

Lawrence Berkeley National Laboratory

LBL Publications

Title

Nuclear Magnetic Resonance Studies of Macroscopic Morphology and Dynamics

Permalink

<https://escholarship.org/uc/item/9487t7tw>

Author

Barrall, G A, Ph.D. Thesis

Publication Date

1995-09-01

Copyright Information

This work is made available under the terms of a Creative Commons Attribution License, available at <https://creativecommons.org/licenses/by/4.0/>



Lawrence Berkeley Laboratory

UNIVERSITY OF CALIFORNIA

Materials Sciences Division

Nuclear Magnetic Resonance Studies of Macroscopic Morphology and Dynamics

G.A. Barrall
(Ph.D. Thesis)

September 1995



REFERENCE COPY
Does Not
Circulate

Bldg. 50 Library.

Copy 1

LBL-37827

DISCLAIMER

This document was prepared as an account of work sponsored by the United States Government. While this document is believed to contain correct information, neither the United States Government nor any agency thereof, nor the Regents of the University of California, nor any of their employees, makes any warranty, express or implied, or assumes any legal responsibility for the accuracy, completeness, or usefulness of any information, apparatus, product, or process disclosed, or represents that its use would not infringe privately owned rights. Reference herein to any specific commercial product, process, or service by its trade name, trademark, manufacturer, or otherwise, does not necessarily constitute or imply its endorsement, recommendation, or favoring by the United States Government or any agency thereof, or the Regents of the University of California. The views and opinions of authors expressed herein do not necessarily state or reflect those of the United States Government or any agency thereof or the Regents of the University of California.

LBL-37827
UC-404

**Nuclear Magnetic Resonance Studies of
Macroscopic Morphology and Dynamics**

Geoffrey Alden Barrall

Department of Chemistry
University of California, Berkeley

and

Materials Sciences Division
Lawrence Berkeley Laboratory
University of California
Berkeley, California 94720

September 1995

This work was supported by the Director, Office of Energy Research, Office of Basic Energy Sciences, Materials Sciences Division, of the U.S. Department of Energy under Contract No. DE-AC03-76SF00098.

Nuclear Magnetic Resonance Studies of Macroscopic Morphology and Dynamics

by

Geoffrey Alden Barrall

B.S. (University of California at Davis) 1990

A dissertation submitted in partial satisfaction of the

requirements for the degree of

Doctor of Philosophy

in

Chemistry

in the

GRADUATE DIVISION

of the

UNIVERSITY of CALIFORNIA, BERKELEY

Committee in charge:

Professor Alexander Pines, Chair

Professor Robert A. Harris

Professor Susan Muller

1995

Abstract

Nuclear Magnetic Resonance Studies of Macroscopic Morphology and Dynamics

by

Geoffrey Alden Barrall

Doctor of Philosophy in Chemistry

University of California at Berkeley

Professor Alexander Pines, Chair

Nuclear magnetic resonance techniques are traditionally used to study molecular level structure and dynamics with a noted exception in medically applied NMR imaging (MRI). In this work, new experimental methods and theory are presented relevant to the study of macroscopic morphology and dynamics using NMR field gradient techniques and solid state two-dimensional exchange NMR. The goal in this work is not to take some particular system and study it in great detail, rather it is to show the utility of a number of new and novel techniques using ideal systems primarily as a proof of principle.

By taking advantage of the analogy between NMR imaging and diffraction, one may simplify the experiments necessary for characterizing the statistical properties of the sample morphology. For a sample composed of many small features, e.g. a porous medium, the NMR diffraction techniques take advantage of both the narrow spatial range and spatial isotropy of the sample's density autocorrelation function to obtain high resolution structural information in considerably less time than that required by conventional NMR imaging approaches. The time savings of the technique indicates that NMR diffraction is capable of finer spatial resolution than conventional NMR imaging techniques.

Radio frequency NMR imaging with a coaxial resonator represents the first use of cylindrically symmetric field gradients in imaging. The apparatus as built has achieved

resolution at the micron level for water samples, and has the potential to be very useful in the imaging of circularly symmetric systems.

The study of displacement probability densities in flow through a random porous medium has revealed the presence of features related to the interconnectedness of the void volumes. The pulsed gradient techniques used have proven successful at measuring flow properties for time and length scales considerably shorter than those studied by more conventional techniques.

Results are presented for the study of particle reorientational dynamics by solid-state two-dimensional exchange NMR. The experimental investigation of rotationally diffusing latex microspheres is presented as an example of the types of classical dynamics accessible by the technique.

**Nuclear Magnetic Resonance Studies of
Macroscopic Morphology and Dynamics**

Copyright © 1995

by

Geoffrey Alden Barrall

The U.S. Department of Energy has the right to use this document
for any purpose whatsoever including the right to reproduce
all or any part thereof

To Noriko and Ivan
(who had to live with me while I wrote this)

Table of Contents

Chapter 1 Introduction	1
Chapter 2 NMR Diffraction	2
2.1 Introduction.....	2
2.2 Basic NMR Theory.....	2
2.3 Magnetic Field Gradients and the Resulting NMR Signal	6
2.4 Slice Selection in NMR Imaging.....	9
2.5 The Imaging Experiment.....	11
2.6 Density Autocorrelation Functions and the Wiener-Khintchin Theorem	13
2.7 Motivation for NMR Diffraction	15
2.8 Historical Background of NMR Diffraction	17
2.9 Principles of NMR Diffraction	19
2.10 Experimental Example of Two-Dimensional NMR Diffraction - Phase Sensitive Detection	19
2.11 Experimental Example of Two-Dimensional NMR Diffraction - Direct Detection of the Diffraction Pattern.....	24
2.12 Dimensionality.....	31
2.12.1 Cylindrical and Spherical Symmetry and the Hankel Transform	32
2.12.2 Noise Effects in Hankel Transforms	37
2.12.3 Application of the Cylindrical Hankel Transform to NMR Diffraction - Theory and Experiment.....	40
2.12.4 Application of the Spherical Hankel Transform to NMR Diffraction - Theory and Experiment.....	44
2.13 Conclusions.....	51
Chapter 3 Radial RF Imaging Using a Coaxial Resonator.....	53
3.1 Introduction.....	53
3.2 Radiofrequency NMR Imaging Theory - Constant Field Gradients	54
3.3 Radiofrequency NMR Imaging - Experimental Methods	56
3.4 The Coaxial Resonator	59
3.5 NMR Imaging with a Coaxial Resonator	62

3.6 Experimental Example of One-Dimensional NMR Imaging with a Coaxial Resonator	65
3.7 Experimental Example of Two-Dimensional NMR Imaging with a Coaxial Resonator - Investigation of Achievable Resolution.....	69
3.8 Conclusions	73
 Chapter 4 Fluid Flow in Porous Media	 74
4.1 Introduction.....	74
4.2 The PGSE Experiment and Position-Displacement Correlations.....	76
4.3 The MSPGSE Experiment.....	79
4.4 Some Aspects of Fluid Flow in Porous Media.....	83
4.4.1 Stochastic Model of Dispersion.....	83
4.4.2 Evidence for Deviations from the Stochastic Dispersion Model for Relatively Short Flow Times	85
4.4.3 The Peclet and Reynolds Numbers.....	87
4.5 Fluid Flow Apparatus	88
4.6 Longitudinal Displacement Distributions of Laminar Fluid Flow in a Pipe.....	91
4.7 Longitudinal Displacement Distributions of Laminar Fluid Flow in a Porous Medium.....	95
4.8 Longitudinal-Transverse Displacement Correlations of Laminar Fluid Flow in a Porous Medium.....	102
4.9 Experimental Measurement of Non-Linear, Longitudinal Variance Evolution	110
4.10 Conclusions.....	114
 Chapter 5 Two-Dimensional Exchange NMR Studies of Particle Reorientational Dynamics	 115
5.1 Introduction.....	115
5.2 Theory - Chemical Shift Anisotropy, Two-Dimensional Exchange NMR and Rotational Diffusion	117
5.2.1 Introduction.....	117
5.2.2 Rotations, Euler Angles and Tensors	117
5.2.3 Chemical Shift Anisotropy	120
5.2.4 NMR Signal from Static Isotropic Samples.....	123
5.2.5 A Word about Probability Densities.....	125

5.2.6	Two-Dimensional Exchange NMR Spectroscopy.....	125
5.2.7	Isotropic Rotational Diffusion	128
5.2.8	Time-Correlation Functions.....	130
5.2.9	Time-Correlation Functions in Two-Dimensional Exchange NMR for the Rotational Diffusion of a Spherical Top	131
5.2.10	Time-Correlation Functions in Two-Dimensional Exchange NMR for the Rotational Diffusion of a Symmetric Top	136
5.3	Simulation of Two-Dimensional Exchange NMR Spectra for the Case of Isotropic Rotational Diffusion	142
5.4	Experimental Example - Isotropic Rotational Diffusion of Latex Spheres in Suspension.....	146
5.4.1	Sample Considerations	146
5.4.2	Preparation of methyl ¹³ C-(carbonyl)-methacrylate	147
5.4.3	Preparation of ¹³ C-(carbonyl)-poly(methyl methacrylate) Microspheres.....	147
5.4.4	Size Characterization of the Latex Microspheres	148
5.4.5	Two-Dimensional Exchange NMR Experiment	150
5.4.6	Experimental Results - Two-Dimensional Exchange NMR of Rotationally Diffusing Latex Microspheres	152
5.5	Conclusions	156
Appendix A Coaxial Resonator Schematics		158
A.1	“Concentric Cylinder” Resonator and Phantom	159
A.2	“Micro-Phantom” Resonator and Phantom.....	173
Appendix B Sample Holder for Fluid Flow in Porous Media Experiments		179
Appendix C Source Code for Rotational Diffusion Simulations.....		185
C.1	Main Program and Internal Subroutines.....	185
C.2	External Subroutines.....	193
C.3	Sample Parameter File.....	202
Bibliography		204

Acknowledgments

Graduate school has been a blast, and now it's time to thank everyone I shared it with. A heartfelt thanks...

To Professor Alexander Pines who gave me the opportunity to work with him and the outstanding group of scientists in his group over the last five years,

To Dr. Gerry Chingas who took me under his wing, and taught me a lot of science you don't find in the books,

To Dr. Young Lee who accompanied me on many a harrowing bike ride and is now freezing his (insert appropriate singular or plural noun) off in Sweden,

To Professor Lucio Frydman who gave me confidence in myself,

To Professor Lyndon Emsley one helluva great softball player and scientist too,

To Dr. Joe Sachleben a great roommate who my other great roommate and I almost killed in the Hoover Wilderness,

To Professor Jay Baltisberger who sparked my interest in softball,

To Professor Jay Shore for being such an amazingly nice guy,

To Professor Klaus Schmidt-Rohr who taught me that it is possible to get a faculty position in less than five minutes,

To all the wonderful people in the Pines' research group that I have had the opportunity to work with who are not listed separately above,

and last of all (not to be confused with *least of all* under any circumstances) to Dione Carmichael who taught me that in *front* of every great professor is an amazing Secretary.

I also want to thank those who have had to put up with me in everyday life and helped me to stay sane in graduate school: my mom and dad, my wife Noriko, my brother and sister, Maryann, Isabel, my cat Ivan, and my roommates over the years Matthew Fishencord, Sara Bloom, David Andres, Joe Sachleben (see above), and James Batteas.

And a special thanks to the Director, Office of Basic Energy Sciences, Materials Sciences Division, and the Director, Office of Health and Environmental Research, Health Effects Research Division, of the U.S. Department of Energy under contract No. DE-AC03-76SF00098 who selflessly supported this research.

Chapter 1 Introduction

Nuclear magnetic resonance (NMR) techniques are generally associated with the study of molecular dynamics, molecular structure and chemical determination. This association is understandable as NMR has proven to be an invaluable tool in the investigation of these fields. This work, however, does not involve the study of molecular level structure and dynamics. On the contrary, the NMR techniques, experiments and theory presented here are directed at the investigation of macroscopic (i.e. much larger than the molecular level) morphology and dynamics. By this, I mean that the phenomena of interest are purely classical, although the origin of the NMR signal is most definitely quantum mechanical in nature^{1,2}.

The various chapters of this thesis are united under this theme, but the approach used in each case is rather different. In order to avoid confusion, the relevant theory for each chapter will be presented with that chapter, as this work will cover a large range of sometimes related and sometimes unrelated topics. The next three chapters are arranged in such a way that much of the theory discussed in the previous sections will be required in order to understand the theory of the following sections. This ordering is actually purely coincidental as the chapters are presented in the chronological order of my research in the different areas.

Chapter 2 NMR Diffraction

2.1 Introduction

Before proceeding with a description of what NMR Diffraction is and why one would want to do it, I will proceed to lay out the basic theory for NMR and NMR imaging as well as a few areas unrelated to NMR but relevant to the understanding of NMR diffraction. For NMR Diffraction and the topics covered in the following two chapters, it is only necessary to consider the dynamics of spin-1/2 nuclei, as the nucleus from which the NMR signal originates is the hydrogen nucleus (protons) present in water. The basic NMR theory presented here is in no way a complete description of the dynamics of spin-1/2 nuclei, but it provides a basis for understanding NMR diffraction and a means of developing a coherent notation. The same may also be said for the NMR imaging theory presented. For a more complete description of spin dynamics as it relates to NMR imaging, I suggest the recently published NMR microimaging book by Callaghan³ as well as the text by Mansfield and Morris⁴ which concentrates more on the medical applications of imaging.

2.2 Basic NMR Theory

The dynamics of isolated spin-1/2 nuclei may be viewed classically, and for NMR field gradient experiments, this viewpoint is very often sufficient. In this case, we may treat the magnetization in a macroscopic sample as a classical magnetization vector, $\mathbf{M} = (M_x, M_y, M_z)$, as opposed to the quantum mechanical case where the same entity would be regarded as an ensemble of spin-1/2 states.

The equation of motion for the classical magnetization vector is

$$\frac{d\mathbf{M}}{dt} = \gamma \mathbf{M} \times \mathbf{B}, \quad (2.1)$$

where we have equated the rate of change of angular momentum to the torque applied to the system. If \mathbf{B} is the static magnetic field in the z direction, the solution of Eq. (2.1) corresponds to precession of the transverse magnetization about B_0 at the Larmor frequency. Application of a radio frequency (rf) field perpendicular to B_0 given by

$$\mathbf{B}_1 = B_1(\cos(\omega_{rf}t)\hat{i} - \sin(\omega_{rf}t)\hat{j}), \quad (2.2)$$

leads to

$$\begin{aligned} \frac{dM_x}{dt} &= \omega_0 M_y + \omega_1 M_z \sin(\omega_{rf}t), \\ \frac{dM_y}{dt} &= \omega_1 M_z \cos(\omega_{rf}t) - \omega_0 M_x, \\ \frac{dM_z}{dt} &= -\omega_1 M_x \sin(\omega_{rf}t) - \omega_1 M_y \cos(\omega_{rf}t). \end{aligned} \quad (2.3)$$

The vectors \hat{i} , \hat{j} and \hat{k} are the unit vectors in the x , y and z directions, respectively, and $\omega_1 \equiv \gamma B_1$. For $\omega_{rf} = \omega_0$ and $\mathbf{M}(t=0) = M_0 \hat{k}$ the solution to Eq. (2.3) is

$$\begin{aligned} M_x &= M_0 \sin(\omega_1 t) \sin(\omega_0 t) \\ M_y &= M_0 \sin(\omega_1 t) \cos(\omega_0 t) \\ M_z &= M_0 \cos(\omega_1 t) \end{aligned} \quad (2.4)$$

In the frame of reference rotating about the static field at the frequency ω_0 (the rotating frame), the magnetization is effectively rotating about the rf field at the frequency ω_1 . After the application of a pulse for which $\omega_1 = \pi/2$, the laboratory frame magnetization is given by

$$\mathbf{M}(t) = M_0(\cos(\omega_0 t)\hat{i} + \sin(\omega_0 t)\hat{j}). \quad (2.5)$$

This may be written in complex notation as

$$M(t) = M_0 \exp(i\omega_0 t). \quad (2.6)$$

This precessing magnetization produces an alternating current in the excitation/receiver coil of the NMR probe. In general, we detect the signal with respect to a reference frequency ω which is offset from the Larmor precession frequency by an amount $\Delta\omega$, which ranges from zero to thousands of Hertz for the experiments presented in this work. Furthermore, the detection may be out of phase with the NMR signal by an amount ϕ . The resulting complex NMR signal may be written

$$S(t) = S_0 \exp(i\phi + i\Delta\omega t), \quad (2.7)$$

where S_0 is the signal at time zero, which is an arbitrary quantity depending upon the electronics of the detection system and the total transverse magnetization of the sample. For the sake of simplicity, we will often ignore ϕ and S_0 as they will have little or no effect upon the basic meaning of the results.

The nonequilibrium magnetization which has been rotated into the xy plane, experiences two relaxation processes which cause the magnetization to return to equilibrium and to dephase in the xy plane itself. In a strong static field, B_0 , equilibrium is characterized by a state of polarization with the magnetization M_0 aligned with B_0 . The return to equilibrium is usually referred to as spin-lattice or T_1 relaxation and, as the former name implies, involves the exchange of energy between the spin system and surrounding thermal reservoir or lattice. Spin-lattice relaxation is assumed to be a first order process and is described by the phenomenological equation

$$\frac{dM_z}{dt} = \frac{-(M_z - M_0)}{T_1}, \quad (2.8)$$

with the solution

$$M_z(t) = M_z(0)\exp\left(-\frac{t}{T_1}\right) + M_0\left(1 - \exp\left(-\frac{t}{T_1}\right)\right). \quad (2.9)$$

T_1 is referred to as the spin-lattice relaxation time and is typically a few seconds for protons in water.

The transverse relaxation or dephasing of the magnetization in the xy plane is caused by the nuclear spins approaching thermal equilibrium among themselves and is referred to as spin-spin or T_2 relaxation. Spin-spin relaxation can as well be described as a first order relaxation process given by

$$\frac{dM_x}{dt} = -\frac{M_x}{T_2}, \quad (2.10a)$$

$$\frac{dM_y}{dt} = -\frac{M_y}{T_2} \quad (2.10b)$$

with the solutions

$$M_x(t) = M_x(0)\exp\left(-\frac{t}{T_2}\right), \quad (2.11a)$$

$$M_y(t) = M_y(0)\exp\left(-\frac{t}{T_2}\right). \quad (2.11b)$$

T_2 is referred to as the spin-spin relaxation time and is shorter than or equal to the spin-lattice relaxation time.

Equations (2.3), (2.8), (2.10a) and (2.10b) may be combined to yield the Bloch equations⁵ which provide a complete description of the classical spin dynamics.

We are primarily interested in relaxation effects which will in some way limit the types of NMR experiments we can perform, as opposed to utilizing relaxation information in an analysis of some molecular system. As we shall see, T_2 relaxation often limits the achievable spatial resolution, and T_1 relaxation limits the frequency of signal averaging. When we begin to study fluid dynamics, we shall see that T_1 relaxation limits the time over which we may observe mass transport, since the T_1 of our tap water is approximately 3 s. The removal of impurities such as oxygen from the tap water increase T_1 to approximately 10 s, but for the sake of convenience, we have decided to just use ordinary and easily available tap water.

2.3 Magnetic Field Gradients and the Resulting NMR Signal

A static magnetic field gradient which can be described by

$$\vec{G} = \begin{bmatrix} \frac{\partial B_x}{\partial x} & \frac{\partial B_x}{\partial y} & \frac{\partial B_x}{\partial z} \\ \frac{\partial B_y}{\partial x} & \frac{\partial B_y}{\partial y} & \frac{\partial B_y}{\partial z} \\ \frac{\partial B_z}{\partial x} & \frac{\partial B_z}{\partial y} & \frac{\partial B_z}{\partial z} \end{bmatrix} \quad (2.12)$$

provides the means of spatially resolving the spin magnetization in the sample. If the static field is much larger than the field gradient producing field, only variations in B_z need be considered, as any effects due to a small static field perpendicular to \mathbf{B}_0 will be averaged out. The field gradient tensor then is effectively reduced to a vector.

$$\mathbf{G} = \left(\frac{\partial B_z}{\partial x}, \frac{\partial B_z}{\partial y}, \frac{\partial B_z}{\partial z} \right) \quad (2.13)$$

Applying a magnetic field gradient in the presence of a large homogeneous static field produces a local Larmor precession frequency given by

$$\begin{aligned}\omega(\mathbf{r}) &= \gamma B_0 + \gamma \mathbf{G} \cdot \mathbf{r}, \\ \text{where } \mathbf{r} &= (x, y, z).\end{aligned}\tag{2.14}$$

For a volume element dV located at point \mathbf{r} with magnetization density $\rho(\mathbf{r})$ (Assuming the magnetization density reflects the sample density of interest, the terms magnetization density and sample density will be used interchangeably), the complex signal arising in the presence of the field gradient is given by

$$dS(\mathbf{r}, t) = \exp(i\gamma \mathbf{G} \cdot \mathbf{r} t) \rho(\mathbf{r}) dV,\tag{2.15}$$

if the signal is acquired with respect to ω_0 or on resonance. The total signal arising from the entire sample is given by the integral over all of the individual signal elements in Eq. (2.15).

$$S(t) = \int \rho(\mathbf{r}) \exp(i\gamma \mathbf{G} \cdot \mathbf{r} t) d\mathbf{r},\tag{2.16}$$

where the integration proceeds over all space. From Eq. (2.16), we see that the signal is simply related to the density or image of the sample by a three-dimensional Fourier transform⁶ with respect to the conjugate variables $(\gamma \mathbf{G} t, \mathbf{r})$.

For the sake of notational simplicity, we will make the substitution

$$\mathbf{k} \equiv \gamma \mathbf{G} t,\tag{2.17}$$

where \mathbf{k} is referred to as the reciprocal space or k-space vector, and restate the Fourier relationship between the signal and the sample density in terms of the k-space vector⁷.

$$S(\mathbf{k}) = \int \rho(\mathbf{r}) \exp(i\mathbf{k} \cdot \mathbf{r}) d\mathbf{r} \quad (2.18a)$$

$$\rho(\mathbf{r}) = \frac{1}{2\pi} \int S(\mathbf{k}) \exp(-i\mathbf{k} \cdot \mathbf{r}) d\mathbf{k}, \quad (2.18b)$$

where the integration proceeds from $-\infty$ to $+\infty$ for all of the components of \mathbf{r} in Eq. (2.18a), whereas in Eq. (2.18b) the integration proceeds from $-\infty$ to $+\infty$ for all of the components of \mathbf{k} . The leading term $1/2\pi$ in Eq. (2.18b) has little relevance in the context of an actual imaging experiment and may be ignored with no loss of generality.

In an actual NMR experiment, the data is acquired over a limited range in \mathbf{k} and at discrete intervals, so Eq. (2.18a) and (2.18b) should be interpreted as discrete Fourier transforms for which there exists a simple relation between the range and resolution in both spaces. For example, the range and resolution of the conjugate pair (x, k_x) are related by

$$\begin{aligned} \text{resolution}(x) = \delta x &= \frac{2\pi}{\text{range}(k_x)}, \\ \text{resolution}(k_x) = \delta k_x &= \frac{2\pi}{\text{range}(x)}. \end{aligned} \quad (2.19)$$

The factor of 2π arises because k_x is measured in radians per unit length. In the specific case of an experiment using an x gradient where N points are acquired in the time domain,

$$\delta x = \frac{2\pi}{N\delta k_x}. \quad (2.20)$$

When performing an imaging experiment, the consequences of Eq. (2.20) are very important. If we choose too large a value for δk_x , i.e. we choose a range which is actually smaller than the spatial extent of the sample, the image will be severely distorted due to aliasing⁶. If on the other hand, we choose too small a value for δk_x , the image resolution will be inadequate for that particular experiment.

2.4 Slice Selection in NMR Imaging

The majority of the images which will be presented here are two-dimensional, but they are derived from three-dimensional samples. In order to avoid having to acquire the entire three-dimensional time domain data set, one may selectively excite a plane in the sample using a frequency selective rf pulse^{3,8-11} in the presence of a static field gradient, where the selective pulse is composed of an on-resonance rf field modulated by a lower frequency envelope of finite duration. The resulting signal will represent only the magnetization from the selected plane or slice, hence the term slice selection. In the following discussion of frequency selective rf pulses, we will assume that the response of the magnetization is linear implying a frequency response equal to the Fourier transform of the applied rf.

A delta function (in time) or “hard” pulse excites resonances at all frequencies, since a delta function is equally composed of all frequencies, whereas a pulse with a finite duration will excite a finite range of frequencies determined by the Fourier response of the pulse. A sinc pulse as used in this work, Fig. (2.1), has an approximately square frequency response, so a well defined frequency range with a sharp cutoff is selected. Since the sinc pulse is not centered about zero time in a real experiment, the magnetization produced is not in phase. Application of a refocussing gradient of equal and opposite strength to the slice selection gradient for a time equal to one half the duration of the rf pulse refocusses the dephased magnetization¹⁰. The refocussing is equivalent to doing a first order (frequency or spatially dependent) phase correction of the magnetization.

For large tilt angles the NMR response is not linear, so the excitation profile will deviate from that predicted by the Fourier transform of the rf pulse^{9,10}. For our purposes, however, the pulses perform well, so we will maintain the assumption that the response is linear.

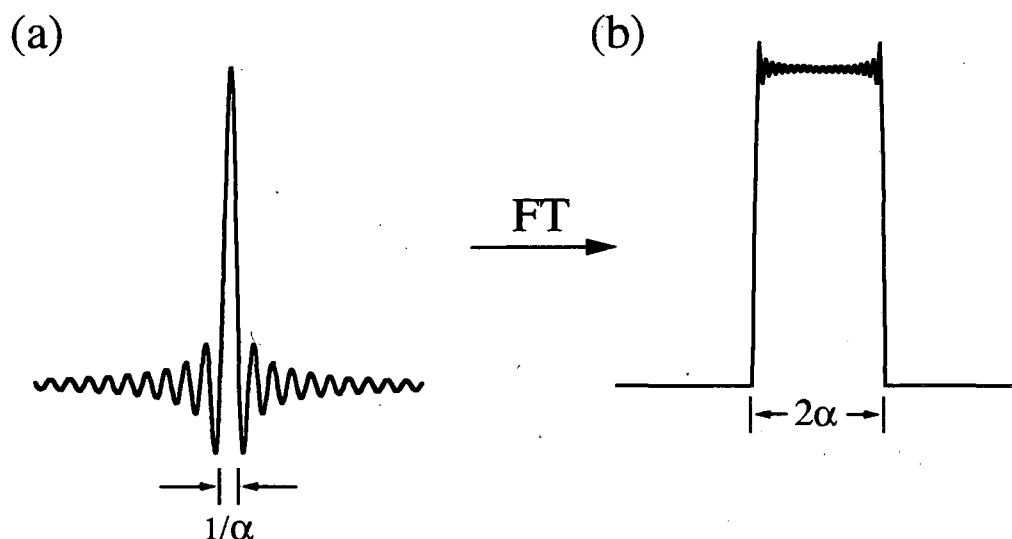


Figure 2.1 Frequency response of a sinc function. The time, frequency and amplitude scales are arbitrary. (a) A sinc function, $\sin(2\pi\alpha t)/(2\pi\alpha t)$, plotted with respect to t . The width $1/\alpha$ denotes the time between zero crossings. (b) Discrete fast Fourier transform of (a). The analytical Fourier transform of the sinc function is a perfect hat or square function, without the high frequency oscillations at either edge. The oscillations are known as the Gibbs phenomenon.

2.5 The Imaging Experiment

An example of a two-dimensional NMR imaging pulse sequence is shown in Fig. (2.2). The selective rf pulse confines the region of interest to a slice in the yz plane within the rf coil. During the interval τ , the read gradient pulse allows the acquisition of an echo, and simultaneously, a variable amount of phase equal to $\gamma G_z \tau$ is encoded along the z direction. In order to acquire the signal necessary to generate the yz image of the slice, a series of N experiments (or excitations) are performed where G_z is incremented in steps δG_z from $(N/2)\delta G_z$ to $-(N/2-1)\delta G_z$.

A graphical representation of the acquired phase in k -space, Fig. (2.3), after the refocussing pulse provides a good picture of what is happening during the experiment. During the time τ , a constant amount of phase $-\gamma G_y \tau$ is encoded along the y direction, whereas a variable amount of phase is encoded along the z direction. This portion of the experiment is referred to as the phase encode period and is represented by the dashed lines

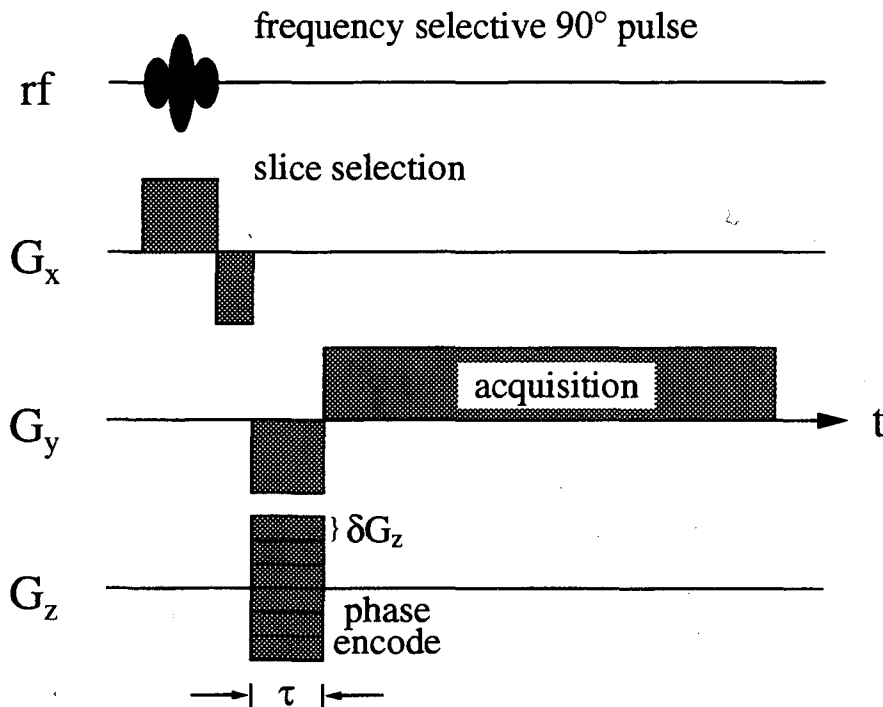


Figure 2.2 Example of a two-dimensional NMR imaging pulse sequence. Slice selection along x allows the acquisition of a 2D image in a 2D experiment. The acquired data is the Fourier transform of a map of the magnetization density in the selected yz plane.

in Fig. (2.3). During acquisition, the phase along y is constantly evolving and the signal is composed of the sum over the frequency contributions from all of the volume elements, Eq. (2.18a), hence the term frequency encoding. Two-dimensional Fourier transformation of the k -space data set yields an image of the magnetization density in the sample.

If one looks at the imaging experiment from the point of view that a certain region of k -space needs to be sampled with some specified resolution in order to obtain an image with the appropriate range and resolution, it is obvious that any imaging scheme will work as long as k -space is appropriately sampled. For example, the reversal in direction of the k -space trajectory along k_y in Fig. (2.3) may be accomplished by either using y gradients of opposite signs as in Fig. (2.2) (one for the phase encoding and one for frequency encoding) or using y phase encode and frequency encode gradients with the same sign

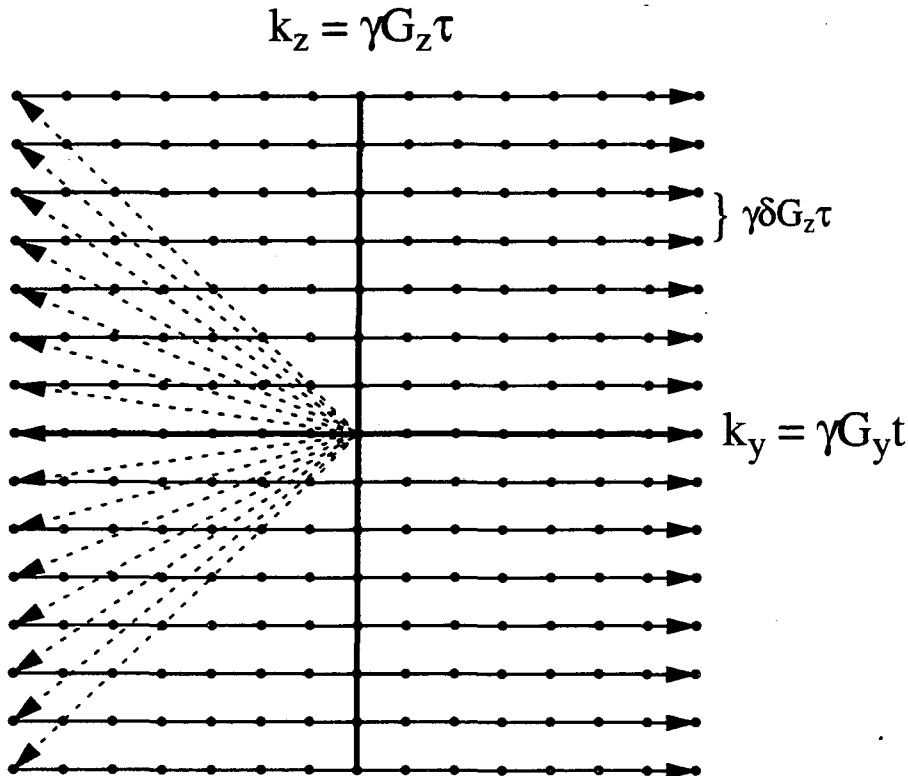


Figure 2.3 Traversal of k -space for the imaging experiment in Fig.(2.2). The phase encode period is represented by the dashed lines, whereas the frequency encode period is represented by solid lines. Data points are acquired at each •.

with a rf π -pulse between the two. Furthermore, the sampling of k-space need not be confined to sampling a Cartesian grid^{3,7,12,13}, but no matter the sampling strategy, a means is required of transforming the acquired data from the time domain to the spatial domain.

If only a one-dimensional experiment is performed (i.e. no G_z), the acquired signal will be the Fourier transform of the projection of the sample density onto the y axis given by

$$\rho_z(y) = \int_{-\infty}^{\infty} \rho(y,z) dz, \quad (2.21)$$

where the subscript z denotes a projection along the z axis, and the sample density is assumed to be two-dimensional. The integration is written as proceeding from $-\infty$ to ∞ , but in actuality one need only consider the integration over the spatial extent of the sample within the coil. In the absence of slice selection, the same experiment yields the projection of the three-dimensional sample density along both the x and z axes onto the y axis, which we shall denote $\rho_{xz}(y)$.

Under certain circumstances, the projection contains all of the information which is required of the experiment, and as will be shown later, in the presence of the appropriate symmetry, one may completely reconstruct the two or three-dimensional sample density from a single projection.

2.6 Density Autocorrelation Functions and the Wiener-Khintchin Theorem

A density image shows the spatial variation of the sample density $\rho(\mathbf{r})$, whereas the density autocorrelation function, $\Phi(\Delta\mathbf{r})$, of the same sample is a measure of how well the sample density comes back into registration with itself when displaced by $\Delta\mathbf{r}$. Alternatively, $\Phi(\Delta\mathbf{r})$, may be viewed as the density encountered $\Delta\mathbf{r}$ from some starting

point weighted by the density at the starting point averaged over all initial positions. Given $\rho(\mathbf{r})$, $\Phi(\Delta\mathbf{r})$ may be determined from the relation,

$$\begin{aligned}\Phi(\Delta\mathbf{r}) &= \int_{\text{all space}} \rho(\mathbf{r})\rho(\mathbf{r} + \Delta\mathbf{r}) d\mathbf{r} \\ &= \langle \rho(\mathbf{r})\rho(\mathbf{r} + \Delta\mathbf{r}) \rangle.\end{aligned}\tag{2.22}$$

In this chapter, angular brackets $\langle \rangle$ denote an average over \mathbf{r} taken within the sample volume. We will see in the next section what relevance $\Phi(\Delta\mathbf{r})$ has to NMR diffraction.

The autocorrelation theorem⁶ often referred to as the Wiener-Khintchin theorem^{14,15} provides an alternative means of obtaining $\Phi(\Delta\mathbf{r})$ from $\rho(\mathbf{r})$. If $S(\mathbf{k})$ is the Fourier transform of $\rho(\mathbf{r})$, then the autocorrelation function of $\rho(\mathbf{r})$ given in Eq. (2.22) is the inverse Fourier transform of $|S(\mathbf{k})|^2$.

$$\Phi(\Delta\mathbf{r}) = \frac{1}{2\pi} \int |S(\mathbf{k})|^2 \exp(-i\mathbf{k} \cdot \Delta\mathbf{r}) d\mathbf{k}.\tag{2.23}$$

The autocorrelation theorem is in fact a special case of the convolution theorem, for which a proof is given in Bracewell⁶.

2.7 Motivation for NMR Diffraction

The properties of many materials are governed by small-scale, morphological features, such as domain boundaries and pores, whose size and distribution are more significant than precise spatial location. Because material structural information resides at short length scales in small, signal-poor regions, applications of NMR imaging to materials have not had the spectacular success of medical applications.

Using NMR imaging to characterize such materials is complicated by the fact that in order to image the entire sample and still resolve small features the image must have very fine resolution over a relatively large spatial range. Acquiring such an image is complicated by two important factors. In the first place, the signal must be acquired over a very large frequency range, since it is not possible to achieve a frequency resolution finer than that dictated by line broadening due to T_2 relaxation and inhomogeneities in the static field. For hydrogen nuclei in water which have a long transverse relaxation time, the latter broadening effect usually dominates due to susceptibility effects produced by the sample and the surrounding probe. As we see from the dependence of the signal to noise ratio on the bandwidth of the receiver^{16,17},

$$\frac{S}{N} \propto \left(\frac{1}{\Delta f} \right)^{\frac{1}{2}}, \quad (2.24)$$

a large receiver bandwidth implies a low signal to noise ratio. Equation (2.24) is obvious since the noise power is independent of frequency and the integrated signal intensity from the sample is a constant. As the bandwidth is increased, more noise is acquired, but the same total amount of signal is still present from the sample. The second difficulty lies in the size of the dataset which must be acquired and the amount of time necessary to acquire the data. If the sample consists of objects which are 1000 times smaller than the sample itself (along one dimension), and if we assume that at least three points are needed along

each dimension to define a resolved object, then a two-dimensional image requires a dataset with at least 3000x3000 points. For a T_1 relaxation time of 1 s, acquisitions should be taken 5 s apart in order to allow the magnetization to return to equilibrium. At a 5 s repetition rate, the image described above would require over four hours to be acquired. For equal sized samples which contain smaller particles, the time required for the experiment becomes considerably larger.

The optimal technique extracts the minimum amount of desired information from the sample without having to acquire the entire image. For the types of materials described above, one may be satisfied with the density auto-correlation function of the sample, since collective properties are often more succinctly described and more easily observed using such a statistical approach. As will be shown later, NMR Patterson functions (density autocorrelation functions) are analogous to the density autocorrelation functions of X-ray diffraction¹⁸, except that nuclear rather than electronic density provides contrast, and resolution is determined by magnetic field gradient strength rather than X-ray wavelength.

Two main benefits accrue. First, the number of data points required for a statistical description (e.g. the density autocorrelation function) is much smaller than for imaging. Although spatial resolution considerations are similar for both diffraction and imaging, the density of data points which determines the extent of the spatial "window" is quite different: as stated above, the image must show the entire sample, but the Patterson function is often appreciable only over several small feature lengths. Hence the required number of points is reduced by approximately the number of features in the sample, which approaches astronomical values for microscopic features in a bulk sample. Further reductions are possible for the important class of spatially isotropic systems, where it will be shown that full statistical information is available for two and three-dimensional isotropic structures from a single one-dimensional projection. In addition, tighter signal filtering and more efficient signal averaging can be applied to increase sensitivity.

Second, with statistical characterization, experimental repeatability is possible even for re-arranging systems. For example, it is impossible to repeat imaging experiments for noise suppression or multi-dimensional purposes for particles undergoing Brownian motion, since the "image" is constantly changing. On the other hand, so long as the system *statistics* remain stationary from one scan to the next, and motion during each acquisition is negligible, repeatability of *statistical* measurements is entirely feasible. To date, an experimental example of this approach has not been demonstrated.

2.8 Historical Background of NMR Diffraction

During early development of nuclear magnetic resonance imaging (MRI) in the 1970's, Mansfield and co-workers explored analogies between scattering amplitudes and NMR signals, and even considered determination of individual nuclear positions from NMR¹⁹⁻²³. Hence the potential of NMR for providing information on the statistics of biological and material microstructures, *for static systems*, was considered nearly two decades ago, although at the time it was set aside in favor of the more direct imaging approach²³.

Structural studies based on *mobility* developed even earlier using gradient echo methods^{24,25}, especially the pulsed-gradient spin echo (PGSE) experiment developed by Stejskal et al.^{26,27} This method not only measures diffusion coefficients, but also provides information on microstructures in the host material when boundaries hinder normal diffusive transport.

In 1983, Kärger and Heink directly obtained the distribution $P(\Delta\mathbf{r}, t)$ of displacements $\Delta\mathbf{r}$ which occurred during a transport time t , by Fourier transforming the PGSE data as a function of magnetic field gradient strength²⁸; the PGSE experiment, position displacement distributions and q-space will be explored in greater detail in Chapter 4. Recently, Cory and Garroway²⁹ demonstrated that for transport times so long that initial and final particle positions become uncorrelated, the distribution $P(\Delta\mathbf{r}, t)$

approaches the fluid density autocorrelation function of the particle container (or an average of such functions when the system consists of an ensemble of such containers). They illustrated this principle for water in yeast cells, inferring the cell size of 5 μm directly from the displacement profile. They also realized that the data, regarded as a function of the gradient strength, is equivalent to that from a diffraction experiment, except that the diffraction "wavevector" is given by gradient pulse strength $\mathbf{q} = \gamma \mathbf{G} \tau$ instead of the momentum transfer $\Delta \mathbf{k}$ appearing in scattering theory³⁰. Here γ is the magnetogyric ratio of the observed nuclear species, \mathbf{G} is the pulsed magnetic field gradient vector, and τ is the duration of each of the pair of magnetic field gradient pulses used in a PGSE experiment. Callaghan et al. have developed this analogy further for porous systems³¹, and have presented data showing an unusual *increase* of the signal amplitude with increasing gradient strength³²⁻³⁴, analogous to Debye-Scherrer rings in crystallography³⁰. Invoking statistical isotropy for their system of 16 μm polystyrene beads immersed in water, they extended data taken along a single direction in q -space to a spherically symmetric three-dimensional function. A three-dimensional Fourier transformation extracted the radial density autocorrelation distribution characteristic of the beads in the sample. These developments (which we shall refer to as diffusive diffraction to avoid confusion with the existing area of X-ray dynamic diffraction³⁰) have been reviewed by Cotts³⁵.

Pulsed gradient methods in general are a powerful way of characterizing systems where diffusion is affected by internal structure. Nevertheless, whether diffractive aspects are considered or not, this technique becomes inapplicable when transport is too slow, fails to reflect structure, or is entirely absent. We now show that structural information related to diffractive principles is still available for stationary objects, based directly on density variation^{36,37}.

2.9 Principles of NMR Diffraction

From Eq. (2.23), it is immediately obvious that the density autocorrelation function is simply related to the time-domain NMR imaging signal. The modulus squared of the time-domain signal, $|S(\mathbf{k})|^2$, is therefore a diffraction pattern of sorts defined by the magnetic field gradient strength. As Mansfield recognized, the nonlinear processing associated with squaring the signal modulus suppresses signal phase and makes image reconstruction impossible²³. Eq. (2.23) shows, however, that the remaining amplitude modulated component extracts statistical information from the original imaging data in a manner analogous to conventional scattering experiments³⁸.

Determining $\Phi(\Delta\mathbf{r})$ from the two-dimensional imaging signal, $S(\mathbf{k})$, using Eq. (2.23) is essentially an image processing step. One can just as easily determine $\Phi(\Delta\mathbf{r})$ from the two-dimensional image $\rho(\mathbf{r})$ using Eq. (2.22). However, as was stated above, far fewer points need be acquired and a considerably smaller receiver bandwidth is necessary for the direct acquisition of $|S(\mathbf{k})|^2$. Experimental examples of both NMR diffraction methods are presented below.

2.10 Experimental Example of Two-Dimensional NMR Diffraction - Phase

Sensitive Detection

We will begin with an experimental example where the density autocorrelation function and the diffraction pattern, $|S(\mathbf{k})|^2$, are determined from the phase sensitive time domain data, $S(\mathbf{k})$. Two-dimensional results of this method are presented in Fig. (2.4). The two phantoms consist of 7 mm I.D. glass tubes into which are packed nylon monofilament fibers (fishing line) of diameter 0.56 mm and 0.33 mm. The tubes are filled with water to provide a proton NMR signal from the interstitial volume.

Imaging data is taken on a Nalorac Cryogenics Quest 4400 spectrometer operating at a proton frequency of 185 MHz. The NMR probe contains a cylindrical gradient set which is capable of producing, with the amplifiers used, 0.65 T/m static field gradients in

all three dimensions (for protons this corresponds to a maximum frequency encoding strength of ~ 28 kHz/mm). The gradient in the z direction is produced by a Maxwell pair³⁹, and the gradients in the x and y directions are produced by quadrupolar coils^{40,41}. The employed spin-warp imaging sequence⁴², c.f. Fig. (2.2), utilizes a sinc modulated rf pulse which selects a transverse slice fully confined to the interior of the rf coil. For the experimental data presented here, a slice of 0.5 mm was selected using a 2 ms, eight-lobed sinc pulse. In terms of the sinc pulse diagrammed in Fig. (2.1), a nine-lobed pulse has a duration of $8/\alpha$.

The unprocessed two-dimensional k -space data consists of complex numbers, has a rapid phase variation, and is not shown, but the derived density images of $\rho(\mathbf{r})$ in Fig. (2.4a) and Fig. (2.4d), each 128 pixels on a side, confirm that the imaging signals $S(\mathbf{k})$ for the phantoms were correctly acquired, and that diffusive and convective motions which produce image distortions are negligible.

Figures (2.4b) and (2.4e) show $|S(\mathbf{k})|^2$, the phase-suppressed imaging data, for each of the two filament sizes. These are the NMR "diffraction patterns", defined in a k -space of spatial frequencies with a range of approximately ± 8 cycles/mm. The diffraction patterns show rings similar to those from powder X-ray diffraction patterns of granular structures, indicating an underlying regularity in the fiber separation³⁰.

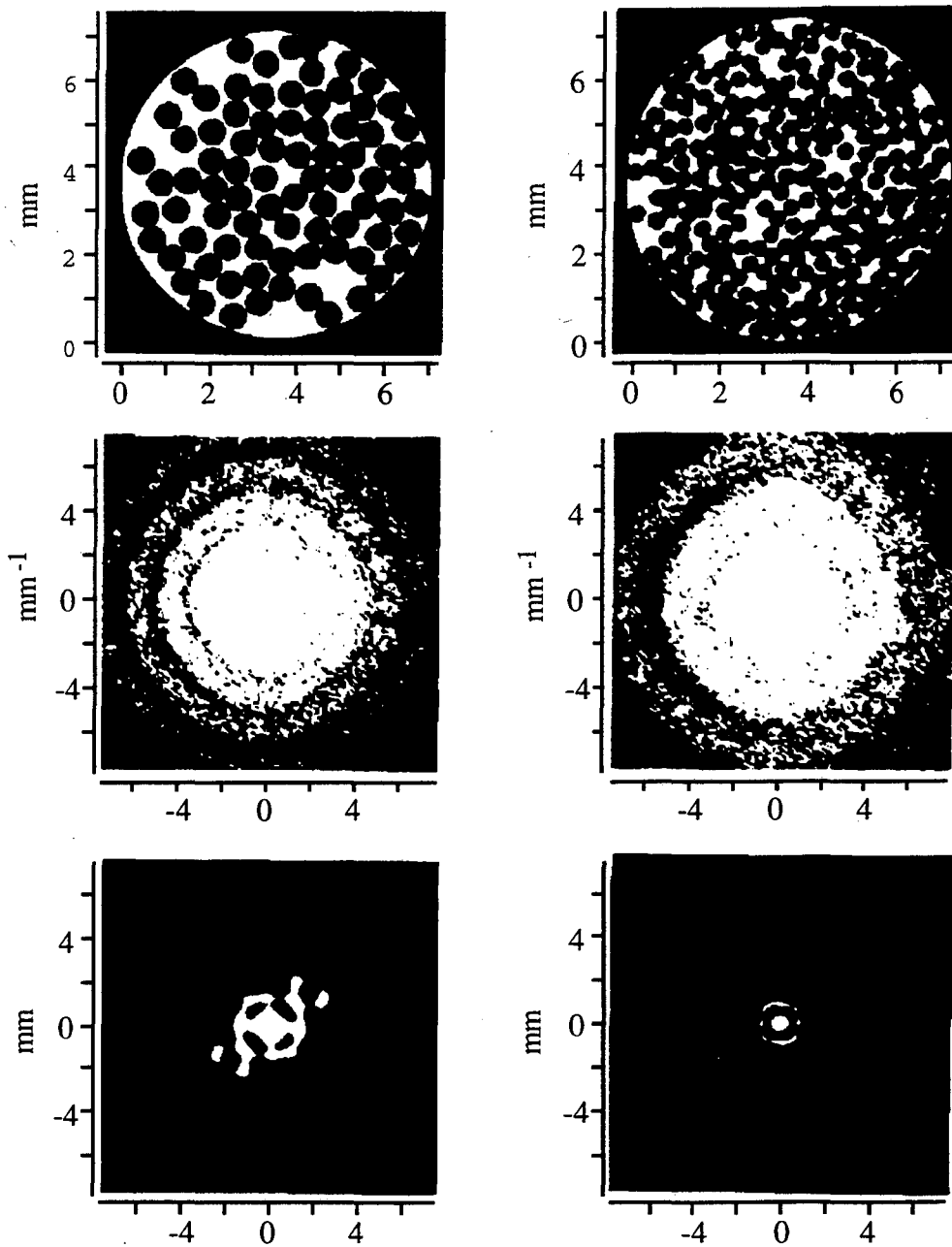


Figure 2.4 (A) Image, (B) diffraction pattern, and (C) Patterson function for 0.56 mm diameter fibers immersed in water in a 7 mm tube. The image shown in (A) is derived by Fourier transformation of NMR data, whose square modulus, the NMR "diffraction pattern", shown in (B) reflects packing statistics. Fourier transformation of the diffraction pattern yields the Patterson function shown in (C). (D) Image, (E) diffraction pattern, (F) and Patterson function for 0.33 mm diameter fibers, to be compared directly with (A) to (C).

The Fourier transform of the diffraction data yields the density autocorrelation function of the volume filled by the water, since the water contributes the NMR signal. It is perhaps easier to envision the density autocorrelation function of the fibers (disks) as the interstitial voids are irregularly shaped. If we express the spatially varying water density $\rho(\mathbf{r})$ as $\rho_0 - \eta(\mathbf{r})$, where ρ_0 is the density of uniform water and $\eta(\mathbf{r})$ the density distribution of *excluded* water occupied by the fibers, the water and fiber Patterson functions are related by

$$\begin{aligned} \langle \rho(\mathbf{r})\rho(\mathbf{r} + \Delta\mathbf{r}) \rangle &= \langle [\rho_0 - \eta(\mathbf{r})][\rho_0 - \eta(\mathbf{r} + \Delta\mathbf{r})] \rangle \\ &= \langle \eta(\mathbf{r})\eta(\mathbf{r} + \Delta\mathbf{r}) \rangle - 2\rho_0\langle \eta(\mathbf{r}) \rangle + \rho_0^2. \end{aligned} \quad (2.25)$$

The last two terms in Eq. (2.25) are constants with respect to $\Delta\mathbf{r}$, so the correlation functions for the fibers and the water filled regions are equal apart from a constant offset. Mansfield and Grannell²² have also discussed this point in terms of Babinet's principle⁴³.

The actual Patterson functions shown in Fig. (2.4c) and (2.4f), obtained by Fourier transforming the diffraction data of Fig. (2.4b) and (2.4e) respectively, are shown on the same scale as their respective images Fig. (2.4a) and (2.4d). The contraction of data toward the origin indicates that the fiber arrangement is ordered over a range much shorter than the image size, consistent with the random packing. The Patterson functions exhibit strong central peaks which are autocorrelations of each fiber with itself; as expected, the diameter of the base of the central peak in each case is approximately two fiber diameters. A low-signal region which indicates the excluded volume between fibers surrounds this peak, and further out, a ring appears which reflects the average separation of the centers of nearest neighbors.

The symmetry and prominence of the nearest-neighbor rings demonstrate the isotropy and short-range order of the packing statistics. The rings occur at ~ 0.7 and ~ 0.45 mm respectively for the 0.56 and 0.33 mm fibers. The location of the nearest

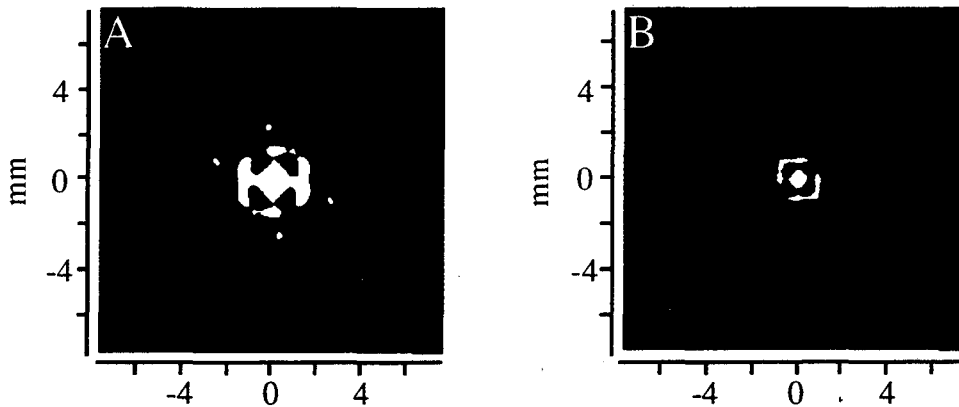


Figure 2.5 Patterson functions for rotated samples. (A) and (B) correspond, respectively, to Fig. (2.4c) and (2.4f) having been obtained from samples rotated 45° from the latter. Although the small fiber data have few features that noticeably follow the rotation, the large fiber data have secondary peaks which do; the latter are attributed to accidental long-range order arising from finite sampling statistics.

neighbor ring gives information about how close the fibers are spaced, but one is not necessarily able to get a good value for the fiber packing fraction. In order to determine a packing fraction from the location of the nearest neighbor rings, one must assume a model for the placement of the fibers within the sample.

To distinguish artifacts from correlations, we repeated the experiments after rotating each sample about the tube axis by approximately 45° ; results shown in Fig. (2.5a) and (2.5b) may be compared with Fig. (2.4c) and (2.4f). The patterns' inversion symmetry about $\Delta r = 0$ follows from their being Fourier transforms of real data. Several features of the large-fiber figures rotate with the sample, notably the large diagonal background swath and two pairs of peaks just outside the nearest-neighbor ring. These features therefore represent true anisotropy and long-range order, appearing here because of the finite statistics of the relatively small number of fibers. This conclusion is borne out by the lack of similar rotated structures for the small fiber data of Fig. (2.5b) and (2.4f), which reflect the statistics of a larger population. On the other hand, the "squareness" of the nearest-neighbor ring, the slightly diamond-shaped pattern of the central peak, and the cross-like bridges between these two structures remain fixed, and therefore must reflect processing

and/or noise artifacts. These latter features persist even when Gaussian apodization is applied to $|S(\mathbf{k})|^2$, ruling out truncation effects as the origin of the artifacts. It is possible that these artifacts represent a correlation between the signal and the noise, however, this issue has not been fully investigated. In the next section, we see that these square features disappear when square law detection is used in conjunction with a spatial window considerably smaller than the total extent of the sample image.

2.11 Experimental Example of Two-Dimensional NMR Diffraction - Direct

Detection of the Diffraction Pattern

The Patterson functions presented in the previous section do not contain any information which is not easily extracted from the images themselves. In fact, the determination of these Patterson functions is basically an image processing technique. The real benefits are accrued if the phase insensitive diffraction pattern is acquired directly without having to acquire the phase sensitive $S(\mathbf{k})$. Since Patterson functions extend over a much smaller spatial/frequency range than the full image, a correspondingly lower sampling rate of $|S(\mathbf{k})|^2$ is required than for $S(\mathbf{k})$, and noise can be reduced by tighter filtering before digitization (assuming the sample is composed of a large number of small objects - I will always assume this to be the case from now on).

In the presence of large static field gradients, the signal produced in the coil will contain high frequency components with respect to the reference frequency. In a normal imaging experiment, this signal is then mixed down (using the reference frequency), filtered at audio frequencies and converted to digital form using an analog to digital converter. In the previous section, this is exactly what was done. The diffraction patterns were then produced digitally by taking the modulus squared of the acquired datasets. In order to directly acquire the diffraction pattern, the magnitude squared of the NMR signal must be generated before detection and preferably before filtering. The squaring operation may be done either before the frequency down-conversion (accomplished by a quadrature

phase sensitive detector or QPD) or after. Since operations such as signal multiplication are relatively simple to do at audio frequencies (kHz), the squaring device is placed after the QPD and before the audio filter.

A schematic of the squaring circuit is shown in Fig. (2.6). The basic function of the squaring circuit is rather simple, but some of the details of the circuit deserve explanation. The input signal voltage emerging from the QPD is composed of real and imaginary parts, V_r and V_i respectively, in the range $\pm 1V$. The operational amplifiers at the input stage serve two purposes. The voltage is amplified by a factor of ten, since the analog multipliers (Analog Devices AD734) can tolerate an input voltage range of $\pm 10V$. The relative amplification of the real and imaginary voltages is controlled by the 550Ω

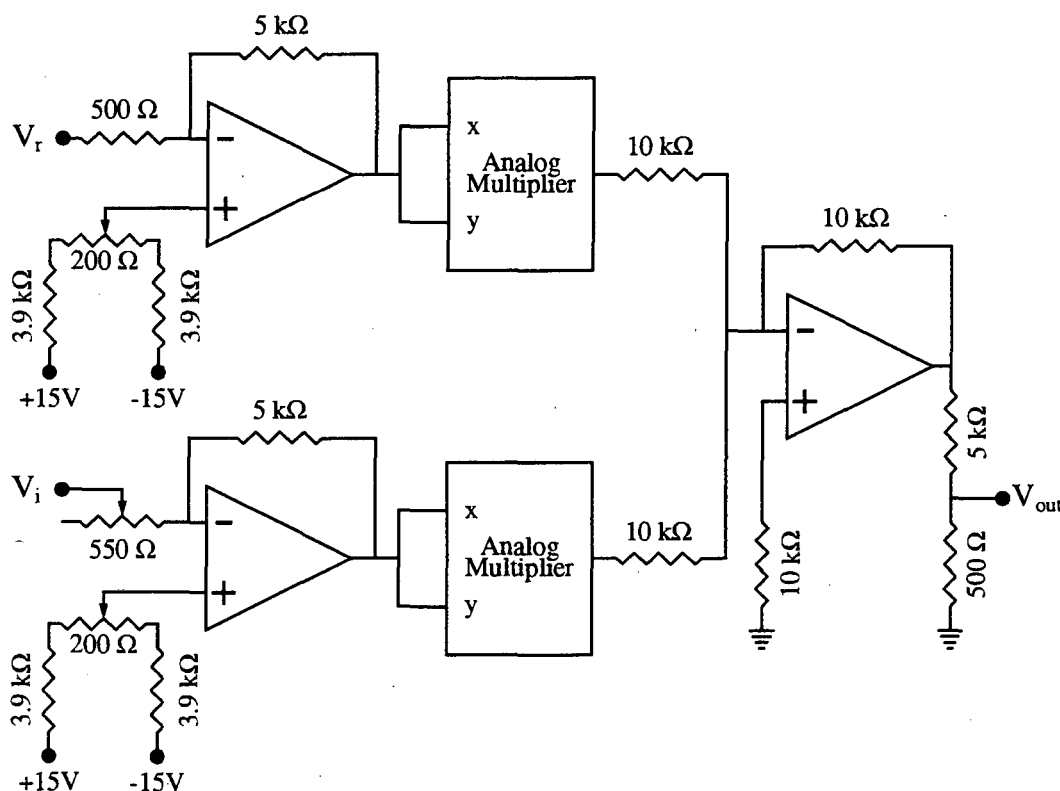


Figure 2.6 Analog squaring device used for the direct acquisition of the NMR diffraction pattern. The real and imaginary voltages are amplified by a factor of ten in the first stage after which the voltages are individually squared by the two analog multipliers (Analog Devices AD734). The resulting voltages are summed and attenuated by a factor of ten before proceeding to the audio filter. All operational amplifiers are Analog Devices AD507.

potentiometer located at the V_i input. Secondly, any DC offset may be removed by adjusting the 200Ω potentiometer in the circuit connected to the positive terminal of each amplifier. With the resistance values shown, a DC offset in the input voltage of $\pm 0.75\text{V}$ may be eliminated. Removal of any DC offset is vital, as the squaring of the signal in the presence of an offset will produce an incorrect result which cannot be accounted for at a later stage. After the squaring operation, the voltages from both multipliers are added and decreased in amplitude by a factor of ten. The final attenuation of the signal assures that the audio filter will see maximum voltages of $\pm 1\text{V}$.

Figure (2.7) shows an image, obtained conventionally (without the square law device), of a 6 mm tube packed with $120\ \mu\text{m}$ diameter monofilament fibers (buttonhole thread), resolved to 128 points per side. Figure (2.8) shows the NMR Patterson function of the same sample, derived from NMR diffraction data, Fig. (2.9), acquired using square law detection prior to filtering and digitization. The gradients used here are four times larger than those used for the image, so the Patterson function has a correspondingly higher resolution even though there are still 128 points on a side. In addition to reducing noise, the audio filter prevents aliasing and isolates the significant central 1.7 mm portion of the Patterson function. The central fiber autocorrelation function in Fig. (2.8) is a cone with a slightly flared base. As expected, the $\sim 220\ \mu\text{m}$ base diameter is equal to two fiber diameters within experimental accuracy. The nearest-neighbor ring radius is $\sim 180\ \mu\text{m}$ which is considerably larger than the $120\ \mu\text{m}$ radius expected for a hexagonally close packed (hcp) system. The large value for the nearest neighbor ring indicates relatively loose packing of the fiber bundle. Portions of the next-nearest neighbor rings are also clearly visible, and a faint third ring is visible but nearly at the level of the noise. This greater detail is available because tighter filtering has greatly suppressed noise and artifacts.

The Nalorac spectrometer uses a 12 bit digitizer which presents difficulties in acquiring all of the squared signal. The amplitude range of the signal far exceeds the range of 4096 intensity levels imposed by the digitizer, so in order to acquire the low intensity

rings in Fig. (2.9) which will give rise to the fine features in the Patterson function, the preamplifier gain must be set such that the signal near the origin in k-space saturates the digitizer (i.e. the signal is clipped at some amplitude determined by the dynamic range of the digitizer). The result is that much of the Patterson function representative of the overall sample geometry is lost, decreasing the baseline offset which would be present if all of the signal were acquired and processed. If the clipped signal is a delta function the baseline will be changed by a constant value, but if the central peak extends over a few points as is the case in Fig. (2.9), the baseline will be curved with the highest amplitude near zero frequency. As long as the saturation occurs over a relatively small range in k-space, there will be little distortion of the width of the central peak and the rings present in Fig. (2.8) as these are relatively low frequency features which are not affected by the digitizer saturation. Saturation effects such as this are also common in X-ray diffraction of powders where the same approach is often taken in analyzing the data³⁰.

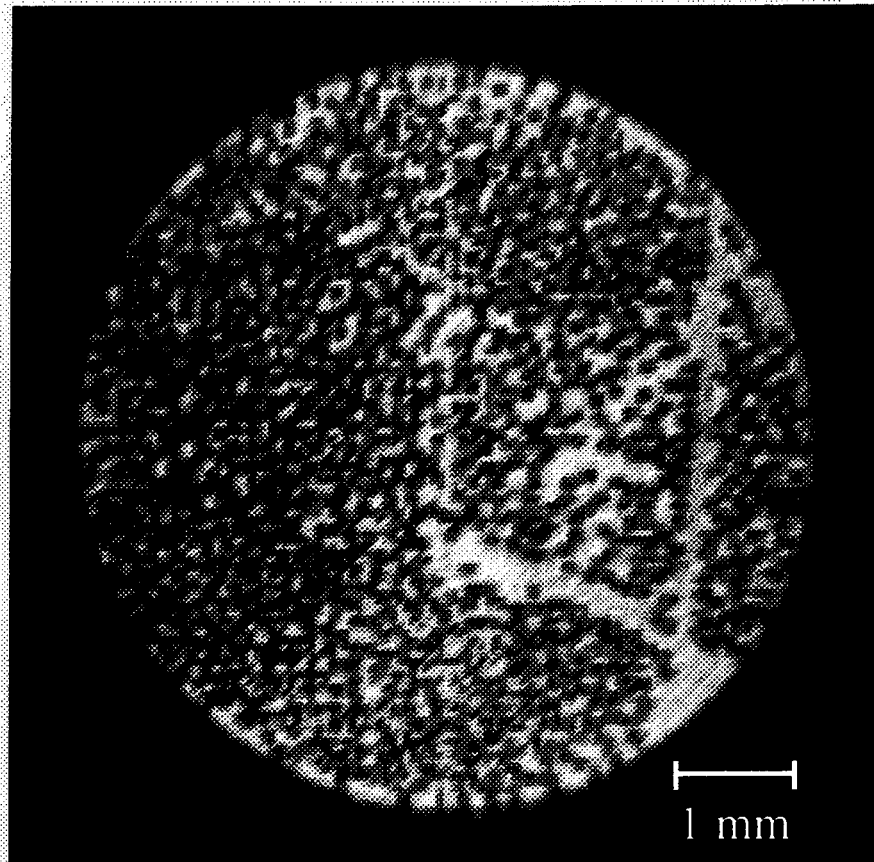


Figure 2.7 Cross sectional image of a 6 mm inner diameter tube containing 120 μm diameter monofilament fibers immersed in water. All signal is derived from the water surrounding the fibers, so the fibers themselves are low signal dark regions. The fibers appear square, since they are resolved by no more than two points in each dimension. The image was acquired with 128 points in each dimension and a digital resolution of 60 μm .

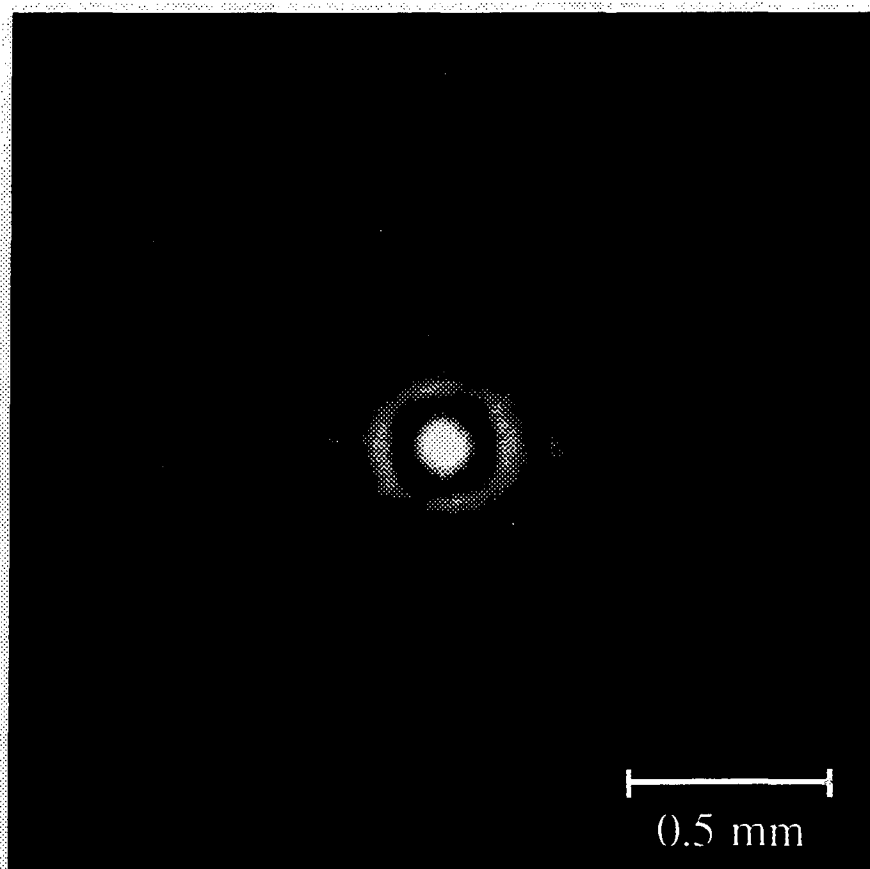


Figure 2.8 NMR Patterson function of 120 μm diameter fibers surrounded by water derived from the square law detected NMR diffraction pattern shown in Fig. (2.9). Two rings are clearly present surrounding the central peak, and a faint third outer ring appears with an amplitude slightly higher than the noise. The image was acquired with 128 points in each dimension and a digital resolution of 17 μm from a 100 μm thick slice. An image of the same sample acquired with phase sensitive detection is shown in Fig. (2.7)

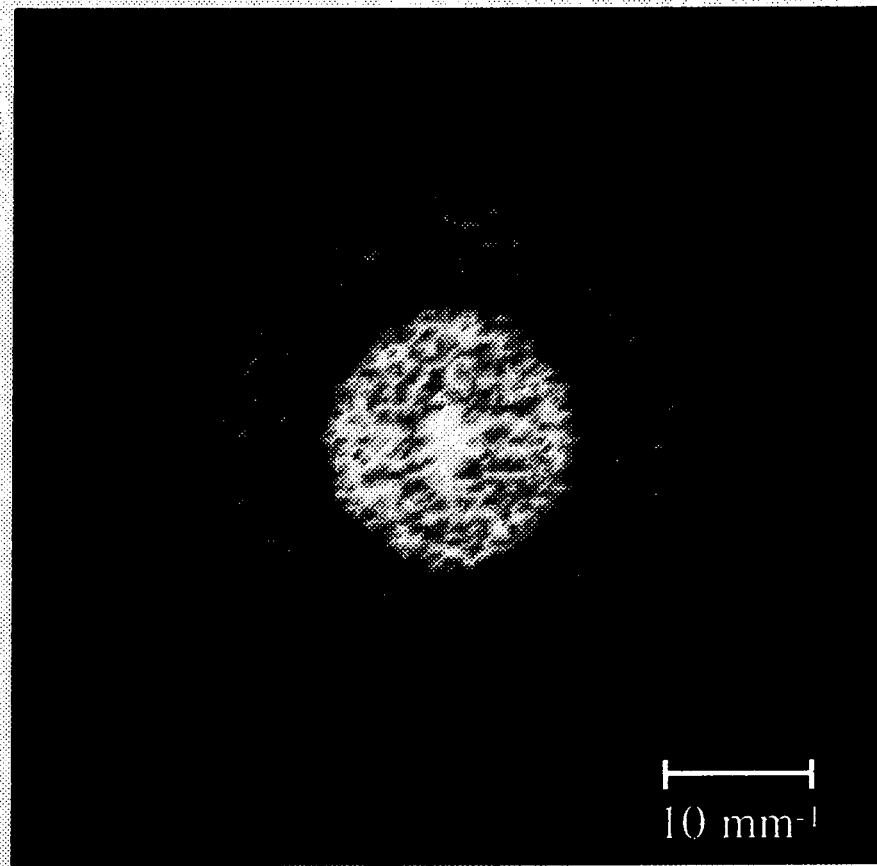


Figure 2.9 Square law detected NMR diffraction pattern of 120 μm diameter fibers surrounded by water. The dataset is 128 points on a side with a total range of 58 mm^{-1} .

There are a number of ways to avoid the saturation problem. 1) The easiest solution is to not square the signal, but then a high density of points must be sampled in k-space. For a one-dimensional experiment this is not usually a problem as will be explained further in the next section, but for the acquisition of multidimensional diffraction patterns, it is desirable to acquire phase insensitive data. 2) We can also replace the 12 bit digitizer with a 24 bit digitizer, but this would entail considerable expense and effort, as high-speed (~0.5 MHz) high-precision (16 to 24 bit) digitizers do not come cheaply, and replacing the digitizer would require considerable modification of the spectrometer software and replacement of hardware such as the signal averaging module. 3) One may put an analog device after the squaring circuit which greatly attenuates the signal at high amplitudes while attenuating the lower amplitude signal considerably less. A common device available for this purpose is a logarithmic amplifier depicted in Fig. (2.10). The square of the signal may be retrieved in post-acquisition processing where high precision is essentially free. This solution was not implemented for the work presented here, since life is just too short.

2.12 Dimensionality

In the previous examples of the NMR Patterson function, the imaging phantom was

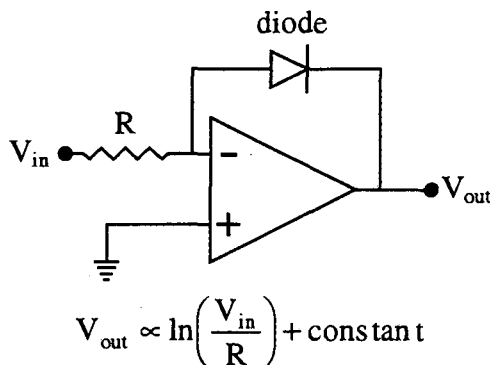


Figure 2.10 Circuit diagram for a simple logarithmic amplifier. Integrated circuit logarithmic amplifiers are also available commercially.

constructed in such a way as to make $\Phi(\Delta\mathbf{r})$ effectively two-dimensional. If the sample were infinitely long along the cylinder axis, the density autocorrelation function along the tube axis would be a delta function, so no generality was lost in looking at a thin cylindrical slice. Looking closely at the Patterson function in Fig. (2.8), there appears to be an even higher degree of symmetry in that $\Phi(\Delta\mathbf{r})$ is roughly circularly symmetric. Therefore, a one-dimensional slice through $\Phi(\Delta\mathbf{r})$ passing through the origin is equivalent to any other slice, if we neglect nonuniformities due to noise and the small deviations from an isotropic distribution of fibers in the yz plane noticeable in Fig. (2.7). Although images have not been presented to demonstrate the effect, $\Phi(\Delta\mathbf{r})$ for an isotropic distribution of small particles (making $\Phi(\Delta\mathbf{r})$ three-dimensional) displays spherical symmetry, hence a one-dimensional slice is equivalent to any other. Given the high degree of symmetry in both cases, we now wish to know whether it is possible to extract $\Phi(\Delta\mathbf{r})$ from experiments with a lower dimensionality than the full Patterson function.

2.12.1 Cylindrical and Spherical Symmetry and the Hankel Transform

The following discussion will be given in terms of the time domain or k -space signal and the corresponding image in xy space encountered in NMR imaging. The results, however, are true in general and have been used in numerous other applications^{6,44,45}.

Consider a density distribution $\rho(x, y)$ which possesses circular symmetry:

$$\begin{aligned} \rho(x, y) &= \rho(r), \\ \text{where } r^2 &= x^2 + y^2. \end{aligned} \tag{2.26}$$

The Fourier transform of $\rho(x, y)$, $S(k_x, k_y)$, will also possess circular symmetry.

$$S(k_x, k_y) = S(k_r), \quad (2.27)$$

where $k_r^2 = k_x^2 + k_y^2$

In light of the symmetry of both functions, we may express the Fourier transform relationship between $\rho(x, y)$ and $S(k_x, k_y)$ in terms of the two sets of polar coordinates defined by $x + iy = r \exp(i\theta)$ and $k_x + ik_y = k_r \exp(i\varphi)$.

$$\begin{aligned} S(k_x, k_y) &= \int_{-\infty}^{\infty} \int_{-\infty}^{\infty} \rho(x, y) \exp(i(xk_x + yk_y)) dx dy \\ &= \int_0^{\infty} \int_0^{2\pi} \rho(r) \exp(ir k_r \cos(\theta - \varphi)) r dr d\theta \\ &= \int_0^{\infty} \rho(r) \left[\int_0^{2\pi} \exp(ir k_r \cos \theta) d\theta \right] r dr \\ &= 2\pi \int_0^{\infty} \rho(r) J_0(r k_r) r dr \\ &= S(k_r), \end{aligned} \quad (2.28)$$

where J_0 is the zeroth-order circular (or cylindrical) Bessel function. Doing the same for the inverse Fourier transform, we arrive at

$$\begin{aligned} S(k_r) &= 2\pi \int_0^{\infty} \rho(r) J_0(r k_r) r dr \\ \rho(r) &= \frac{1}{2\pi} \int_0^{\infty} S(k_r) J_0(r k_r) k_r dk_r. \end{aligned} \quad (2.29)$$

The transform in Eq. (2.29) is referred to as either a cylindrical Hankel or zeroth-order Fourier-Bessel transform. In this discussion, the product $k_r r$ has units of radians in

keeping with the previous definition of the k-space vector, Eq. (2.17), so the coefficients in front of the two integrals in Eq. (2.29) are not the same. Traditionally, the Hankel transform is defined with k_r unitless⁶, making the coefficients in front of both integrals 2π . No matter which units are used, the Hankel transform is its own inverse, as long as one keeps in mind the units of the spaces between which the transform is performed, so we will not make a distinction between forward and reverse Hankel transforms.

As was mentioned earlier in connection with the one-dimensional imaging experiment, the Fourier transform of a slice through $S(k_x, k_y)$, e.g. $S(k_r) = S(k_x, k_y = 0)$, yields the projection of the density $\rho(x, y)$ onto the y axis and is written

$$\begin{aligned}
 \rho_y(x) &= \int_{-\infty}^{\infty} \rho(x, y) dy \\
 &= \frac{1}{2\pi} \int_{-\infty}^{\infty} S(k_x, k_y = 0) \exp(ik_x x) dk_x \\
 &= \frac{1}{2\pi} \int_{-\infty}^{\infty} S(k_r) \exp(ik_r x) dk_r.
 \end{aligned} \tag{2.30}$$

Since we have assumed $\rho(x, y)$ and $S(k_x, k_y)$ to be circularly symmetric, we will obtain the same result by transforming any radial slice from the k-space data. From Eq. (2.29) and (2.30) we see that the Hankel transform is equivalent to doing a Fourier transform followed by an inverse projection⁴⁵ (by this I mean the operation, given that one exists, inverse to the projection operation). Although our primary concern is the determination of $\rho(r)$ from a single slice in k-space, it is instructive to further investigate the transformations associated with projections and inverse projections and how these relate to the Fourier and Hankel transforms.

We begin by rewriting the projection transformation in polar coordinates for a circularly symmetric function as defined in Eq. (2.26).

$$\begin{aligned}
\rho_y(x) &= \int_{-\infty}^{\infty} \rho(x,y) dy \\
&= 2 \int_x^{\infty} \frac{\rho(r)r}{\sqrt{r^2 - x^2}} dr,
\end{aligned} \tag{2.31}$$

where we have used the fact that $r^2 = x^2 + y^2$. The second integral in Eq. (2.31) is commonly referred to as the Abel transform⁶. One may further show that the Abel transform is invertible, where the inverse Abel transform is given by⁴⁵

$$\rho(r) = -\frac{1}{\pi} \int_r^{\infty} \frac{1}{\sqrt{x^2 - r^2}} \frac{d}{dx} [\rho_y(x)] dx. \tag{2.32}$$

Given that there exists an analytic form for the inverse Abel transform, we can go about doing the transformations in Eq. (2.29) as either Hankel transforms or combinations of Fourier and Abel/Inverse Abel transforms. The relationships between slices and projections in the two two-dimensional conjugate spaces⁴⁵ (real space and k-space in our case) are summarized in Fig (2.11). As we can see, from a single slice in the time domain, one can generate the projection of the sample density as well as the equivalent of a slice through the sample density.

For objects which display spherical symmetry, we follow a similar procedure as in Eq. (2.28) to determine the spherical Hankel transform given by

$$\begin{aligned}
S(k_r) &= (2\pi)^{\frac{3}{2}} \int_0^{\infty} \rho(r) \frac{J_{1/2}(rk_r)}{\sqrt{k_r}} r^{\frac{3}{2}} dr \\
\rho(r) &= \left(\frac{1}{2\pi}\right)^{\frac{3}{2}} \int_0^{\infty} S(k_r) \frac{J_{1/2}(rk_r)}{\sqrt{r}} k_r^{\frac{3}{2}} dk_r,
\end{aligned} \tag{2.33}$$

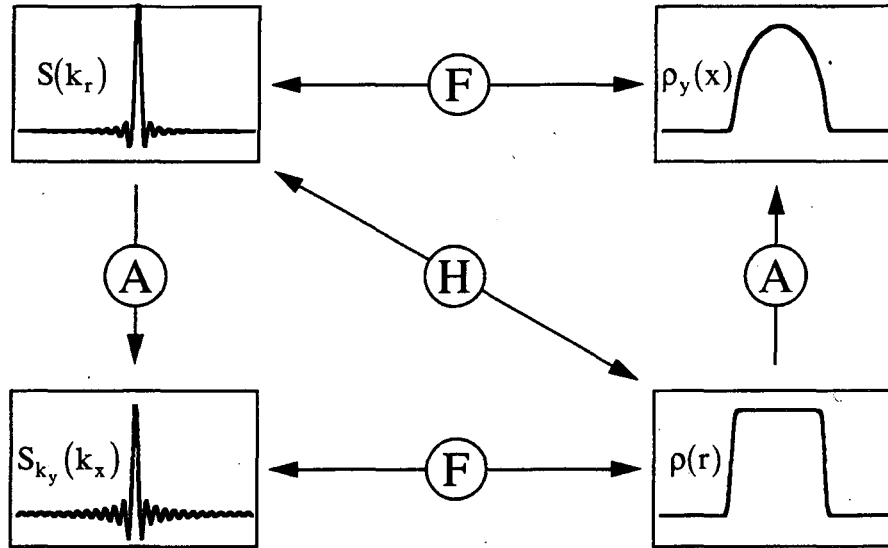


Figure 2.11 Transforms relating slices and projections in both domains to each other. The two-dimensional object represented is a solid disk in xy space centered at the origin. Abbreviations : (H)ankel, (A)bel, and (F)ourier transform. The Hankel transform takes a slice $S(k_r)$ from the k -space domain and produces a slice through the density distribution $\rho(r)$, whereas a Fourier transform of $S(k_r)$ produces the projection $\rho_y(x)$. The double arrows imply a transform which is its own inverse, whereas the single arrows are for the Abel transform which is not its own inverse.

where

$$J_{1/2}(rk_r) = \sqrt{\frac{2}{\pi rk_r}} \sin(rk_r). \quad (2.34)$$

In practice, the spherical Hankel transform is less computationally intensive as the evaluation of $J_{1/2}(rk_r)$ requires fewer operations than the evaluation of $J_0(k_r r)$. Due to the large number of computations which must be performed in a brute force implementation of the Hankel and inverse Abel transforms, numerous algorithms have been developed for fast cylindrical Hankel⁴⁶⁻⁵³ and inverse Abel⁵⁴⁻⁵⁶ transforms. For the work presented here, the Hankel transform is integrated explicitly since only a few transforms need to be performed at any given time; a 1024 point dataset requires approximately 1s of CPU time (~10 s of real time on average) on a Silicon Graphics R4000 Iris Indigo Computer.

2.12.2 Noise Effects in Hankel Transforms

In many applications the desired signal is acquired in the presence of either white or bandwidth limited noise, where white noise is characterized by a constant variance and noise power independent of frequency. For bandwidth limited noise, the noise power is confined to a finite frequency range. In NMR applications, the preamplifier contributes the major source of white noise. To eliminate aliasing of high frequency noise, the input signal is filtered (time averaged) at or slightly above the sampling frequency. As the noise power is not dependent on the frequency, Fourier transformation of noise produces noise with a constant variance within the spectral window defined by the filter. This is not the case, however, for the Hankel and inverse Abel transforms^{44,57}.

The noise generated by the inverse Abel transform of a noise dataset with variance σ^2 and bandwidth B is approximately⁵⁷

$$\sigma_{abel}^2(r) = \frac{\sigma^2 B}{2r} \quad (2.35)$$

for large values of $2\pi rB$. Since the Fourier transform deals with noise equally, Eq. (2.35) also applies to the cylindrical Hankel Transform, where σ^2 is then the noise variance of the dataset after the implied Fourier transformation and before the inverse Abel transform. Although Eq. (2.35) is not correct for small values of $2\pi rB$, it serves as a guide for the behavior of the noise variance of Hankel transformed data. It is very important to keep this effect in mind for NMR diffraction, since the data of interest appears near the origin where the noise variance is greatest.

We have not found an analytical study of the effect on noise by the spherical Hankel transform, but the approximate dependence of the noise variance can be determined by numerical experiment. To do this a number of white noise data sets are generated and the spherical Hankel transform is applied to each dataset. An example of a noise data set and

its spherical Hankel transform are shown in Fig. (2.12). It is immediately apparent in Fig. (2.12b), that the noise variance is strongly dependent upon r . The magnitude squared of the noise datasets are then added together, producing the envelope, $E(r)$, of the square of the transformed data, c.f. Fig. (2.13). As the envelope has the same dependence upon r as does the variance, a fit yields the radial dependence of the variance. In Fig. (2.13), the data is fit to

$$E(r) = \frac{a}{r^b}, \quad (2.36)$$

where a and b are the fitting parameters. The fit yields a value of 2.08 for b . As we might have expected from Eq. (2.35), the application of the inverse Abel transform two times yields a noise variance approximately inversely proportional to the radius squared.

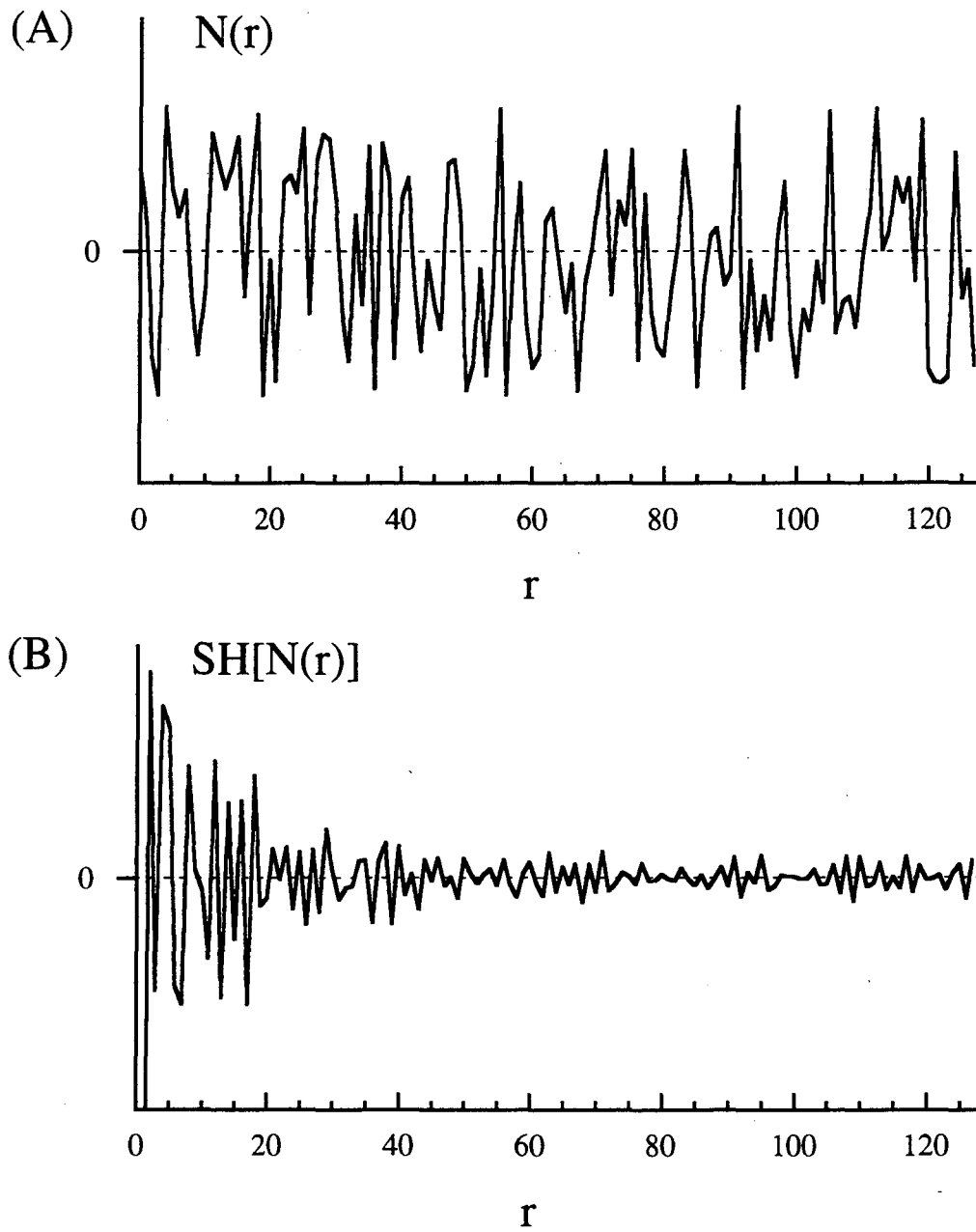


Figure 2.12 (A) White noise trace, $N(r)$, with constant variance. (B) Spherical Hankel transform of $N(r)$, $SH[N(r)]$, truncated at 8% of the maximum (negative) amplitude. The nonlinear treatment of noise by the Hankel transform is readily apparent in (B). Radial values are given in points.

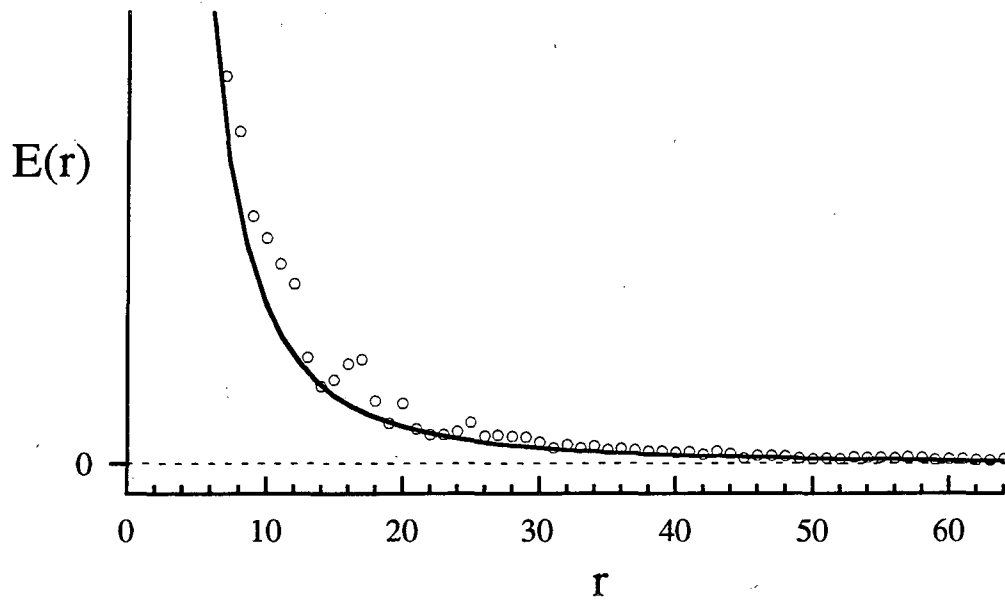


Figure 2.13 $E(r)$, circles, is the magnitude squared of the spherical Hankel transform summed over 64 noise traces each containing 128 points. $E(r)$ is equivalent to the envelope of the magnitude squared of spherically Hankel transformed white noise and displays the same dependence upon r as the noise variance. The fit, black line, shows that the noise variance is approximately inversely proportional to the radius squared. For clarity, $E(r)$ is truncated at 1% of maximum. Radial values are given in points.

In the following applications of the cylindrical and spherical Hankel transforms of diffraction data, the noise is reduced by filtering and signal averaging but can never be completely eliminated. In some cases, the noise produces a noticeable zero frequency glitch.

2.12.3 Application of the Cylindrical Hankel Transform to NMR

Diffraction - Theory and Experiment

The Hankel transform relations in Eq. (2.29) have great relevance to NMR imaging and diffraction. Given a circularly symmetric image or density autocorrelation function, one need only acquire a single ray in k -space in order to completely determine that function. In order for the transformation to proceed correctly, the object must possess true cylindrical

symmetry (neglecting noise contributions) and be centered in the frequency window, since asymmetry and misalignment produce noticeable artifacts in the resulting distribution⁵⁸. For the case of NMR diffraction, the situation is simplified in that the Patterson function is necessarily centered in the frequency window, and if the sample statistics are isotropic, the Patterson function is circularly symmetric.

From Eq. (2.23) and (2.29), we can determine the transform relating the time domain diffraction data to a cylindrically symmetric Patterson function.

$$\begin{aligned}\Phi(\Delta r) &= \frac{1}{2\pi} \int_0^{\infty} |S(k_r)|^2 J_0(\Delta r k_r) k_r dk_r \\ |S(k_r)|^2 &= 2\pi \int_0^{\infty} \Phi(\Delta r) J_0(\Delta r k_r) \Delta r d\Delta r\end{aligned}\tag{2.37}$$

The Fourier transform of the one-dimensional diffraction data yields the Abel transform of $\Phi(\Delta r)$, c.f. Eq. (2.30). To distinguish between the slices and projections, we will refer to the unprojected density autocorrelation function as $\Phi_0(\Delta r)$ and the projected distribution as $\Phi_1(\Delta r)$. By definition, $\Phi_0(\Delta r)$ is the autocorrelation of the point density (pointwise autocorrelation density), whereas $\Phi_1(\Delta r)$ may be viewed as the correlation of discrete strips or lines of density (stripwise autocorrelation density).

As was noted before, the Patterson function in Fig. (2.8) displays approximate circular symmetry, so the same sample (120 μm monofilaments) was used to demonstrate the utility of the cylindrical Hankel transform approach. By implementing the Hankel transform approach on the same sample, we will also be able to compare the full two-dimensional autocorrelation distribution in Fig. (2.8) to the Hankel transform result.

Figure (2.14) compares the Fourier and cylindrical Hankel transforms of one-dimensional square law detected diffraction data to a slice from the two-dimensional Patterson function in Fig. (2.8). All three density autocorrelation functions have a digital

resolution of $16.5 \mu\text{m}$. To ensure the isotropy of the data, the one-dimensional data was averaged over 64 equally spaced gradient directions, hence the superior signal to noise and smoothness of Fig. (2.14a), $\Phi_1(\Delta r)$, and Fig. (2.14c), $\Phi_0(\Delta r)$, with respect to Fig. (2.14b). In Fig. (2.14c) peaks appear at 0, 160, 280 and $410 \mu\text{m}$; these numbers should be compared to those expected for two-dimensional hcp : 0, 120, 207 and $240 \mu\text{m}$. As the measured values are considerably larger than those for hcp, the porosity of the sample, the ratio of the void volume (water) and the total physical volume of the selected region, is necessarily larger than the porosity of a hcp system, 0.09. The larger porosity value agrees with the imperfect packing noticeable in Fig. (2.7). Previously, it was noted that a faint third ring appears in Fig. (2.8); the third ring or peak is clearly seen in Fig. (2.14c). As expected, the stripwise autocorrelation distribution, Fig. (2.14a) has less pronounced nearest neighbor peaks than $\Phi_0(\Delta r)$ and has a monotonically decreasing baseline. In determining the location of the peaks, one should use Fig. (2.14c), since the baseline of the projected distribution makes the peaks appear at a smaller radial value.

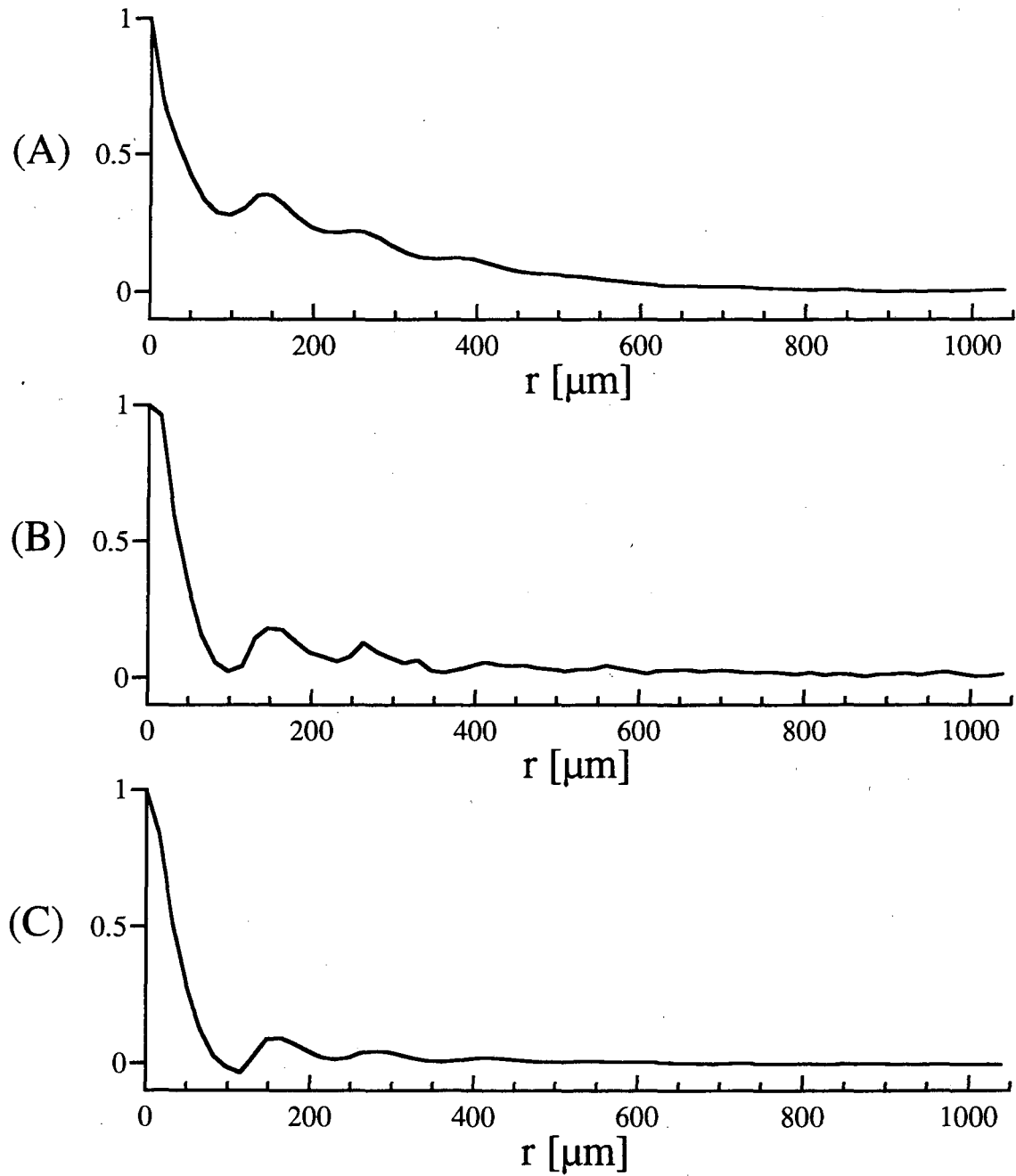


Figure 2.14 (A) One-dimensional Fourier transform of square law detected diffraction data from the 120 μm diameter fiber sample, averaged over 64 equally spaced gradient directions. The glitch at zero frequency is likely due to noise. (B) Slice taken from the two-dimensional autocorrelation distribution in Fig. (2.8). (C) Cylindrical Hankel transform of the same radial diffraction data as used to produce (A). Differences between (B) and (C) are primarily due to the circular averaging used to produce the radial diffraction data from which (C) is derived. Each dataset has a digital resolution of 16.5 μm

For samples with a more homogeneous distribution of fibers, only a single slice from the diffraction data need be acquired, but we were unable to produce fiber samples with adequate isotropy. However, we were able to fabricate samples with a nearly isotropic distribution of small particles.

2.12.4 Application of the Spherical Hankel Transform to NMR Diffraction - Theory and Experiment

For samples which display spherically symmetric statistics, the density autocorrelation distribution is determined from a one-dimensional diffraction dataset by the spherical Hankel transform.

$$\begin{aligned}\Phi(\Delta r) &= \left(\frac{1}{2\pi}\right)^{\frac{3}{2}} \int_0^{\infty} |S(k_r)|^2 \frac{J_{1/2}(\Delta r k_r)}{\sqrt{r}} k_r^{\frac{3}{2}} dk_r \\ |S(k_r)|^2 &= (2\pi)^{\frac{3}{2}} \int_0^{\infty} \Phi(\Delta r) \frac{J_{1/2}(\Delta r k_r)}{\sqrt{k_r}} \Delta r^{\frac{3}{2}} d\Delta r\end{aligned}\tag{2.38}$$

A cylindrical Hankel transform of the diffraction data generates the Abel transform of the density autocorrelation distribution, and a Fourier transform generates the Abel transform of the Abel transform of $\Phi(\Delta r)$.⁴⁵ We will refer to the true density autocorrelation distribution as $\Phi_0(\Delta r)$, the Abel transform of $\Phi_0(\Delta r)$ as $\Phi_1(\Delta r)$, and the Abel transform of $\Phi_1(\Delta r)$ as $\Phi_2(\Delta r)$. As noted previously, $\Phi_0(\Delta r)$ is the density autocorrelation of discrete points in the sample or the pointwise correlation. $\Phi_1(\Delta r)$ represents a slice from the projection of $\Phi_0(\Delta r)$ onto a two-dimensional plane and may be thought of as the density autocorrelation distribution of discrete strips. $\Phi_2(\Delta r)$ is the projection of $\Phi_0(\Delta r)$ onto a single line and may be thought of the density autocorrelation distribution of discrete planes in the sample.

The sample consists of 140 μm diameter polystyrene microspheres (Duke Scientific) packed into a 7 mm inner diameter glass tube which is filled with water. Air bubbles are avoided by slowly adding the particles to a water filled tube and allowing them to settle. Tubes prepared in this way consistently have a porosity of ~ 0.38 , whereas the smallest achievable porosity corresponding to a face centered cubic (fcc) configuration is 0.26.⁵⁹

The diffraction data in this case was not acquired using square law detection, since little is gained by square law detection in a one-dimensional experiment. After acquisition, the square magnitude of the time domain data is filtered using a Gaussian convolution function given by

$$G(\Delta r) = \exp\left(\frac{-\Delta r^2}{\sigma^2}\right), \quad (2.39)$$

where $\sigma^2 = 770\mu\text{m}$.

The Gaussian convolution is the computational equivalent to an audio filter following square law detection. Although the response of a Gaussian filter is not as flat as the commonly used electronic Hadamard filter, it serves the purpose of reducing the total noise power in the data set, and for reasons to be explained below, a Gaussian filter insures that the geometry of the sample appears spherically symmetric.

Since we acquire the data without square law detection, we are able to acquire the entire echo amplitude. The density autocorrelation distribution will therefore show the autocorrelation of the bulk sample with the small fluctuations due to the spherical particles riding atop and located near the origin. Formally, we may separate the density distribution of the sample into two parts

$$\rho(\mathbf{r}) = \rho^b(\mathbf{r}) + \rho'(\mathbf{r}). \quad (2.40)$$

$\rho^b(\mathbf{r})$ has the same bulk geometry as $\rho(\mathbf{r})$ but has an intensity equal to the average local intensity of $\rho(\mathbf{r})$ within the sample volume. By average, we mean that the intensity is averaged over a larger area than the fluctuations created by the sample inhomogeneities. For the experiment described above with Gaussian filtering, $\rho^b(\mathbf{r})$ is a spherical Gaussian. $\rho'(\mathbf{r})$ arises from the fluctuations about the average value of $\rho^b(\mathbf{r})$ due to the presence of the introduced heterogeneities. In terms of Eq. (2.40), the autocorrelation of $\rho(\mathbf{r})$ is

$$\begin{aligned}\Phi_0(\Delta r) &= \langle \rho(\mathbf{r})\rho(\mathbf{r} + \Delta\mathbf{r}) \rangle \\ &= \langle \rho^b(\mathbf{r})\rho^b(\mathbf{r} + \Delta\mathbf{r}) \rangle + \langle \rho^b(\mathbf{r})\rho'(\mathbf{r} + \Delta\mathbf{r}) \rangle \\ &\quad + \langle \rho'(\mathbf{r})\rho^b(\mathbf{r} + \Delta\mathbf{r}) \rangle + \langle \rho'(\mathbf{r})\rho'(\mathbf{r} + \Delta\mathbf{r}) \rangle\end{aligned}\tag{2.41}$$

where the brackets represent integration over \mathbf{r} and, in light of the spherical symmetry, a final integration over the angular components of $\Delta\mathbf{r}$. Since $\rho'(\mathbf{r})$ has an average value of zero, the middle two terms in the sum of Eq. (2.41) vanish. We are left with the sum of the autocorrelation of the mean bulk sample and the autocorrelation of fluctuations in the sample density.

$$\Phi_0(\Delta r) = \Phi_0^b(\Delta r) + \Phi_0'(\Delta r)\tag{2.42}$$

Taking successive Abel transforms of Eq. (2.42), we arrive at similar expressions for $\Phi_1(\Delta r)$ and $\Phi_2(\Delta r)$.

$$\Phi_1(\Delta r) = \Phi_1^b(\Delta r) + \Phi_1'(\Delta r)\tag{2.43}$$

$$\Phi_2(\Delta r) = \Phi_2^b(\Delta r) + \Phi_2'(\Delta r)\tag{2.43}$$

Note that Abel transformation is a linear operation, so $\Phi_1'(\Delta r)$ is the projection of $\Phi_0'(\Delta r)$, etc.

Since the data is processed with a Gaussian filter with a bandwidth considerably narrower than the sample geometry, the bulk autocorrelation function $\Phi_0^b(\Delta r)$ and its projections $\Phi_1^b(\Delta r)$ and $\Phi_2^b(\Delta r)$ are all almost perfect Gaussians, hence they represent autocorrelations of a spherically symmetric distribution, namely a spherical Gaussian. This is an important point, since in applying the Hankel transformation, we are assuming spherical symmetry, whereas the sample is actually a cylindrical section.

Figure (2.15) shows the experimentally obtained $\Phi_0'(\Delta r)$, $\Phi_1'(\Delta r)$ and $\Phi_2'(\Delta r)$ for the sampled described at the beginning of the section with a slice thickness of ~ 7 mm and a digital resolution of $15.5 \mu\text{m}$. As was shown in Fig. (2.14b), the projections of $\Phi_0'(\Delta r)$, namely $\Phi_1'(\Delta r)$ and $\Phi_2'(\Delta r)$, display peaks riding atop a monotonically decreasing baseline. This is not the baseline due to the bulk sample, $\Phi_0^b(\Delta r)$. Rather, it is a consequence of the projection operation. For the projections, the peaks appear to be at smaller values than do those in $\Phi_0'(\Delta r)$, so in order to be able to pick off particle separations simply, one should use the unprojected density autocorrelation distribution. Figure (2.16a) shows $\Phi_0'(\Delta r)$ over a smaller amplitude range, which reveals the presence of a total of five peaks at 0, 150, 270, 390, and 510 μm . For a fcc packing structure (porosity=0.26), peaks should appear at 0, 140, 240, 280, and 370 μm . Comparing the two sets of numbers, we may surmise that the particles are relatively well packed over short length scales, however, the close packing does not continue over much more than two particle diameters. This may be due to the particles grouping into small, well ordered domains which are randomly oriented with respect to one another.

Unexpectedly, $\Phi_0'(\Delta r)$ in Fig. (2.16a) does not go appreciably below zero between the peaks as might be expected for a density autocorrelation function derived from a density distribution with zero mean. For a thinner slice, shown in Fig. (2.16b), $\Phi_0'(\Delta r)$ does go appreciably below zero. The discrepancy between the two distributions may be due to an inaccurate subtraction of the Gaussian baseline $\Phi_0^b(\Delta r)$ which is much larger than $\Phi_0'(\Delta r)$ for the 7 mm slice than for the 0.4 mm slice; data taken for a large number of slice

thicknesses indicate that the area of the magnitude of $\Phi'_0(\Delta r)$ decreases approximately linearly with respect to the slice thickness, whereas the area of $\Phi_0^b(\Delta r)$ is inversely proportional to the square of the slice thickness. In spite of the discrepancy, Fig. (2.16a) reveals a significant amount of information for a one dimensional experiment.

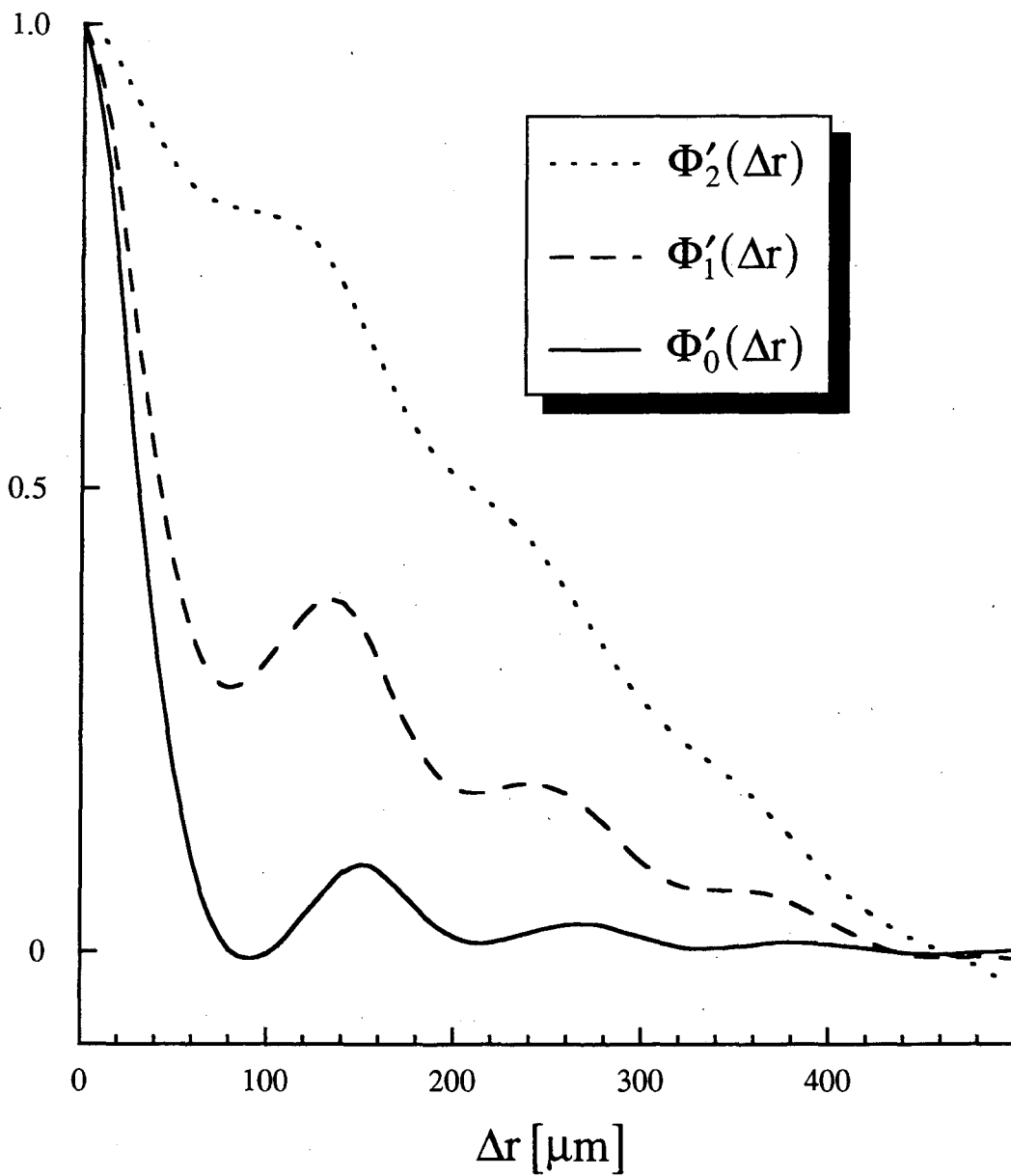


Figure 2.15 Comparison of the Fourier, cylindrical Hankel, and spherical Hankel transformed data, Φ_2' , Φ_1' and Φ_0' respectively, for a sample composed of 140 μm microspheres. The amplitude scale is arbitrary, and the digital resolution in each case is 15.5 μm .

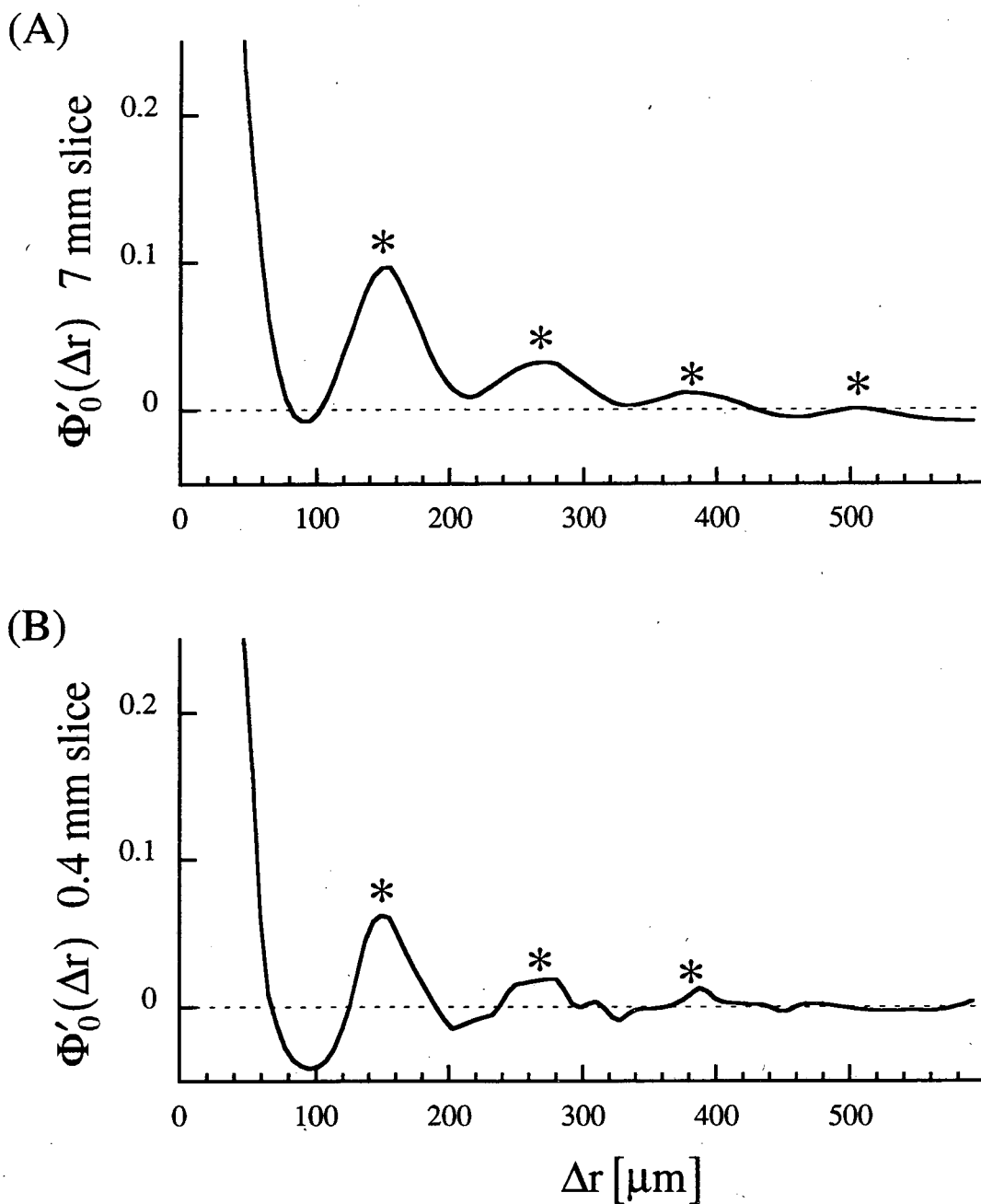


Figure 2.16 Comparison of Φ'_0 for two slice thicknesses: (A) 7 mm and (B) 0.4 mm with a digital resolution of $15.5 \mu\text{m}$. The * symbols indicate the peaks at 150, 270, 390 and 510 μm referred to in the text. The 510 μm peak is not indicated in (B) since the noise level makes it impossible to determine the existence of a peak at that location. Note that the range of the horizontal scale is larger than that in Fig. 2.15. To better display the peaks, the vertical range in (A) and (B) is only one-quarter of the maximum amplitude.

2.13 Conclusions

We have shown how direct diffraction and associated NMR Patterson functions can characterize the spatial statistics of small structures. Of course, it is always possible to extract statistical information from an image by digital processing, but there are compelling advantages for adopting the diffraction viewpoint (and square law detection), which fall under the headings of acquisition economy and, most generally, statistical regularity.

Acquisition economy refers to the fact that fewer points are often required to specify the Patterson function of a sample compared to its image. Although *range* in k-space (maximum gradient level and duration) must be maintained for good spatial resolution for both diffraction and imaging, the *density* of data points in k-space determines the spatial range, and this is quite different in the two cases. This was shown in Figs. (2.7) and (2.8), where the same number of data points were used to display the Patterson function with a resolution 4 times higher than the corresponding image. As discussed in Section 2.7, the statistical experiment reduces the number of points required by approximately the number of features in the sample length. If there are 100 features on a side, for example, obtaining a three dimensional Patterson function requires about a million times fewer points than for a comparably resolved image. This corresponds to a considerable time savings in multidimensional experiments.

Statistical regularity refers to the fact that statistical descriptions of systems, such as the Patterson functions discussed here, often possess higher symmetry than the system itself. We have already mentioned above how statistical characterization permits repeated signal acquisition even for re-arranging systems because statistical data are time invariant but imaging data are not. A similar situation arises for orientation when features are distributed isotropically. The rotational symmetry of Fig. (2.4c), (2.4f), and (2.8) demonstrates such angular independence. In Section 2.12.3 and 2.12.4, we took advantage of the sample symmetry to reduce the dimensionality of the required experiment to *one* by using the cylindrical and spherical Hankel transforms respectively to process

one-dimensional diffraction datasets. These temporal and orientational symmetries are two instances of *statistical regularity*, by which we mean symmetries possessed by system statistics but not by the system (or image) itself. In fact, the underlying mechanism behind acquisition economy is actually another statistical regularity, translational invariance: the rapid (phase) variations in k-space associated with macroscopic translations are absent from the correlation statistics.

Finally, the fact that diffraction information resides in an intrinsically narrower bandwidth than data for comparably resolved images implies that NMR diffraction techniques will be able to achieve a finer spatial resolution than that which can be achieved in a reasonable time (an important consideration in the theoretical resolution of NMR imaging) by NMR imaging techniques. Theoretical work presented by Callaghan indicates that NMR imaging is able to resolve three-dimensional objects only as small as 10 μm on a side¹⁷.

Chapter 3 Radial RF Imaging Using a Coaxial Resonator

3.1 Introduction

NMR imaging conventionally employs magnetic field gradients which produce planes of constant field strength of either the static field B_0 ,^{3,60,61} or, as will be discussed in this chapter, the excitation field B_1 .⁶² In both cases, the field strength increases linearly along one direction of the Cartesian coordinate system (x,y,z) producing spatially dependent Larmor or nutation frequencies respectively. Such gradients are appropriate for medical imaging where the object being studied has no particular symmetry. However, for systems having cylindrical symmetry (e.g. the flow between counter-rotating cylinders or in a pipe) it may be possible to reduce the dimensionality of the experiment by producing magnetic field gradients of cylindrical symmetry, i.e. cylinders of constant field strength, for faster acquisition or improved signal to noise. This approach requires a different coil geometry from previous imaging methods^{3,4,39,63}, so a novel means of producing magnetic field gradients will need to be developed.

In this chapter, we present a method for producing cylindrically symmetric rf magnetic field gradients and a means of interpreting the NMR results from such a system⁶⁴. Although the work on this system did not proceed beyond the initial testing stages of the apparatus, we foresee that these results open up the possibility of efficiently investigating phenomena previously difficult or impossible to measure.

3.2 Radiofrequency NMR Imaging Theory - Constant Field Gradients

Unlike the type of NMR imaging described in Chapter 2, radio frequency or rotating frame NMR imaging (rf imaging) employs a gradient in the excitation field as a means of obtaining a spatially resolved sample density distribution. In the following discussion, we assume that the coil which generates the rf field gradient is also used to acquire the NMR signal, no appreciable T_1 or T_2 relaxation occurs in the course of the experiment, and the rf field is applied at the Larmor precession frequency (note that this also implies the absence of inhomogeneities in the static field). Also, we will take the standpoint of the reference frame rotating in phase with the excitation magnetic field, i.e. the rotating frame.

Consider, for example, a coil and sample configuration such as that shown in Fig. (3.1). The B_1 field directed along the coil axis increases approximately linearly between $x = 0.5R$ to $1.2R$, where R is the radius of the coil, and the region considered lies along the line which determines the central axis of the coil⁶⁵. We will define the x axis

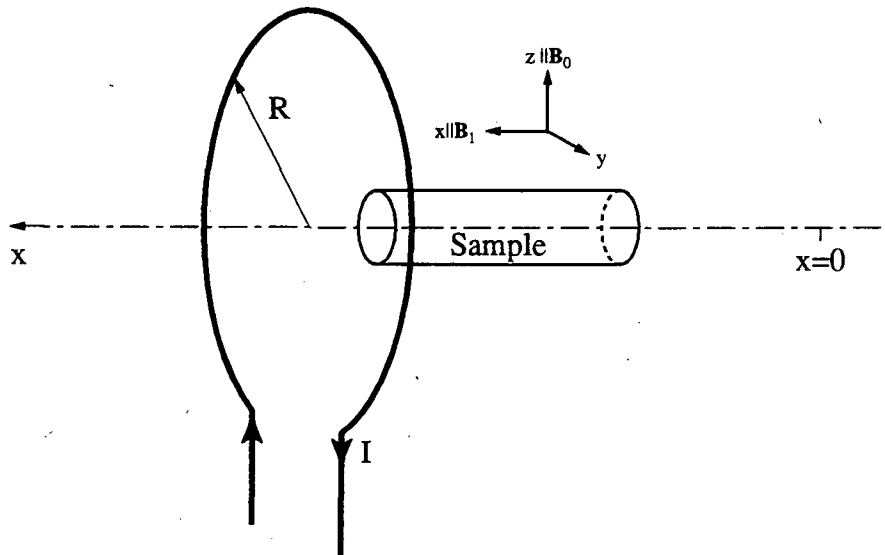


Figure 3.1 Schematic of coil and sample configuration for a possible rf NMR imaging experiment. The excitation field is aligned with the x axis and is linearly increasing with respect to x in the region $x = 0.5R$ to $1.2R$. Note that the orientation of the x axis is from right to left. The arrowheads on the coil indicate the direction of the instantaneous current through the coil.

origin as the imaginary point where the excitation field goes through zero if one extrapolates from the linear region. This point lies at a distance of $1.4R$ from the coil center. If we define the positive direction as moving towards the center of the coil from $x = 0$, then the magnetic field strength as a function x is given by

$$B_1(x) = g_1 x, \quad (3.1)$$

where $g_1 = 0.76 B_{1c}/R$ and B_{1c} is the field at the center of the coil. When the on-resonance excitation field is applied, the magnetization within the region of linearity indicated above will nutate about the rf field at a frequency given by

$$\omega_1(x) = \gamma g_1 x. \quad (3.2)$$

In the rotating frame, the component of the magnetization in the plane transverse to the static magnetic field for a volume element dV located at x_0 following a pulse of length τ will be

$$M_{xy}(t) \propto \sin(\omega_1(x_0)\tau)\rho(x_0)dV, \quad (3.3)$$

where $\rho(x_0)$ is a projection of the sample density along the y and z axes. The NMR signal arising from the same volume element is given by

$$dS(x_0, \tau) \propto \omega_1(x_0)\rho(x_0)\sin(\omega_1(x_0)\tau)dV. \quad (3.4)$$

The leading term $\omega_1(x_0)$ appears as a consequence of reciprocity^{16,66}. Simply stated, the voltage or current produced in a coil by a magnetic dipole is proportional to the magnetic field produced at the position of the dipole by a unit current in the coil. Therefore, the

NMR signal from a given point is weighted by the strength of the magnetic field produced by the resonator at that point, and since the magnetic field strength is proportional to ω_1 , the signal is weighted by ω_1 . Integrating over the entire sample volume and neglecting any proportionality constants outside the integral, we obtain the total NMR signal given by

$$S(\tau) = \int_V \omega_1(x) \rho(x) \sin(\omega_1(x) \tau) dx. \quad (3.5)$$

If $\omega_1(x)$ is given by Eq. (3.2), the signal becomes

$$S(\gamma g_1 \tau) = \gamma g_1 \int_V x \rho(x) \sin(\gamma g_1 \tau x) dx. \quad (3.6)$$

It is now possible to obtain the density distribution by doing a sine transform with respect to the conjugate variables $(\gamma g_1 \tau, x)$.

$$x \rho(x) \propto \int_V S(\gamma g_1 \tau) \sin(\gamma g_1 \tau x) d(\gamma g_1 \tau). \quad (3.7)$$

Although the sine transform does not directly yield the sample density distribution, $\rho(x)$ may be obtained trivially from Eq. (3.7).

The range and resolution of the experiment in both spaces may be determined by Eq. (2.19) and (2.20) replacing k_x with $\gamma g_1 \tau$.

3.3 Radiofrequency NMR Imaging - Experimental Methods

We will consider three basic approaches to rf imaging. As was the case for static field gradient imaging, the goal is to adequately sample the space determined by $\gamma g_1 \tau$. Unlike static field gradient imaging, it is impossible to sample the NMR signal while the

gradient is applied. However, as we will show in the third example, it is still possible to do a frequency encoding type experiment, cf. Section 2.5.

The first method, Fig. (3.2a), is an inherently two-dimensional experiment. A rf pulse of constant duration τ is applied with a variable amplitude increasing from zero to the maximum value in equal increments. Of course, the first pulse does not produce any signal, but this is necessary in order to ensure the proper implementation of the sine transform. The second method, Fig. (3.2b), is also inherently a two-dimensional experiment, but instead of varying the amplitude of a pulse of constant duration, one applies constant amplitude pulses with a variable duration increasing from zero to the maximum value in equal increments. In both cases, one may either acquire only the first point in the resulting free induction decays (FIDs), or acquire the entire FID. By acquiring the entire FID, one may perform a Fourier transform along the acquisition dimension to separate resonances due to different chemical species⁶⁷⁻⁶⁹ or to compensate for small inhomogeneities in the static field. Both experiments may also be turned into two-dimensional imaging experiments by applying static field gradients in a manner similar to that described in Section 2.5, cf. Fig. (2.2). An example of a mixed rf and static field imaging experiment will be presented in Section 3.7.

The third type of rf imaging experiment, Fig. (3.2c), unlike the other two, is a one-dimensional experiment. Short, constant duration rf pulses are applied between which a single point is acquired. Nutation sequences such as this have been used previously in solid-state decoupling experiments^{70,71} and, by myself, to quickly determine the rf field homogeneity in NMR imaging probes.

The first two experimental methods, Fig. (3.2a) and (3.2b), are phase encoding methods, whereas the nutation experiment is a frequency encoding experiment.

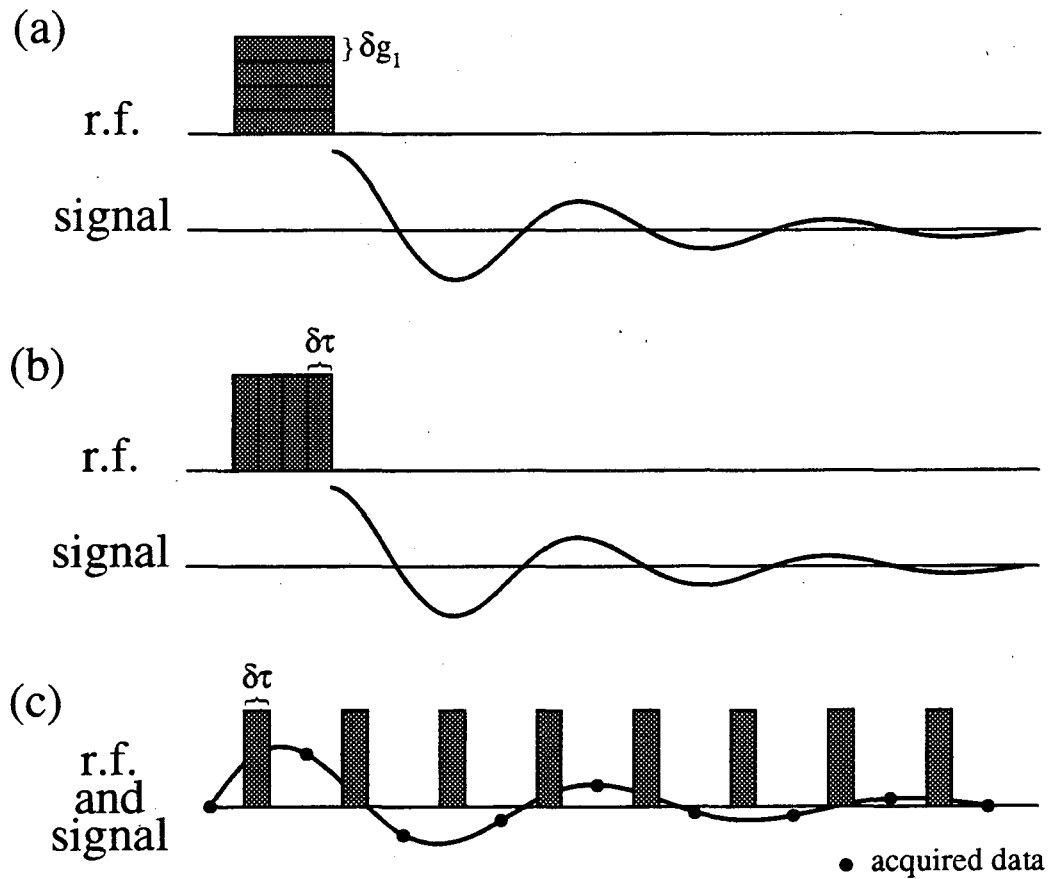


Figure 3.2 Pulse sequences for three types of rf imaging experiments. In (a) constant duration gradient pulses of increasing amplitude are used. In (b) constant amplitude pulses of increasing duration are applied. In (c) we see the equivalent of acquisition during the application of the excitation field gradient. The signal represented in (a) and (b) is the FID resulting from the individual excitation pulses and contains *no* imaging information by itself. The imaging information is contained in the amplitude modulation of the signal between excitations. In (c) the signal does contain imaging information and is equivalent to the time domain signal in Eq. (3.5).

3.4 The Coaxial Resonator

As mentioned above, the primary goal of this work is to develop a system which generates cylindrically symmetric gradients in the excitation field strength. There does not appear to be a way to do this for static field gradients unless a conductor is run through the central part of the sample. Inductive coupling of the gradient coil to the resonator and a dramatic lowering of the Q of the resonator circuit due to the presence of what is effectively a conductive sample rule out the use of static field gradients. However, cylindrically symmetric gradients in the excitation field are present in coaxial resonators. In an infinite coaxial transmission line, Fig. (3.3), the magnetic field produced between the two conductors is given by^{72,73}

$$B_{\phi} = \frac{\mu I(z,t)}{2\pi r}, \quad (3.8)$$

where (r, ϕ, z) define the cylindrical coordinate system aligned with the central conductor, $I(z,t)$ is the current at a given distance z down the line at time t , and μ is the permeability of the region between the two conductors.

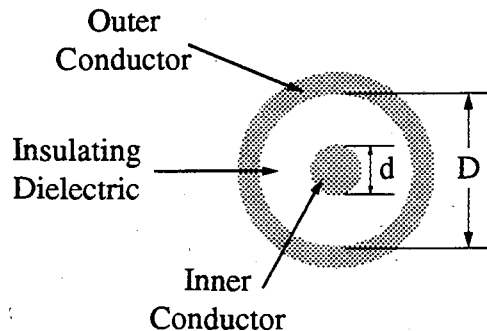


Figure 3.3 Cross section of a coaxial transmission line. Generally the outer conductor is grounded and current travels down the internal conductor. The magnetic fields produced are confined to the insulating dielectric region and produce cylinders of constant field strength concentric with the inner conductor.

A coaxial resonator may be constructed using an open-ended (open circuit at both ends) half-wavelength, $\lambda/2$, section of coaxial transmission line, where λ is the wavelength of the excitation rf field. For the field strengths we will be using, the half wavelength in free space of the resonant excitation field is approximately 80 cm, which is inconveniently long. Of course, the introduction of insulating dielectrics between the two conductors will reduce the length of a $\lambda/2$ line, but the segment will still be quite long. In addition, the rf field gradient is only close to cylindrically symmetric in the central (axial) portion of the resonator due to the sinusoidal dependence of the current in the axial direction.

Transmission line theory^{74,75} suggests a means of shortening the coaxial segment and achieving a nearly cylindrically symmetric rf field, while still maintaining the resonant characteristics of a half-wave line. The input impedance with respect to ground, Z_S , of a lossless transmission line segment of length l (in our case a coaxial line) with a terminating impedance of Z_R is given by

$$Z_S = Z_0 \frac{Z_R \cos(\beta l) + iZ_0 \sin(\beta l)}{Z_0 \cos(\beta l) + iZ_R \sin(\beta l)}, \quad (3.9)$$

$$\beta = \frac{2\pi}{\lambda_r}, \quad (3.10)$$

where λ_r is the rf wavelength in the material between the two conductors and is equal to the wavelength in free space divided by $\sqrt{\epsilon_r}$. ϵ_r is the ratio of the dielectric constant of the insulating material between the two conductors and the dielectric constant of free space. Z_0 is the characteristic impedance of the transmission line, which for a coaxial line, Fig. (3.3), is given by

$$Z_0 = \frac{60}{\sqrt{\epsilon_r}} \ln\left(\frac{D}{d}\right). \quad (3.11)$$

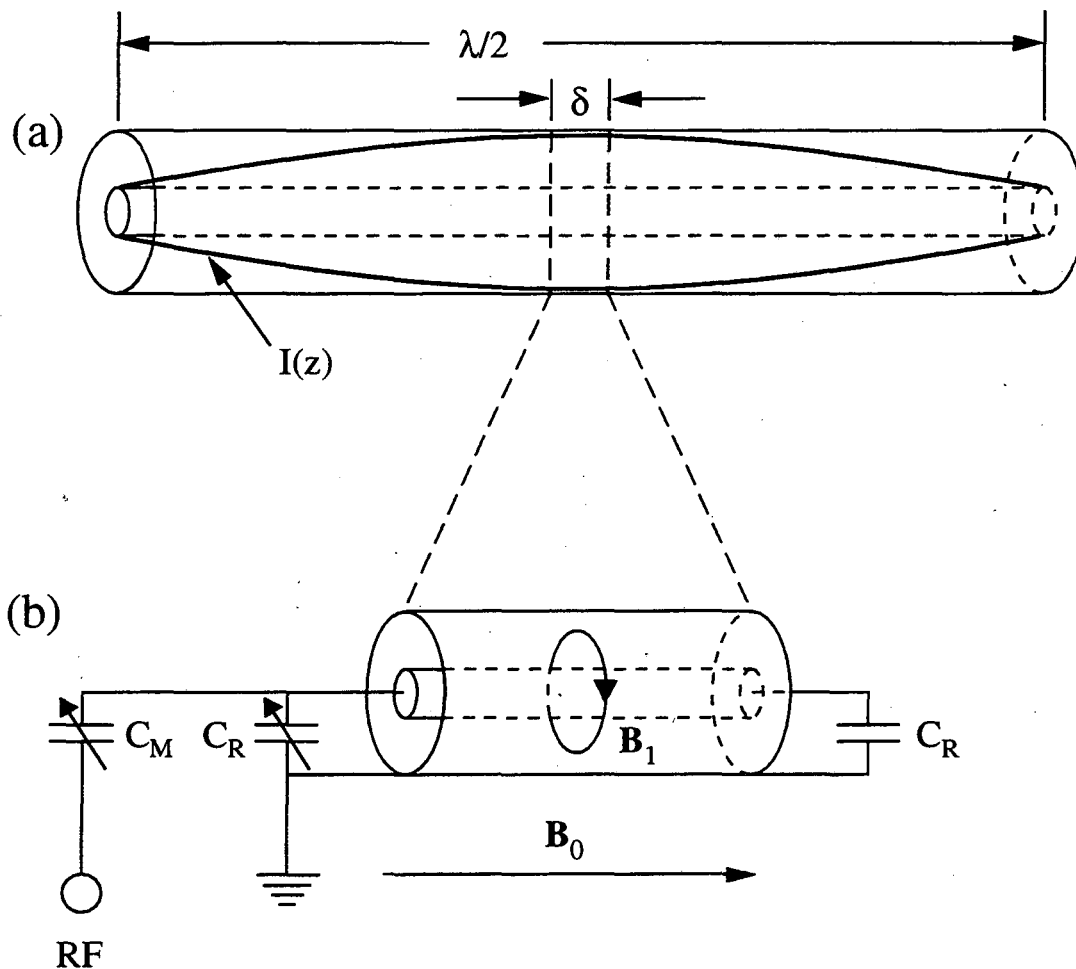


Figure 3.4 A coaxial resonator may be constructed either (a) from a half-wave line or (b) by terminating both ends of a shorter line with the appropriate capacitance, C_R . One of the terminating capacitors is made variable to allow for balancing of the end capacitance. C_R may be determined from Eq. (3.13) given the resonator dimensions, the dielectric constant of the material between the coaxial conductors, and the frequency of the applied current. The match capacitor, C_M , provides a means of matching the input impedance of the circuit to the characteristic impedance of the line connecting the amplifier to the resonator, 50Ω .

For an open line, $Z_R \rightarrow \infty$, so the input impedance simplifies to

$$Z_S = -iZ_0 \cot(\beta l). \quad (3.12)$$

Now we may ask ourselves, if we only wish to keep the central section of the half-wave line, what can we use to replace the two pieces which were cut off either end? Since the two pieces are each shorter than a quarter-wavelength, Eq. (3.12) implies that they have a negative imaginary impedance, i.e. they are equivalent to capacitors to ground. If we use a coaxial line of length δ , then the required capacitance at either end is

$$C_R = \frac{1}{2\pi f Z_0} \cot\left(\frac{\pi\delta}{\lambda_r}\right), \quad (3.13)$$

where f is the frequency of the excitation field. A diagram of the circuit is shown in Fig. (3.4). The matching capacitor, C_M , is used to match the impedance of the resonant circuit near resonance to the impedance (in our case 50Ω) looking towards the input from resonant the circuit⁷⁶.

3.5 NMR Imaging with a Coaxial Resonator

For the coaxial resonator, we wish to express the rf imaging signal in terms of the cylindrical coordinate system. From Eq. (3.5),

$$S(t) = \int_0^{\infty} \omega_1(r) \rho_{\varphi z}(r) \sin(\omega_1(r)t) r dr, \quad (3.14)$$

where $\rho_{\varphi z}(r)$ is the average volume density taken over a cylinder of radius r and length L given by

$$\rho_{\varphi z}(r) = \frac{1}{2\pi L} \int_0^{2\pi} d\varphi \int_{-L/2}^{L/2} dz \rho(r, \varphi, z). \quad (3.15)$$

We will neglect proportionality constants appearing in front of the integral in the following signal equations. These constants are not essential in the following discussion, so no generality will be lost; we will not, however, neglect proportionality constants appearing inside functions within the integrals.

Using the magnetic field strength indicated in Eq. (3.8), we arrive at the form of the radially dependent nutation frequency

$$\omega_1(r) = \gamma B_\phi = \frac{\gamma \mu I}{2\pi r} = \frac{\gamma g_1}{r}, \quad (3.16)$$

where we are assuming that the current is a constant in the short section of coaxial line used. The gradient g_1 in this case is the derivative of the excitation field with respect to $1/r$ as opposed to r .

Rewriting Eq. (3.14) in terms of ω_1 , Eq. (3.16), yields

$$S(t) = \int_0^\infty \frac{\rho_{\varphi z}(r)}{\omega_1^2} \sin(\omega_1 t) d\omega_1. \quad (3.17)$$

We define the nutation spectrum of $S(t)$ as the sine transform of the signal according to

$$\sigma(\omega_1) \equiv \int_0^\infty S(t) \sin(\omega_1 t) dt. \quad (3.18)$$

Combining Eq. (3.17) and (3.18) provides a relationship between the average radial density and the nutation spectrum.

$$\begin{aligned}\rho_{\varphi z}(r) &= \omega_1^2 \sigma(\omega_1) \\ &= \frac{\sigma\left(\frac{\gamma \mathcal{B}_1}{r}\right)}{r^2}\end{aligned}\quad (3.19)$$

Since the resolution of the nutation spectrum with respect to ω_1 is constant and Eq. (3.16) relating ω_1 to r is non-linear, the resolution of $\rho_{\varphi z}(r)$ with respect to r will not be constant. The radially dependent resolution is

$$\begin{aligned}\delta r &\approx \frac{dr}{d\omega_1} \delta\omega_1 = \frac{r^2}{\gamma \mathcal{B}_1} \delta\omega_1 \\ &\text{for } r \gg \delta r,\end{aligned}\quad (3.20)$$

where $\delta\omega_1$ is the resolution of the nutation spectrum. For data obtained from N time-domain points sampled with a dwell time $\delta\tau$, Fig. (3.2c), Eq. (3.20) becomes

$$\delta r = \frac{2\pi r^2}{\gamma \mathcal{B}_1 N \delta\tau}.\quad (3.21)$$

Therefore, the technique is expected to yield density distributions with considerably better resolution at small radii than at large radii.

The noise power and frequency are also a function of radius for $\rho_{\varphi z}(r)$. Given wide-sense white noise in the nutation spectrum, we see from Eq. (3.19) that the noise variance for $\rho_{\varphi z}(r)$ scales by $1/r^2$ and from Eq. (3.20) that the noise frequency scales by $1/r^2$. These effects are clearly seen in the one-dimensional rf imaging data shown in the next section.

3.6 Experimental Example of One-Dimensional NMR Imaging with a Coaxial Resonator

A cutaway view of the coaxial resonator and a concentric cylinder phantom along with relevant dimensions are shown in Fig. (3.5). More detailed schematics of the resonator and concentric cylinder phantom are given in Appendix A.1. The terminating capacitors are soldered to the end plates, but they are only held to the outer conductor by a metal clamp (not shown). This design allows loading of the sample without having to unsolder the capacitors every time. With the sample loaded, the resonator has a measured Q of ~ 200 . Driving the loaded resonator with a 100 W rf amplifier produces a maximum nutation frequency of 42 kHz at the inner 3.85 mm radius, which implies that the resonator carries a maximum current of 19.2 A according to Eq. (3.16).

The phantom is composed of 94% plexiglass, $\epsilon_r = 2.3$, and 6% water, $\epsilon_r = 80$, so the wavelength of a 185 MHz signal is ~ 61 cm, and the characteristic impedance, Eq. (3.11), is 25Ω . Using these parameters, the dimensions of the resonator shown in Fig. (3.5) and Eq. (3.13), we find that each end of the resonator should be terminated by a capacitance of 147 pF. In practice, we found that a capacitance of 110 pF was sufficient. The discrepancy between the two values may be due to the presence of unaccounted for stray capacitance or an average relative dielectric constant different from the predicted value of $\epsilon_{r,ave} = 7$.

The imaging experiments were performed using the same spectrometer as that described in Section 2.10 operating at 185 MHz. The nutation imaging sequence, Fig. (3.2c), employed 1024 $10 \mu\text{s}$ rf pulses separated by a $90 \mu\text{s}$ delay to allow for data acquisition, probe ringdown, filter rise time and amplifier blanking. Great care is taken to ensure that the static field is spatially homogeneous in the sample region and the excitation pulses are applied on resonance. The time domain signal, $S(t)$, is shown in Fig. (3.6a), and the sine transform of this signal, the spectrum $\sigma(\omega_1)$, is shown in Fig. (3.6b). The

average radial density $\rho_{\varphi z}(r)$ shown in Fig. (3.6c) is obtained from $\sigma(\omega_1)$ using Eq. (3.16) and (3.19).

Because Eq. (3.16) relating ω_1 to r is non-linear, the uniformly spaced points (constant resolution in ω_1) of $\sigma(\omega_1)$ are mapped into the unevenly spaced points of $\rho_{\varphi z}(r)$; see Eq. (3.20) and (3.21). For display uniformity, Fig. (3.6c) actually shows $\rho_{\varphi z}(r)$ defined for evenly spaced points with amplitudes determined by cubic spline interpolation. The true digital resolution at the smallest inner radius, 3.85 mm, is 8.6 μm . Based on the rise of $\rho_{\varphi z}(r)$ at this position, the achieved resolution is approximately 100 μm . Since the root-mean-square displacement due to self-diffusion of the water in the sample is $\sim 20 \mu\text{m}$ over the course of the 102 ms experiment, diffusion accounts for some loss in resolution. In addition, the z dependence of ω_1 due to the finite wavelength of the applied field produces a barrel-shaped as opposed to a purely cylindrical field profile. Thus, a surface of constant ω_1 located at a radius r at the resonator center will constrict slightly inward to $r - \Delta r$ at the resonator ends, where

$$\frac{\Delta r}{r} = 1 - \cos\left(\frac{\pi \delta}{\lambda_r}\right). \quad (3.22)$$

δ is the length of the resonator, and λ_r is the wavelength of the current in the resonator (i.e. the wavelength of the excitation radiation). At the 3.85 mm radius the value of Δr is approximately 10 μm , so the bulk of the 100 μm spread in the signal is likely due to sample or conductor misalignment. In the next section, we will present results from a phantom which better tests the resolution of the apparatus.

The nonuniformity of the noise variance of $\rho_{\varphi z}(r)$ is immediately apparent in Fig. (3.6c). As expected, the noise increases for smaller radial values and the noise frequency decreases.

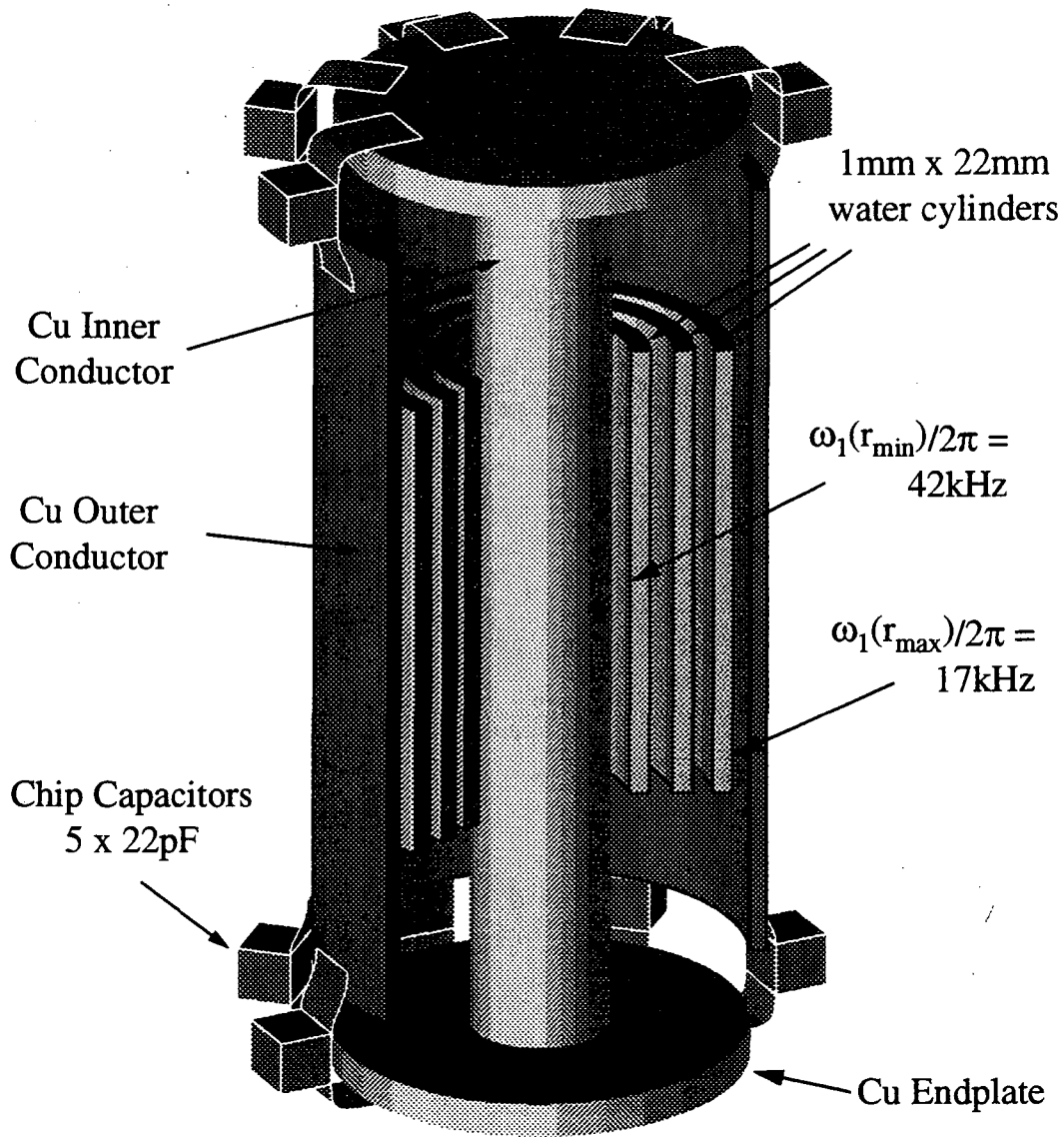


Figure 3.5 Cutaway of coaxial resonator and concentric cylinder phantom. The plastic internal support is not shown. The resonator is 4.45 cm long with a 0.625 cm O.D. inner conductor and a 1.875 cm I.D. outer conductor. The phantom consists of three 1 mm thick, 22 mm long, concentric cylinders of water with inner radii of 3.85, 5.85 and 7.85 mm supported by a plexiglass holder. Each end is shorted to the outer conductor (ground) by five ~22 pF ATC low power chip capacitors. The lower endplate is also shorted to ground by a variable Voltronics capacitor used to balance the capacitance between the two ends.

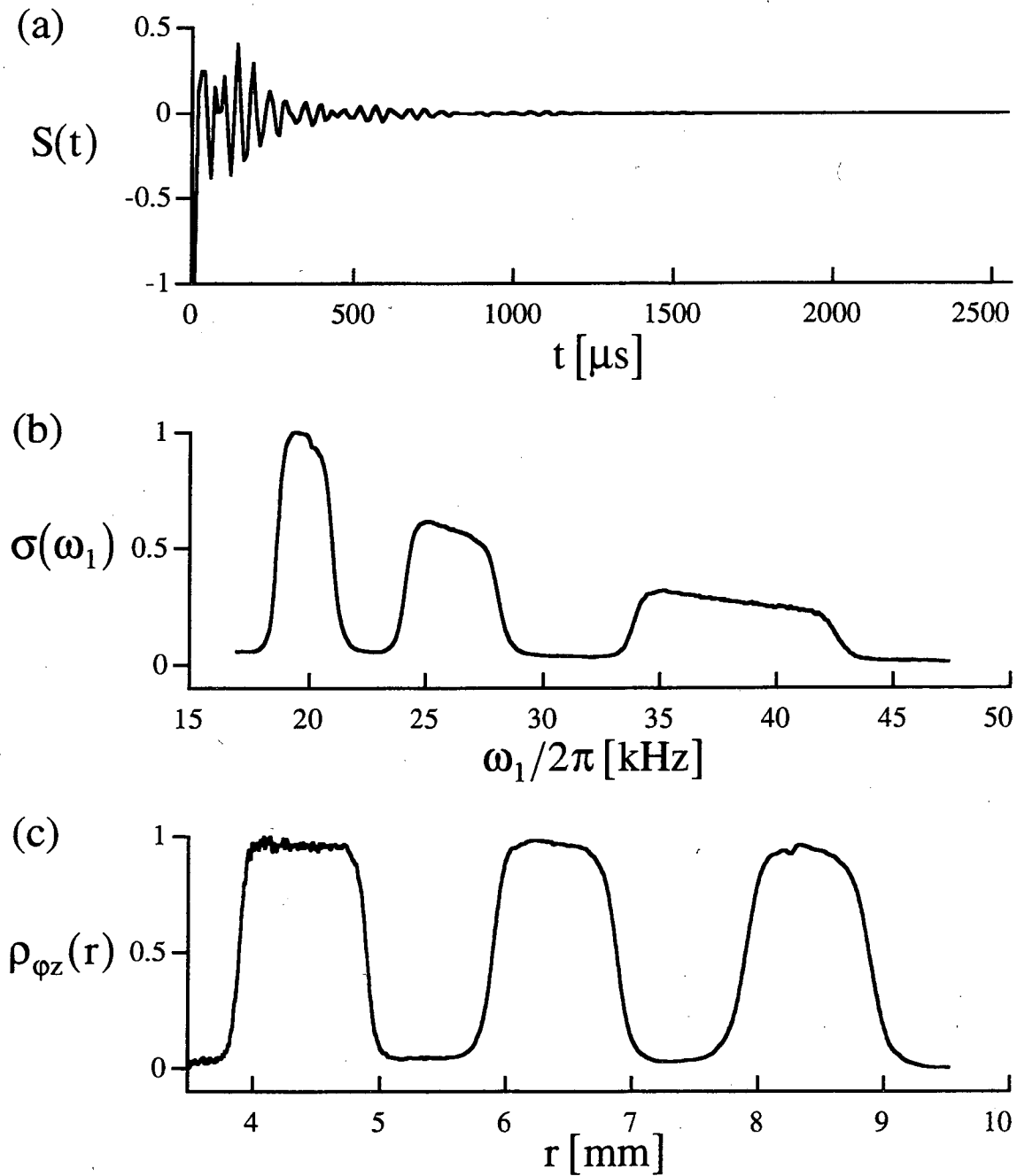


Figure 3.6 One-dimensional rf imaging data for the sample in Fig. (3.5). (a) The first 256 points of the time domain data, $S(t)$, with the time axis labeled according to the total duration of the rf pulses, $10 \mu\text{s}$ each, applied prior to each single point acquisition. (b) The frequency spectrum $\sigma(\omega_1)$ obtained from a sine transformation of $S(t)$. The frequency scale corresponds to the nutation rate of the magnetization about the excitation field. (c) The average radial density distribution, $\rho_{\phi z}(r)$, plotted with respect to the distance from the center of the inner coaxial conductor.

3.7 Experimental Example of Two-Dimensional NMR Imaging with a Coaxial Resonator - Investigation of Achievable Resolution

The phantom and the experimental technique used in the last section do not allow a good test of the spatial resolution achievable by the coaxial resonator system. The concentric cylinder phantom does not possess any features near the size of the digital resolution, and misalignment of the cylinders with respect to the inner conductor may produce large effects upon the apparent resolution. Two phantoms were constructed to address the former problem; see Fig. (3.7). The water in each case is confined between two cylinders, where the outer cylinder has a constant inner diameter, whereas the inner cylinder is tiered with three steps (the top step is not counted, since the water does not go over the top). One phantom has $\sim 25 \mu\text{m}$ steps and the other has $\sim 100 \mu\text{m}$ steps. Schematics of the sample design are presented in Appendix A.2. To address the misalignment problem, we will employ static field gradient imaging along the axial direction in combination with radial rf imaging. Figure (3.8) shows the layout of the two-dimensional imaging pulse sequence used. Note that the rf gradient is used in the phase encoding dimension.

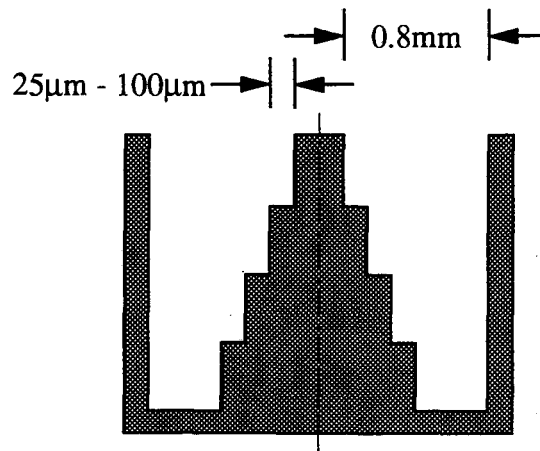


Figure 3.7 Cross sectional view of the circularly symmetric micro-phantom (not to scale). The water sample is placed in the ~ 0.8 mm gap. Steps of $25 \mu\text{m}$ and $100 \mu\text{m}$ provide a fine measure of the technique's resolution. The dashed line indicates the location of the central conductor. Machine shop schematics for the micro-phantom are given in Appendix A.2.

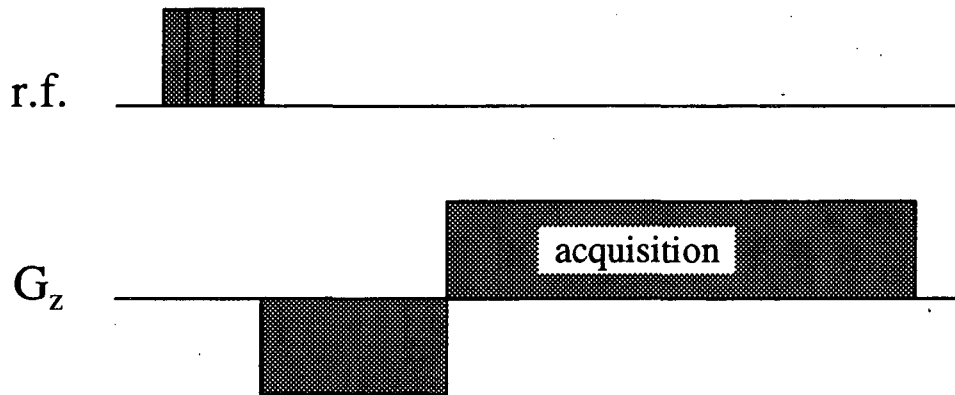


Figure 3.8 Basic layout of a two-dimensional imaging experiment with radial phase encoding by the rf gradient and axial frequency encoding by the static field gradient.

The micro-phantom resonator requires terminating capacitances of ~ 88 pF (compare to the 110 pF required for the concentric cylinder phantom). A reduction in the capacitance, Eq. (3.13), is expected due to an increase in the characteristic impedance of the coaxial line segment. The increase in the characteristic impedance, Eq. (3.11), arises from the decrease in the average relative dielectric constant of the phantom (less water, more plastic) and the decrease in the diameter of the central conductor. See schematics in Appendix A.2.

Results for the $100\ \mu\text{m}$ step phantom using water as a contrast agent, Fig. (3.9), clearly show the three steps, signifying resolution better than $100\ \mu\text{m}$. A number of artifacts appear in the image which are not completely understood. The lack of signal in the top left hand corner could be due to a trapped air bubble, although the gap is so small that any air bubble would be expected to fill the entire $0.8\ \text{mm}$ width. The lower signal level adjacent to the lowest step and the spreading out of the signal to anomalously large radial values at the base are not understood.

For the $25\ \mu\text{m}$ phantom, Fig. (3.10), the steps are clearly seen, however, they appear distorted, with the distortion appearing as a low signal region extending radially outward from the corner of the step, but since the steps are clearly seen, we may conclude a resolution as good as $25\ \mu\text{m}$.

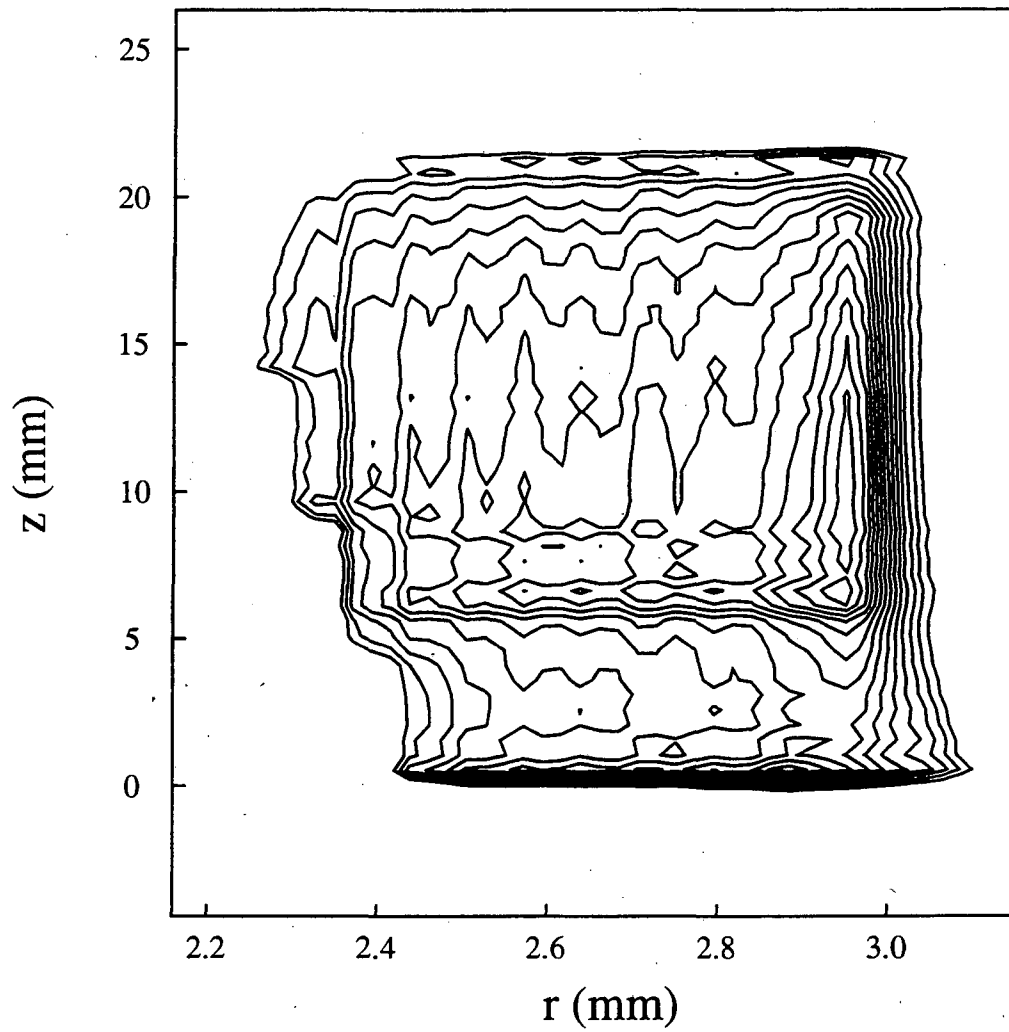


Figure 3.9 Contour plot of a two-dimensional image of the 100 μm step phantom. Compare to Fig. (3.7). Contour levels appear at the 5% levels, beginning at the 20% level.

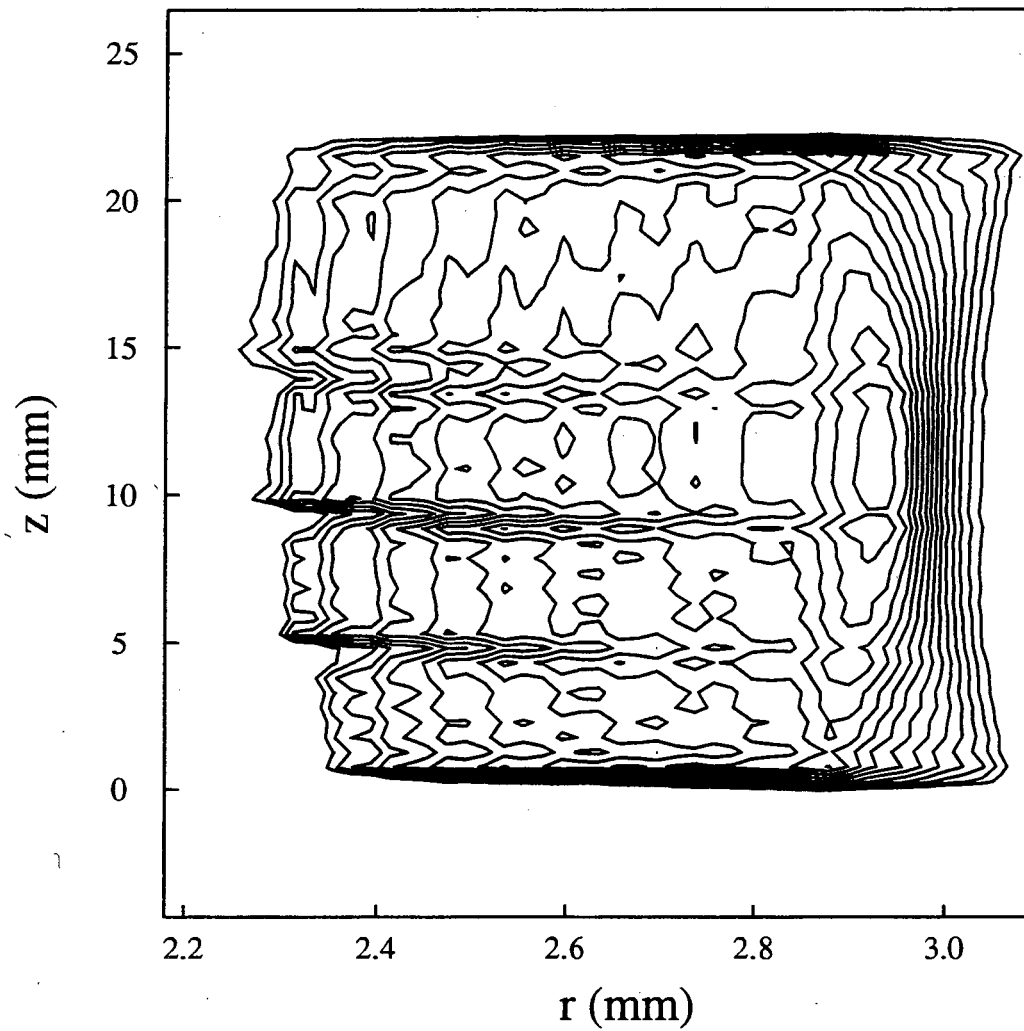


Figure 3.10 Contour plot of a two-dimensional image of the 25 μm step phantom. Compare to Fig. (3.7). Contour levels appear at the 5% levels, beginning at the 20% level.

Further experiments were not done to investigate the image artifacts, so there is little information upon which to make an informed guess as to their origin. Some of the artifacts could be due to static field inhomogeneities, local susceptibility changes or perhaps paramagnetic impurities introduced in the machining process. The results do, however, indicate that the technique has the potential for very good resolution in the radial direction.

3.8 Conclusions

The findings presented here demonstrate the feasibility of high resolution, radial, spatial encoding using a coaxial resonator in conjunction with rf nutation encoding. By taking advantage of the cylindrical symmetry of the system, coaxial resonator imaging is likely to prove useful in the study of Taylor-Couette and other circularly symmetric flows, and the improved resolution at small radii should be useful for imaging boundary layer flow effects. In a broader sense, the work addresses the idea of designing the NMR apparatus around the experiment being performed as opposed to the more common approach of modifying the system to fit the more traditional NMR apparatus.

Chapter 4 Fluid Flow in Porous Media

4.1 Introduction

The mechanics of fluid flow in porous media is of great importance in understanding oil recovery, chemical separation, heterogeneous catalysis, ground water flow and a number of other systems. Classical methods to study flow in these systems generally focus on the long-time, long-distance behavior of the flow. Comprehensive reviews of such methods may be found in the books by Bear⁷⁷, Dullien⁷⁸ and Greenkorn⁷⁹. A few noted exceptions to the long-time long-distance perspective include the investigation of two-dimensional micromodels by Lenormand⁸⁰ and the real time studies of longitudinal and lateral dispersion by Han, et. al.⁸¹

A large number of nuclear magnetic resonance (NMR) techniques have also been employed in the investigation of fluid flow in porous media including straightforward imaging techniques to monitor the movement of fluid in previously unsaturated media⁸²⁻⁸⁵ and in multiphase (e.g. oil and water) systems^{83,86,87}, spatial mapping of velocity⁸⁸⁻⁹⁰, measurement of the transverse displacement probability density for flowing systems⁹¹, and measurement of fluid displacement due to self diffusion^{32-34,92}.

In this chapter, we discuss the application to fluid flow in porous media of a modification of the NMR pulsed gradient spin echo (PGSE) experiment known as the multiple stepped pulsed gradient spin echo technique (MSPGSE). Using MSPGSE, we can generate a series of time resolved fluid displacement distributions in a two-dimensional experiment. The spatial resolution (where by spatial we refer to the displacement dimension) of the technique is on the order of microns, and the flow may be studied for time scales on the order of milliseconds to seconds. With such space and time resolution, we are able to directly observe the evolution of the fluid before random processes have destroyed information about the sample microstructure. Longitudinal (parallel to the flow direction) displacement distributions as well as joint longitudinal-transverse (radial)

displacement correlations of water flow through a packed column of disordered monodisperse polymer microspheres reveal interesting features associated with stagnation in the interparticle volume and the pore structure itself. Although we have not had the opportunity to adequately explore the connection between these results and theoretical predictions, we are convinced that these techniques will be able to provide new and important experimental data useful in understanding the microscopic properties of fluid flow in porous media.

4.2 The PGSE Experiment and Position-Displacement Correlations

Unlike NMR imaging experiments which encode a phase dependent upon spatial location, pulsed gradient spin echo (PGSE) experiments encode a phase dependent upon relative spatial displacement^{27,28}. The most common use of PGSE type experiments is in the measurement of molecular diffusion in a variety of systems, a subject which is reviewed in detail by Kärger⁹³ and Stilbs⁹⁴. In the following study, we intend to apply a modification of the PGSE or stepped PGSE technique to the measurement of coherent flow, so we will not go into detail about the various means of measuring diffusion using the technique.

Consider the stepped PGSE sequence in Fig. (4.1). During the initial gradient pulse, a spin or fluid particle located at x_0 acquires a phase of $\gamma G_x \tau x_0$, the sign of which is reversed after a time $T/2$ by the rf π -pulse located midway between the two gradient pulses. After another delay of $T/2$, the second gradient pulse imparts a phase of $\gamma G_x \tau x_1$ on the spin, where x_1 is the new particle position at the time the second gradient is applied. The total accumulated phase for the spins under consideration is then $\gamma G_x \tau \Delta x$, where

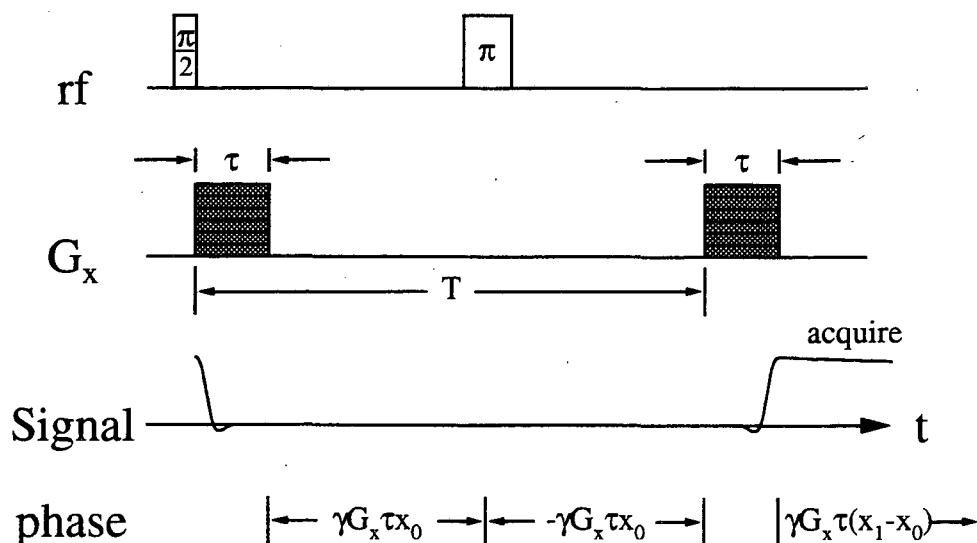


Figure 4.1 PGSE sequence utilizing x encode gradients. The time T is considered to be much greater than the gradient duration τ . Furthermore, motion in the x direction is assumed to be negligible with respect to the displacement resolution during the application of the pulsed gradients.

$\Delta x = x_1 - x_0$. The signal arising from all of the particles initially located near x_0 which have moved a net distance of approximately Δx is then

$$dS(T) = \rho(x_0)P(\Delta x, x_0; T)\exp(i\gamma G_x \tau \Delta x)dx_0 d\Delta x, \quad (4.1)$$

where $\rho(x)$ is the magnetization or sample density and $P(\Delta x, x_0; T)$ is the conditional probability that a particle initially located at position x_0 will undergo a net displacement in the x direction of magnitude Δx in time T . Averaging over all initial positions in the sample and all possible displacements, we obtain the total integrated signal intensity given by

$$S(\gamma G_x \tau, T) = \int_{-\infty}^{\infty} P(\Delta x; T)\exp(i\gamma G_x \tau \Delta x)d\Delta x, \quad (4.2)$$

where

$$P(\Delta x; T) \equiv \int_V \rho(x_0)P(\Delta x, x_0; T)dx_0. \quad (4.3)$$

$P(\Delta x; T)$ is referred to as either the displacement probability density/distribution or averaged propagator²⁸ and, as is apparent from Eq. (4.2), can be obtained from the Fourier transformation of the echo amplitudes obtained by the pulsed gradient experiment, where the gradient strength is incremented in equal steps to provide the traversal of q -space; in analogy to the concept of k -space presented in Chapter 2, we define the quantity

$$q_x \equiv \gamma G_x \tau. \quad (4.4)$$

The Fourier relationship between the signal and the displacement probability density can then be rewritten as

$$S(q_x; T) = \int_{-\infty}^{\infty} P(\Delta x; T) \exp(iq_x \Delta x) d\Delta x, \quad (4.5a)$$

$$P(\Delta x; T) = \int_{-\infty}^{\infty} S(q_x; T) \exp(-iq_x \Delta x) dq_x, \quad (4.5b)$$

where we have purposefully neglected to include any proportionality constants appearing in front of the integrals. Using the stepped PGSE experiment, we are therefore able to directly extract information about mass transport in the system of interest.

The experiment may be extended to more than one spatial dimension by including another pair of pulsed gradients varied independently of the other pairs. In this way, one may acquire the entire three-dimensional displacement probability density. The general form for Eq. (4.5a) and (4.5b) is given by

$$S(\mathbf{q}; T) = \int P(\Delta \mathbf{r}; T) \exp(i\mathbf{q} \cdot \Delta \mathbf{r}) d\Delta \mathbf{r}, \quad (4.6a)$$

$$P(\Delta \mathbf{r}; T) = \int S(\mathbf{q}; T) \exp(-i\mathbf{q} \cdot \Delta \mathbf{r}) d\mathbf{q}, \quad (4.6b)$$

where the integrations proceed over all space or q-space for the necessary number of dimensions (up to three in each case).

Another modification entails combining the basic PGSE sequence with a one, two, or three dimensional imaging sequence to obtain position-displacement correlations in what is sometimes referred to as dynamic NMR microscopy⁹⁵⁻⁹⁷; an example pulse sequence is shown in Fig. (4.2). The point of such an experiment is of course to obtain a spatially

resolved mapping of the displacement probability density, where the form of the time domain signal is given by

$$S(\mathbf{k}, \mathbf{q}; T) = \int \rho(\mathbf{r}) \exp(i\mathbf{k} \cdot \mathbf{r}) \int P(\Delta\mathbf{r}, \mathbf{r}; T) \exp(i\mathbf{q} \cdot \Delta\mathbf{r}) d\mathbf{r} d\Delta\mathbf{r}. \quad (4.7)$$

For the specific case shown in Fig. (4.2) $\mathbf{r} = (y, z)$ and $\Delta\mathbf{r} = \Delta x$ with the corresponding k and q -space variables.

In the instance that the imaging and displacement dimensions coincide, one must insure that negligible motion occurs during the course of the k -space evolution. Frydman et al.^{36,98} have also presented a means of obtaining position-displacement correlations directly from the pulsed gradient spin echo shape using a mixed dimensional approach.

4.3 The MSPGSE Experiment

In order to acquire a one-dimensional displacement distribution for a single flow

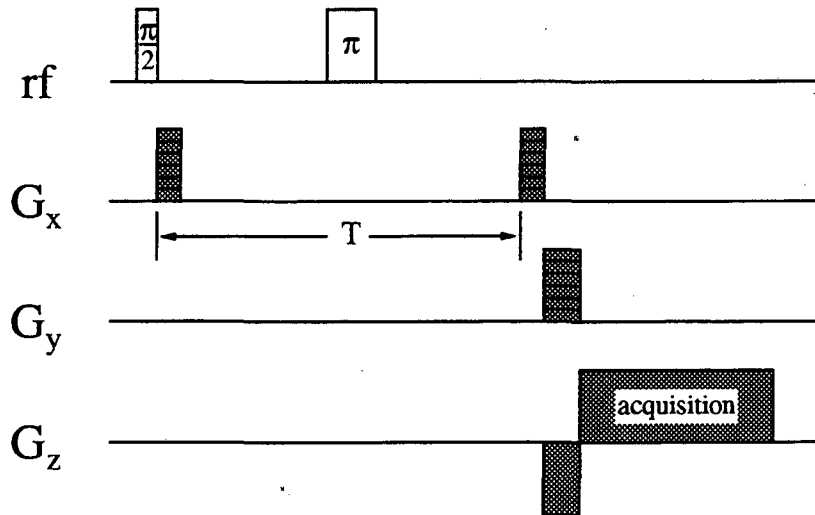


Figure 4.2 Position-displacement correlation sequence. Displacement phase encoding is applied along x , imaging phase encoding is done along the y direction and imaging frequency encoding is done during acquisition along the z direction. No slice selection is explicitly shown during the excitation pulse, but generally one would perform slice-selection of a yz plane.

time, one must perform what is effectively a two-dimensional experiment, since the stepped PGSE experiment provides phase encoding but not frequency encoding. This means that a three-dimensional experiment is required to acquire a time resolved set of displacement distributions in order to characterize the displacement history.

Since it is not clear if it is possible to acquire a single displacement distribution in a one-dimensional experiment, we will investigate a means of acquiring a single point in q -space for a number of evolution times in a one-dimensional experiment. The possibility of repeatedly forming PGSE signals (i.e. constant q value but increasing T) has been discussed by Sotak and Li⁹⁹, who used a related strategy to obtain a pulsed gradient echo train to measure diffusion. Here we discuss stepping the amplitudes of all of the gradient pulses synchronously, as indicated in Fig. (4.3), so that the variation of multiple echo peaks as a function of pulsed gradient amplitude may be used to determine a series of time-resolved displacement distributions in a single two-dimensional experiment.

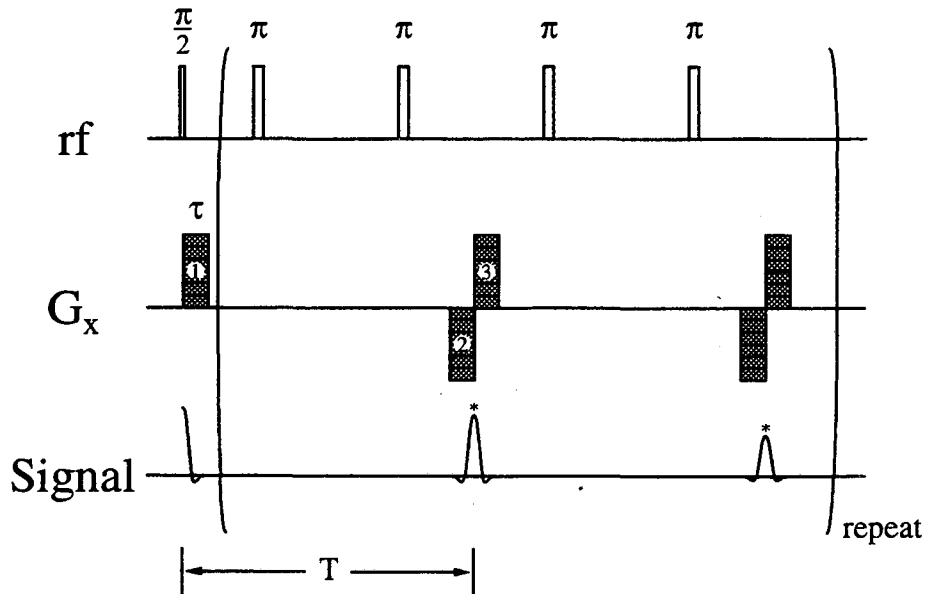


Figure 4.3 Multiple Stepped Pulsed Gradient Spin Echo (MSPGSE) sequence. The region in brackets may be repeated a number of times in order to acquire signal for a number of flow times T . Signal acquisition occurs at *.

Consider the MSPGSE pulse sequence in Fig. (4.3). The sequence begins with a slice selective excitation pulse (slice selection not shown), followed immediately by an encoding gradient (1) of duration τ , so a particle located at x_0 acquires a phase $\gamma G_x \tau x_0$. Since there are an even number of rf π -pulses separating the gradient pulses, gradient (2) has the opposite sign of gradient (1), thus imparting a phase given by $-\gamma G_x \tau x_1$, where x_1 is the position of the particle during the application of gradient (2) - assuming motion is negligible during the application of the gradient. The net phase acquired by the particle of interest at this point is given by $-\gamma G_x \tau \Delta x_1$ where $\Delta x_1 = (x_1 - x_0)$. If we terminate the sequence before gradient (3) and acquire signal for the appropriate range of gradient amplitudes, we will generate the one-dimensional q-space signal for a single time T , cf. Eq. (4.5a). The trick at this point is to apply gradient (3) after gradient (2) to completely negate the phase imposed by gradient (2), so the net phase accumulation after gradient (3) is $\gamma G_x \tau x_0$. If complete cancellation is achieved, it is as if gradients (2) and (3) are not present. We are now free to repeat the series of rf π -pulses followed by the application of a gradient identical to gradient (2), acquire the signal, and then reset the phase to $\gamma G_x \tau x_0$ using a gradient identical to gradient (3). The resulting two-dimensional data set has the form

$$S(q_x; mT) = \int_{-\infty}^{\infty} P(\Delta x; mT) \exp(iq_x \Delta x) d\Delta x, \quad (4.8)$$

where the quantity mT signifies that a series of m time resolved displacement distributions with flow time mT are acquired.

As shown, Fig. (4.3), the MSPGSE sequence contains two rf π -pulses between acquisitions as opposed to the single π -pulse shown in the PGSE sequence, Fig. (4.1). The use of more than one π -pulse between acquisitions is recommended in order to minimize dephasing caused by the particles moving through inhomogeneities in the static

field caused by local internal gradients¹⁰⁰ and poor shimming. For longer flow times, more than two rf π -pulses per acquisition may be inserted. Although the sequence as shown contains an even number of π -pulses, one may also use an odd number; this requires that the sign of gradients (1) and (2) be reversed for the sample acquisitions where m is odd. Because the fluid may move appreciably between subsequent π -pulses, rf homogeneity compensation should be performed within each π -pulse¹⁰¹, rather than between them¹⁰²⁻¹⁰⁴.

In practice, approximately eight points are acquired surrounding the echo maximum in the presence of the gradient (2). Careful centering of the echo insures that the echo maximum is acquired. We have also found that the even number π -pulse version of MSPGSE is inferior to the odd number π -pulse version. If the gradients are not perfectly balanced a small amount of phase will build-up and the echoes will move outside of the assigned acquisition window if one uses the even number π -pulse version. When using the odd number π -pulse version, however, the unwanted phase will be canceled on alternate acquisitions, resulting in no appreciable movement of the echo within the acquisition window.

As with the PGSE experiment, another displacement dimension may be added by applying another set of gradients independently of the first. In the case of a combination of x and y gradients, the multiple flow time q -space signal is given by

$$S(q_x, q_y; mT) = \int_{-\infty}^{\infty} P(\Delta x, \Delta y; mT) \exp(iq_x \Delta x) \exp(iq_y \Delta y) d\Delta x d\Delta y, \quad (4.9)$$

with the inverse q -space Fourier transform of the signal yielding

$$P(\Delta x, \Delta y; mT) = \int_{-\infty}^{\infty} S(q_x, q_y, mT) \exp(-iq_x \Delta x) \exp(-iq_y \Delta y) dq_x dq_y \quad (4.10)$$

An example of this type of experiment is presented in Section 4.8.

4.4. Some Aspects of Fluid Flow in Porous Media

Before proceeding with the NMR results for fluid flow in porous media, we will present some of the basic principles used in describing such flow. The material presented here is very important for understanding the NMR results, but should not be considered a comprehensive summary of the field.

4.4.1 Stochastic Model of Dispersion

In its simplest interpretation, dispersion refers to the fact that some fluid may move farther than other fluid in a flowing system. For laminar pipe flow the fluid in the center of the pipe will move considerably farther than the fluid at the edges (see Section 4.6), hence pipe flow produces dispersion of the fluid. In the absence of diffusion, the dispersion in the pipe flow system is entirely due to the radial velocity gradient which is present due to viscous drag with the pipe walls. Of course, for sufficiently slow flow or for long flow times, molecular diffusion will contribute a substantial amount to the dispersion of the fluid.

For laminar fluid flow in porous media, there exists an additional mechanism for dispersion, tortuosity. Consider the drawing of a porous medium in Fig. (4.4). Two fluid elements, *A* and *B*, start at nearly the same location. The one which begins at *A* takes a relatively straight route along the general direction of the flow (left to right) and ends up at location *A'*. The fluid element starting at *B* takes a more tortuous route ending at point *B'* at the same time that the other element is at *A'*. Both fluid elements have moved nearly the same total distance, but they are displaced from one another both in the direction of the

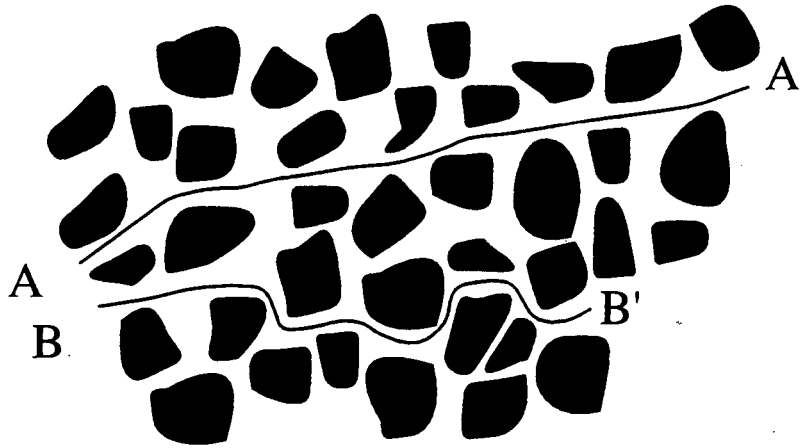


Figure 4.4 An example of the effect of tortuosity in a porous medium. Flow direction is from left to right.

flow and in the direction transverse to the average flow direction. An accumulation of such events can lead to a significant amount of dispersion

A common quantitative description of dispersion for laminar viscous flow in porous media assumes a stochastic model. The individual fluid elements undergo random fluctuations in both transverse and longitudinal displacements. If we consider a dot of tagged fluid inserted in to flow stream, it will spread out or disperse, with the variance of its concentration profile in the longitudinal or x direction given by⁷⁹

$$D_L = \frac{\overline{(\Delta x - v_x T)^2}}{2T}, \quad (4.11)$$

where D_L is referred to as the longitudinal dispersion coefficient, the bar denotes an average over all possible displacements, and v_x is the average longitudinal velocity of the fluid. The term in the numerator is the variance, which may be written as σ_x^2 . The longitudinal displacement distribution is then given by

$$P_L(\Delta x; T) \propto \exp\left(-\frac{(\Delta x - v_x T)^2}{4D_L T}\right), \quad (4.12)$$

which is a Gaussian distribution centered at $v_x T$.

The transverse dispersion coefficient, D_T , is related to the variance in transverse displacements by

$$D_T = \frac{\overline{\Delta y^2}}{2T}, \quad (4.13)$$

and, as in the longitudinal case, the transverse displacement distribution is Gaussian:

$$P_T(\Delta y; T) \propto \exp\left(-\frac{\Delta y^2}{4D_T T}\right). \quad (4.14)$$

One may equally well consider any other direction perpendicular to the x direction for the transverse dispersion.

So, in this stochastic model which naturally assumes flow through a large number of pores (long distance) over a period of time sufficient to traverse said pores (long time), the two-dimensional longitudinal-transverse displacement distribution is a two-dimensional Gaussian given by the product of Eq. (4.12) and (4.14).

4.4.2 Evidence for Deviations from the Stochastic Dispersion Model for Relatively Short Flow Times

For short times and short displacements, Carbonell et al.¹⁰⁵ determined that for a three-dimensional porous system, the longitudinal dispersion coefficient will have the form of Eq. (4.11) if the following condition is satisfied:

$$\frac{D_m t}{l_\beta^2} \gg 1, \quad (4.15)$$

where D_m is the molecular diffusion coefficient of the tracer, t is the time of flow after injection of a tracer into the porous medium, and l_β is a characteristic length associated with the pore spaces in the system. In other words, the longitudinal variance of the displacement distribution will increase linearly with time if Eq. (4.15) is satisfied.

Consider the following specific experiment. An ionic tracer compound is inserted at one end of a column packed with single sized, spherical particles while an effluent is simultaneously pumped through the column. The concentration of the tracer is then measured by a platinum conductivity probe at a fixed axial position as a function of time. If the detector is located a distance L from the injection point, the particles have diameter d , the column has a porosity given by ϕ , the fluid velocity in the longitudinal direction is v_x , and the tracer has a molecular diffusion coefficient in the effluent given by D_m , then Eq. (4.15) may be rewritten for the described apparatus as⁸¹

$$\frac{L}{d} \frac{1-\phi}{\phi} \gg 1, \quad (4.16)$$

where

$$Pe \equiv \frac{v_x d}{D_m} \left(\frac{\phi}{1-\phi} \right). \quad (4.17)$$

Pe is referred to as the Peclet number and is a measure of the relative magnitude of convective and diffusive transport. For such an experiment, the characteristic length l_β is given by

$$l_\beta = d \left(\frac{\phi}{1-\phi} \right). \quad (4.18)$$

For a porous medium not composed of uniform spherical particles, the characteristic length will have a different form.

Han et al.⁸¹ have performed experiments as described in the previous paragraph for a large range of Peclet numbers and a number of values of L , and have concluded that Eq. (4.16) is too restrictive. Their results indicate that one can expect constant longitudinal dispersion coefficients if

$$\frac{L}{dPe} \frac{1-\phi}{\phi} \geq 0.3. \quad (4.19)$$

In Section 4.9, we will present results which indicate that Eq. (4.19) is perhaps too restrictive.

4.4.3 The Peclet and Reynolds Numbers

The longitudinal Peclet number in the form shown in Eq. (4.17) is attributed to Whitaker¹⁰⁶. We may rewrite Eq. (4.17) as the ratio of the time τ_D required for diffusive transport across a pore to the time τ_C required for convective (coherent) transport across the pore as follows:

$$Pe = \frac{v_x l_\beta}{D_m} = \frac{l_\beta^2 / D_m}{l_\beta / v_x} = \frac{\tau_D}{\tau_C} \quad (4.20)$$

In this form, the Peclet number has obvious meaning. When diffusive transport dominates, the Peclet number is small; when convective transport dominates, the Peclet number is large.

Another unitless quantity indicative of the nature of the fluid motion is the Reynolds number, Re , which quantifies the relative strength of inertial and viscous forces in viscous flow. For viscous fluid flow in a porous medium we may define Re by

$$Re = \frac{v_x l_\beta}{\nu}, \quad (4.21)$$

where ν is the kinematic viscosity of the fluid. For Reynolds numbers of approximately 10 or above, the fluid flow is not laminar⁷⁷. For small Reynolds numbers, the fluid flow is laminar and may be considered to be composed of discrete, unbroken streamlines.

4.5 Fluid Flow Apparatus

All pulsed gradient experiments are performed on a Nalorac Cryogenics Quest 4400 spectrometer operating at a proton frequency of 185 MHz. The NMR probe consists of a cylindrical gradient set and is capable of producing, with the amplifiers used, 0.65 T/m static field gradients in all three dimensions. At maximum power, the rise time of the gradients is approximately 100 μ s, which is substantially shorter than the 1 ms gradient pulses used in the experiments reported here.

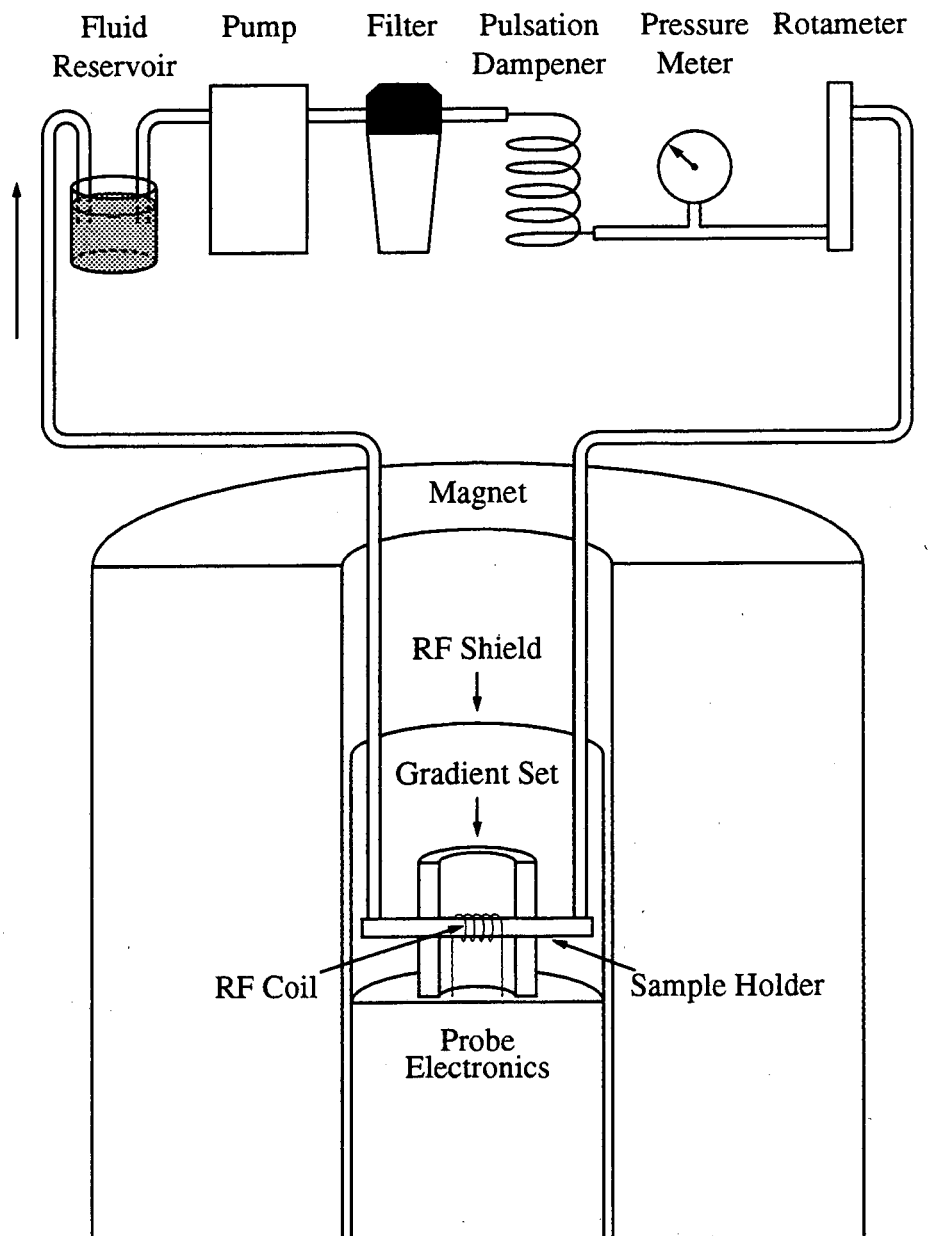


Figure 4.5 Schematic of the fluid flow apparatus showing a cross section through the superconducting magnet and NMR probe. Direction of flow is indicated by arrows on the left and right.

A schematic of the fluid flow system is shown in Fig. (4.5), and detailed drawings of the sample holder assembly are given in Appendix B. Water is pumped from the reservoir using a Rainin Rabbit-Plus™ peristaltic pump with 10 rollers capable of flow rates from 0.0005 to 41.0 ml/min at pressures up to 75 psi. The water is then run through a 10 μm filter followed by a length of Tygon tubing used to minimize the pulsation caused by the peristaltic pump. A rough estimate of the flow rate is given by the flow meter (rotameter), which also indicates the degree of pulsation caused by the pump; the pressure buildup in the line is monitored by the pressure meter inserted before the rotameter. Tygon tubing directs the fluid to the sample column which is inserted in the probe with its long axis perpendicular to the static magnetic field. After exiting the sample, the water is then directed back to the fluid reservoir to be recirculated.

The 6.35 mm inner diameter, 50 mm long sample column contains a porous medium composed of either 140 or 300 μm polystyrene microspheres produced by Duke Scientific. The particles are prevented from exiting the column by the placement of medium coarseness ($\sim 40\text{-}60$ μm hole size) sintered glass frits. In addition to securing the particles, the glass frits distribute the inflow and outflow, thus reducing end-effects caused by the short length of the column and the small input orifice.

The column is prepared by having the particles settle into the water filled cylinder with one of the end pieces (plungers) already screwed in. The holder is then inserted into the probe and the other end is screwed down. By using right handed threads on one end and left handed threads on the other, the plungers may be tightened down by rotating the sample cylinder. Samples prepared in this way are free of bubbles and consistently have a mean porosity between ~ 0.37 and 0.42. Porosity is measured by removing the microspheres at the end of a series of experiments, finding their volume using their weight and the density of polystyrene, subtracting the particle volume from the total volume and then dividing by the total volume of the sample.

In the initial stages of the work, problems were encountered with algae growing in the system and depositing on the inlet glass frit. The deposition created an obstruction to flow, which led to excessive pressures, eventually causing Tygon connections to disconnect and release water into the bore of the magnet. To avoid algae growth, a small quantity of bleach was introduced to the water. In addition, the apparatus was periodically dismantled and carefully cleaned. Other possible impurities were removed by running the sample water through a wound 10 μm filter. Interestingly, a wound cloth filter which was used originally introduced small fibers into the system, creating an obstruction at the glass frit. From this point forward, we used wound polycarbonate filters which did not produce the same problem.

4.6 Longitudinal Displacement Distributions of Laminar Fluid Flow in a Pipe

As a initial test of the system, we applied the MSPGSE technique to fluid flow in an empty pipe. Of course it is also possible to observe the molecular self-diffusion of the water, but the time scales for appreciable diffusive motion are much longer than those anticipated in the porous media experiments.

The velocity profile of a viscous fluid undergoing steady, incompressible, laminar flow in a cylindrical pipe of radius a , Fig. (4.6), is given by¹⁰⁷

$$v(r) = v_{max} \left(1 - \frac{r^2}{a^2} \right), \quad (4.22)$$

$$\text{where } v_{max} = -\frac{a^2}{4\nu} \frac{dp}{dx}.$$

The kinematic viscosity of the fluid is ν and dp/dx is the change in the hydrostatic pressure along the axis of the pipe.

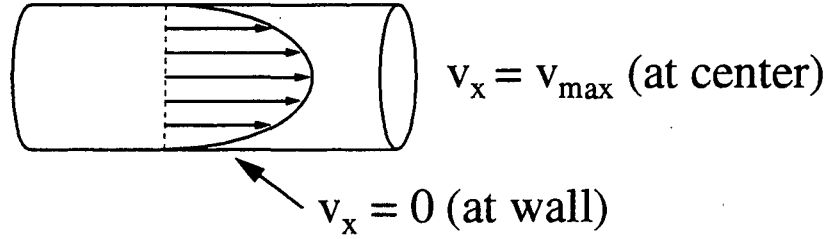


Figure 4.6 Parabolic distribution of axial velocity in pipe flow. Flow direction is from left to right with interior arrows indicating relative velocity.

The task now at hand is to use the relation between the velocity and the radial value in Eq. (4.22) to determine the axial displacement probability density. Since the velocity is assumed to be constant in time, the displacement distribution is proportional to the velocity distribution or spectrum, so we will first determine the functional form of the velocity distribution. The area under the velocity distribution over a range of velocities

$$\Delta v = v(r_1) - v(r_2) \quad (4.23)$$

is equal to the area under the sample radial density distribution over the corresponding radial range

$$\Delta r = r_2 - r_1. \quad (4.24)$$

The previous statement implies that

$$P(v)\Delta v = \rho(r)\Delta r, \quad (4.25)$$

where $P(v)$ is the velocity distribution in units of mass per unit velocity, and $\rho(r)$ is the radial sample density in units of mass per unit length. For a sample of length L with a uniform density, $\rho(r)$ is given by

$$\begin{aligned}\rho(r) &= \int_{-L/2}^{L/2} \int_0^{2\pi} \rho_0 r d\phi dz \\ &= 2\pi L r \rho_0,\end{aligned}\tag{4.26}$$

where ρ_0 is the density of the fluid (mass per unit volume). Since the sample is limited to a cylinder of radius a :

$$\rho(r) = \begin{cases} 0 & r > a \\ 2\pi L r \rho_0 & r \leq a \end{cases}\tag{4.27}$$

Substituting Eq. (4.26) into Eq. (4.25), we have that

$$P(v) = -2\pi L r \rho_0 \frac{dr}{dv},\tag{4.28}$$

where we have gone to the limit of infinitesimal intervals. The minus sign arises from the definitions of the two intervals in Eq. (4.23) and (4.24). Evaluating the derivative and substituting into Eq. (4.28) yields

$$P(v) = \frac{\pi L \rho_0 a^2}{v_{\max}}.\tag{4.29}$$

The corresponding displacement probability density is given by

$$P(\Delta x; T) = \frac{\pi L \rho_0 a^2}{v_{\max} T}.\tag{4.30}$$

Normalizing Eq. (4.30) to one yields the less constant ridded expression

$$P(\Delta x; T) = \frac{1}{v_{max} T}. \quad (4.31)$$

From all of this, we conclude that $P(\Delta x; T)$ for laminar pipe flow in the absence of diffusion is a hat function (rectangle) with amplitude $(v_{max} T)^{-1}$ for displacements from zero to $v_{max} T$ and amplitude zero everywhere else. One may similarly derive the expected displacement distributions for any flow for which the velocity is related to r and $v(r)$ is invertible. Seymour et al.¹⁰⁸ have used this approach to obtain the velocity distributions for power law and Bingham fluids¹⁰⁹ in addition to the Newtonian case presented here.

An experimental example of $P(\Delta x; T)$ for laminar pipe flow is shown in Fig. (4.7). Slice selection of a 2 mm thick slice in the middle of the column perpendicular to the flow direction ensures that the flow has stabilized before entering the region in which the displacement distributions are measured. For the displacement times shown, the

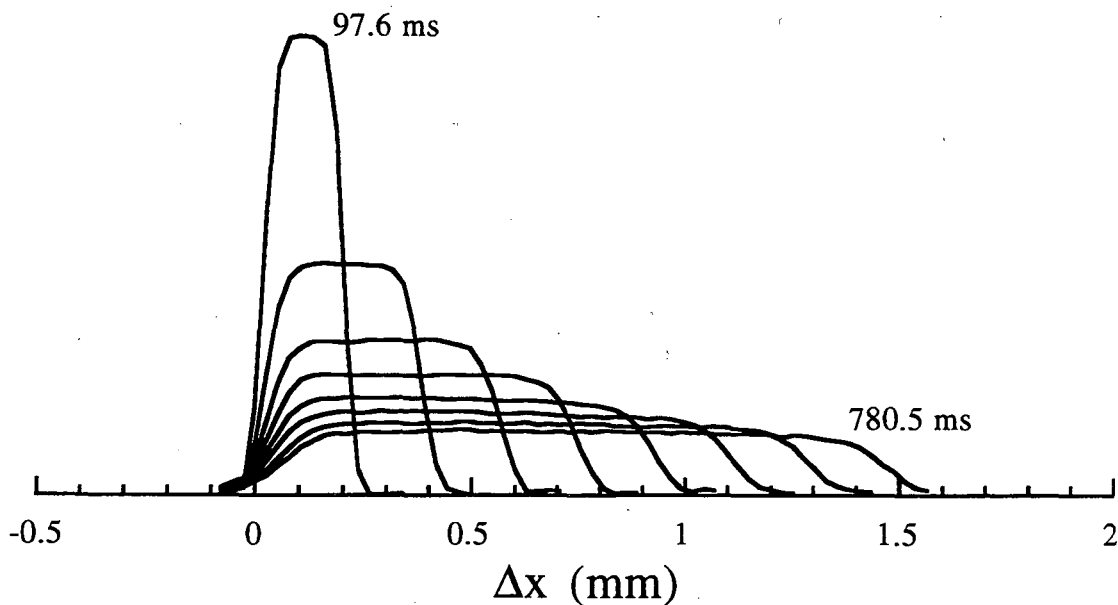


Figure 4.7 Experimentally obtained displacement distributions for laminar fluid flow in a pipe. Distributions shown at 97.6 ms intervals. For clarity, the baseline of each distribution is zeroed below a given threshold.

selected fluid does not move far enough to exit the resonant coil. The data shown are one-half of the distributions acquired using a MSPGSE sequence with π -pulses placed approximately every 8 ms, and an initial encode gradient (gradient (1) in Fig. (4.3)) of 1.0 ms. The displacement times are at 97.6 ms intervals, the average velocity $v_{max}/2$ is 0.95 mm/s, and the digital displacement resolution is 26.1 μm . The rounding of the corners for each distribution is due to both molecular self-diffusion between constant velocity streamlines and along streamlines. These results agree very well with the expected rectangular distributions described above.

4.7 Longitudinal Displacement Distributions of Laminar Fluid Flow in a Porous Medium

Using the MSPGSE sequence and the apparatus described in Section 4.5, longitudinal displacement distributions were acquired for a number of average flow velocities and times, and for both 140 μm and 300 μm diameter particles. In each case a slice of ~ 2 mm thickness is selected perpendicular to the direction of flow, 64 echo peaks are acquired for each displacement distribution, the digital resolution in Δx is 26.1 μm , and the porosity of the sample is ~ 0.38 .

Figure (4.8) shows displacement distributions for the 140 μm particles with a volume flow rate of 3.68 ml/min and a mean flow rate of 5.23 mm/s. The flow time for the first distribution is 16.25 ms and the flow times for the following distributions follow in steps of 16.25 ms. One immediately notices that the short time distributions are distinctly not Gaussian in nature. As the flow develops, peaks with a periodicity of ~ 125 μm appear, with later distributions exhibiting up to three noticeable peaks. The separation of the peaks is close to the expected average separation of void spaces in the sample. In addition to the bumps, the short time distributions are more heavily weighted to short displacements with a long tail extending to larger displacements. For longer flow times, the distributions approach the expected long time Gaussian form.

Figure (4.9) shows displacement distributions for the 300 μm particles with a volume flow rate of 4.07 ml/min and a mean flow rate of 5.56 mm/s. The flow time for the first distribution is 16.25 ms and the flow times for the following distributions follow in steps of 16.25 ms. The same features which appear for the 140 μm particles appear for the 300 μm particles, but they are more pronounced for the larger particles. The periodic structure in this case occurs at ~ 300 μm intervals. One also notices a very distinct peak at zero displacement apparently due to stagnating fluid. This peak disappears for longer flow times. The non-zero density apparent at negative displacements is actually aliasing of the longer time displacement distributions. Aliasing may cause some distortion in the last two distributions, but not in the shorter time data.

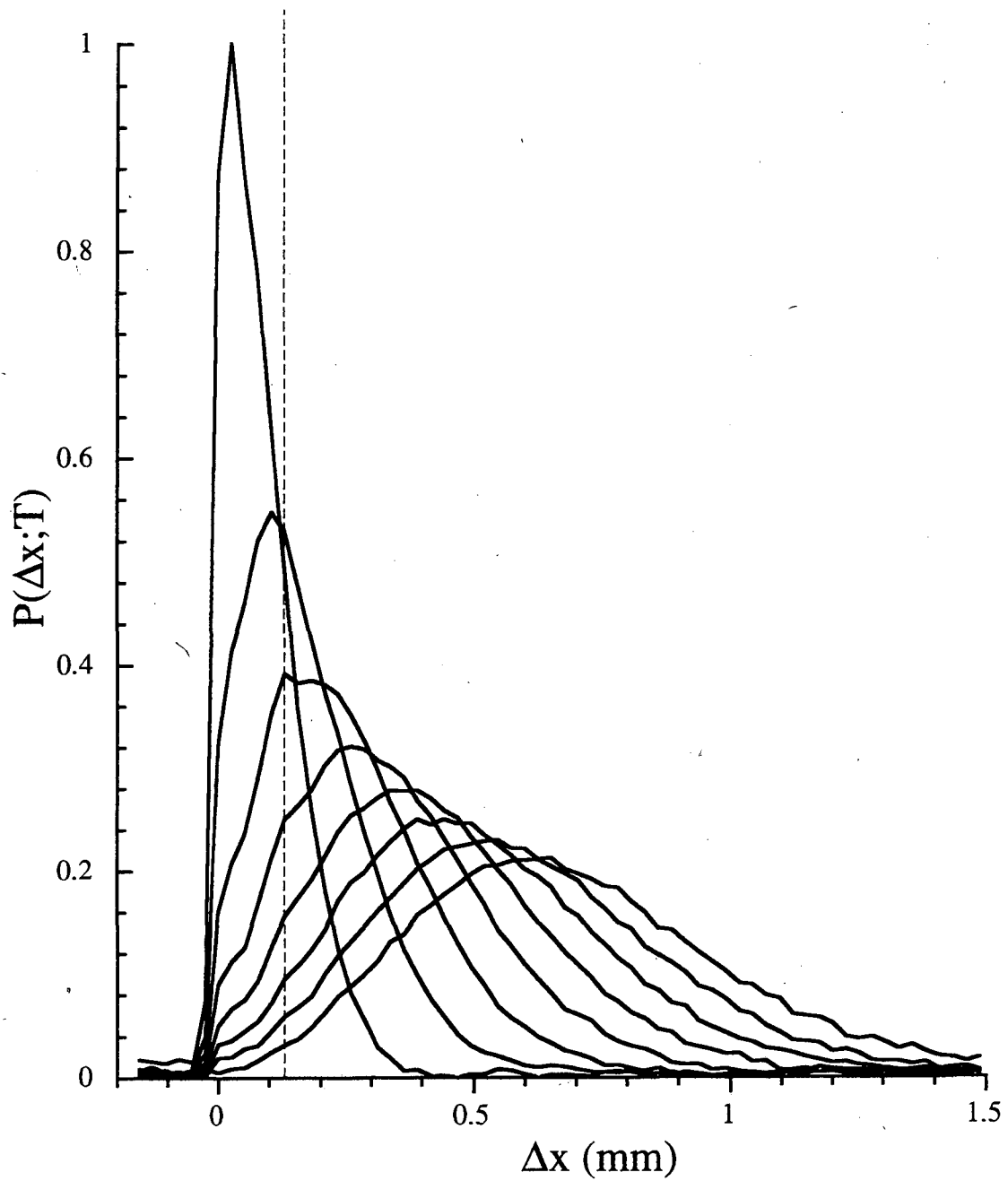


Figure 4.8 Displacement distributions for $140 \mu\text{m}$ particles separated by 16.25 ms each. Volume flow rate = 3.68 ml/min , mean longitudinal flow rate = 5.23 mm/s , porosity = 0.38 , $Pe = 180$, $Re = 0.45$. The dashed line indicates the presence of a structure with a $\sim 125 \mu\text{m}$ periodicity.

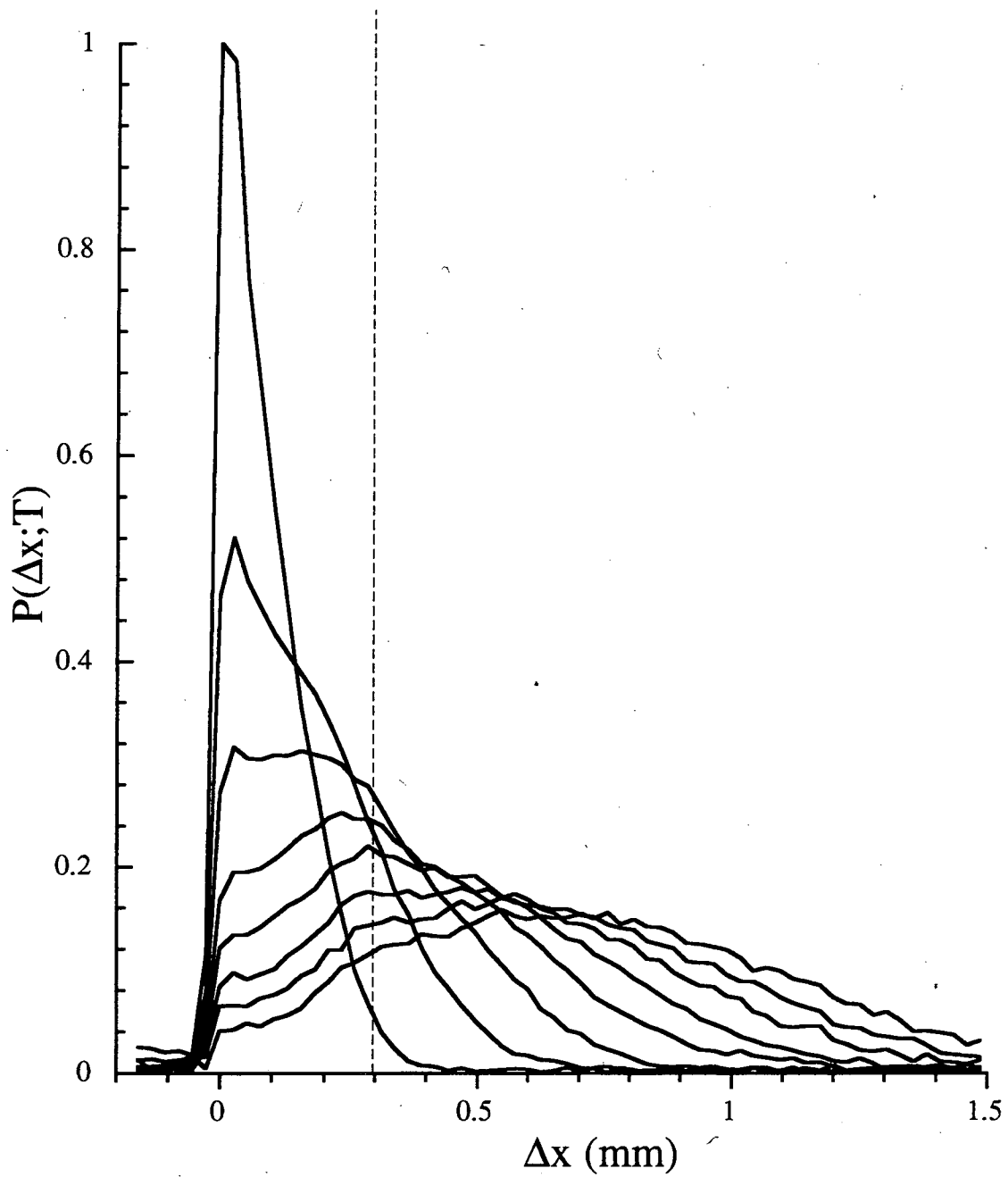


Figure 4.9 Displacement distributions for 300 μm particles separated by 16.25 ms each. Volume flow rate = 4.07 ml/min, mean longitudinal flow rate = 5.56 mm/s, porosity = 0.38, $Pe = 409$, $Re = 1.02$. The dashed line indicates the presence of a structure with a $\sim 300 \mu\text{m}$ periodicity.

The periodic features evident in both Fig. (4.8) and Fig. (4.9) are most probably due to relatively slow motion in the large void spaces between the particles as compared to faster motion in the regions connecting these voids. This implies a system model composed of discrete voids connected by narrow, fast flow channels. Similar features have also been observed in PGSE measurements of displacement distributions for diffusive motion, for which the same physical model of the porous medium is invoked^{33,34}. For diffusive motion in such a system, in the long time limit the displacement distribution approaches the density autocorrelation function of the sample²⁹. These PGSE experiments are generally referred to as dynamic NMR diffraction. Unlike dynamic NMR diffraction, where the equilibrium or long time displacement distribution displays features indicative of inter-pore spacing, the features present in coherent flow through porous media are only present for short time displacements and disappear in the long time limit when the displacement distribution has reached an equilibrium form, i.e. a Gaussian distribution with a linearly increasing variance and mean displacement. The features are not due to any sort of recirculation in the void spaces, since the small Reynolds numbers in each case insure the flow is entirely laminar.

Displacement distributions using the same 300 μm sample as used for Fig. (4.9) were also acquired at slower flow rates in order to determine the dependence of the periodic structures and the "tail" on the mean flow rate. Slow flow experiments were also done on the 140 μm sample and for more flow rates than are shown here; the data shown here is only for the fastest and slowest flow rates used for the 300 μm sample. Two comparisons are shown in Fig. (4.10) with all of the relevant parameters given in the figure caption. In both Fig. (4.10a) and (4.10b), the periodic structure mentioned previously is far more pronounced in the faster flow data. Longitudinal diffusion alone cannot account for these differences, since the root-mean-square displacement due to molecular diffusion which is expected to take place in the time difference between the slow and fast distributions is

$\sim 18 \mu\text{m}$ for Fig. (4.10a) and $\sim 31 \mu\text{m}$ for Fig. (4.10b). Obviously another mechanism is at work.

The likely mechanism for the dramatic difference between the fast and slow flow rate data is diffusion between streamlines; see Fig. (4.11). If there is a large amount of

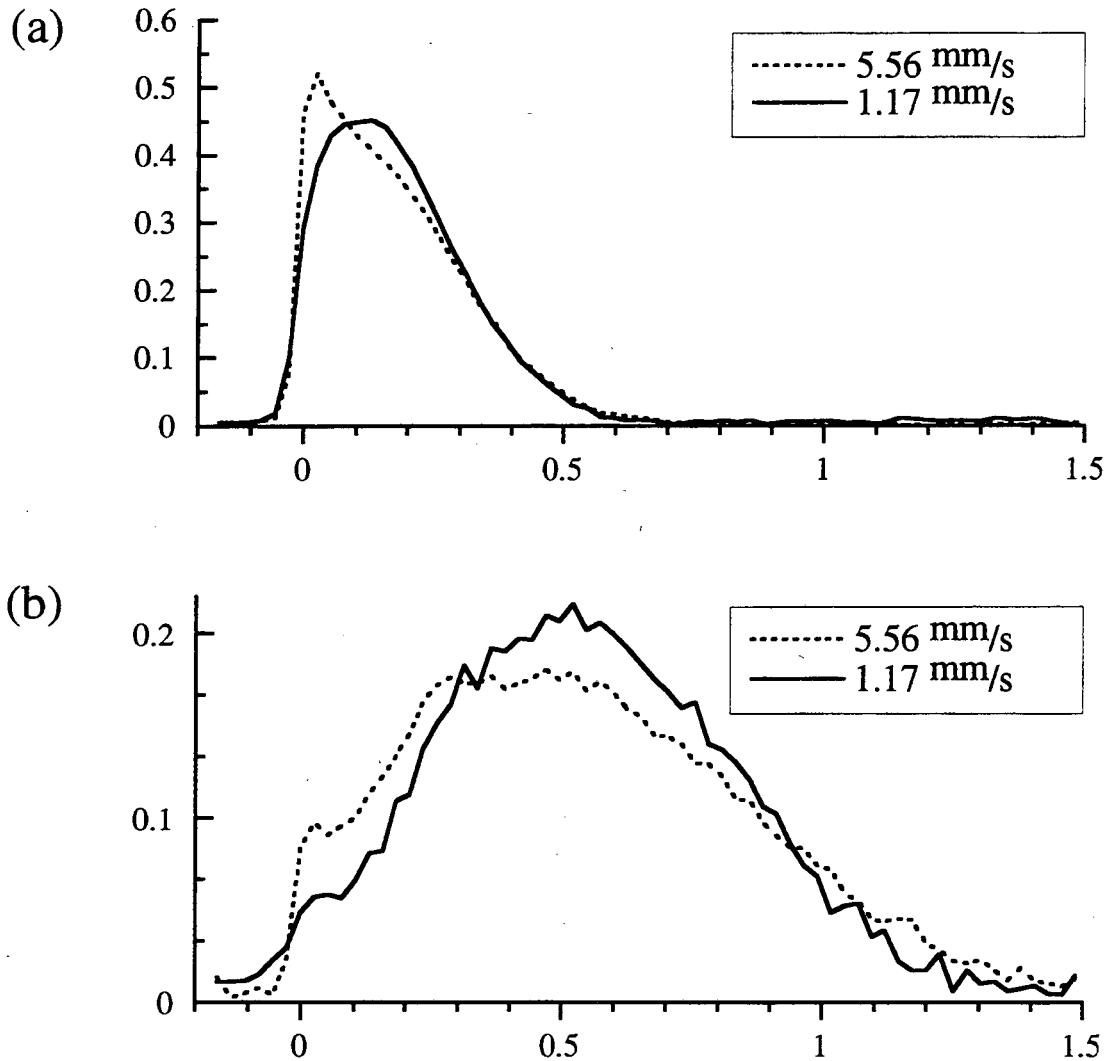


Figure 4.10 Comparison of longitudinal displacement distributions at two different flow rates, 1.17 and 5.56 mm/s. (a) Mean displacement of $\sim 0.19 \text{ mm}$. Faster flow - $Pe = 409$, flow time = 32.5 ms. Slower flow - $Pe = 86$, flow time = 162.5 ms. (b) Mean displacement of $\sim 0.55 \text{ mm}$. Faster flow - $Pe = 409$, flow time = 97.5 ms. Slower flow - $Pe = 86$, flow time = 487.5 ms. Resolution in each case is $26 \mu\text{m}$.

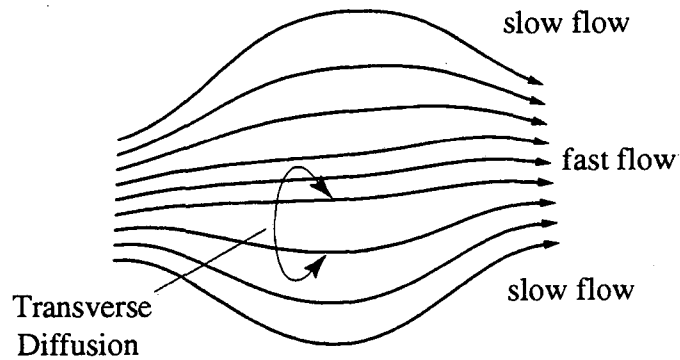


Fig 4.11 Diffusion between adjacent streamlines in a void space. Outer streamlines are assumed to be nearer to the boundaries of the void space and are therefore slower than the streamlines near the center of the flow. For laminar flow, the streamlines are stable and continuous.

shear, inter-streamline diffusion will cause considerable mixing and make the displacement distributions more Gaussian by producing less differentiation between discrete streamlines. This explanation agrees well with the previous explanation for the periodic structures in Fig. (4.8) and (4.9); slow streamlines go quickly through the narrow channels and slow down in the large void spaces, whereas the fastest streamlines go through unimpeded, producing the long displacement tail. Any mixing between streamlines should reduce the periodic structure as well as shorten the “tail”. The tail is definitely shorter for the slower flow data in Fig. (4.10).

4.8 Longitudinal-Transverse Displacement Correlations of Laminar Fluid Flow in a Porous Medium

To gain a more complete picture of the transport in the system, MSPGSE experiments were performed to correlate longitudinal displacements with displacements orthogonal to the flow direction using the multi-dimensional pulse sequence described in Section 4.3.

The displacement distribution referred to in Eq. (4.10), $P(\Delta x, \Delta y; mT)$, is actually a projection along the Δz axis of the full three dimensional displacement distribution $P(\Delta x, \Delta y, \Delta z; mT)$. In light of the obvious cylindrical symmetry of $P(\Delta x, \Delta y, \Delta z; mT)$ about the Δx axis, we may also obtain a slice through the axis of symmetry of $P(\Delta x, \Delta y, \Delta z; mT)$ by applying an inverse Abel transform to $P(\Delta x, \Delta y; mT)$ along the Δy axis (see Section 2.6) with the resulting displacement distribution given by $P(\Delta x, \Delta r; mT)$. In practice, a Hankel transform in q -space along q_y is used as opposed to an inverse Abel transform along Δy . In the following section, examples of both $P(\Delta x, \Delta y; mT)$ and $P(\Delta x, \Delta r; mT)$ for the 140 μm sample described in Section 4.7 will be presented. Similar experiments were also conducted with the 300 μm sample, but the results do not reveal any significant features not present in the 140 μm data.

Figure (4.12) shows a series of six displacement distributions correlating x and y displacements for the 140 μm sample. As one might expect, fluid which has moved only a short longitudinal distance does not move appreciably in the transverse direction. As the fluid progresses farther along the direction of the average flow, the transverse dispersion increases until reaching a maximum. For fluid which has undergone appreciable longitudinal displacement, the transverse dispersion decreases from its maximum. Due to the nature of the contour plots, it is difficult to discern any structure corresponding to the periodic peaks displayed in the longitudinal displacement distributions, Fig. (4.8).

The central $\Delta y = 0$ dataset from each of the two-dimensional plots in Fig. (4.12) is shown in Fig. (4.13). The structure with 125 μm periodicity is much more pronounced

than the equivalent structure in Fig. (4.8) with the 97.5 ms dataset displaying four discernible peaks including the zero displacement peak. Mixed time and displacement domain data (meaning a plot with independent variable axes q_x and Δy) for the 65 ms displacement time indicate that the periodic feature is only present out to $\Delta y = 25 \mu\text{m}$ and has a constant periodicity of $\sim 125 \mu\text{m}$. For all of the flow times, the zero displacement stagnation peak is very prominent. The narrow width of this peak as shown in Fig. (4.12), however, indicates that only a small percentage of the fluid is actually stagnant. Displacement distributions acquired with much longer flow times (not shown) have shown that the peak at zero displacement is below the level of the noise after about 0.25 s of flow at $\sim 5 \text{ mm/s}$, so the stagnation peak is not due to fluid which is completely immobile.

The plots of $P(\Delta x, \Delta r; mT)$ in Fig. (4.14) show considerably more detail than do those of $P(\Delta x, \Delta y; mT)$ in Fig. (4.12); this is to be expected, since the process of projection has a tendency to smooth out details. The $\Delta r = 0$ datasets shown in Fig. (4.15) differ from those in Fig. (4.13) primarily in the height of the stagnation peak. In addition, they are considerably more noisy, due to the unequal treatment of noise by the inverse Abel transform (see Section 2.12.2, in particular Eq. (2.35)).

The periodic structures in Fig. (4.14) appear to extend into the transverse direction for nearly the entire width of the distributions, a phenomenon not present in Fig. (4.12). Line plots of the longitudinal displacement for increasing transverse displacements, Fig. (4.16), better illustrate the radial extent of the periodic features. From the inverse Fourier transform (along the Δx dimension) of the 65 ms displacement distribution in Fig. (4.14), Fig. (4.16), we find that the spacing of the features becomes smaller for increasing transverse displacement with the period equal to $143 \mu\text{m}$ at $\Delta r = 24 \mu\text{m}$, $125 \mu\text{m}$ at $\Delta y = 49 \mu\text{m}$, and $100 \mu\text{m}$ at $\Delta y = 73 \mu\text{m}$. For larger transverse displacements, the signal to noise ratio of the time domain data does not allow an accurate estimate of the feature periodicity in the longitudinal displacement direction.

It is difficult to draw any meaningful conclusions from the results discussed above, since we do not have a theoretical model with which to predict the distributions presented. The very presence of certain features such as the pronounced stagnation peak and the behavior of the periodic structures are very interesting in and of themselves, since we have not found any model in the literature which predicts these features.

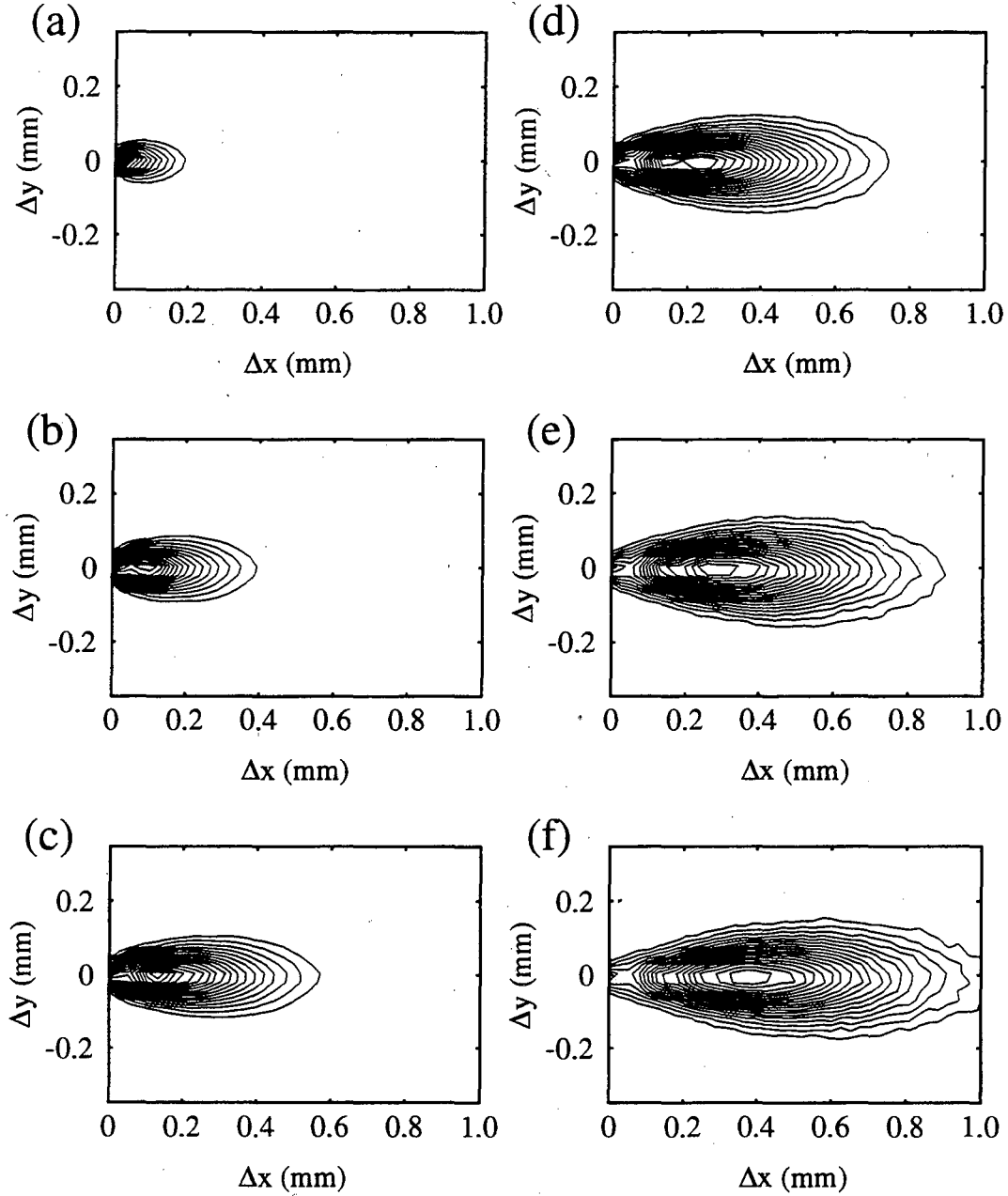


Figure 4.12 $P(\Delta x, \Delta y; mT)$ for $mT =$ (a) 16.25 ms, (b) 32.5 ms, (c) 48.75 ms, (d) 65 ms, (e) 81.25 ms, and (f) 97.5 ms. Mean longitudinal flow rate = 5.25 mm/s, porosity = 0.38, $Pe = 180$, Δx resolution = $26.1 \mu\text{m}$ and Δy resolution = $24.45 \mu\text{m}$. The Δx and Δy axes are scaled equally. Contours at 5% intervals with the lowest contour at 10%. All distributions are normalized to a maximum height of one.

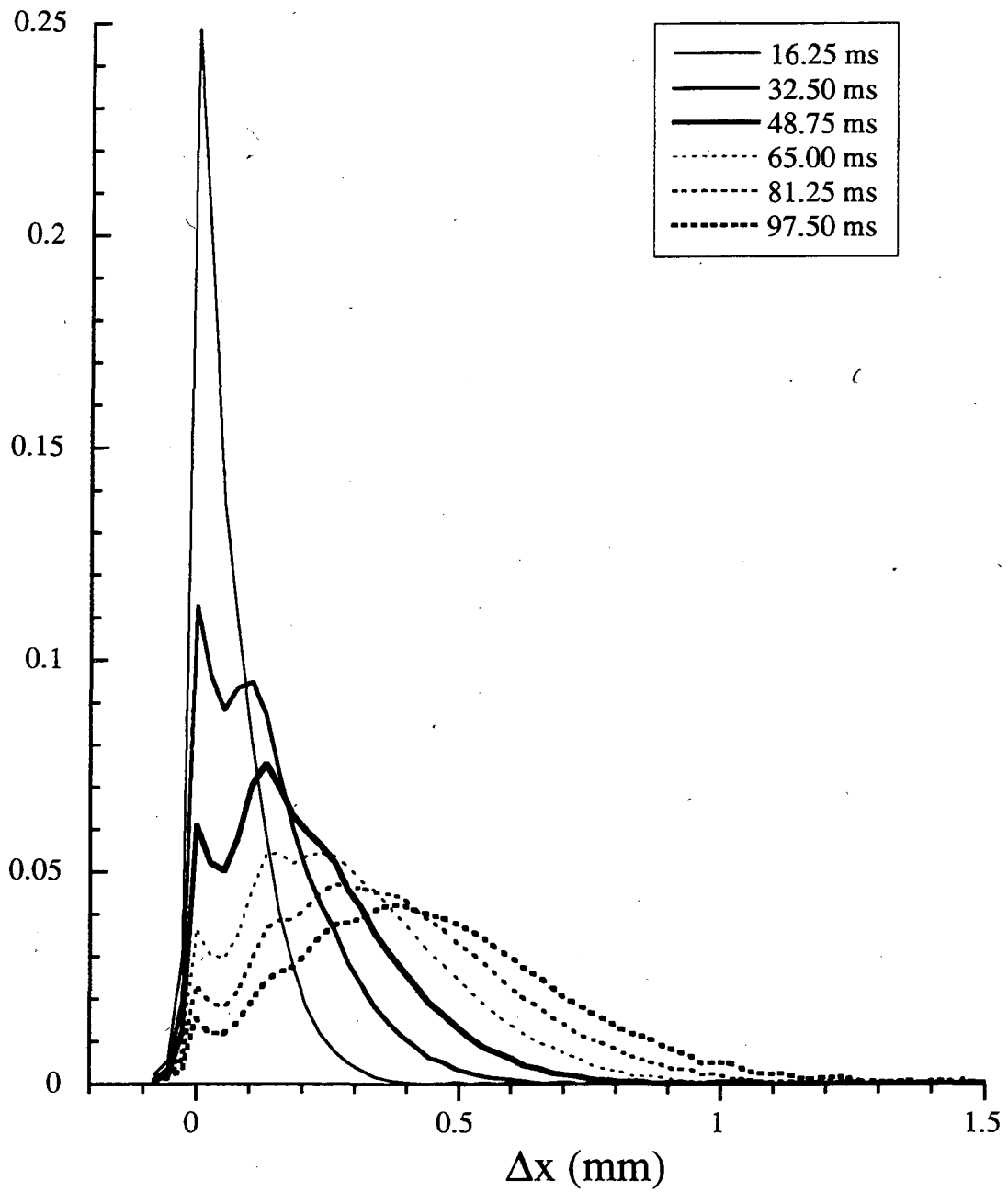


Figure 4.13 $P(\Delta x, \Delta y = 0; mT)$ for the flow times indicated in the legend. Mean longitudinal flow rate = 5.25 mm/s, porosity = 0.38, $Pe = 180$ and Δx resolution = 26.1 μm . The total area of each distribution is normalized to the same value.

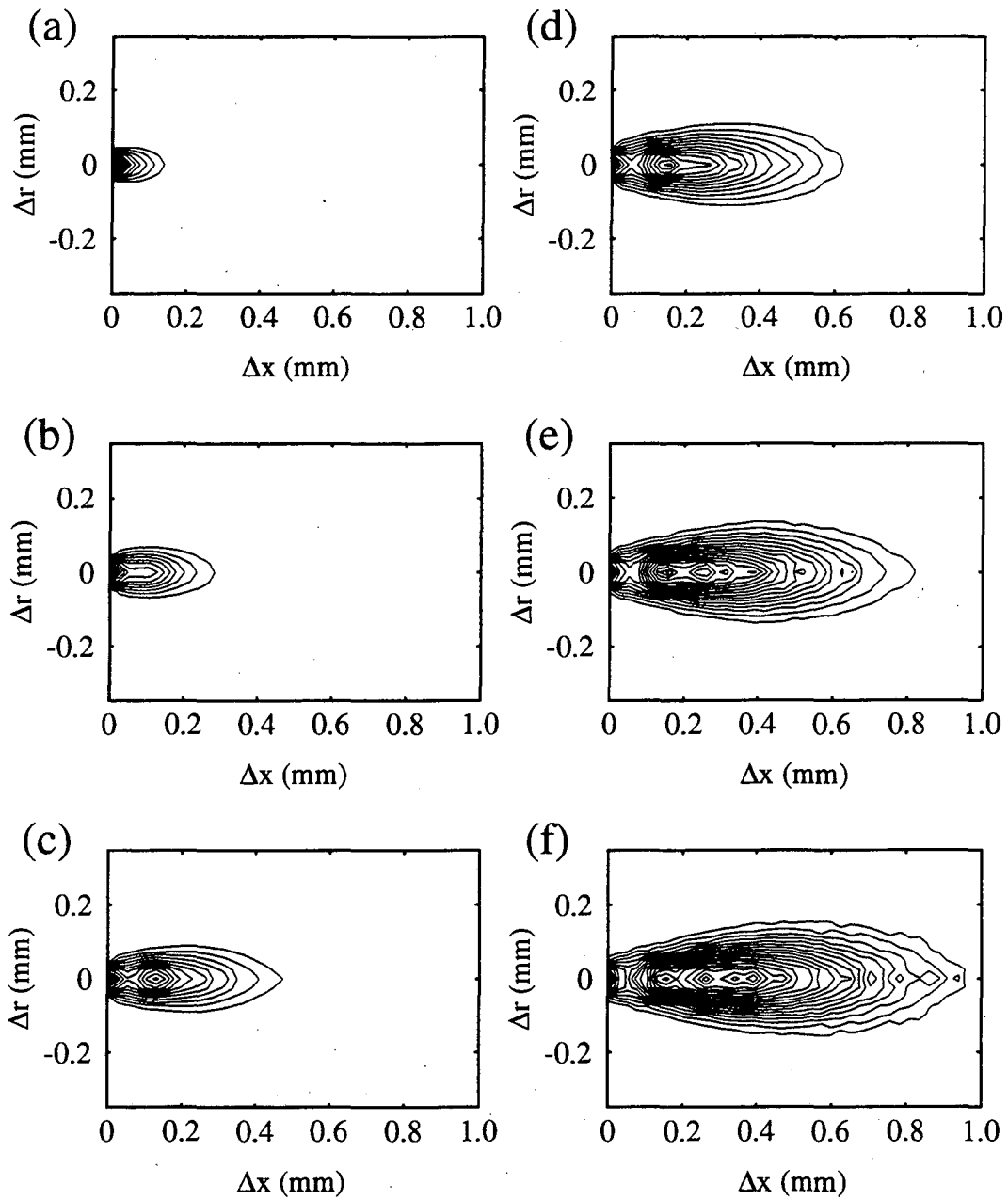


Figure 4.14 $P(\Delta x, \Delta r; mT)$ for $mT =$ (a) 16.25 ms, (b) 32.5 ms, (c) 48.75 ms, (d) 65 ms, (e) 81.25 ms, and (f) 97.5 ms. Mean longitudinal flow rate = 5.25 mm/s, porosity = 0.38, $Pe = 180$, Δx resolution = 26.1 μm and Δy resolution = 24.45 μm . The Δx and Δy axes are scaled equally. Contours at 5% intervals with the lowest contour at 10%. All distributions are normalized to a maximum height of one.

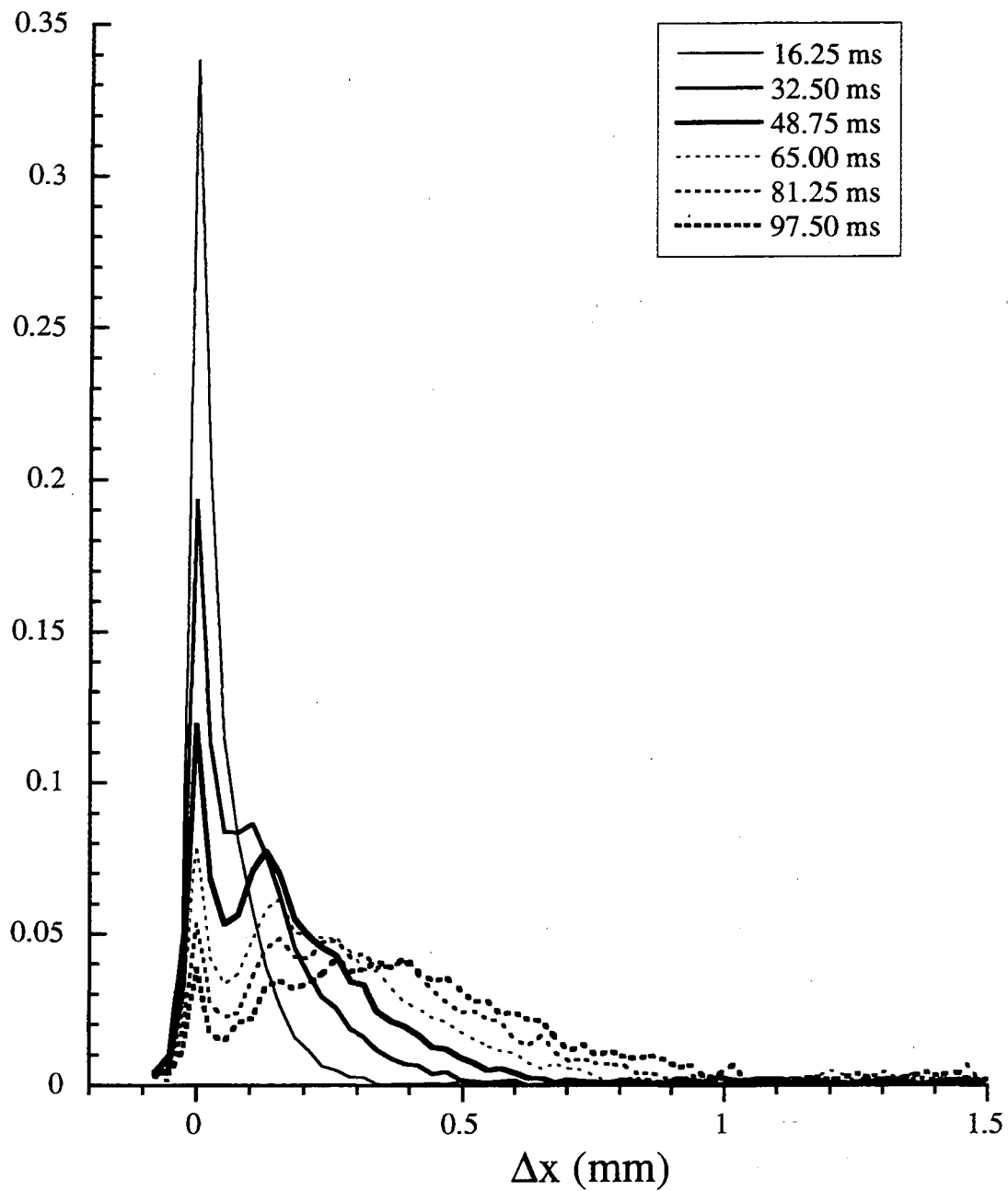


Figure 4.15 $P(\Delta x, \Delta r = 0; mT)$ for the flow times indicated in the legend. Mean longitudinal flow rate = 5.25 mm/s, porosity = 0.38, $Pe = 180$ and Δx resolution = 26.1 μm . The total area of each distribution is normalized to the same value.

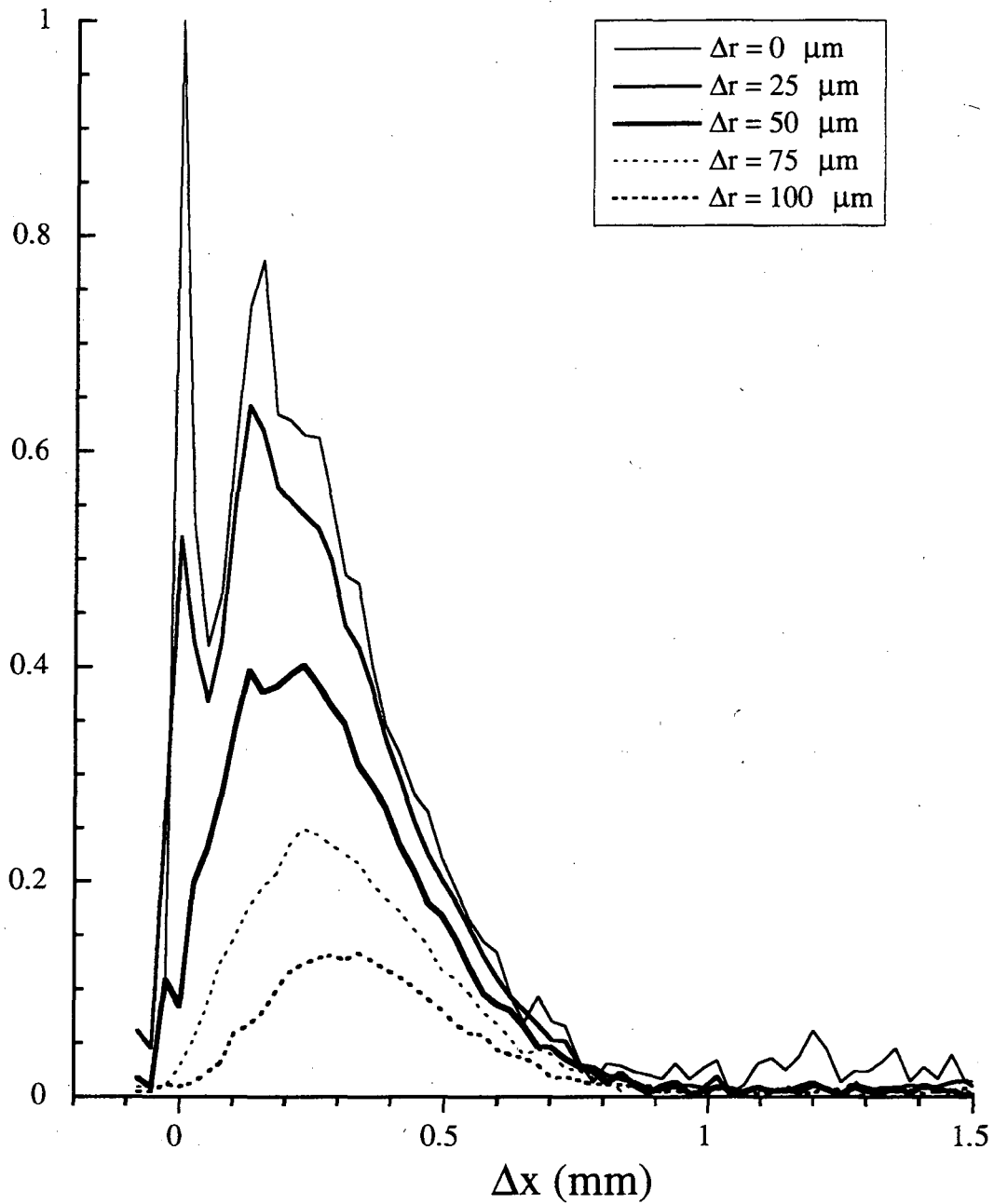


Figure 4.16 $P(\Delta x, \Delta r; mT = 65 \text{ ms})$ for the values of Δr indicated in the legend. Mean longitudinal flow rate = 5.25 mm/s, porosity = 0.38, $Pe = 180$ and Δx resolution = 26.1 μm .

4.9 Experimental Measurement of Non-Linear, Longitudinal Variance Evolution

As was mentioned Section 4.4.2, the variance of the longitudinal displacement distribution is expected to evolve non-linearly in time unless the condition of Eq. (4.19) is satisfied. In this section we present preliminary results of the time evolution of the longitudinal displacement distribution variance, σ_x^2 , for a 140 μm sample at a single flow rate. A more complete study with different particle sizes and flow rates is planned.

In order to apply the condition of Eq. (4.19) to the displacement experiments it is necessary to determine how to measure L . Han et al.⁸¹ measured the concentration of a tracer compound as a function of the flow time, T , at discrete points along the length of a packed column. The time $T = 0$ corresponds to the injection of the tracer into one end of the column, and L is the distance from the injection point of the tracer to the measurement probe. From the resulting time dependence of the concentration a longitudinal dispersion coefficient may then be determined⁷⁹. If the dispersion coefficient depends upon the position L , the system is assumed to not have reached equilibrium. The point in the column at which the flow has reached equilibrium determines the value of the constant on the right hand side of Eq. (4.19). This minimum flow distance we will refer to as L_t where the subscript t refers to the transition between non-equilibrium and equilibrium flow

We will measure the evolution of σ_x^2 as determined from longitudinal displacement distributions such as those in Fig. (4.8) and (4.9) to locate the time T_t when the evolution becomes linear, i.e. equilibrium has been reached. If we take the maximum displacement of the distribution which corresponds to the beginning of linearity (from this point forward this distribution will be referred to as $P_t(\Delta x; T_t)$ or the transition distribution with T_t referred to as the transition flow time) as L_t , we will then be assured of choosing a value of L_t which will produce a condition at least as restrictive as the one measured reported by Han et al.⁸¹. Perhaps a more reasonable choice in our case for L_t is the mean displacement of $P_t(\Delta x; T_t)$, however, the use of the mean displacement will not allow a good comparison with the restriction imposed by Eq. (4.19).

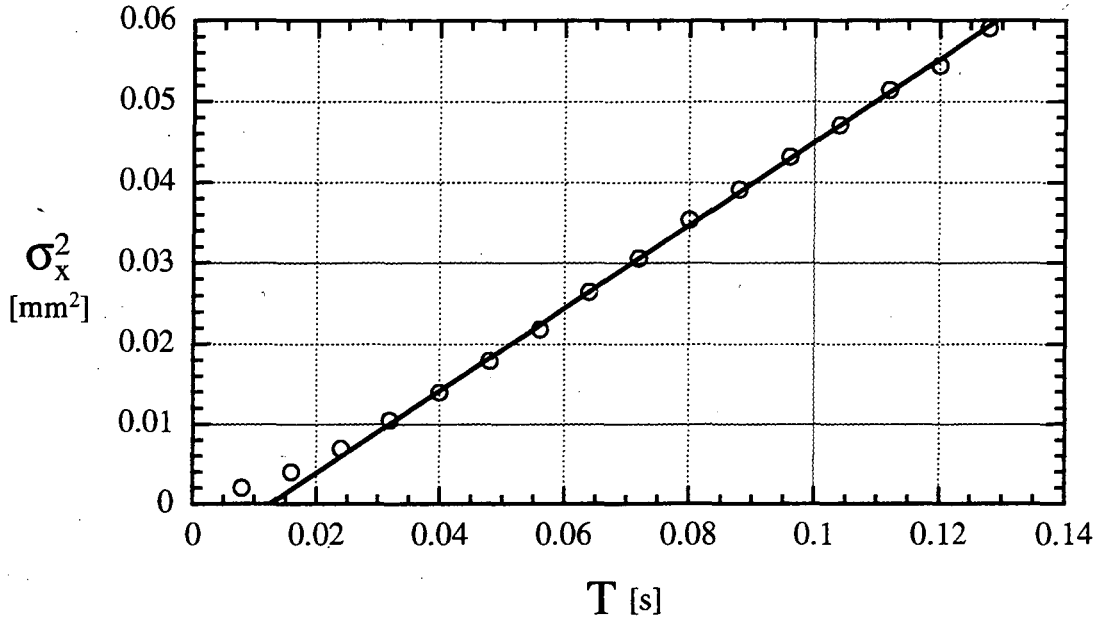


Figure 4.17 Variance of the longitudinal displacement distribution as a function of time. A linear fit to the variance for times greater than and including 0.04 s is shown to guide the eye. For times below approximately 0.04 s, the variance noticeably deviates from the linear assumption. Relevant parameters: particle diameter (d) = 140 μm , porosity (ϕ) = 0.4, mean longitudinal flow rate (v_x) = 4.36 mm/s, Peclet number (Pe) = 162.7.

The variance of the longitudinal displacement distribution $P(\Delta x; T)$ is defined as

$$\sigma_x^2(T) = \frac{\int_{-\infty}^{\infty} (\Delta x)^2 P(\Delta x; T) d\Delta x}{\int_{-\infty}^{\infty} P(\Delta x; T) d\Delta x} \quad (4.32)$$

Using Eq. (4.32), the variance as a function of flow time was determined for a sample containing 140 μm particles with a porosity of ~ 0.4 at an average flow rate of 4.36 mm/s. The results shown in Fig. (4.17) indicate that $T_t \cong 0.04$ s for this system.

Some of the displacement distributions used to compute the variances of Fig. (4.17) are shown in Fig. (4.18). The displacement distribution at $T = 0.04$ s has a

mean displacement of 188 μm and a maximum displacement of approximately 517 μm (the point near the leading edge of the distribution with an amplitude 5% of the maximum). If we choose the maximum displacement value, Δx_{max} , as L_t we have the restriction for equilibrium flow given by

$$\frac{\Delta x_{max}}{dPe} \frac{1-\phi}{\phi} \geq 0.034. \quad (4.33)$$

On the other hand, if the mean displacement, $\overline{\Delta x}$ is used we have the restriction

$$\frac{\overline{\Delta x}}{dPe} \frac{1-\phi}{\phi} \geq 0.012. \quad (4.34)$$

Clearly, the condition imposed by Eq. (4.33) is far less restrictive than that proposed by Han et al.⁸¹, Eq. (4.19). It is possible that in their system, end effects or the invasive nature of the conductivity probe contributed to a much larger value for L_t , however, at this time there is no means of verifying these assumptions. Before making any final conclusions as to the validity of Eq. (4.33) for our system, more measurements need to be done over a large range of Peclet numbers and particle sizes.

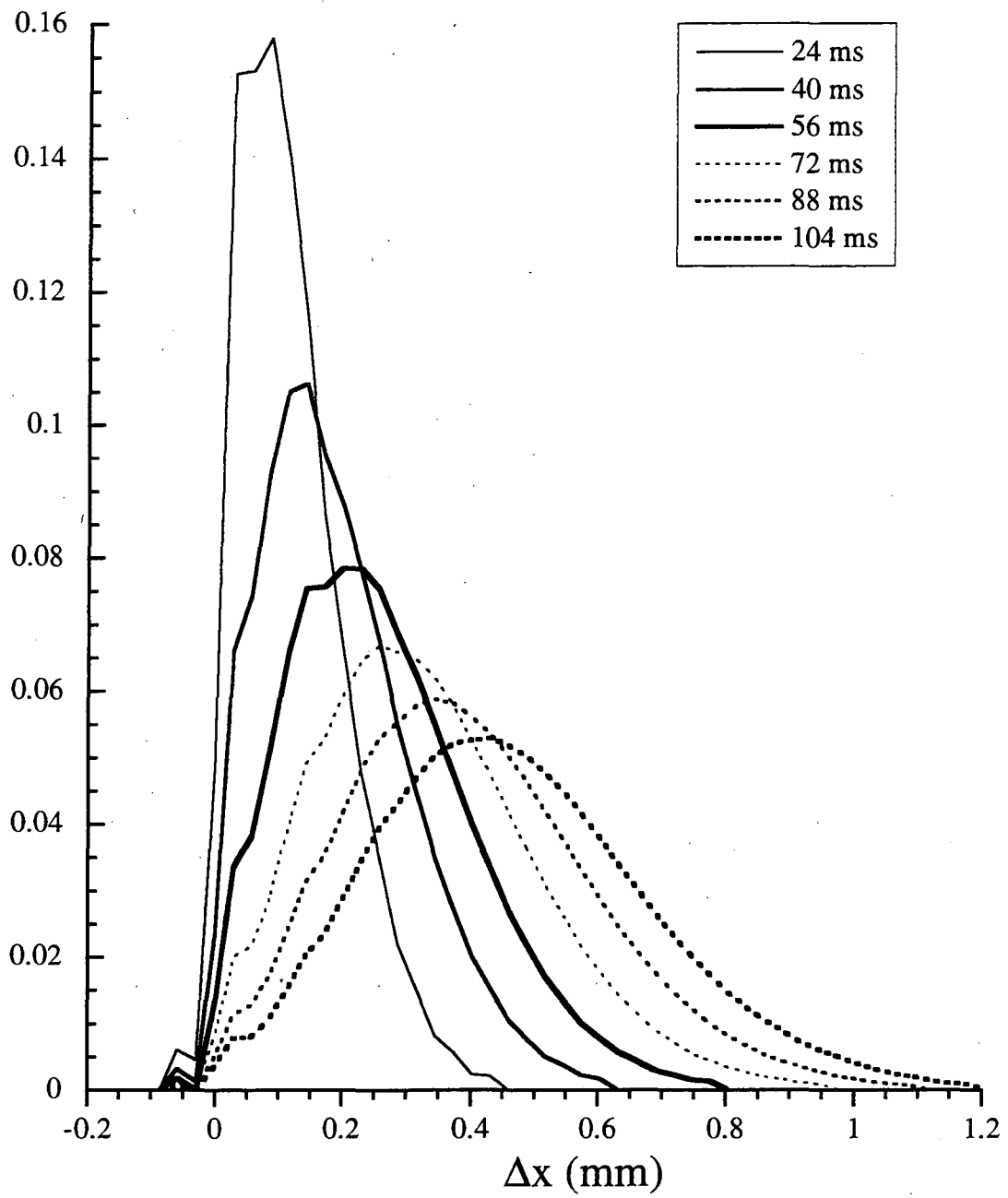


Figure 4.18 Some of the longitudinal displacement distributions used to determined the variance values in Fig. (4.17).

Unexpectedly, the periodic feature described previously is clearly present well after T_1 , so it is not necessary for the displacement distribution to be Gaussian in the region of linearly increasing variance.

4.10 Conclusions

The ability of NMR pulsed gradient techniques to non-invasively probe short time flow phenomena in porous media provides a unique opportunity to efficiently study non-equilibrium fluid dynamics in these systems. Both the longitudinal and joint longitudinal transverse displacement distributions presented here reveal interesting features which reflect the microstructure of the porous medium. These observations have been primarily qualitative, but future results from this technique may provide a means of determining the validity of fluid flow models in the short time and length scale limit. In the one quantitative comparison of these results to another joint theoretical/experimental study, we noted a disagreement between our results and those of another group⁸¹. In light of this discrepancy, further progress should be made to determine the advantages of the techniques presented here to those more commonly applied to the study of fluid flow in porous media.

Chapter 5 Two-Dimensional Exchange NMR Studies of Particle Reorientational Dynamics

5.1 Introduction

Up to this point, all of the techniques developed have employed some sort of gradient in the strength of the static or excitation magnetic field in order to achieve spatial encoding. These techniques are useful for investigating morphology and translational motion, but they are not ideal or in some cases appropriate for the investigation of the reorientational dynamics of small particles. We are particularly interested in measuring particle reorientation as this could prove to be an indirect measure of local vorticity in turbulent flow and also would be valuable in studying particle dynamics in systems with a high particulate concentration. One particularly interesting area is the study of particle reorientation in the flow of suspensions. The effects of particle reorientation in these systems has been studied extensively¹¹⁰⁻¹¹², but the actual reorientational dynamics of the suspended particles has not been experimentally investigated in depth.

In an initial study, we wish to first look at a simple system, which is well understood. This is generally a good philosophy to adhere to when one is developing a new technique. The simplest system which displays some sort of easily understood reorientational dynamics consists of a colloidal suspension of latex spheres which, if small enough, will reorient due to Brownian motion with correlation times on the order of milliseconds. In addition, the equations of motion for the rotational diffusion of spherical particles at low concentration have an analytical solution^{113,114}. To date, dynamic light scattering (DLS) and depolarized dynamic light scattering (DDLS) have been the most widely used experimental techniques to study the dynamics of colloidal suspensions, and have provided a wealth of information about the translational and rotational diffusion of suspended particles and macromolecules¹¹⁵⁻¹¹⁷. The technique, however, suffers from a number of drawbacks. The solution must be free of any impurities which may cause

unwanted scattering, solutions which are opaque to the light source are not accessible, and in order to observe rotational diffusion, the scatterer must be optically anisotropic^{115,116} or have some physical anisotropy. Further complications arise in the study of dense systems which produce large amounts of multiple scattering.

Before proceeding with the background theory necessary to understand the experiments performed, we will consider the line of reasoning used to develop the experiment. The details necessary to explain the line of reasoning will be developed later in this chapter. What we first need is some sort of NMR interaction which has a dependence upon the relative orientation of the static magnetic field. NMR abounds with such interactions including the chemical shift anisotropy (CSA), quadrupolar, and dipolar interactions. For a variety of reasons, we chose to utilize the CSA interaction of the ^{13}C nucleus as our orientation probe. This makes sense, as latex spheres of uniform size are easy to make, and they contain a lot of carbon. There is the little difficulty that they do not contain very much ^{13}C (approximately 1% of naturally occurring carbon is ^{13}C), but one can always make samples enriched in ^{13}C . The experiment could also have been performed using the quadrupole interaction of deuterium¹¹⁸. We chose, however, not to use deuterium as the synthesis of labelled microspheres would have proven to be too difficult.

We will also need an experiment which will yield information about the particle reorientation which we can use in some reasonable way. Two-dimensional exchange NMR spectroscopy has been used by many groups to study the reorientational dynamics of large and small molecules in the solid or near solid state for time scales from milliseconds to seconds¹¹⁹⁻¹²¹. The technique offers a number of advantages to DLS. Chemical selectivity allows the measurement of dynamics in the presence of impurities, the sample need not be optically clear, and solutions of very high concentration may be easily studied. In fact, solutions of high concentration are preferred due to the low sensitivity of the NMR technique.

5.2 Theory - Chemical Shift Anisotropy, Two-Dimensional Exchange NMR and Rotational Diffusion

5.2.1 Introduction

Previous explanations of the nature of the magnetization in NMR have been approached from the classical viewpoint. This was possible since we only had to deal with the dephasing of the magnetization of spin-half nuclei in the presence of a magnetic field gradient of either the static or excitation field. We could treat all of the nuclei as classical dipoles precessing about the static magnetic field at the Larmor frequency. Although one must use quantum mechanics to prove the existence of a nuclear spin¹, once that is done, one can usually treat imaging experiments in a purely classical way. In describing the Hamiltonian for an immobile nucleus possessing a chemical shift anisotropy, we must adopt a quantum mechanical description. I will refrain from going into too much detail in explaining the basic principles necessary for a quantum mechanical treatment of the many Hamiltonian's encountered in NMR, but it is necessary to go over some of the ideas in order to avoid any confusion in interpreting the results derived here, i.e. notational differences, sign conventions, etc.

The conventions used here agree with those used by Haeberlen¹²² and Rose¹²³. For a more detailed description of the following theoretical development, I highly recommend these two books. One will probably notice that Section 4.2.3 follows Haeberlen's work very closely.

5.2.2 Rotations, Euler Angles and Tensors

In order to succinctly describe the orientation of CSA tensors and particles in solution, a standard way of representing orientation must be developed. In NMR and many other fields, the Euler angle representation of orientation is perhaps the most commonly used system. Depending upon which text you read, the conventions will vary

in both the order of rotations, the sign of the rotation and the axis about which any particular orientation occurs. Furthermore, some conventions represent reorientation as the rotation of a physical object from one system to another, whereas others choose to represent the process as the rotation of the coordinate system itself. At least for myself, the conventions used by Rose¹²³ (the former) make the most sense.

Using the three Euler angle rotations, we may represent any arbitrary rotation in three-dimensional space. Figure 5.1 shows the sequence of rotations used to perform an arbitrary rotation of one coordinate system to another. Consider a tensor of rank l with elements given by ψ_{lm} in the (X, Y, Z) coordinate system. In the rotated frame of reference (x'', y'', z'') the interaction has matrix elements R_{lm} given by

$$R_{lm} = \sum_{n=-l}^l \mathcal{D}_{nm}^l(\alpha, \beta, \gamma) \psi_{ln}, \quad (5.1)$$

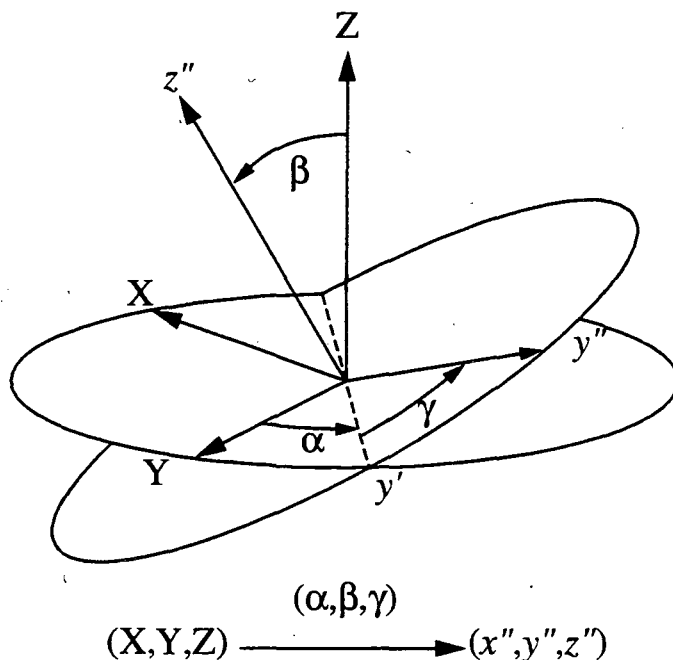


Figure 5.1 Definition of the Euler angle triplet. All rotations are right-handed about the specified axis. The first rotation by α is about the Z axis, the second rotation by β is about the intermediate axis y' , and the final rotation by γ is about the z'' axis. This set of rotations takes the (X, Y, Z) coordinate system into the (x'', y'', z'') coordinate system.

where the term $\mathcal{D}_{nm}^l(\alpha, \beta, \gamma)$ denotes a Wigner rotation matrix element. The rotation matrix elements may be written in terms of the reduced Wigner rotation matrix elements, $d_{mn}^l(\beta)$.

$$\mathcal{D}_{nm}^l(\alpha, \beta, \gamma) = \exp(-im\alpha) d_{mn}^l(\beta) \exp(-in\gamma) \quad (5.2)$$

A list of the reduced Wigner rotation matrix elements of rank 2 is given in Table (5.1). We are only concerned here with zero and second rank matrix elements as these are the only terms which will be of interest in the derivation of the CSA Hamiltonian. The zero rank rotation matrix is a scalar with a value equal to one.

The Wigner rotation matrix elements are not normalized to one, however, they are orthogonal. The orthogonality relation over the unit sphere is expressed in the form

$$\int d\bar{\Omega} \mathcal{D}_{m'n'}^l(\bar{\Omega}) \mathcal{D}_{mn}^l(\bar{\Omega})^* = \frac{8\pi^2}{2l+1} \delta_{l'l} \delta_{m'm} \delta_{n'n}, \quad (5.3)$$

n	m				
	2	1	0	-1	-2
2	$\frac{(1+\cos\beta)^2}{4}$	$-\frac{1+\cos\beta}{2} \sin\beta$	$\sqrt{\frac{3}{8}} \sin^2\beta$	$-\frac{1-\cos\beta}{2} \sin\beta$	$\frac{(1-\cos\beta)^2}{4}$
1	$\frac{1+\cos\beta}{2} \sin\beta$	$\cos^2\beta - \frac{1-\cos\beta}{2}$	$-\sqrt{\frac{3}{8}} \sin 2\beta$	$\frac{1+\cos\beta}{2} - \cos^2\beta$	$-\frac{1-\cos\beta}{2} \sin\beta$
0	$\sqrt{\frac{3}{8}} \sin^2\beta$	$\sqrt{\frac{3}{8}} \sin 2\beta$	$\frac{3\cos^2\beta - 1}{2}$	$-\sqrt{\frac{3}{8}} \sin 2\beta$	$\sqrt{\frac{3}{8}} \sin^2\beta$
-1	$\frac{1-\cos\beta}{2} \sin\beta$	$\frac{1+\cos\beta}{2} - \cos^2\beta$	$\sqrt{\frac{3}{8}} \sin 2\beta$	$\cos^2\beta - \frac{1-\cos\beta}{2}$	$-\frac{1+\cos\beta}{2} \sin\beta$
-2	$\frac{(1-\cos\beta)^2}{4}$	$\frac{1-\cos\beta}{2} \sin\beta$	$\sqrt{\frac{3}{8}} \sin^2\beta$	$\frac{1+\cos\beta}{2} \sin\beta$	$\frac{(1+\cos\beta)^2}{4}$

Table 5.1 Reduced Wigner rotation matrix elements of rank $l=2$, $d_{mn}^l(\beta)$. A means of generating all possible matrix elements is given in Rose¹²³.

where $\bar{\Omega} = (\alpha, \beta, \gamma)$, the differential $d\bar{\Omega} = \sin(\beta)d\alpha d\beta d\gamma$, and the integration proceeds from 0 to 2π for α and γ , and from 0 to π for β . The δ_{mn} terms are the Dirac delta function which is zero for $m \neq n$ and one for $m = n$.

5.2.3 Chemical Shift Anisotropy

The chemical shift (CS) interaction refers to the magnetic coupling between the orbital angular momentum of the electrons and the nuclear spin angular momentum¹²⁴. The magnetic field produced by the orbital angular momentum of the electrons effectively changes the local field of the nucleus producing a shift in the resonant frequency, hence the name chemical shift.

The CS Hamiltonian in the laboratory system, LS, which is defined by the orientation of the static magnetic field may be written in the the form

$$H_{cs} = \gamma \mathbf{I} \cdot \bar{\sigma} \cdot \mathbf{B}_0, \quad (5.4)$$

where \mathbf{I} is the angular momentum operator, \mathbf{B}_0 is the static magnetic field, and $\bar{\sigma}$ is the second rank CS or CSA tensor for a given nuclear site. It perhaps has more meaning if we note that $-\bar{\sigma} \cdot \mathbf{B}_0$ is the magnetic field induced by the nearby electrons at the nucleus.

For our purposes, Eq. (5.4) is not immediately useful and may be rewritten as

$$H_{cs} = \gamma \sum_{\alpha, \beta=1}^3 \sigma_{\alpha\beta} T_{\beta\alpha}. \quad (5.5)$$

The terms $T_{\beta\alpha}$ are elements of the dyadic product of the angular momentum vector and the static field vector. $\sigma_{\alpha\beta}$ is an element of the second rank reducible chemical shift tensor, $\bar{\sigma}$, which is diagonal in the chemical shift principal axis system, PAS_{cs} . The diagonal elements are referred to as σ_{xx} , σ_{yy} , and σ_{zz} , where by convention

$$|\sigma_{zz} - \sigma| \geq |\sigma_{yy} - \sigma| \geq |\sigma_{xx} - \sigma|$$

$$\text{with } \sigma = \frac{1}{3} \text{Tr } \bar{\bar{\sigma}}.$$
(5.6)

In order to more conveniently manipulate the chemical shift Hamiltonian, it is desirable to rewrite Eq. (5.5) in terms of irreducible spherical tensor operators¹²³. In doing so, we arrive at the relation

$$H_{cs} = \gamma \sum_l \sum_{m=-l}^l (-1)^m R_{l,-m} T_{lm}$$
(5.7)

where the terms R_{lm} come from $\sigma_{\alpha\beta}$ and the terms T_{lm} from $T_{\beta\alpha}$. As $\bar{\bar{\sigma}}$ is a symmetric second rank cartesian tensor, only terms with $l = 0, 2$ will be nonzero. The components R_{lm} in PAS_{cs} are given by

$$\rho_{00} = \frac{1}{3} \text{Tr } \bar{\bar{\sigma}} = \sigma,$$

$$\rho_{20} = \sqrt{\frac{3}{2}} (\sigma_{zz} - \sigma) = \sqrt{\frac{3}{2}} \delta,$$

$$\rho_{2\pm 2} = \frac{1}{2} (\sigma_{yy} - \sigma_{xx}) = \frac{1}{2} \eta \delta,$$
(5.8)

where σ is the isotropic chemical shift, δ is the chemical shift anisotropy, and η is the assymetry parameter. We may relate the terms R_{lm} in the laboratory system, LS, to the terms ρ_{lm} in PAS_{cs} by rotating PAS_{cs} into the LS using Eq. (5.1).

$$R_{lm} = \sum_{n=-l}^l \mathcal{D}_{nm}^l(\bar{\bar{\Omega}}) \rho_{ln},$$
(5.9)

where we now use $\bar{\bar{\Omega}}$ as the relative orientation of PAS_{cs} with respect to the LS.

The irreducible tensor elements, T_{lm} , with $l = 0, 2$ are given by

$$\begin{aligned}
 T_{00} &= I_0 B_0, \\
 T_{20} &= \sqrt{\frac{2}{3}} I_0 B_0, \\
 T_{2\pm 1} &= \frac{1}{\sqrt{2}} I_{\pm 1} B_0, \\
 T_{2\pm 2} &= 0,
 \end{aligned} \tag{5.10}$$

where

$$\begin{aligned}
 I_0 &= I_z, \\
 I_{+1} &= -\frac{1}{\sqrt{2}} (I_x + iI_y), \\
 I_{-1} &= \frac{1}{\sqrt{2}} (I_x - iI_y).
 \end{aligned} \tag{5.11}$$

Substituting Eq. (5.9) as well as the expressions for T_{lm} into Eq. (5.7), we arrive at the expression

$$H_{cs} = \gamma B_0 I_0 \left[\sigma + \delta \left(\mathcal{D}_{00}^2 + \frac{\eta}{\sqrt{6}} (\mathcal{D}_{20}^2 + \mathcal{D}_{-20}^2) \right) \right], \tag{5.12}$$

where we have ignored the terms containing $I_{\pm 1}$, since these terms will average out in the presence of a large static magnetic field aligned along the z axis of the LS.

If we absorb the term γB_0 into the CSA parameters (this is done to avoid having to write γB_0 every time), we may write the frequency of the observed CSA interaction as

$$\omega_{cs}(\bar{\Omega}) = \sigma + \delta \left[\mathcal{D}_{00}^2(\bar{\Omega}) + \frac{\eta}{\sqrt{6}} (\mathcal{D}_{20}^2(\bar{\Omega}) + \mathcal{D}_{-20}^2(\bar{\Omega})) \right], \tag{5.13a}$$

$$= \sigma + \delta \left(\frac{3 \cos^2 \beta - 1}{2} + \frac{\eta}{2} \sin^2 \beta \cos 2\gamma \right). \tag{5.13b}$$

Depending upon the specifics of the calculation one may choose to use either Eq. (5.13a) or Eq. (5.13b).

5.2.4 NMR Signal from Static Isotropic Samples

The complex time domain signal from a single isolated spin possessing a CSA and oriented by $\bar{\Omega}$ with respect to the static magnetic field is $\exp[i(\omega_{cs} - \omega_0)t]$, where ω_0 is the reference frequency. We will ignore from this point forward the reference frequency and generally assume that it is set somewhere close to the isotropic chemical shift. For a sample composed of an isotropic distribution of such nuclei, the signal is given by a sum over the unit sphere.

$$F(t) = \frac{1}{8\pi^2} \int d\bar{\Omega} \exp[i\omega(\bar{\Omega})t] \quad (5.14)$$

From this point forward we will neglect the subscript *cs* for the frequency, since we will be dealing only with signal arising from a nucleus possessing a CSA. Note that Eq. (5.14) completely ignores all relaxation mechanisms, but introducing such quantities into the argument would hopelessly confuse the issue. The frequency domain signal, $S(\omega)$, is given by the Fourier transform of $F(t)$ with respect to the conjugate variables (ω, t) .

$$S(\omega) = \int_{-\infty}^{\infty} F(t) \exp(i\omega t) dt \quad (5.15)$$

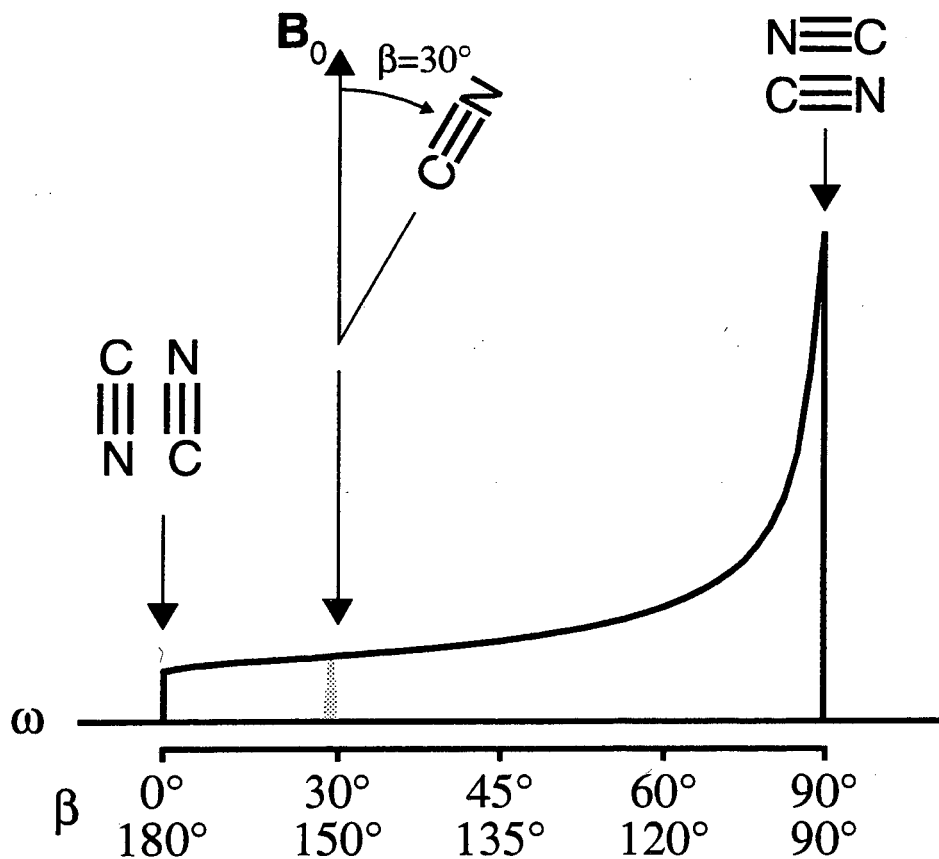


Figure 5.2 Simulation of a ^{13}C powder pattern for an axially symmetric CSA interaction demonstrated for ^{13}C in a cyano group. The angle β refers to the relative orientation of the carbon-nitrogen bond with the static magnetic field. Various physical orientations of the cyano group are related to a resulting NMR frequency. Note that the frequency axis is linear, whereas the orientation axis is not.

Often one is not able to acquire the time domain signal for both positive and negative times, so the integration may proceed from 0 to ∞ . In a one-dimensional experiment, it is sufficient to acquire only the positive time data. An example of a spectrum for an axially symmetric CSA interaction is shown in Fig. (5.2).

5.2.5 A Word about Probability Densities

In the following sections, joint and conditional probability densities will be used extensively. Consider a function that represents the probability that an object with a given initial orientation $\bar{\Omega}_0$ with respect to some reference frame will reorient to $\bar{\Omega}_1$ in a given amount of time t . We call such a probability density a *conditional* probability density, as it is conditional upon the object having an initial orientation given by $\bar{\Omega}_0$ at time $t = 0$. Symbolically we will represent this probability density as $P(\bar{\Omega}_1, t | \bar{\Omega}_0, 0)$. Now suppose that we have a large collection of these objects with a distribution of initial orientations with the probability that there is an object at $\bar{\Omega}_0$ given by $W(\bar{\Omega}_0)$, where $W(\bar{\Omega}_0)$ is normalized such that the integral over all possible orientations is unity. For the case of an isotropic distribution of initial orientations, $W(\bar{\Omega}_0) = 1/8\pi^2$. Knowing $W(\bar{\Omega}_0)$, we now may ask what the probability is that an object will undergo a reorientation from $\bar{\Omega}_0$ to $\bar{\Omega}_1$ in time t with no *a priori* knowledge of the object's initial orientation. Such a probability density is referred to as a *joint* probability density. In this case, the joint reorientational probability density is given by $W(\bar{\Omega}_0)P(\bar{\Omega}_1, t | \bar{\Omega}_0, 0)$ and is assumed to be normalized to unity.

5.2.6 Two-Dimensional Exchange NMR Spectroscopy

The standard assumptions for this type of experiment concerning the nature of the NMR interaction and the evolution of the nuclear spin magnetization, will be made, namely: the NMR interaction will consist only of the chemical shift anisotropy of a spin-half nucleus such as ^{13}C , complete dipolar decoupling of ^{13}C and ^1H nuclei is achieved during evolution and acquisition, all CSA parameters are constant in time, all rf pulses are "hard", i.e. they will be assumed to be delta functions in time, there is no spin diffusion, and spin-lattice relaxation is independent of the orientation of the CSA tensor.

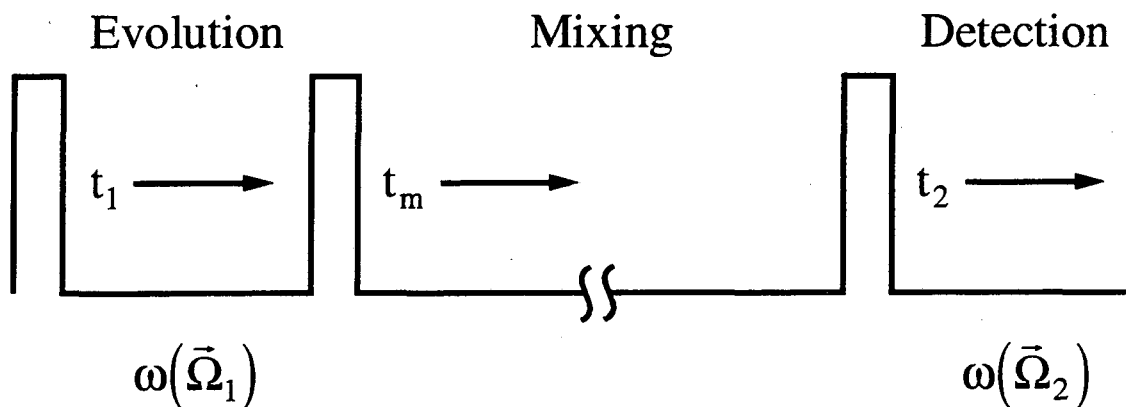


Figure 5.3 Basic layout of a two-dimensional NMR exchange experiment¹²⁵. Magnetization produced by the first pulse evolves with a frequency related to the initial orientation of the interaction. Evolution of the magnetization ceases during the mixing period to resume during the detection period. During the detection period the magnetization evolves at frequencies determined by the final orientation of the interaction. The mixing period is assumed to be much longer than both the evolution and detection periods.

The basic form of the two-dimensional NMR spectroscopy experiment¹²⁵ is given in Fig. (5.3). After the initial excitation of the ¹³C magnetization, each spin evolves for a time t_1 at the frequency dictated by its initial PAS orientation,

$$\omega(\bar{\Omega}_1) = \sigma + \delta \left[\frac{3\cos^2(\beta_1) - 1}{2} - \frac{\eta}{2} (\sin^2(\beta_1) \cos(2\gamma_1)) \right]. \quad (5.16)$$

The initial orientation $\bar{\Omega}_1$ will be referred as PAS1, Fig. (5.4). After the evolution period, a second pulse stores one component of the magnetization parallel to \mathbf{B}_0 for a mixing time t_m , during which time physical reorientation may occur, thus changing the relative orientation of the PAS to the LS. The third pulse returns the spin magnetization to the transverse plane for detection. During detection, each spin will evolve at a frequency determined by the new orientation $\bar{\Omega}_2$, PAS2.

$$\omega(\bar{\Omega}_2) = \sigma + \delta \left[\frac{3\cos^2(\beta_2) - 1}{2} - \frac{\eta}{2} (\sin^2(\beta_2) \cos(2\gamma_2)) \right] \quad (5.17)$$

The resulting two-dimensional time domain signal represents an ensemble average of the spin isochromats over all possible initial and final orientations weighted by the joint probability density for the reorientation from PAS1 to PAS2:

$$\begin{aligned} F(t_1, t_2) &= \left\langle \exp[i\omega(\bar{\Omega}_1)t_1] \exp[i\omega(\bar{\Omega}_2)t_2] \right\rangle \\ &= \int d\bar{\Omega}_1 \int d\bar{\Omega}_2 W(\bar{\Omega}_1, 0) P(\bar{\Omega}_2, t_m | \bar{\Omega}_1, 0) \\ &\quad \times \exp[i\omega(\bar{\Omega}_1)t_1] \exp[i\omega(\bar{\Omega}_2)t_2]. \end{aligned} \quad (5.18)$$

where $P(\bar{\Omega}_2, t_m | \bar{\Omega}_1, 0)$ is the conditional probability density that a CSA tensor with an initial PAS orientation $\bar{\Omega}_1$ will reorient to a final PAS at $\bar{\Omega}_2$ in a time t_m . In this case, $W(\bar{\Omega}_1, 0)$ represents the probability that the CSA tensor is oriented at $\bar{\Omega}_1$ at time $t = 0$, and as we are dealing with isotropic samples, this term is a constant, $1/8\pi^2$. Two-dimensional Fourier transformation of the time domain signal yields the frequency spectrum

$$\begin{aligned} S(\omega_1, \omega_2; t_m) &= \int d\bar{\Omega}_1 \int d\bar{\Omega}_2 \delta[\omega(\bar{\Omega}_1) - \omega_1] \delta[\omega(\bar{\Omega}_2) - \omega_2] \\ &\quad \times W(\bar{\Omega}_1, 0) P(\bar{\Omega}_2, t_m | \bar{\Omega}_1, 0). \end{aligned} \quad (5.19)$$

Note that in Eq. (5.19) δ is the Dirac delta function not the anisotropy parameter. Equation (5.19) is of particular interest, as it will provide the means to extract information about reorientational dynamics directly from the frequency domain NMR signal.

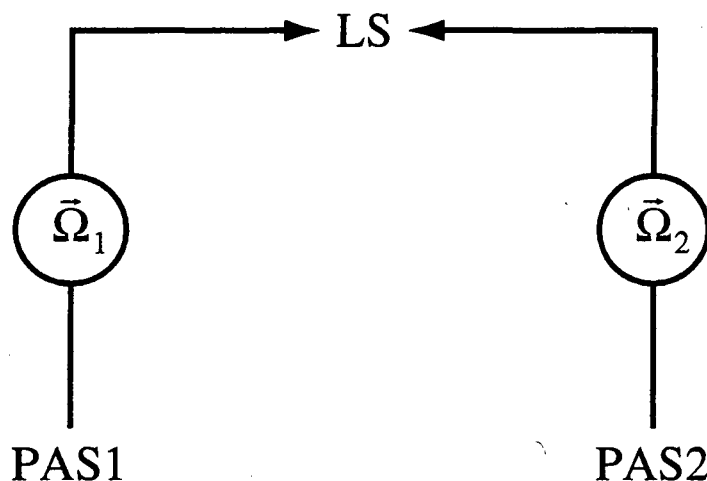


Figure 5.4 Rotations relating the principal axis systems (PAS1 and PAS2) of the CSA tensor during mixing and detection to the laboratory system (LS).

Depending upon the nature of the reorientational process, one will need to consider different functional forms for the joint reorientational probability density. In this study, we assume that the particles undergo isotropic rotational diffusion for which the basic theory is presented in the next section. We also desire some means of extracting quantitative information about the isotropic rotational diffusion constant, from which one may determine the size of the latex microspheres in solution. In analogy to DLS where such information is often extracted from the time-correlation function of the scattered light, we will develop equations describing the time-correlation function of the NMR frequency and also a means of extracting the NMR frequency time-correlation function directly from the two-dimensional exchange spectrum.

5.2.7 Isotropic Rotational Diffusion

The equation of motion for an isolated rigid particle undergoing rotational Brownian diffusion is given by

$$\frac{\partial W(\bar{\Omega}, t)}{\partial t} + (\mathbf{L} \cdot \mathbf{D} \cdot \mathbf{L})W(\bar{\Omega}, t) = 0, \quad (5.20)$$

where $W(\bar{\Omega}, t)$ is the probability density for the particle (i.e. its principle axis system) to have orientation $\bar{\Omega}$ at time t , \mathbf{L} is the infinitesimal rotation operator, and \mathbf{D} is the rotational diffusion tensor. The formal solution to Eq. (5.20) is¹¹⁴

$$W(\bar{\Omega}, t) = \int d\bar{\Omega}_1 W(\bar{\Omega}_1, 0) P(\bar{\Omega}_2, t | \bar{\Omega}_1, 0), \quad (5.21)$$

where $W(\bar{\Omega}_1, 0)$ is the probability that the particle is initially oriented at the angle $\bar{\Omega}_1$, and $P(\bar{\Omega}_2, t | \bar{\Omega}_1, 0)$ is the conditional probability that if the particle was initially at $\bar{\Omega}_1$, then it will have the orientation $\bar{\Omega}_2$ at time t . For the case of isotropic rotational diffusion, it has been shown that^{113,114}

$$\begin{aligned} W(\bar{\Omega}_1, 0) P(\bar{\Omega}_2, t | \bar{\Omega}_1, 0) &= \frac{1}{8\pi^2} \sum_{l=1}^{\infty} \left[\frac{2l+1}{8\pi^2} \exp(-l(l+1)D^r t) \right. \\ &\quad \left. \times \sum_{m=-l}^l \sum_{n=-l}^l \mathcal{D}_{mn}^l(\bar{\Omega}_1)^* \mathcal{D}_{mn}^l(\bar{\Omega}_2) \right]. \end{aligned} \quad (5.22)$$

D^r is the isotropic rotational diffusion constant in Hz.

At infinite dilution, D^r has a particularly simple form¹²⁶:

$$D_0^r = \frac{k_B T}{8\pi \nu a^3}, \quad (5.23)$$

where k_B is the Boltzmann constant, T is the temperature, ν is the kinematic viscosity of the suspending fluid, and a is the hydrodynamic radius of the colloidal particle. For

finite dilution and short observation times the diffusion coefficient varies with the relative volume fraction, ϕ , of the colloidal particles¹²⁷

$$D^r = D_0^r(1 - C^r\phi). \quad (5.24)$$

The coefficient C^r is dependent upon the nature of the interaction between the particles and the suspending fluid and has the value 0.63 for the case of hard spheres with stick hydrodynamic boundary conditions¹²⁷. In the following discussions of rotational diffusion, we will use the corrected form of the rotational diffusion coefficient, Eq. (5.24).

5.2.8 Time-Correlation Functions

The diffusion statistics can be fully described by the normalized orientational time-correlation functions given by¹²⁸:

$$C_{l'm'n',lmn}(t) = \frac{\left\langle \mathcal{D}_{m'n'}^{l'}(\bar{\Omega}_1(0)) \mathcal{D}_{mn}^l(\bar{\Omega}_2(t))^* \right\rangle}{\left\langle \left| \mathcal{D}_{m'n'}^{l'}(\bar{\Omega}_1(0)) \right|^2 \right\rangle}. \quad (5.25)$$

The $\langle \rangle$'s denote integration over all possible initial and final orientations weighted by the joint reorientational probability density, $W(\bar{\Omega}_1, 0)P(\bar{\Omega}_2, t | \bar{\Omega}_1, 0)$. The orientational time-correlation functions play a central role in DLS, and as we will show in the next section, they also play an important role in interpreting two-dimensional exchange spectra. From the orthogonality of the Wigner rotation matrices, Eq. (5.3), and using the joint reorientational probability density in Eq. (5.22), we find

$$\left\langle \mathcal{D}_{m'n'}^{l'}(\bar{\Omega}_1) \mathcal{D}_{mn}^l(\bar{\Omega}_2)^* \right\rangle_{ird} = \frac{1}{2l+1} \exp(-l(l+1)D^r t) \delta_{l'l} \delta_{m'm} \delta_{n'n}, \quad (5.26)$$

where the subscript *ird* signifies that the reorientational process is isotropic rotational diffusion. In the two-dimensional exchange NMR experiment we will be particularly interested in the time-correlation functions with $l = 2$.

$$C_{2,m}^{ird}(t) = \frac{\left\langle \mathcal{D}_{m0}^2(\bar{\Omega}_1) \mathcal{D}_{m0}^2(\bar{\Omega}_2)^* \right\rangle_{ird}}{\left\langle \left| \mathcal{D}_{m0}^2(\bar{\Omega}_1) \right|^2 \right\rangle} = \exp(-6D^r t), \quad (5.27)$$

$$\text{where } \left\langle \left| \mathcal{D}_{m0}^2(\bar{\Omega}_1) \right|^2 \right\rangle = \frac{1}{5}.$$

For time-correlation functions of this type, it is convenient to define a correlation time given by

$$\tau_c = \frac{1}{6D^r}. \quad (5.28)$$

Theoretical evidence predicts non-exponential behavior for $C_{2,m}(t)$ in colloidal suspensions of finite dilution, but it is unlikely this behavior will be seen for volume fractions below 0.1.¹²⁹

5.2.9 Time-Correlation Functions in Two-Dimensional Exchange NMR for the Rotational Diffusion of a Spherical Top

The objective in this section is to develop a method to extract the time-correlation function and, therefore, information about the rotational diffusion constant for a spherically symmetric diffusor directly from the two-dimensional exchange spectrum.

First, we rewrite the frequency of the CSA interaction, Eq. (5.13a) with $\sigma = 0$ and $\delta = 1$ in terms of the Wigner rotation matrices.

$$\omega(\bar{\Omega}) = \mathcal{D}_{00}^2(\bar{\Omega}) + \frac{\eta}{\sqrt{6}} \left[\mathcal{D}_{20}^2(\bar{\Omega}) + \mathcal{D}_{-20}^2(\bar{\Omega}) \right] \quad (5.29)$$

Although it is not necessary to set the isotropic chemical shift to zero, we have decided to do so in the actual calculations of the NMR frequency time-correlation function. The case where σ is not set to zero will be discussed later in this section where we will investigate the consequences of overlapping CSA powder patterns arising from chemically distinct sites. Because $\omega(\bar{\Omega})$ is real, we may express the NMR frequency time-correlation function in terms of the time-correlation functions discussed in the previous section.

$$\begin{aligned} \langle \omega(\bar{\Omega}_1) \omega(\bar{\Omega}_2) \rangle &= \langle \omega(\bar{\Omega}_1) \omega(\bar{\Omega}_2)^* \rangle \\ &= \langle \mathcal{D}_{00}^2(\bar{\Omega}_1) \mathcal{D}_{00}^2(\bar{\Omega}_2)^* \rangle \\ &\quad + \sqrt{\frac{2}{3}} \eta \langle \mathcal{D}_{00}^2(\bar{\Omega}_1) \left[\mathcal{D}_{20}^2(\bar{\Omega}_2)^* + \mathcal{D}_{-20}^2(\bar{\Omega}_2)^* \right] \rangle \\ &\quad + \frac{\eta^2}{6} \left\langle \left[\mathcal{D}_{20}^2(\bar{\Omega}_1) + \mathcal{D}_{-20}^2(\bar{\Omega}_1) \right] \left[\mathcal{D}_{20}^2(\bar{\Omega}_2)^* + \mathcal{D}_{-20}^2(\bar{\Omega}_2)^* \right] \right\rangle \end{aligned} \quad (5.30)$$

Using Eq. (5.22) and the relation derived in Eq. (5.26), we arrive at the desired expression for the normalized isotropic rotational diffusion time-correlation function of the CSA frequency, which we shall denote $C_2^{cs}(t_m)$.

$$C_2^{cs}(t_m) = \frac{\langle \omega(\bar{\Omega}_1) \omega(\bar{\Omega}_2)^* \rangle_{ird}}{\langle |\omega(\bar{\Omega}_1)|^2 \rangle} = \exp(-6D^r t_m), \quad (5.31)$$

$$\text{where } \langle |\omega(\bar{\Omega}_1)|^2 \rangle = \frac{1}{5} \left(1 + \frac{\eta^2}{3} \right).$$

This is identical to the time-correlation function found in Eq. (5.27) except the normalization is given by $(1 + \eta^2/3)/5$ as opposed to $1/5$. In the case of an axially symmetric CSA interaction ($\eta = 0$), the normalization factors in Eqs. (5.31) and (5.27) are identical.

In deriving Eq. (5.31), we did not need to consider the relative orientation of the CSA interaction within the diffusing particles. Due to the symmetry of the motion, one may in fact view the situation as merely the isotropic rotational diffusion of a collection of CSA tensors. We shall see in the next section that this viewpoint is not correct when the diffusor is non-spherical.

There exists one more crucial step to developing a method to determine C_2^{cs} directly from the experimentally obtained two-dimensional exchange spectrum. Using a modification of the expression for the frequency domain NMR signal given in Eq. (5.19) where we have replaced $\omega(\bar{\Omega}_2)$ by its complex conjugate, one may easily show that

$$\int d\omega_1 \int d\omega_2 S(\omega_1, \omega_2; t_m) \omega_1 \omega_2 = \int d\bar{\Omega}_1 \int d\bar{\Omega}_2 W(\bar{\Omega}_1) \times P(\bar{\Omega}_2, t_m | \bar{\Omega}_1, 0) \omega(\bar{\Omega}_1) \omega(\bar{\Omega}_2)^*, \quad (5.32)$$

where we have assumed that the exchange spectrum is normalized to one.

$$\int d\omega_1 \int d\omega_2 S(\omega_1, \omega_2; t_m) = 1 \quad (5.33)$$

From Eq. (5.31) and Eq. (5.32)

$$C_2^{cs}(t_m) = \frac{\int d\omega_1 \int d\omega_2 S(\omega_1, \omega_2; t_m) \omega_1 \omega_2}{\frac{1}{5} \left(1 + \frac{\eta^2}{3}\right)}. \quad (5.34)$$

This result for the case of $\eta = 0$, where $C_2^{cs}(t_m) = C_{2,0}(t_m)$, was previously reported by Schmidt-Rohr and Spiess^{119,130}. In Eqs. (5.32) and (5.34), we are assuming that the weighted integral of the spectrum is carried out from $-(1+\eta)/2$ to 1 for both ω_1 and ω_2 , in a frequency space which is scaled such that $\delta = 1$ and $\sigma = 0$. In order to do this, of course, it is necessary to know all three CSA parameters.

We now have a relatively direct method of extracting isotropic rotational diffusion information from the two-dimensional exchange NMR experiment. In fact, the exchange experiment is actually simpler to interpret than the DDLS experiment as the light-scattering time-correlation functions also contain an exponential decay arising from translational diffusion¹²⁸.

Although we are primarily concerned with measuring time-correlation functions in a system with an isolated chemical shift where it is possible to zero the isotropic frequency by changing the reference frequency, many potentially interesting systems contain multiple sites with overlapping CSA powder patterns. In this case, it is not generally possible to choose a single reference frequency which simultaneously sets all of the isotropic frequencies to zero. We then have an NMR spectrum which consists of a sum over the spectra produced by each site

$$S(\omega_1, \omega_2; t_m) = \sum_{i=1}^{n_{sites}} C_i S_i(\omega_1, \omega_2; t_m), \quad (5.35)$$

where n_{sites} is the number of chemically distinct sites being observed, and C_i is the relative population of the i^{th} site. Using Eq. (5.32) and the distributive property of integration,

$$\begin{aligned}
& \int d\omega_1 \int d\omega_2 S(\omega_1, \omega_2; t_m) \omega_1 \omega_2 \\
&= \sum_{i=1}^{n_{\text{sites}}} C_i \int d\omega_1 \int d\omega_2 S_i(\omega_1, \omega_2; t_m) \omega_1 \omega_2 \\
&= \sum_{i=1}^{n_{\text{sites}}} C_i \langle \omega_i(\bar{\Omega}_1) \omega_i(\bar{\Omega}_2)^* \rangle.
\end{aligned} \tag{5.36}$$

We now must compute the time-correlation function for NMR frequencies of the form

$$\omega_i(\bar{\Omega}) = \sigma_i + \delta_i \left[\mathcal{D}_{00}^2(\bar{\Omega}) + \frac{\eta_i}{\sqrt{6}} \left(\mathcal{D}_{20}^2(\bar{\Omega}) + \mathcal{D}_{-20}^2(\bar{\Omega}) \right) \right], \tag{5.37}$$

where this time we have included the isotropic chemical shift and anisotropy parameters. For any of the given sites we find that the isotropic rotational diffusion NMR frequency time-correlation function is

$$\left\langle \omega_i(\bar{\Omega}_1) \omega_i(\bar{\Omega}_2)^* \right\rangle_{\text{ird}} = \sigma_i^2 + \left[\frac{\delta_i^2}{5} \left(1 + \frac{\eta_i^2}{3} \right) \right] \exp(-6D^r t_m). \tag{5.38}$$

The frequency weighted integral over the NMR spectrum is then

$$\begin{aligned}
& \int d\omega_1 \int d\omega_2 S(\omega_1, \omega_2; t_m) \omega_1 \omega_2 \\
&= \exp(-6D^r t_m) \sum_{i=1}^{n_{\text{sites}}} C_i \left[\frac{\delta_i^2}{5} \left(1 + \frac{\eta_i^2}{3} \right) \right] + \sum_{i=1}^{n_{\text{sites}}} C_i \sigma_i^2.
\end{aligned} \tag{5.39}$$

The limits of the integration in this case should be set so that all of the relevant powder patterns are included in the integration region.

Although Eq. (5.39) is more complicated than the expression for a single CSA interaction with zero isotropic shift, Eq. (5.31), if one knows all of the relevant CSA

parameters, the determination of the rotational diffusion constant is relatively simple. In the event that one does not know the CSA parameters, one may determine the rotational diffusion constant by treating the two terms containing the CSA parameters as adjustable parameters in a fit of the experimental data.

The treatment presented here will also be useful for a quantitative analysis of ^2H NMR spectra, where the powder patterns of two NMR transitions overlap. Since the powder patterns have the same center of gravity, σ_i can be chosen to be zero. In addition, the magnitude of δ is the same for both patterns. For the quadrupolar interaction of deuterons bonded to aliphatic carbons, $\eta \cong 0$. Therefore, the frequency-weighted integral over the ^2H NMR 2D spectrum, Eq. (5.39), simplifies to $(\delta^2/5)\exp(-6D^r t_m)$.

5.2.10 Time-Correlation Functions in Two-Dimensional Exchange NMR for the Rotational Diffusion of a Symmetric Top

Although we intend in this study to investigate the rotational diffusion of spherical particles, it is important to understand the form of the correlation function if the particles are not spherical. In fact, the development of this work was prompted by the appearance of multiple correlation times in the experimental data which will be presented later. Consider, for example, a rod-like particle whose reorientation about the axis of symmetry is rapid with respect to the mixing time, but whose reorientation perpendicular to the axis of symmetry is slow. An axially symmetric CSA interaction parallel to the symmetry axis of the rod will show relatively little frequency exchange for the given mixing time. On the other hand, considerable frequency exchange will occur if the CSA tensor is perpendicular to the symmetry axis of the rod. It is therefore necessary to discuss the orientation of the CSA tensor not only in terms of how the particles are moving, but also in terms of the relative orientation of the CSA tensor and the particle.

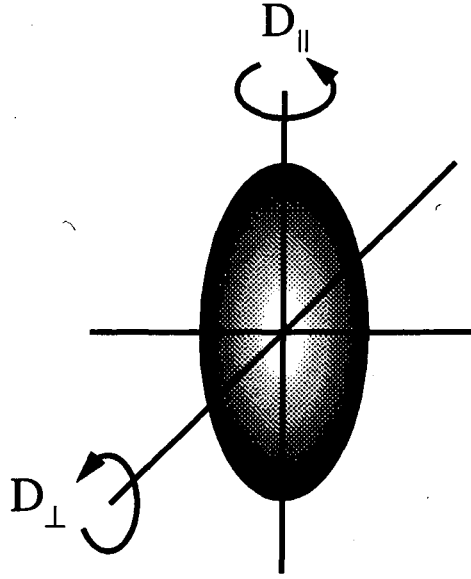


Figure 5.5 Relation between the two rotational diffusion coefficients of a symmetric top to the geometry of a prolate ellipsoid. The diffusion coefficient D_{\parallel} refers to diffusion about the axis of symmetry, whereas D_{\perp} refers to diffusion perpendicular to the axis of symmetry.

The diffusion tensor for a symmetric top may be represented by two diffusion constants, D_{\parallel} and D_{\perp} , in the reference frame, PAS_{diff} , which diagonalizes the diffusion tensor. D_{\parallel} describes the diffusion about the axis of symmetry, whereas D_{\perp} describes the diffusion perpendicular to the symmetry axis as shown in Fig. (5.5). As with isotropic rotational diffusion, one may obtain an analytical solution of Eq. (5.20) for a symmetric top. In this case, the joint reorientational probability density is given by^{113,114}

$$\begin{aligned}
 & W_{\text{diff}}(\bar{\Omega}_1, 0) P_{\text{diff}}(\bar{\Omega}_2, t | \bar{\Omega}_1, 0) \\
 &= \frac{1}{8\pi^2} \sum_{l=1}^{\infty} \left[\frac{2l+1}{8\pi^2} \exp[-l(l+1)D_{\perp}t - m^2(D_{\parallel} - D_{\perp})t] \right. \\
 & \quad \left. \times \sum_{m=-l}^l \sum_{n=-l}^l \mathcal{D}_{mn}^l(\bar{\Omega}_1)^* \mathcal{D}_{mn}^l(\bar{\Omega}_2) \right]. \tag{5.40}
 \end{aligned}$$

Depending upon one's definition of the Euler angles, the m^2 contained in the exponential will either be the first or the second subscript of the Wigner rotation matrix elements. As stated before, we have chosen to adopt the convention used by Rose¹²³.

Unlike the case of the spherical top, where the diffusion tensor is diagonal in any PAS, for the symmetric top the diffusion tensor is only diagonal in PAS_{diff} . Therefore, we must first rotate the PAS of the chemical shift interaction during the encode period, $PAS1_{cs}$, into the PAS which diagonalizes the diffusion tensor during the same period, $PAS1_{diff}$. As we observe the CSA frequency in the LS, we must perform another rotation of $PAS1_{diff}$ to LS. We will denote the first rotation from $PAS1_{cs}$ to $PAS1_{diff}$ by the triplet $\bar{\Omega}'$, and the rotation from $PAS1_{diff}$ to the LS by $\bar{\Omega}_1$, the initial orientation of the diffusor. The total rotation from $PAS1_{cs}$ to the LS will be denoted $\bar{\Omega}_1''$. During the acquisition period we repeat the process substituting 1's for 2's in the previous explanation. See

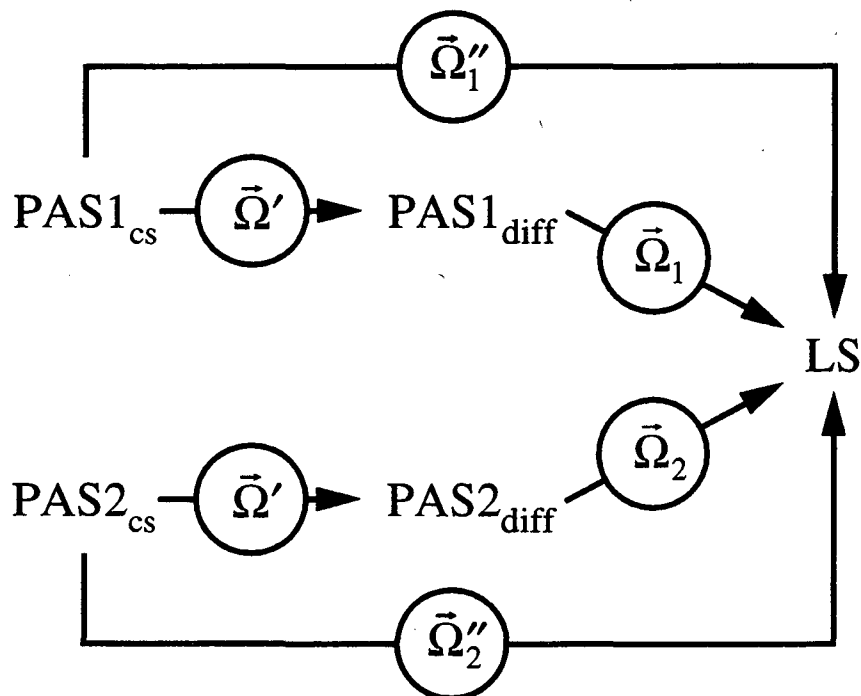


Figure 5.6 Rotations relating the PAS of the CSA tensor, the PAS in which the diffusion tensor of the symmetric top is diagonal, and the LS. Note that $PAS1_{cs}$ and $PAS2_{cs}$ remain fixed with respect to the PAS of the diffusor.

Fig. (5.6). From Eq. (5.29), the NMR frequency as a function of $\bar{\Omega}'$ and $\bar{\Omega}_1$ is given by

$$\omega(\bar{\Omega}_1, \bar{\Omega}') = \sum_{n'=-2}^2 \mathcal{D}_{n'0}^2(\bar{\Omega}_1) \left[\mathcal{D}_{0n'}^2(\bar{\Omega}') + \frac{\eta}{\sqrt{6}} (\mathcal{D}_{2n'}^2(\bar{\Omega}') + \mathcal{D}_{-2n'}^2(\bar{\Omega}')) \right]. \quad (5.41)$$

Determination of the time-correlation function requires specifying the orientation ensemble average of the CSA tensor in the particles. In general, we must take into account the probability at $t = 0$, $W_{cs}(\bar{\Omega}', 0)$, that PAS1_{cs} has orientation $\bar{\Omega}'$ with respect to PAS1_{diff} , and the conditional probability density, $P_{cs}(\bar{\Omega}', t_m | \bar{\Omega}', 0)$, that PAS2_{cs} is then at the same relative orientation at time t_m . For the case of an isotropic distribution of CSA tensors rigidly embedded in the particles,

$$\begin{aligned} W_{cs}(\bar{\Omega}', 0) &= \frac{1}{8\pi^2}, \\ P_{cs}(\bar{\Omega}', t_m | \bar{\Omega}', 0) &= 1. \end{aligned} \quad (5.42)$$

Combining Eq. (5.40), (5.41) and (5.42) we arrive at

$$\begin{aligned} &\langle \omega(\bar{\Omega}_1, \bar{\Omega}') \omega(\bar{\Omega}_2, \bar{\Omega}')^* \rangle \\ &= \left(\frac{1}{8\pi^2} \right)^2 \int d\bar{\Omega}_1 \int d\bar{\Omega}_2 \int d\bar{\Omega}' \\ &\times \sum_{n'=-2}^2 \mathcal{D}_{n'0}^2(\bar{\Omega}_1) \left[\mathcal{D}_{0n'}^2(\bar{\Omega}') + \frac{\eta}{\sqrt{6}} (\mathcal{D}_{2n'}^2(\bar{\Omega}') + \mathcal{D}_{-2n'}^2(\bar{\Omega}')) \right] \\ &\times \sum_{n''=-2}^2 \mathcal{D}_{n''0}^2(\bar{\Omega}_2)^* \left[\mathcal{D}_{0n''}^2(\bar{\Omega}')^* + \frac{\eta}{\sqrt{6}} (\mathcal{D}_{2n''}^2(\bar{\Omega}')^* + \mathcal{D}_{-2n''}^2(\bar{\Omega}')^*) \right] \\ &\times \sum_{l=0}^{\infty} \sum_{m,n=-l}^l \mathcal{D}_{mn}^l(\bar{\Omega}_1)^* \mathcal{D}_{mn}^l(\bar{\Omega}_2) \exp[-l(l+1)D_{\perp}t - m^2(D_{\parallel} - D_{\perp})t]. \end{aligned} \quad (5.43)$$

After carrying out the integrations we obtain

$$\begin{aligned}
& \left\langle \omega(\bar{\Omega}_1, \bar{\Omega}') \omega(\bar{\Omega}_2, \bar{\Omega}')^* \right\rangle \\
&= \frac{1}{5} \left(\frac{1}{5} + \frac{\eta^2}{15} \right) \left(2 \exp[-6D_{\perp}t - 4(D_{\parallel} - D_{\perp})t] \right. \\
& \quad \left. + 2 \exp[-6D_{\perp}t - (D_{\parallel} - D_{\perp})t] + \exp[-6D_{\perp}t] \right). \tag{5.44}
\end{aligned}$$

One obtains a similar triexponential expression for the depolarized light scattering time-correlation function in DDLS¹²⁸.

The equation for the NMR exchange spectrum originally presented in Eq. (5.19) may be restated as an ensemble average similar to that used in the definition of the time-correlation function above.

$$\begin{aligned}
S(\omega_1, \omega_2; t_m) &= \int d\bar{\Omega}_1 \int d\bar{\Omega}_2 \int d\bar{\Omega}' \delta[\omega(\bar{\Omega}_1, \bar{\Omega}') - \omega_1] \delta[\omega(\bar{\Omega}_2, \bar{\Omega}')^* - \omega_2] \\
& \quad \times W_{cs}(\bar{\Omega}', 0) P_{cs}(\bar{\Omega}', t_m | \bar{\Omega}', 0) W_{diff}(\bar{\Omega}_1, 0) P_{diff}(\bar{\Omega}_2, t_m | \bar{\Omega}_1, 0) \tag{5.45}
\end{aligned}$$

Using this form for the two-dimensional exchange spectrum, it is simple to show (see Eq. (5.32) and (5.34)) that the frequency weighted integral of the two-dimensional NMR spectrum is equal to the NMR frequency time-correlation function given in Eq. (5.44).

The diffusion coefficients derived from the NMR frequency time-correlation function may be used to determine the major and minor semi-axes of revolution of an ellipsoid, a and b respectively, using^{131,132}

$$D_{\parallel} = \frac{3kT}{32\pi\eta} \frac{2a - b^2 G(a, b)}{(a^2 - b^2)b^2}, \tag{5.46a}$$

$$D_{\perp} = \frac{3kT}{32\pi\eta} \frac{(2a^2 - b^2)G(a, b) - 2a}{a^4 - b^4}, \tag{5.46b}$$

where

$$G(a,b) = \frac{2}{\sqrt{a^2 - b^2}} \ln \left(\frac{a + \sqrt{a^2 - b^2}}{b} \right) \quad (5.47a)$$

for $a > b$ (prolate ellipsoid), and

$$G(a,b) = \frac{2}{\sqrt{b^2 - a^2}} \arctan \left(\frac{\sqrt{b^2 - a^2}}{a} \right) \quad (5.47b)$$

for $a < b$ (oblate ellipsoid). Although the two diffusion coefficients in Eq. (5.46a) and (5.46b) are indeterminate at $a = b$, they tend towards the value for the isotropic rotational diffusion coefficient given in Eq. (5.23) as $a \rightarrow b$.

5.3 Simulation of Two-Dimensional Exchange NMR Spectra for the Case of Isotropic Rotational Diffusion

Up to this point we have focused on extracting time-correlation functions from the two-dimensional exchange spectrum with the assumption that the motional process is rotational diffusion. Even if the particle reorientation is not described by rotational diffusion, the frequency weighted integral of the exchange spectrum may still yield a monotonically decreasing function which may be fit with a sum of decaying exponentials. Unlike the time-correlation function, two-dimensional exchange spectra can show features which are characteristic of anisotropic motions, discrete jumps, coherent rotation, etc.¹¹⁸⁻¹²¹. In order to gain more insight into the actual dynamics which we are observing, we need to develop a method of simulating two-dimensional exchange spectra based upon the rotational diffusion model. Simulations will allow us to determine if the process *looks* like rotational diffusion and to check for experimental artifacts.

The task of simulating two-dimensional exchange spectra using Eq. (5.19) appears very formidable. One must integrate over six separate angles over the interval $(0, 2\pi)$ for four of the angles and $(0, \pi)$ for the other two. Such a simulation would prove very difficult to solve in any reasonable amount of time. A simpler equation which takes into account redundant integrations has been derived previously by Wefing et al.^{120,121} In the simplification, Wefing approaches the problem from the point of view of a fixed chemical shift PAS where the LS appears to reorient from LS1 to LS2. The relative orientation of the two laboratory systems is $\vec{z}' = (\alpha', \beta')$, and the orientation of LS1 with respect to the PAS is $\vec{z}_1 = (\alpha_1, \beta_1)$. In the case of isotropic rotational diffusion and non-zero assymetry parameter ($\eta \neq 0$), Eq. (5.19) reduces to

$$\begin{aligned}
S(\omega_1, \omega_2; t_m) &= \int_0^{\pi/2} d\beta' \sin(\beta') \Gamma^g(\beta', t_m) \int_0^{\pi/2} d\alpha_1 \\
&\times \int_0^{\pi/2} d\beta_1 \sin(\beta_1) \delta[\omega(\alpha_1, \beta_1) - \omega_1] \\
&\times \int_0^{2\pi} d\alpha' \delta[\omega(\alpha', \beta', \alpha_1, \beta_1) - \omega_2],
\end{aligned} \tag{5.48}$$

where

$$\Gamma^g(\beta', t_m) = \sum_{l=0}^{\infty} \frac{4l+1}{8\pi^2} \exp(-2l(2l+1)D't_m) P_{2l}(\cos(\beta')), \tag{5.49}$$

$\omega(\alpha_1, \beta_1)$ is given in Eq. (5.13a) (note that $\alpha_1 \rightarrow \gamma$ and $\beta_1 \rightarrow \beta$), and $\omega(\alpha', \beta', \alpha_1, \beta_1)$ may be determined using Eq. (5.41). Γ^g is referred to as either the jump or reorientation angle distribution.

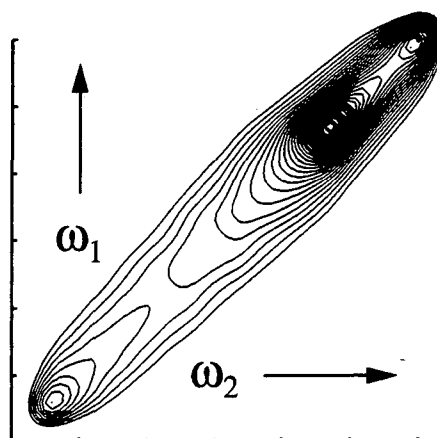
As an example, Fig. (5.7) shows two-dimensional exchange spectra with non-zero asymmetry parameter for a number of correlation times with a fixed mixing time. The simulations were performed with steps of $\pi/64$ radians with each simulation requiring approximately 43 s of CPU time on a Silicon Graphics Indigo computer running a MIPS R4000 CPU. At zero mixing time, the spectrum should lie entirely along the diagonal from the bottom left hand corner to the top right hand corner.

We have chosen to perform the simulation in the frequency domain as opposed to the time domain to reduce the number of numerical operations. Each angle is independently sampled using equally spaced intervals which are chosen to produce acceptable gridding artifacts after the convolution of the spectrum with a two-dimensional Gaussian line broadening function chosen to simulate the dipolar line broadening inherent in the experiment. CSA parameters are scaled in such a way that the

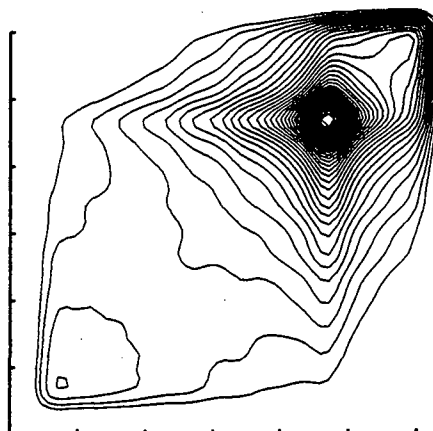
computed angle dependent frequency corresponds to the appropriate matrix index of the spectrum, thus avoiding the need to rescale the NMR frequency at each point of the sampled grid of orientations. Instead, the resulting frequency is converted to an integer and the appropriate weighting is added to the spectrum elements indicated by the computed frequencies. Wefing has pointed out that simulation in the time domain is a better approximation to the real signal¹²⁰, but the difference between the two methods is not important when one only wishes to use the simulation as a qualitative comparison to the experimental data. We have performed both time domain and frequency domain simulations and found no noticeable qualitative difference after the convolution of the spectrum with a Gaussian apodization function. In addition, NMR frequency time-correlation values derived from the simulated spectra using Eq. (5.34) agree with the correlation times used in the simulation.

Simulation of equivalent sites undergoing isotropic rotational diffusion with different correlation times involves almost no extra computation. It is sufficient to compute a reorientation angle distribution for each site independently and then add the distributions together weighted by the respective fractional population of each site. The resulting reorientation angle distribution may then be used in the simulation in the same way as the single correlation time reorientation angle distribution is used. As the calculation time of the reorientation angle distribution is much smaller than the total time required for the simulation, this method is more efficient than simulating the exchange spectrum separately for each correlation time and then adding the spectra. Examples of this sort of simulation will be presented later in this paper in association with the experimental results.

(a) $t_m/\tau_c = 0.1$



(b) $t_m/\tau_c = 1.0$



(c) $t_m/\tau_c = 10$

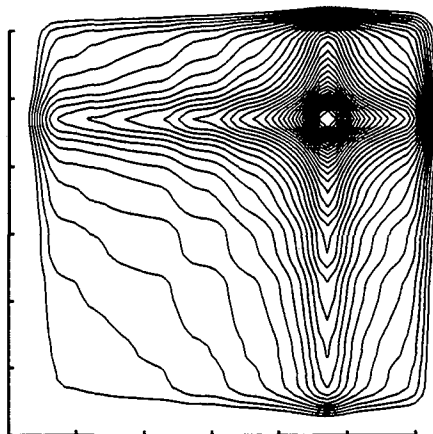


Figure 5.7 Simulated ^{13}C two-dimensional exchange spectra with $\sigma = 6.2$ ppm, $\delta = 90$ ppm, and $\eta = 0.45$. Frequency axes extend from -106 ppm to 80 ppm. Some features present in the spectra are due to an inadequate sampling of orientations. Spectra are normalized to a maximum height of one.

5.4 Experimental Example - Isotropic Rotational Diffusion of Latex Spheres in Suspension

5.4.1 Sample Considerations

Latex microspheres are often used as prototypical spherical colloidal particles in DLS studies of rotational diffusion. Monodisperse latex microspheres are relatively easy to produce using emulsion polymerization reactions, have a density near that of water and, therefore, remain in suspension for long periods of time without the need for agitation of the sample. Furthermore, crystalline latex microspheres have been produced with an intrinsic optical anisotropy¹¹⁵ which is useful if one wishes to measure the rotational diffusion of spherical particles using DDLS.

The requirements for an acceptable colloidal suspension to be studied using two-dimensional exchange NMR differ somewhat from those in DDLS. As is the case for optical techniques, the particles should be monodisperse, relatively easy to synthesize and neutrally buoyant in the suspending fluid. If the ^{13}C CSA interaction is to be used as the orientational probe, the particles should be relatively easy to enrich in ^{13}C at a site which is, preferably, not directly bonded to hydrogen; an absence of directly bonded protons considerably reduces the necessary decoupling power during the evolution and acquisition periods. Since spin-lattice relaxation times of ^{13}C nuclei in solid polymers are on the order of 1 s and the inhomogeneous linewidths are on the order of 100 ppm, measurable correlation times range from 5 ms to 1 s. At room temperature with water as the suspending fluid, these correlation times require the particles have a radius between 170 and 1000 nm.

In order to avoid excessive background signal, the suspending solvent should be free of ^{13}C nuclei, so common organic solvents are not appropriate. In light of its ease of use and availability, water is used as the suspending fluid in this study. Alternative

solvents such as ^{13}C depleted organic solvents and silanes may be preferable for specialized applications.

The results reported here are for a colloidal suspension of PMMA microspheres enriched to approximately 20% ^{13}C at the carbonyl site with a target radius of 300 nm. The method of synthesis for small batches of the particles is presented in detail below.

5.4.2 Preparation of methyl ^{13}C -(carbonyl)-methacrylate

Methacrylic acid enriched to 100% ^{13}C at the carboxylic acid group is synthesized by the low temperature carboxylation of isopropenyl magnesium bromide with barium carbonate- ^{13}C .¹³³ The acid is then isolated as the sodium salt and dried at 110°C under high vacuum. Esterification of the salt proceeds with trimethylphosphate on a vacuum manifold system in the presence of hydroquinone to inhibit polymerization. The resulting methyl ^{13}C -(carbonyl)-methacrylate is isolated by low temperature distillation. The final yield with respect to the barium carbonate- ^{13}C reactant is between 75% and 80%. Both the yield and sample purity obtained by this synthesis are higher than a previously reported reaction sequence via acetone cyanohydrine (from acetone and potassium cyanide- ^{13}C).¹³⁴

5.4.3 Preparation of ^{13}C -(carbonyl)-poly(methyl methacrylate) Microspheres

To conserve the enriched reactant, 300 nm radius ^{13}C -(carbonyl)-poly(methyl methacrylate) (PMMA) latex microspheres are synthesized in a two-step semicontinuous emulsion polymerization.

In the first step, seed particles of unlabeled MMA with a radius of 125 nm are synthesized in a 1 L reaction vessel in the presence of nitrogen to avoid the reaction of oxygen with the monomer. For the synthesis 200 ml of H_2O , 25.0 ml of a 0.5% solution of polyethyl ether (AD33[®], Atochem, France) to act as an emulsifier, 20 ml of a 1.57% solution of $(\text{NH}_4)_2\text{S}_2\text{O}_8$ to act as an initiator, and 15.0 g unenriched MMA are initially

placed in the reactor. After a nucleation time of 2 h at 20 °C, a pre-emulsion composed of 177 g MMA, 50 ml of a 1.0% solution of AD33®, and 200 ml of H₂O is pumped into the main reactor at a rate of 3.6 ml/min. Simultaneously, 25 ml of a 1.57% solution of the initiator (NH₄)₂S₂O₈ is added at a rate of 0.21 ml/min. The reaction temperature is stabilized at 72°C with a stirring speed of 250 rpm. After the addition is complete, the temperature is raised to 85 °C for 5 h in order to obtain high conversion and to dissociate the remainder of the initiator. The final solids content is 27.3% by weight.

In the second step, the labeled MMA is polymerized onto the surface of the latex 125 nm seed particles in a 50 ml reactor. The synthesis of 300 nm particles is very difficult because the MMA has a tendency to spontaneously nucleate during the addition of the monomer. To avoid the formation of new particles in this step of the synthesis, the addition rate is slowed down, and the concentration of emulsifier is reduced to suppress unwanted nucleation in micelles formed by the emulsifier. It should be noted that a certain amount of emulsifier is necessary for the stabilization of the emulsion, so the emulsifier cannot be completely removed.

For the reaction, 462 mg of the seed latex and 13.4 g of H₂O are added to the main reactor. A pre-emulsion composed of 917 mg of the enriched MMA, 983 mg of a 1% solution of AD33®, 1.68 g of a 1.57% solution of (NH₄)₂S₂O₈, and 1.54 g of H₂O is added over a period of 4 h with a 5 ml syringe. The temperature in the 50 ml reactor is stabilized at 72 °C during the addition and is then raised to 85 °C for 26 h after the addition to ensure completion of the polymerization. The final solids content of the colloidal suspension is ~10% by weight.

5.4.4 Size Characterization of the Latex Microspheres

The size of the latex microspheres was investigated by both dynamic light scattering techniques and by scanning electron microscopy (SEM).

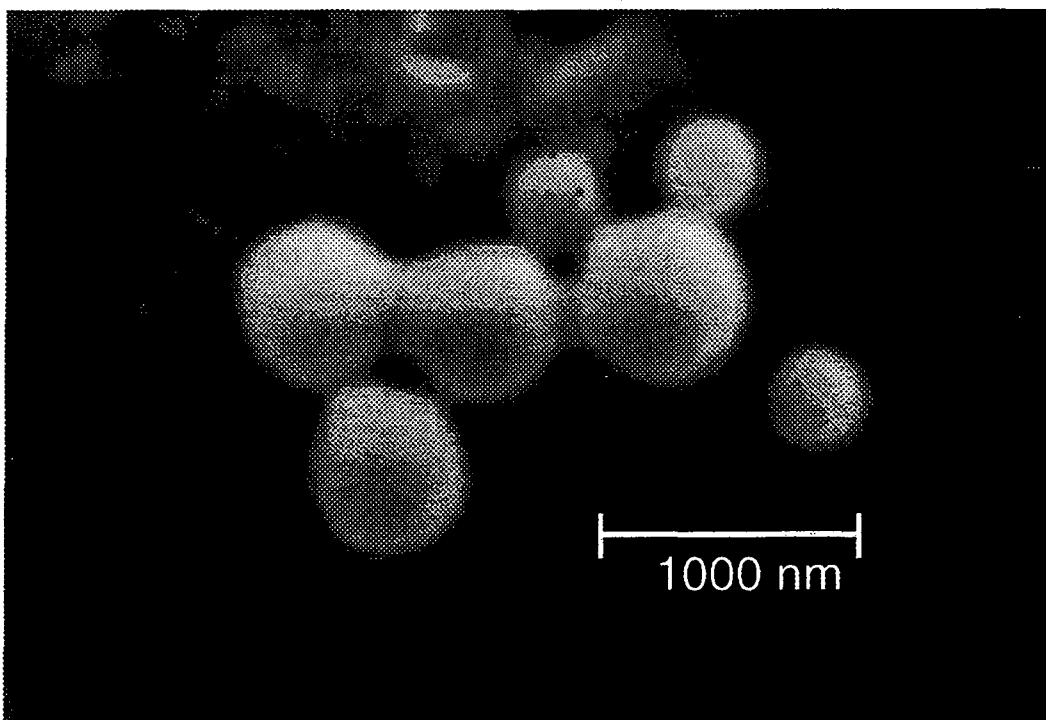


Figure 5.8 Scanning electron micrograph of the PMMA microspheres coated with approximately 25 nm of gold. Measurements from this image indicate particle radii of 320 ± 40 nm and 180 ± 40 nm. These values take into account the 25 nm layer of gold on the surface of the particles. The error arises from the 80 nm wide indistinct outline of the particles in the image. Radius measurements were made from the central point of the indistinct outline using the image analysis program NIH Image 1.52.

DLS, being the customary method for size characterization, was used initially. Measurements performed on an Autosizer 4700 (Malvern) indicated a particle radius of approximately 313 nm with a polydispersity of 10%. There was no indication of particles with a substantially different size. Rotational diffusion measurements made using two-dimensional exchange NMR did not agree with this result as will be shown below.

To resolve the discrepancy, SEM measurements were made using a Microscope Stereoscan (Cambridge Instruments) with an acceleration voltage of 8 kV. One droplet of the latex was diluted with 2 ml of water, applied to an aluminum support, freeze dried, and gold coated using an Auto Sputter Coater (Bio-Rad, Polaron Division). Particle sizes determined from the SEM micrograph in Fig. (5.8) indicate the presence of particles with two distinct radii, 320 ± 40 nm and 180 ± 40 nm. The uncertainty reflects blurring of the

microsphere edges in the picture. It appears that a second nucleation at a relatively early stage in the reaction has taken place. This would imply that the larger particles contain a 125 nm radius unenriched core, whereas the smaller particles are composed entirely of enriched PMMA.

5.4.5 Two-Dimensional Exchange NMR Experiment

Figure (5.9) shows the pulse sequence used in the two-dimensional exchange experiment. The initial ^{13}C magnetization is created through cross polarization with ^1H nuclei, and evolves for a time t_1 . During the evolution period, a decoupling field is applied in order to quench the dipolar interaction between the ^{13}C and ^1H nuclei. After the evolution period, a $\pi/2$ -pulse stores one component of the ^{13}C magnetization along the direction of the static field. Neglecting spin-lattice relaxation, the stored magnetization does not evolve during the mixing period. The second ^{13}C $\pi/2$ -pulse returns the stored magnetization to the plane perpendicular to the static field for detection accompanied by decoupling. In order to ensure that the signal at $t_2 = 0$ is acquired, a π -pulse is performed to create a spin echo. The addition of the spin echo makes it unnecessary to apply a first order phase correction along t_2 , so we are only required to apply a zero order phase correction to the resulting two-dimensional exchange spectrum. The experiment is repeated with increasing values of t_1 until a sufficient number of t_1 points have been acquired. In order obtain a pure phase absorption spectrum we utilize the States method¹³⁵.

The $t_1 = 0$ slice in each two-dimensional exchange experiment was analyzed in order to determine the CSA parameters of the carbonyl carbon in the PMMA sample. These parameters are necessary in the determination of the NMR frequency time-correlation function. Calculations yielded a value of 90 ppm for δ and 0.45 for η . Values for the isotropic shift varied between some experiments depending upon the reference frequency. These values of the isotropic shift were taken into account

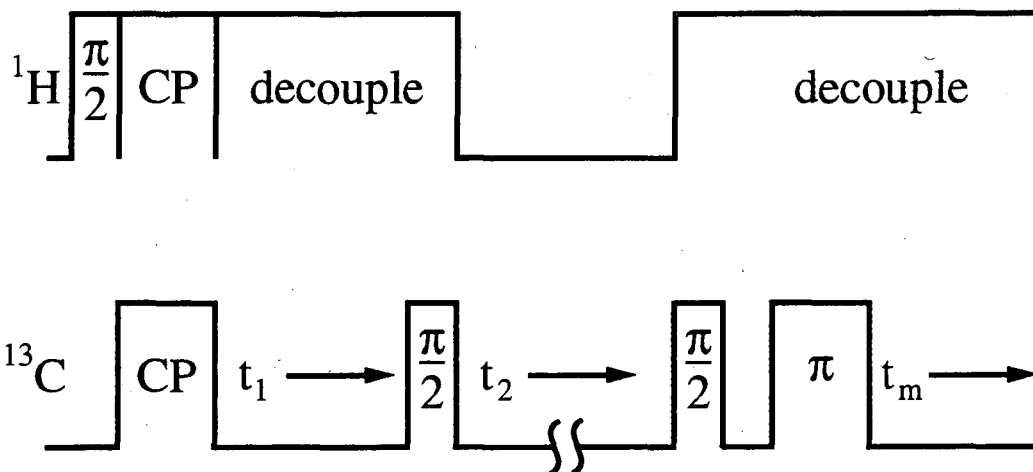


Figure 5.9 NMR pulse sequence for the two-dimensional NMR exchange experiment. ^1H excitation pulse 9 μs , crosspolarization contact time 1.5 ms, and acquisition time of 2.1 ms for a spectral window of 15 kHz. The spectrometer used in this study is not capable of changing the rf power on a given channel during the course of the sequence, so the large duty cycle decoupling pulses limit the nutation frequency to 27 kHz.

individually in the calculation of each point of the time-correlation function. All experiments were performed on a 300 MHz home-built homodyne spectrometer¹³⁶ with a Tecmag pulse programmer run by a Macintosh IIfx computer. As configured, the system achieved a 27 kHz ^1H nutation frequency. The rf power level provided acceptable decoupling of the ^{13}C - ^1H dipolar interaction in addition to pulse times short enough to make it unnecessary to perform a first order phase correction along the encode dimension, t_1 .

The PMMA- ^{13}C latex microspheres studied were produced with an expected mean radius of 300 nm, density of 1.19 g/mm³, and 10% solids content by weight with respect to the water solution. At the size and density of the latex microspheres, it is expected that the particles will completely settle out of a room temperature water suspension in approximately two to three days. As the experiment takes approximately

12 hours to complete, a significant amount of settling is expected to occur. We corrected for this problem by fabricating a sample holder which could be slowly rotated while the NMR probe is in the magnet. The sample holder consists of a KelF tube with a pulley cap supported on KelF/teflon bearings. A belt and pulley system connects the sample holder to an electric motor driven at ca. 0.05 Hz. Sample reorientation at this rate is at least 100 times slower than the reorientation of the latex spheres due to rotational diffusion, so we expect there to be no detectable effect upon the two-dimensional exchange spectrum. Settling of the sample, however, is effectively eliminated at this rotation rate.

5.4.6 Experimental Results - Two-Dimensional Exchange NMR of Rotationally Diffusing Latex Microspheres

Two-dimensional NMR exchange experiments were performed for a number of mixing times chosen to adequately sample the decay of the NMR frequency time-correlation function. Figure (5.10), a plot of the natural logarithm of the time-correlation function *versus* the mixing time, shows the presence of at least two exponentially decaying components corresponding to distinct correlation times. A biexponential function,

$$f(A, p_1, \tau_1, \tau_2; t_m) = \ln \left[A \left(p_1 \exp\left(-\frac{t_m}{\tau_1}\right) + (1 - p_1) \exp\left(-\frac{t_m}{\tau_2}\right) \right) \right], \quad (5.50)$$

shown as a solid line in Fig. (5.10) fits the data well. The adjustable parameters used in the fitting process are as follows: A takes into account effects of line broadening due to ^{13}C - ^1H dipolar coupling, p_1 is the fraction of signal contributed by particles with a rotational diffusion correlation time τ_1 , and τ_2 is the correlation time for the other sized particles. The following values yield the best fit:

$$\begin{aligned}
 \tau_1 &= 6.4 \pm 1.5 \text{ ms} \\
 \tau_2 &= 41.8 \pm 2 \text{ ms} \\
 p_1 &= 0.49 \pm 0.015 \\
 A &= 0.85 \pm 0.04
 \end{aligned}
 \tag{5.51}$$

The reported errors reflect the uncertainty in determining the proper limits of integration for the extraction of the time-correlation function from the exchange spectrum.

Assuming a temperature of 300 K and a viscosity of 1.0×10^{-2} Poise, the two correlation times correspond to the radii 180 ± 13 nm and 338 ± 5 nm. These values

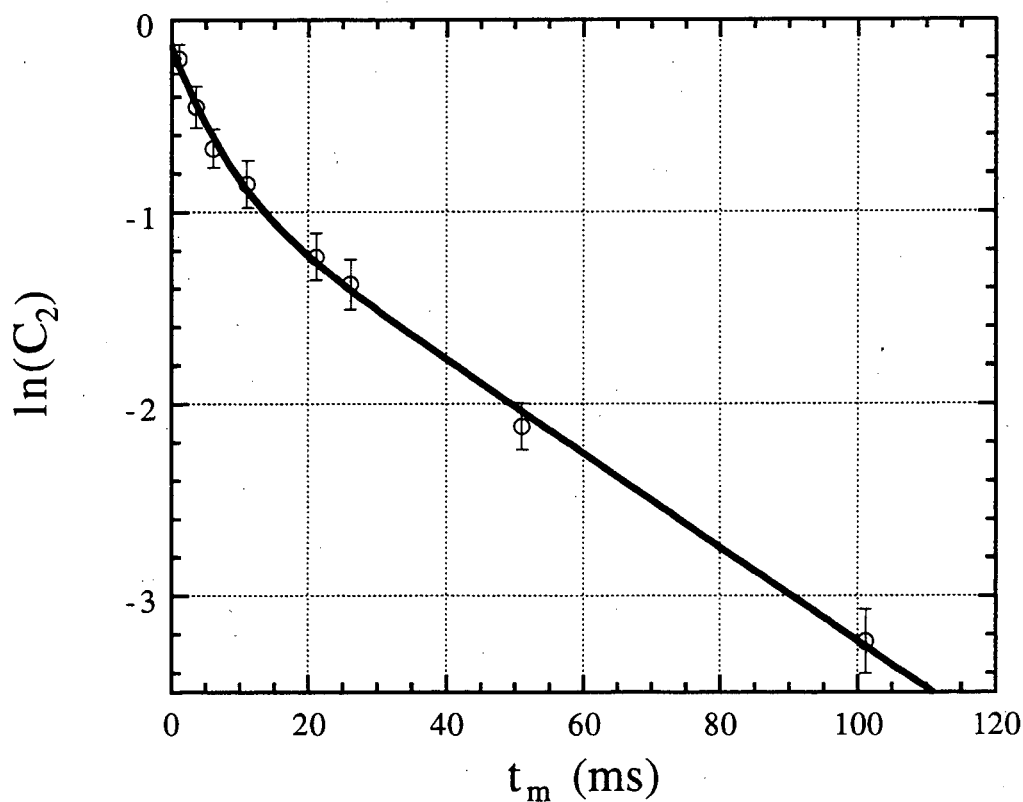


Figure 5.10 Plot of the natural logarithm of the time-correlation function vs mixing time derived from two-dimensional NMR exchange experiments. The data are fit to a four parameter biexponential function. The parameters account for two particle diameters, relative signal contribution of each particle size, and line broadening due to ^{13}C - ^1H dipolar couplings. The form of the fitting function is given in the text. Vertical error bars represent possible error in determining the CSA parameters. Due to the finite time involved in signal acquisition and evolution during t_1 , an error of ± 1 ms in time exists for each point.

agree very well with those determined by scanning electron microscopy, and the presence of two particle sizes is attributed to spontaneous nucleation during the second step of the polymerization reaction. The relative number of small to large particles is calculated to be 6:1 assuming the smaller particles are composed entirely of the 20% enriched PMMA and the larger particles contain a core of unenriched PMMA.

Due to the finite duration of the acquisition and encode times (~ 2.1 ms), each point in Fig. (5.10) has an uncertainty of ± 1 ms. This uncertainty is substantial compared to the shorter correlation time, so it is surprising that the particle size determined from this correlation time agrees so well with the SEM data. On the other hand, the uncertainty is substantially shorter than the longer correlation time, so we would expect the NMR data to provide a reasonably accurate estimate of the larger particle size.

The data were also fit to the symmetric top model, which yielded values of $D_{\parallel} \cong 30$ Hz and $D_{\perp} \cong 2.6$ Hz. Assuming the particles to be prolate ellipsoids, Eq. (5.46a), (5.46b) and (5.47a) indicate a major semi-axis of 740 nm and a minor semi-axis of 104 nm. These values definitely do not agree with either of the apparent particle sizes in the SEM picture, Fig. (5.8). Furthermore, the two diffusion coefficients do not agree with the model of a prolate ellipsoid, Eq. (5.47b).

Figure (5.11) shows a comparison of some of the experimentally obtained exchange spectra with simulations using the two measured correlation times in Eq. (5.51). The simulations are line broadened in the time domain using a 2 kHz Gaussian apodization function, and the experimental data has been line broadened by 1 kHz to reduce the effect of noise in the plot. All of the datasets have been normalized with respect to the volume under the spectrum, so a comparison of the contour levels between experiment and simulation is justified. Qualitatively, the simulations agree very well with the experimental data.

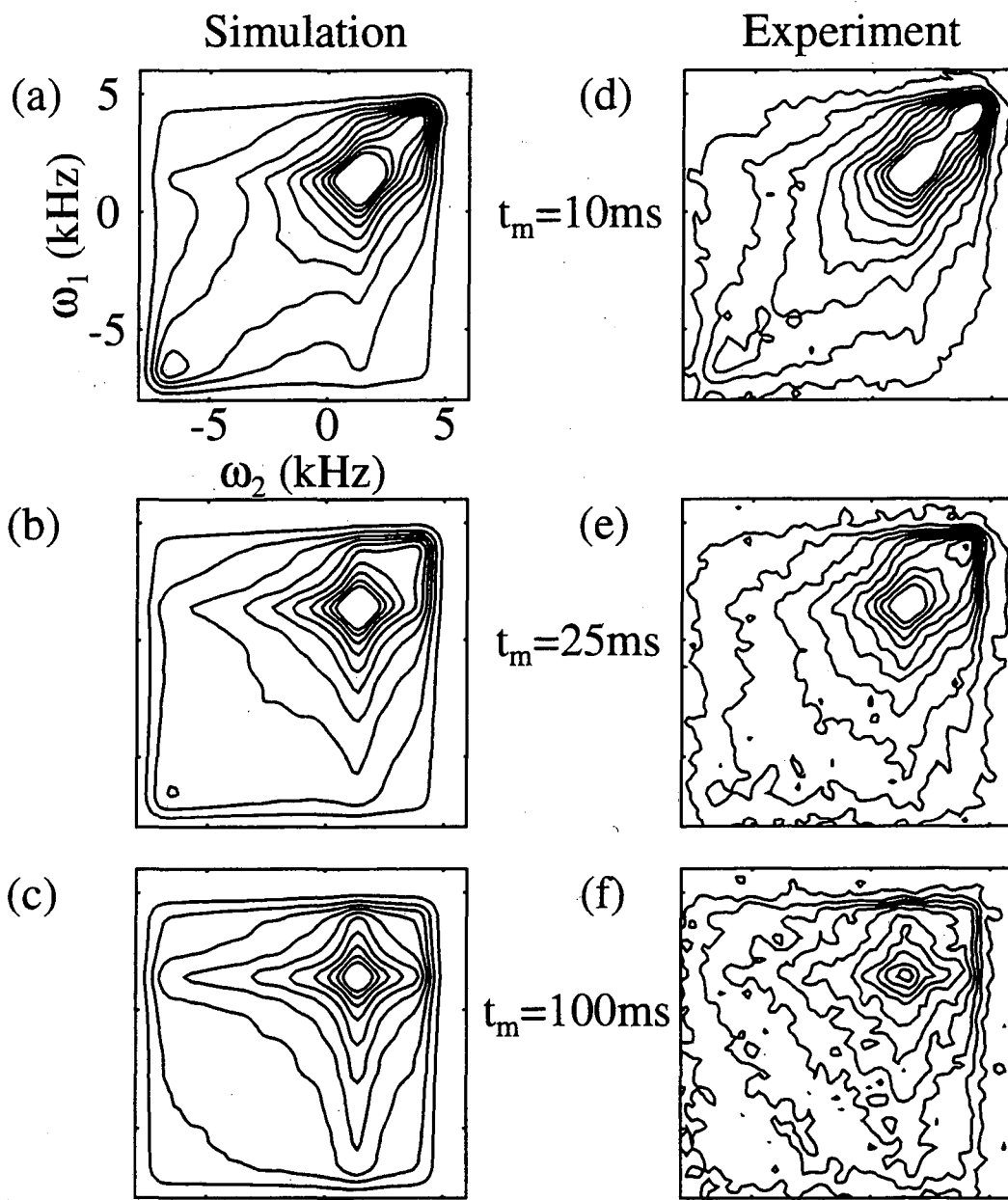


Figure 5.11 Experimentally obtained two-dimensional exchange spectra and their corresponding simulations. The simulations assume two correlation times, 6.4 ms and 41.8 ms, with equal weighting. All spectra are normalized with respect to the integral over the entire spectrum, and are plotted from -8 kHz to 6 kHz along both frequency axes. The 10 ms mixing time experimental spectrum is slightly shifted to positive frequency with respect to the other spectra due to a difference in the shim currents used during that experiment, but for the sake of uniformity (d) is plotted in the same frequency range as the other spectra. Contour levels represent steps of 10% with respect to the maximum amplitude in (f).

5.5 Conclusions

The results presented here show that two-dimensional exchange NMR provides a means of investigating the reorientational dynamics of particles for correlation times ranging from milliseconds to seconds. In fact, while DLS measurements indicate a single particle size in the sample prepared for these experiments, the NMR exchange experiments correctly indicate the presence of two distinct particle sizes determined by SEM.

For the colloidal suspension used in this study, it was necessary to signal average for approximately 12 h for each two-dimensional exchange spectrum in order to obtain spectra with a sufficiently high signal to noise ratio (S/N) to clearly show all spectral features. However, a considerably lower S/N is tolerable when the only purpose of the experiment is to obtain values of the time-correlation function. The length of the experiment may then be reduced by as much as a factor of ten, allowing the determination of a single point of the time-correlation function in approximately one hour. For a more concentrated sample, the length of the experiment may again be reduced. An increase in the particle concentration by a factor of four allows the acquisition of a two-dimensional exchange spectrum with S/N comparable to the spectra presented in this work in 45 min, and a single point in the time-correlation function can be acquired in as little as 5 min.

The improved performance of two-dimensional exchange NMR for concentrated samples makes it ideally suited for studying reorientational processes in sediments, slurries, pastes, or any other system with high particle concentrations. The technique also promises to be useful in studying particle dynamics in turbulent, non-Newtonian, and solid particle flow. Given sufficient signal, NMR exchange experiments may be combined with imaging techniques to correlate reorientational dynamics with spatial maps or translational motion. Stimulated echo exchange experiments¹³⁷ which do not

require the acquisition of the entire two-dimensional time domain data set may be especially useful in this case.

The orientational probe used in this work, the CSA of the ^{13}C nucleus, is suitable for measuring reorientational processes with correlation times ranging from milliseconds to one or two seconds. Using deuterium as a probe allows the investigation of time scales approximately one order of magnitude shorter^{118,121}. For shorter times, two-dimensional exchange pulsed EPR may prove useful.

Appendix A Coaxial Resonator Schematics

The following sections contain schematics for both of the coaxial resonator imaging probe heads described in Chapter 3. These are only some of the schematics originally given to the machine shop, and do not contain drawings for all aspects of the probe, but they do provide guidelines for the production of a coaxial resonator probe head. The two resonators and phantoms are constructed in such a way that they are both easily interchangeable with the same probe body (not shown). The resonator effectively takes the place of the normal coil and sample in a NMR probe suitable for use in a super-wide bore superconducting magnet. Variable capacitors indicated in Fig. (3.4) should be located below the platform which supports the coaxial resonator. The gradient coil holders were never utilized for the production of static field gradients, but they did serve as a means of supporting the resonator.

In most of the drawings the object possesses circular symmetry, so the views presented are cross sectional and from the top or the bottom. Assembly drawings are generally just cross-sectional views of all or part of the resonator and phantom. I have decided not to number these figures as they are never specifically referred to in the text.

The program which was used to produce the drawings, Claris CAD v. 2.03, does not transfer drawings well to other programs. In this case the drawings were transferred from Claris CAD to Microsoft Word. For this reason, in some of the drawings, some circles which should appear to be concentric are not, and some lines which should be joined are not. As a good rule of thumb in interpreting the drawings, everything is centered about the center of the object unless explicitly stated to the contrary.

A.1 "Concentric Cylinder" Resonator and Phantom

The following schematics represent the resonator and phantom used in Section 3.6. The clamps and outer conductor shown are also used in the construction of the micro-phantom of Section 3.7.

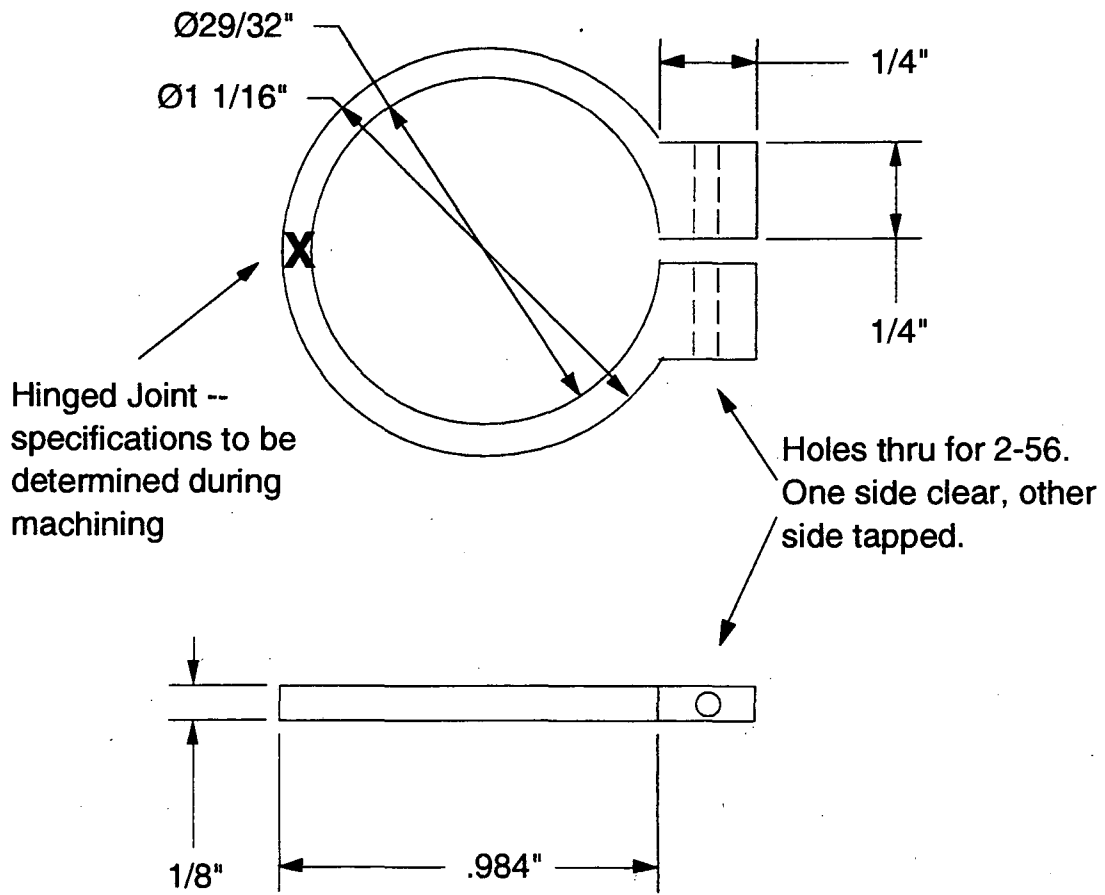
Clamp

material : aluminum

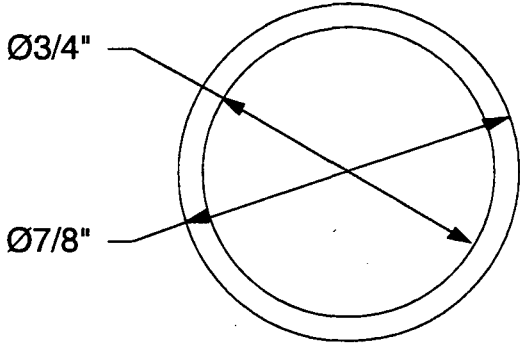
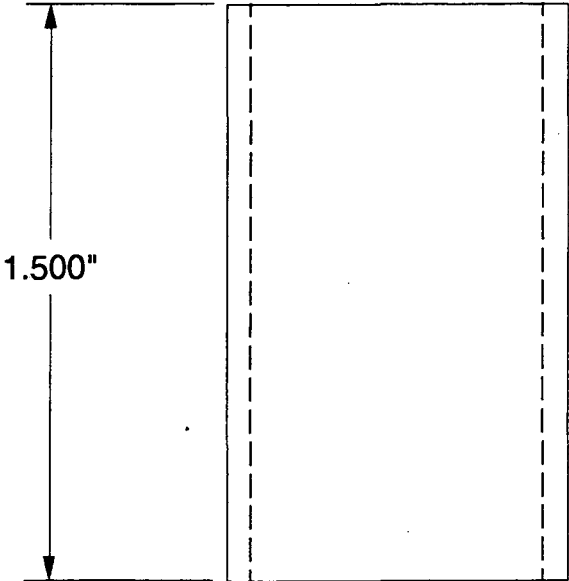
required : 2

scale 1:2

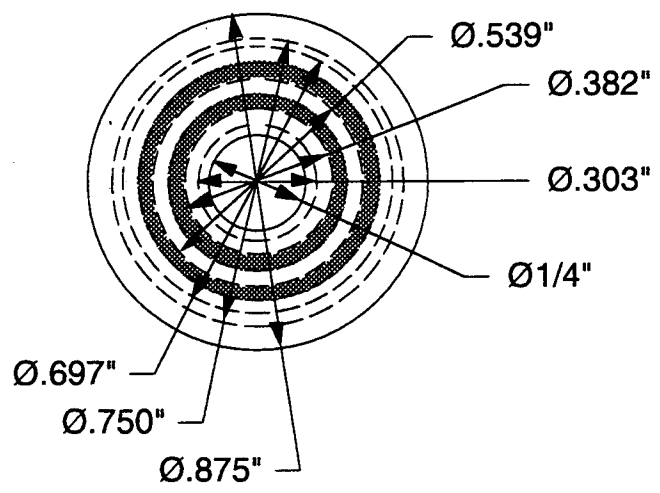
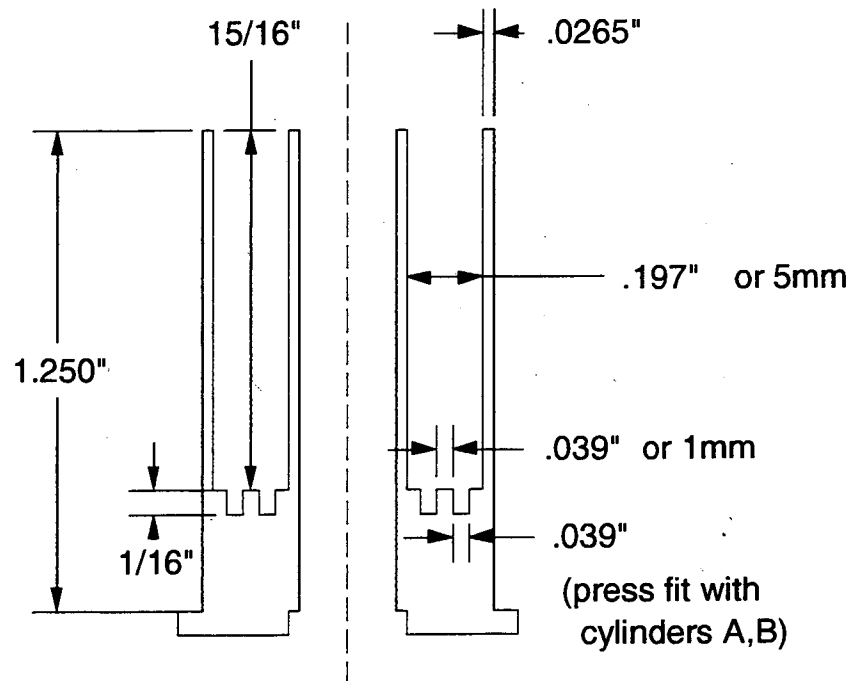
screw : brass or aluminum



Outer Conductor
Material : copper
required : 1
scale 1:2



Sample Cup
Material : plexiglass
required : 1
scale 1:2



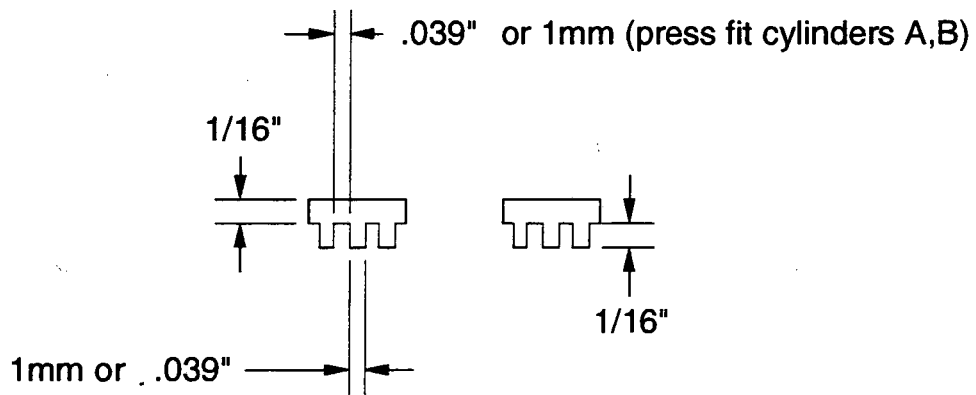
Inner and outer cylinder may need to be made separately and glued onto the base of the sample cup.

Cylinder Holder

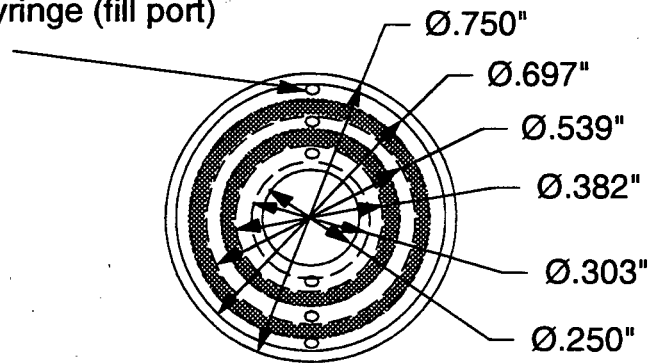
Material : plexiglass

required : 1

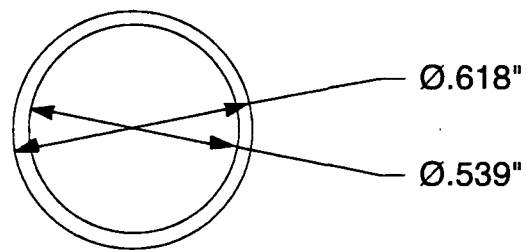
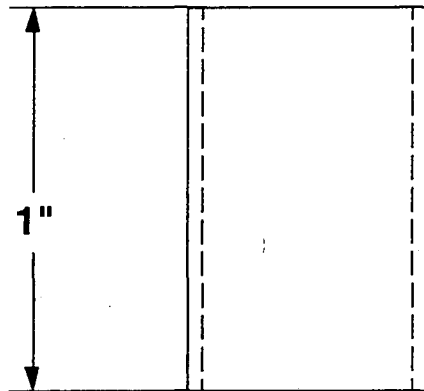
scale 1:2



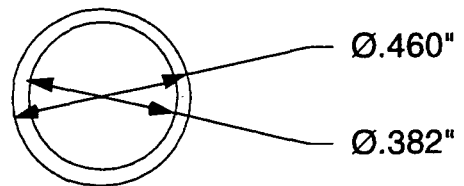
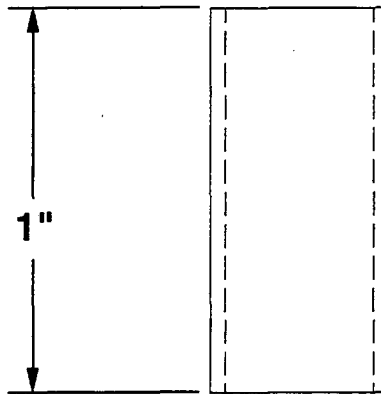
6 holes $\approx 1/32''$ diameter.
For syringe (fill port)



Cylinder A
Material : plexiglass
required : 1
scale 1:2

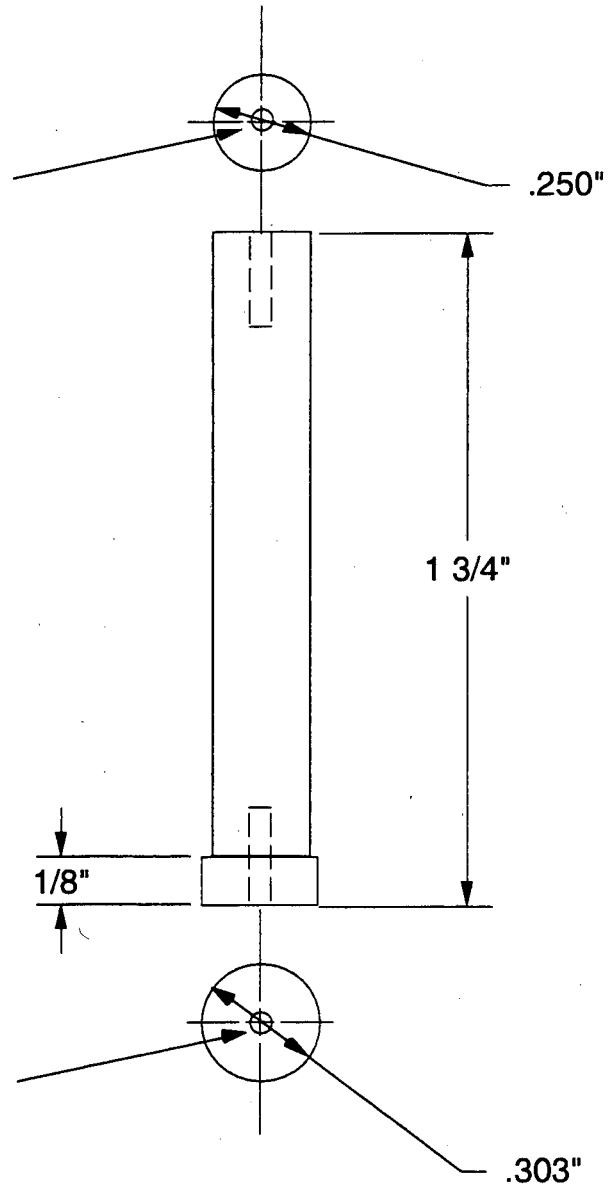


Cylinder B
Material : plexiglass
required : 1
scale 1:2



Inner Conductor
material: copper
no required: 1
scale: 1:2

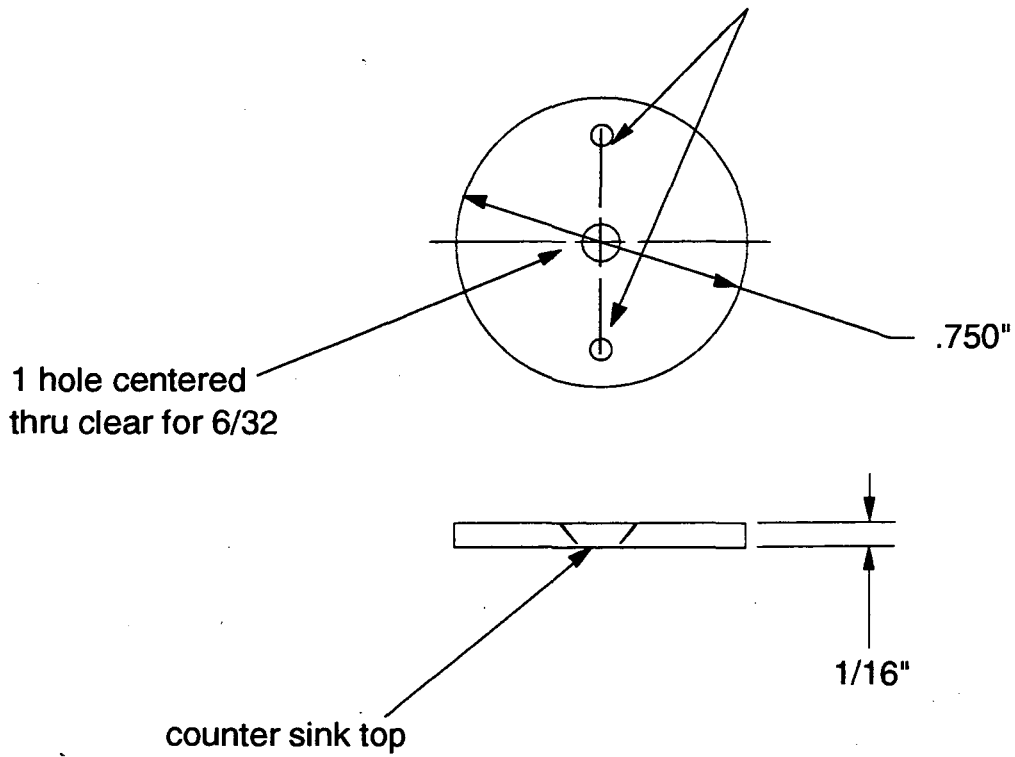
1 hole tapped for
6-32
centered 1/4" deep



1 hole tapped for
6-32
centered 1/4" deep

Capacitor plates
material: copper
no required: 2
scale: 1:2

2 holes thru to hold 1/16" pegs
to fit into Gradient Holder

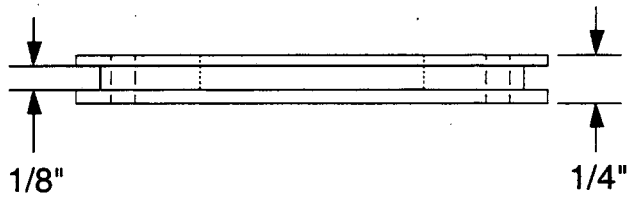
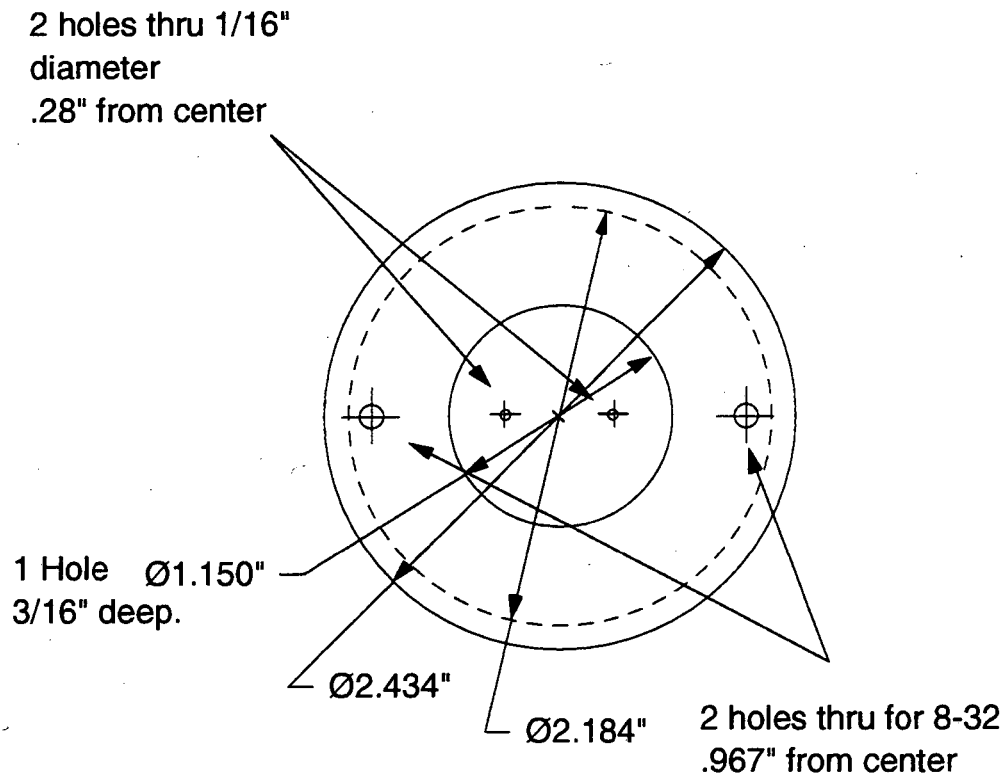


Gradient Coil Holder 1

Material; Glass reinforced phenolic

Number Required : 1

scale 1:1

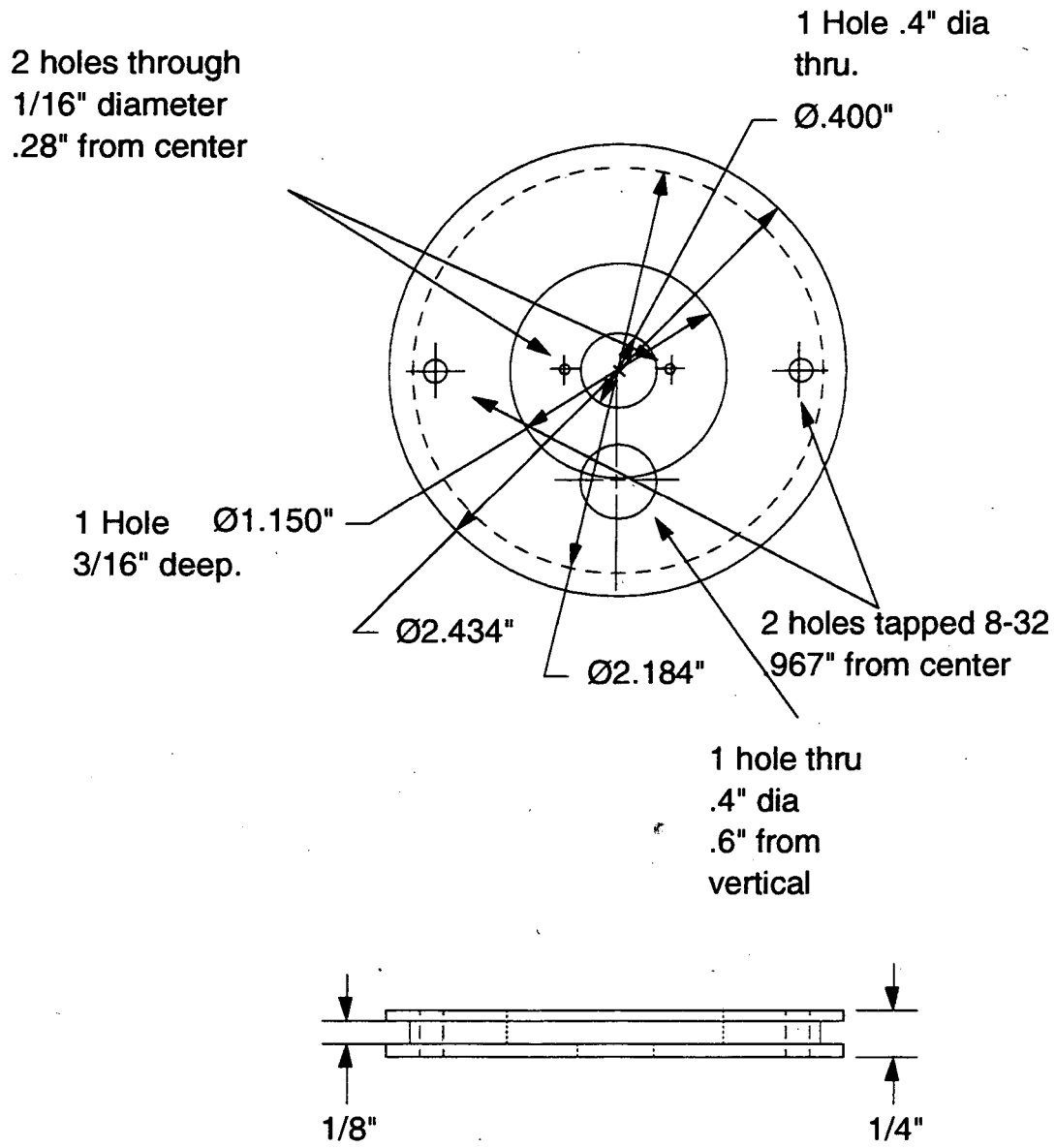


Gradient Coil Holder 2

Material; Glass reinforced phenolic

Number Required : 1

scale 1:1

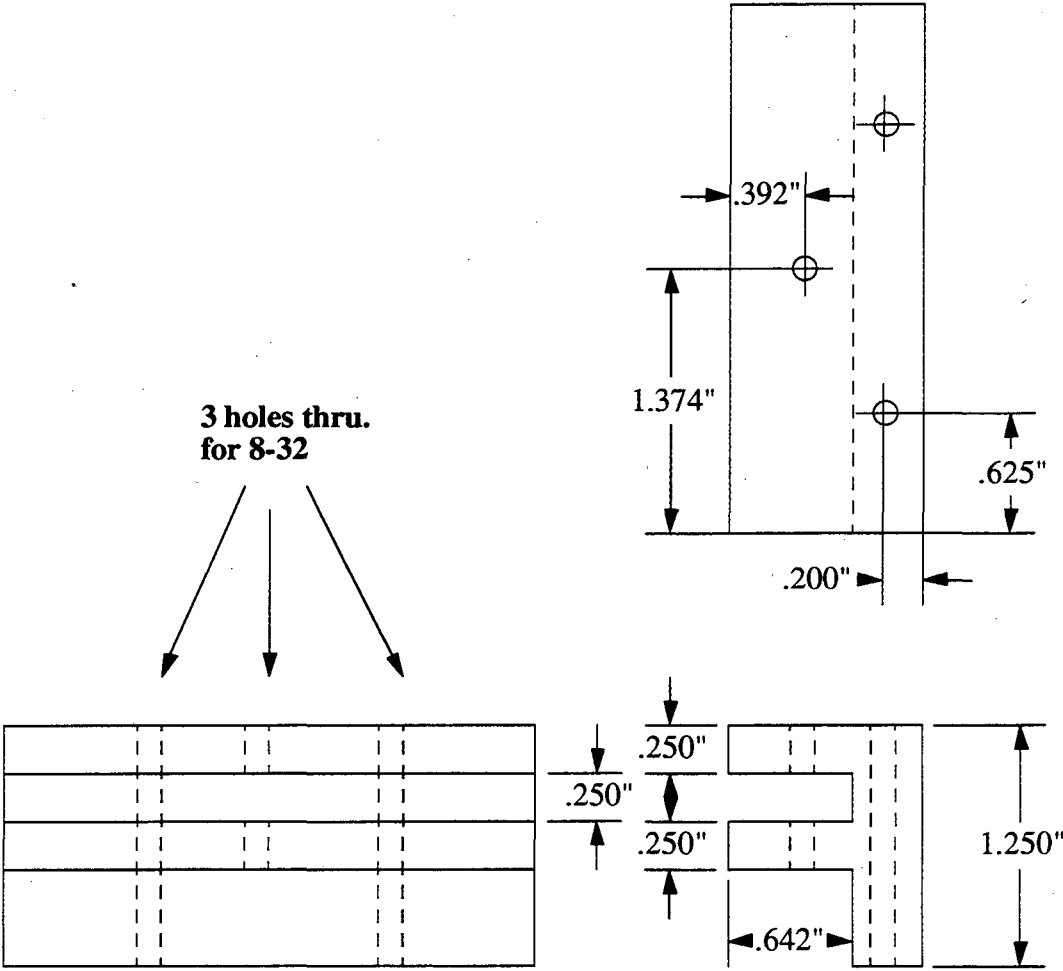


Gradient Top Bracket

Material : Glass reinforced phenolic

Number required : 2

scale 1:1



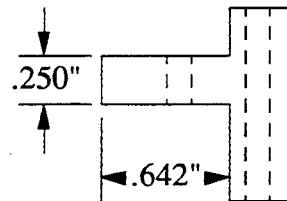
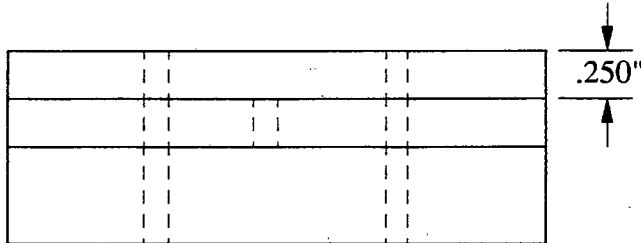
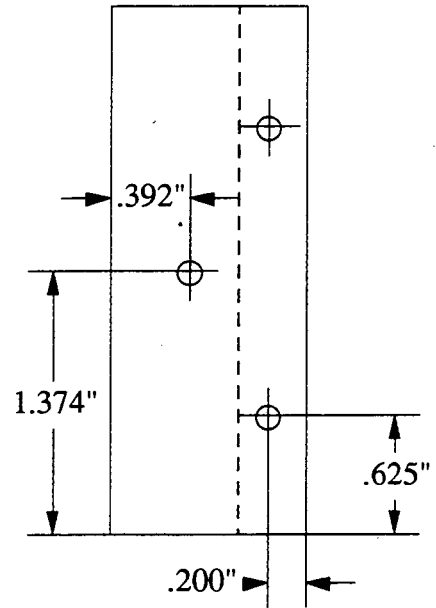
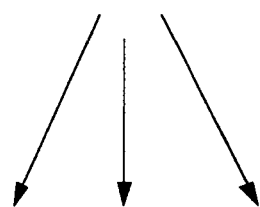
Gradient Bottom Bracket

Material : Glass reinforced phenolic

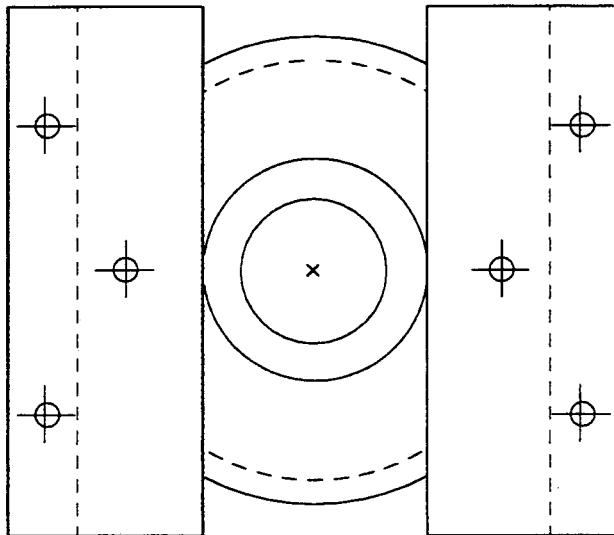
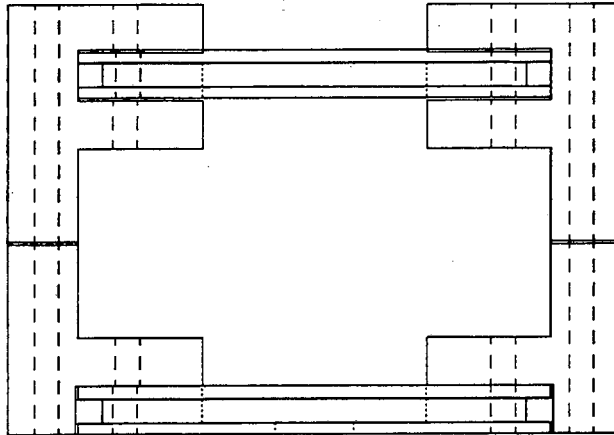
Number required : 2

scale 1:1

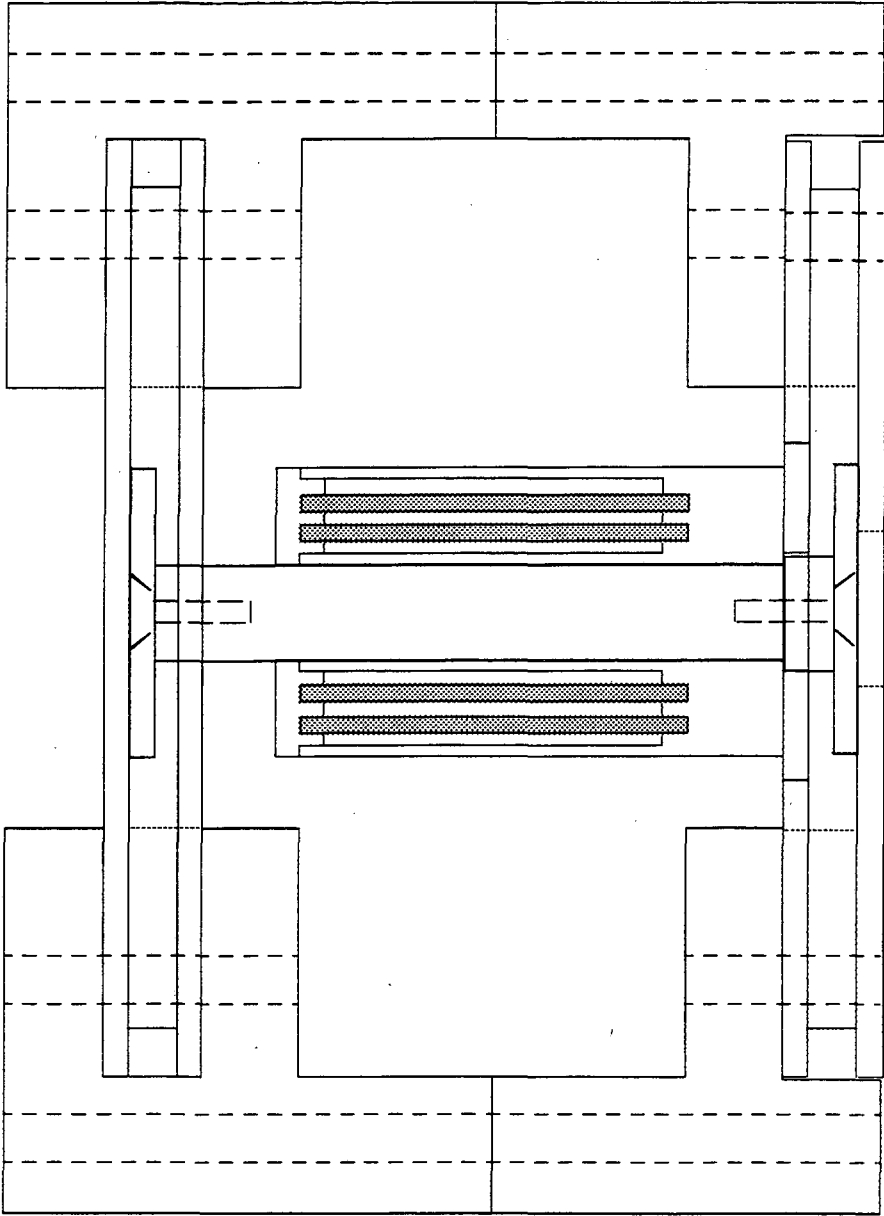
**3 holes thru.
for 8-32**



Gradient Holder and Bracket Assembled
scale 1:2



Probe Head Assembled
(rotated 90°)
Scale 1:2



A.2 "Micro-Phantom" Resonator and Phantom

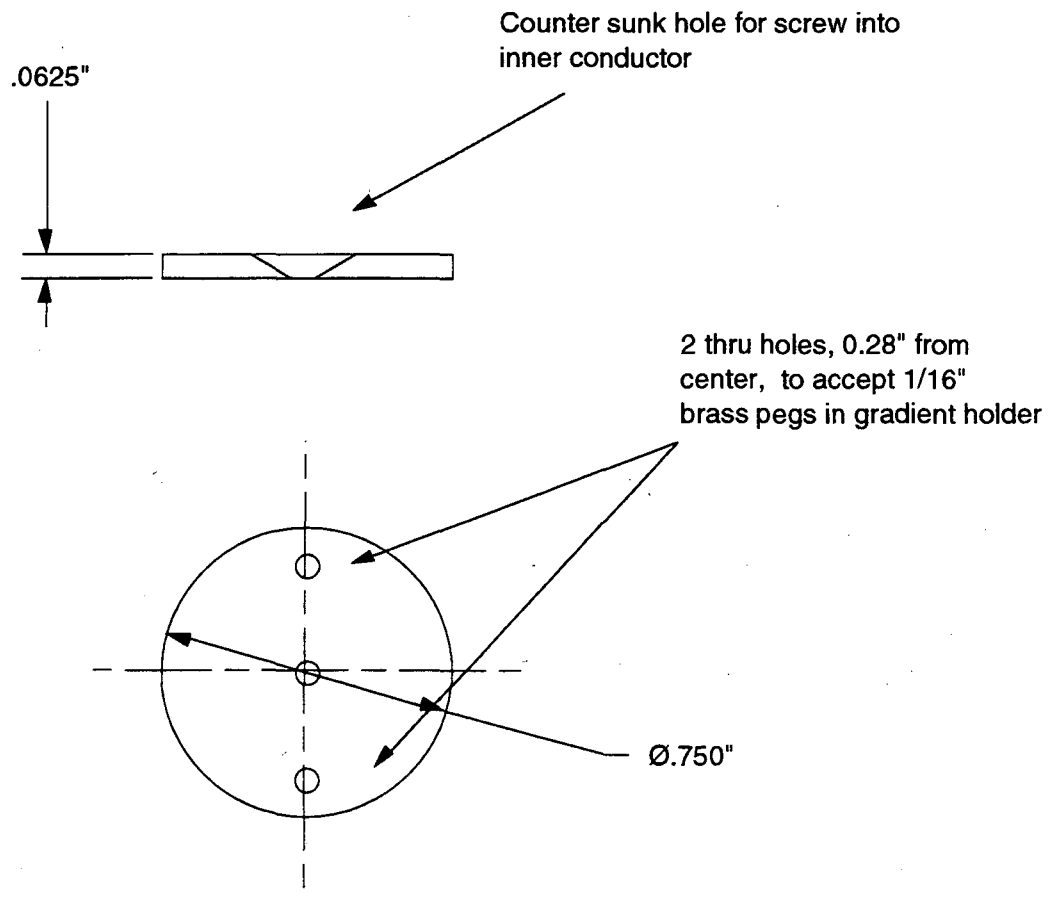
The following schematics represent the resonator and phantom used in Section 3.7. Parts of the assembly which are shared with the concentric cylinder phantom and resonator are not shown (i.e. outer conductor, capacitor clamp, z-gradients, etc.). The phantom with 25 μm steps is not shown.

Capacitor Plates

Material: Copper

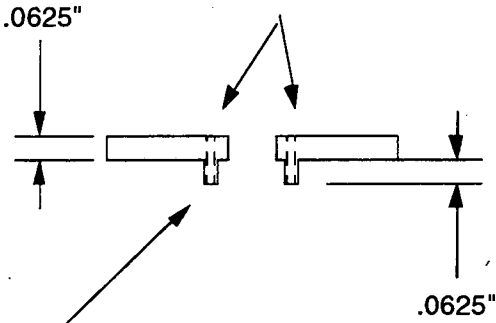
required : 2

scale 1:2

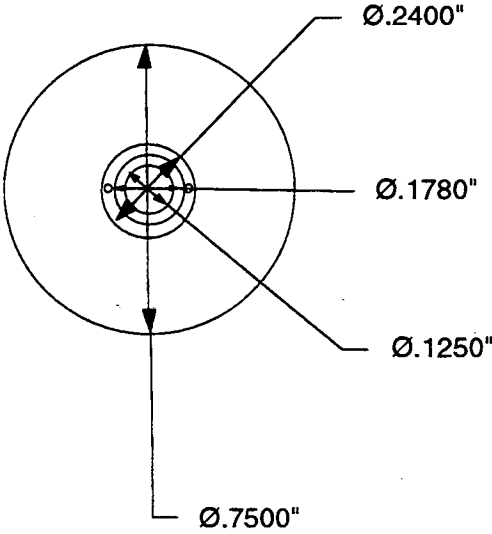


Cylinder Cap
Material: Plexiglass
required : 1
scale 1:2

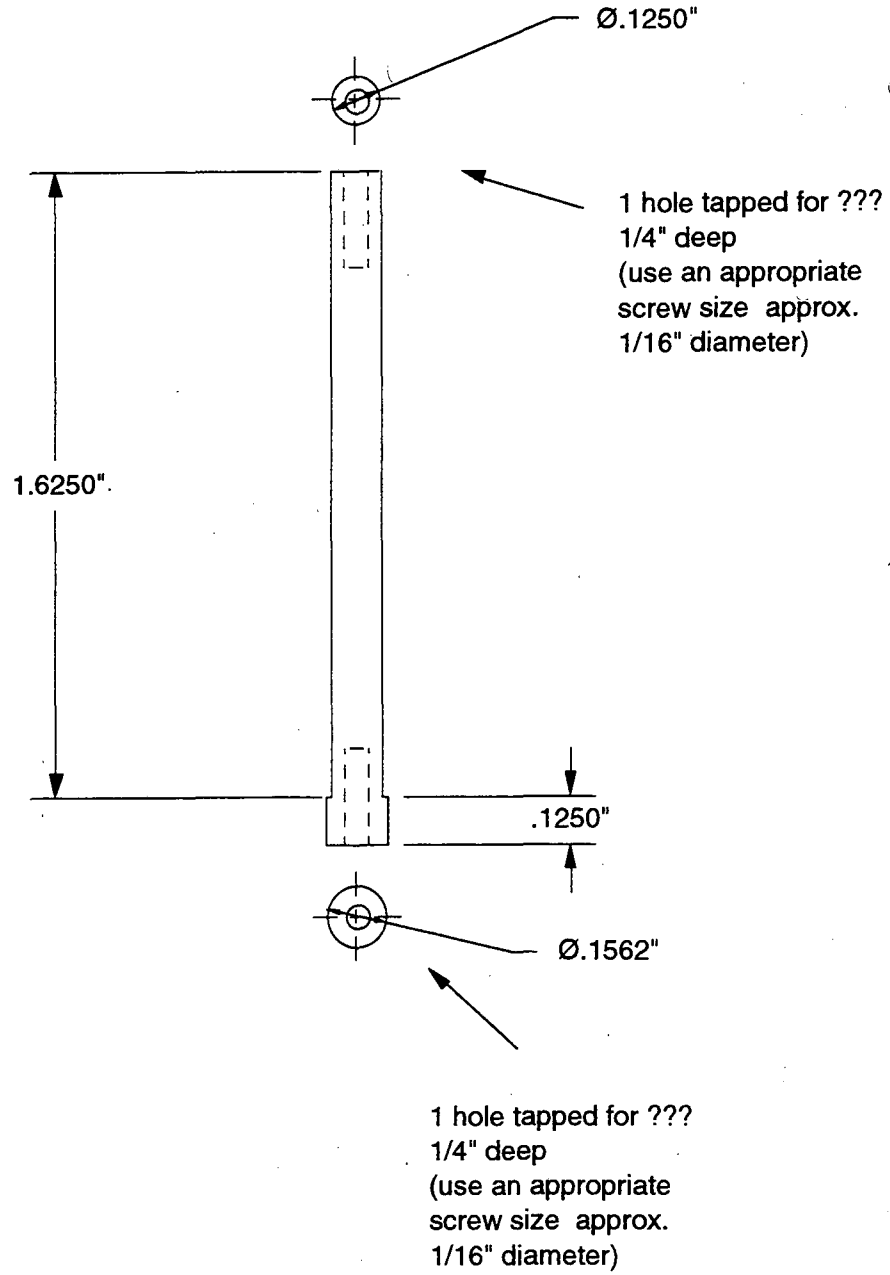
Two holes approx .024" diameter to fit .020" diameter syringe needle (needle provided)



circular ridge used for locating cap between inner and outer cylinder

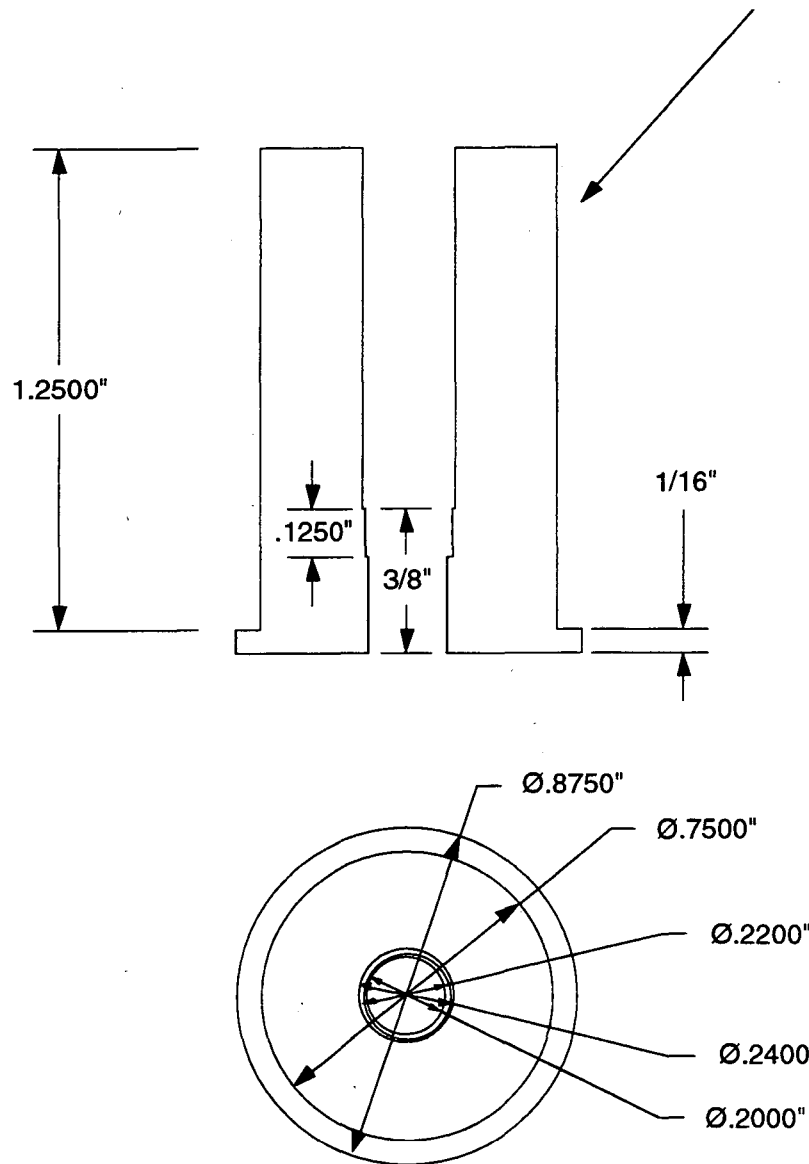


Inner Conductor
Material: Copper
required : 1
scale 1:2



Outer Cylinder
Material: Plexiglass
required : 1
scale 1:2

An easy press fit with
copper cylinder provided



Inner Cylinder (0.004" Steps)

Material: Plexiglass

required : 1

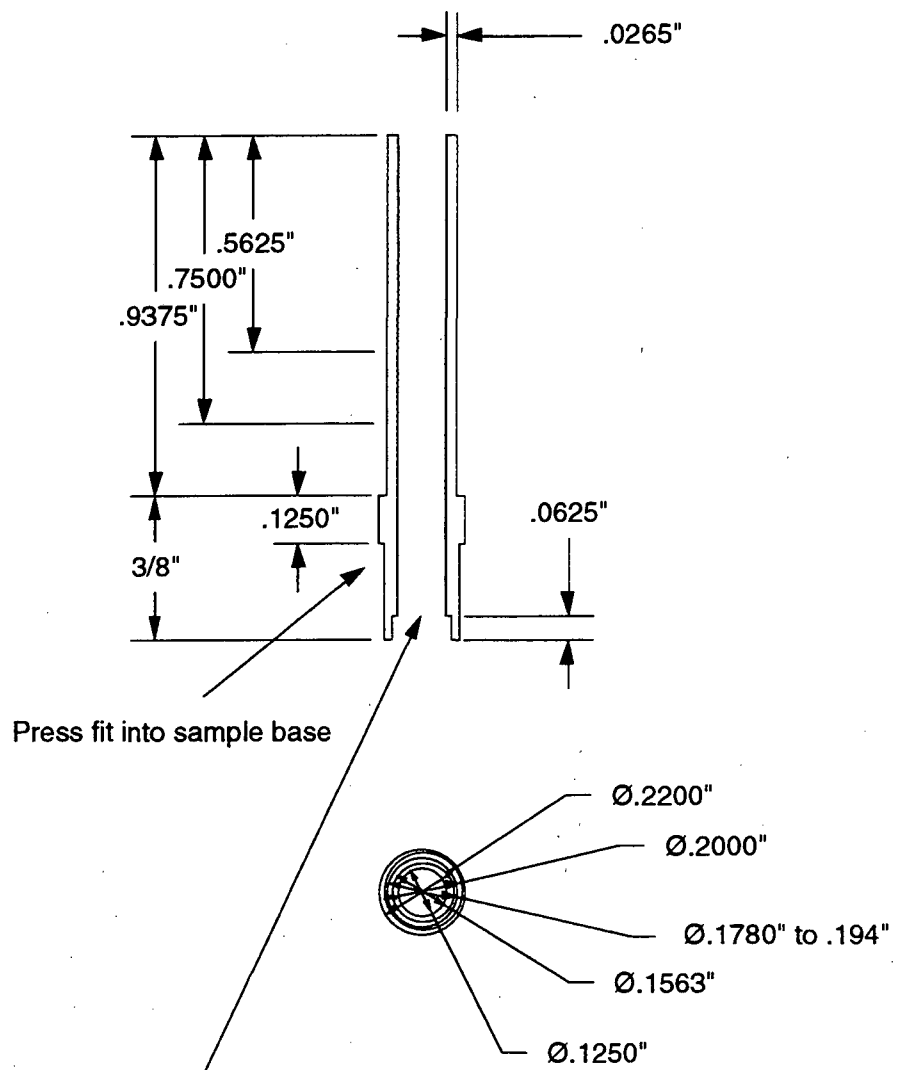
scale 1:2

The step sizes are critical. The steps should be as square as possible under the circumstances.

OD of cylinder from top to 0.5625" is 0.178"

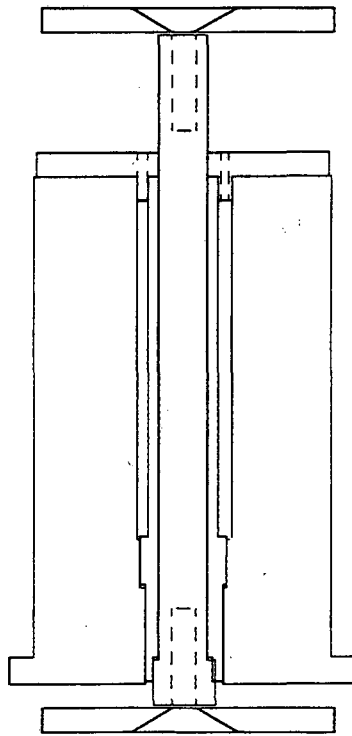
OD from 0.3750" to 0.750" is .186"

OD from 0.5625" to 0.9375" is .194"



An easy press fit over inner conductor

Assembly Drawing

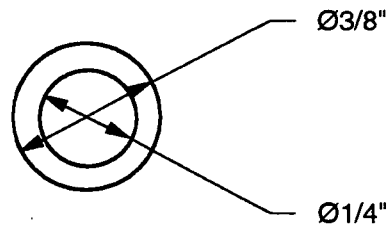
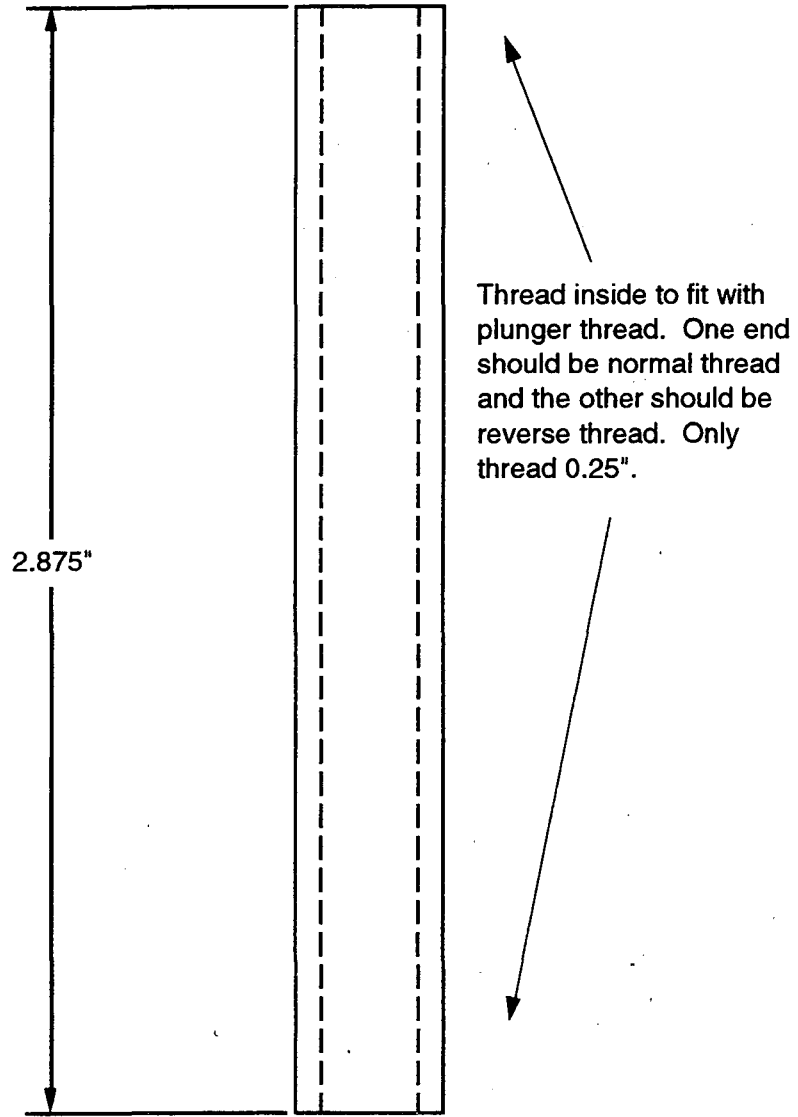


Appendix B Sample Holder for Fluid Flow in Porous Media Experiments

The following section contains schematics for the fluid flow apparatus referred to in Chapter 4. I have decided not to number these figures as they are never specifically referred to in the text.

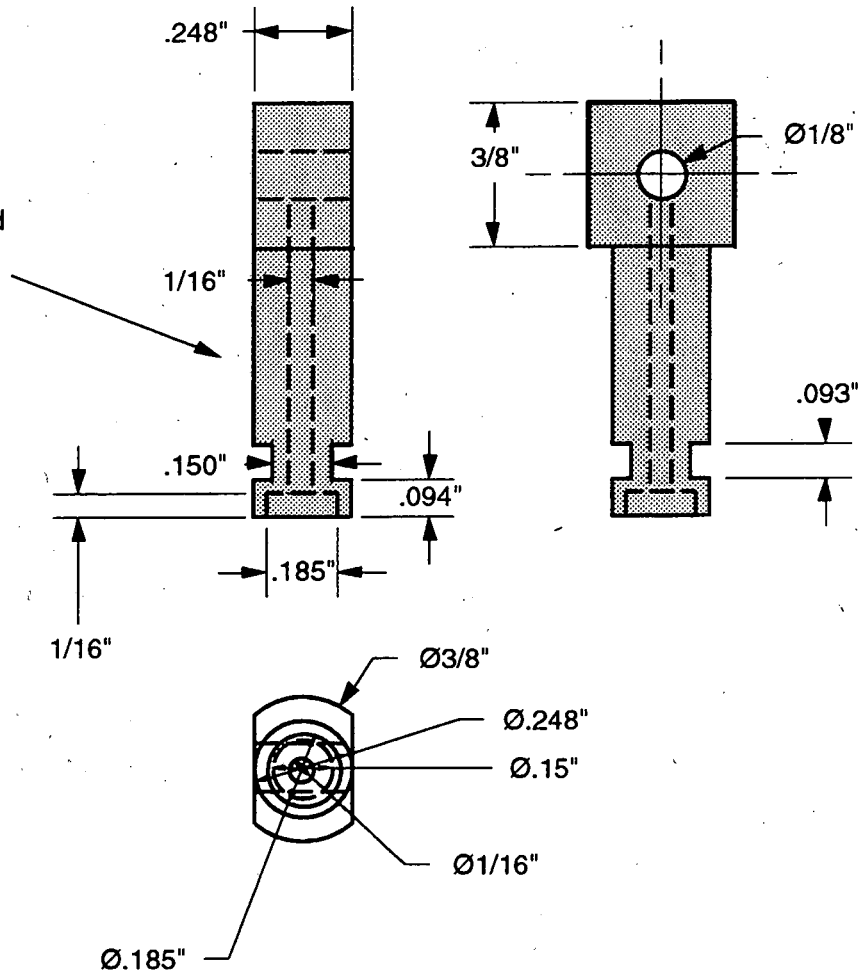
The program which was used to produce the drawings, Claris CAD v. 2.03, does not transfer drawings well to other programs. In this case the drawings were transferred from Claris CAD to Microsoft Word. For this reason, in some of the drawings, some circles which should appear to be concentric are not, and some lines which should be joined are not. As a good rule of thumb in interpreting the drawings, everything is centered about the center of the object unless explicitly stated to the contrary.

Sample Tube
Material: polycarbonate (Lexan)
Side View and end view
quantity: 1
scale: 1:2



Plunger
 material: polycarbonate (Lexan)
 side views and end view
 quantity: 4
 scale: 1:2

Thread 0.375" starting
 from 3/8" diameter.
 O.D. here should be a
 little larger than
 0.248" in order to get
 a tight fit with the
 sample tube. Thread
 two with normal thread
 and the others with
 reverse thread.



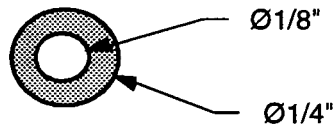
Washer

material: copper or brass

side view and end view

quantity: 4

scale: 1:2



This will be soldered on to the inlet tube such that the edge of the washer is approximately 0.6" from the threaded end of the tube. (see assembly)

If no standard washer exists which will do the job then you may need to make a washer.

Inlet tube
material: copper or brass
side views and end view
quantity: 4
scale: 1:2

Solder on a tygon hose adapter
for 3/8" ID tygon tubing.

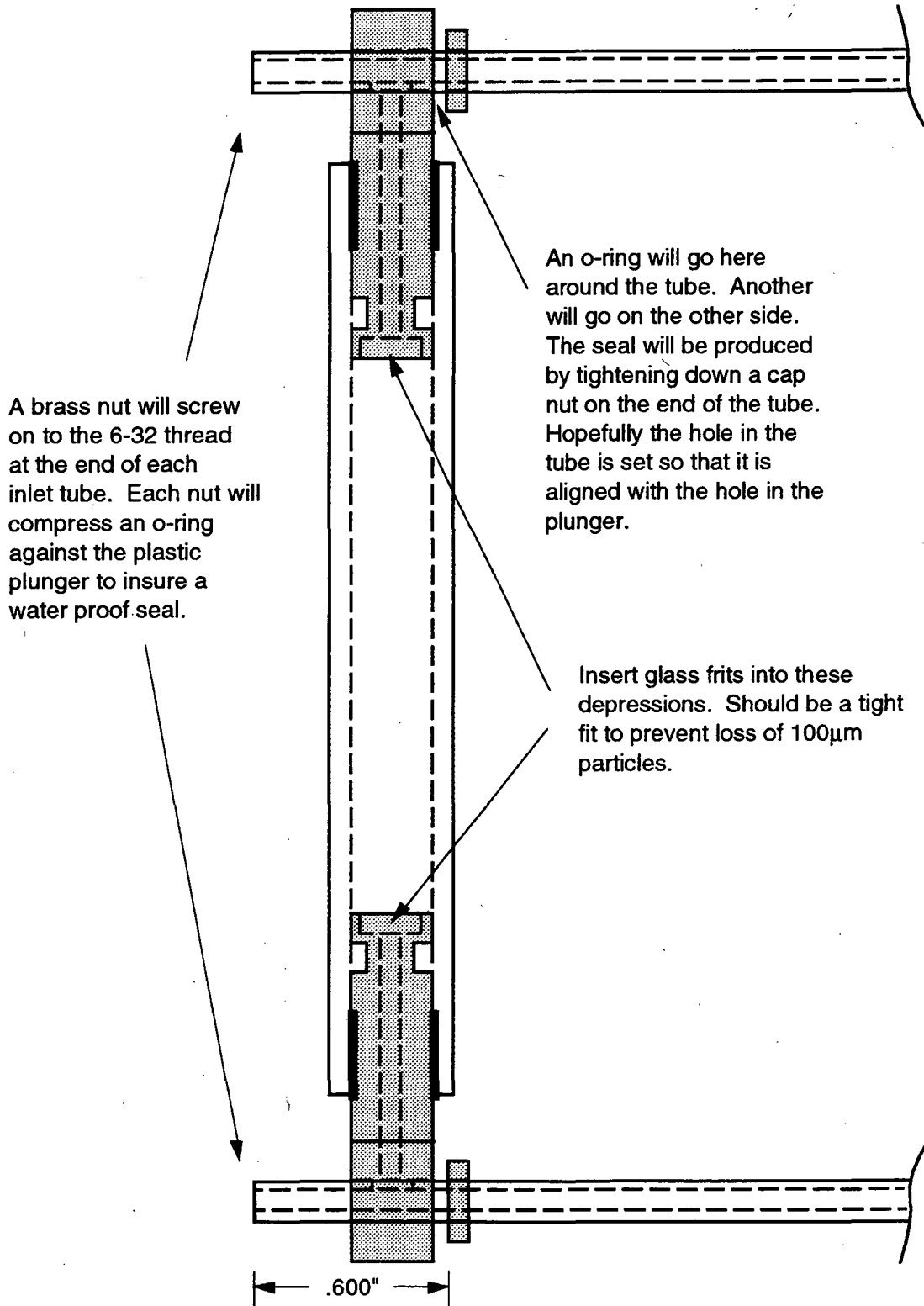
Mill a hole 0.0625" across
with height 0.125" through
one side. Center hole 0.43"
from end of tube.

Thread last 0.25" on the
outside with 6-32. To get
snug fit with appropriate
nut

Solder end for a water
tight seal.



Assembly Drawing
side view
scale: 1:2



Appendix C Source Code for Rotational Diffusion Simulations

The following sections contain the source code and parameter file used in the simulation of two-dimensional exchange spectra for particles undergoing isotropic rotational diffusion. All source code is written in C and should be portable between different UNIX systems. Some modifications will be necessary to have the simulation run on a non-UNIX system or computer. Not included are the complex number and memory allocation libraries which may be found in Numerical Recipes in C.¹³⁸ In addition, the header files "complex.h", "memalloc.h" and "csaexchsubs.h" are not included, but these files may be written using the information contained here.

C.1 Main Program and Internal Subroutines

The following is a complete listing of the main source file "csaexch.c" used for the simulation of the two-dimensional exchange spectra in Chapter 5. The program uses the parameter file "csaexch.par" for all of the necessary input parameters. See Section B.3. Output consists of both the Gaussian line broadened pure-absorption spectrum and non-line broadened spectrum. One may choose to output the data as either a binary floating point (single precision) file or as tab delimited text. The commenting in this file is rather complete and should provide sufficient guidance for modification of the code.

```
#include "./complex.h"
#include "./memalloc.h"
#include "./csaexchsubs.h"
#include <stdio.h>
#include <math.h>
#include <time.h>
#define Pi (3.141592654)

/*****
  Simulates CSA 2d exchange spectrum for a site undergoing rotational
  diffusion. Spectrum simulated in the frequency domain. Does this for
  multiple correlation times. Only works for one set of CSA parameters.
```

This version is the self-contained version and requires the subroutine files complex.c, memalloc.c and csaexchsubs.c. complex.c contains the Numerical Recipes complex number subroutines. memalloc.c contains the Numerical Recipes memory allocation subroutines.

*****/

main()

```
{
    FILE *par;
    char str[100][100], spec_file[100], speclb_file[100], CT_file[100];

    void C11();
    double gCSA(), hCSA();
    double *ST, *CT, *CTsq;
    double **C11_dist, *C11_dist_holder, C11_sum;
    dcomplex **spectrum;
    double **spectrumReal;
    double sigma, delta, eta;
    double sb1, sb1_holder, omega1, omega2, delta_omega;
    int istr, ii, i, j, k, l;
    /** b2 is actually a difference of b for pas1 and pas2 ***/
    double b1, b1min, b1max, b1inc, b2, b2min, b2max, b2inc;
    double a1, almin, almax, alinc, a2, a2min, a2max, a2inc;
    double population[50], tm[50], Dr[50], sw1, sw2, lb1, lb2, normalization;
    int alnpts, a2npts, b1npts, b2npts;
    int wlnpts, w2npts, Lmax[50], output_type, exchange, output;
    int nCorrTimes;

    time_t Tbefore, Tafter;

    istr=0;
    /** input parameters ***/
    par=fopen("csaexch.par", "r");
    fscanf(par, "%s %lf %lf %lf", str[++istr], &sigma, &delta, &eta);
    fscanf(par, "%s %lf %lf %d", str[++istr], &almin, &almax, &alnpts);
    fscanf(par, "%s %lf %lf %d", str[++istr], &a2min, &a2max, &a2npts);
    fscanf(par, "%s %lf %lf %d", str[++istr], &b1min, &b1max, &b1npts);
    fscanf(par, "%s %lf %lf %d", str[++istr], &b2min, &b2max, &b2npts);
    fscanf(par, "%s %lf %d %lf %lf %d
%lf", str[++istr], &sw1, &wlnpts, &lb1, &sw2, &w2npts, &lb2);
    fscanf(par, "%s %s", str[++istr], spec_file);
    fscanf(par, "%s %s", str[++istr], speclb_file);
    fscanf(par, "%s %d", str[++istr], &output_type);
    fscanf(par, "%s %lf", str[++istr], &normalization);
    fscanf(par, "%s %d", str[++istr], &output);
    fscanf(par, "%s %d", str[++istr], &nCorrTimes);
    for(i=1; i<=nCorrTimes; i++)
        fscanf(par, "%s %lf %lf %lf
%d", str[++istr], &population[i], &tm[i], &Dr[i], &Lmax[i]);

    fclose(par);
    /** check parameter input ***/
    ii=0;
    if (output==1)
    {
        printf("%s %lf %lf %lf\n", str[++ii], sigma, delta, eta);
        printf("%s %lf %lf %d\n", str[++ii], almin, almax, alnpts);
    }
}
```

```

        printf("%s %lf %lf %d\n",str[++ii],a2min,a2max,a2npts);
        printf("%s %lf %lf %d\n",str[++ii],b1min,b1max,b1npts);
        printf("%s %lf %lf %d\n",str[++ii],b2min,b2max,b2npts);
        printf("%s %lf %d %lf %lf %d
%lf\n",str[++ii],sw1,wlnpts,lb1,sw2,w2npts,lb2);
        printf("%s %s\n",str[++ii],spec_file);
        printf("%s %s\n",str[++ii],speclb_file);
        printf("%s %d\n",str[++ii],output_type);
        printf("%s %lf\n",str[++ii],normalization);
        printf("%s %d\n",str[++ii],output);
        printf("%s %d\n",str[++ii],nCorrTimes);
        for(i=1;i<=nCorrTimes;i++)
            printf("%s %lf %lf %lf
%d\n",str[++ii],population[i],tm[i],Dr[i],Lmax[i]);
    }

    /*** get marginal distributions C11 ***/
    C11_dist=dmatrix(1,nCorrTimes,0,b2npts-1);
    C11_dist_holder=dvector(0,b2npts-1);
    for(i=1;i<=nCorrTimes;i++)
    {
        C11(C11_dist_holder,b2min,b2max,b2npts,tm[i],Dr[i],Lmax[i],output);
        C11_sum = 0.00;
        for(j=0;j<=b2npts-1;j++)
        {
            C11_dist[i][j] = population[i]*C11_dist_holder[j];
            C11_sum +=C11_dist[i][j]*b2max/(double)b2npts;
        }
        if (output==1)
            printf("Area under C11_dist[%d] = %lf\n",i,C11_sum);
    }

    /** these output statements are for debugging use **/
    wr_explld_ascii_general(C11_dist[1],0,b2npts-
1, "/usr/people/geoff/pro/sims/c11_1");
    if (nCorrTimes>=2)
        wr_explld_ascii_general(C11_dist[2],0,b2npts-
1, "/usr/people/geoff/pro/sims/c11_2");

    /***
    Modify sigma, delta and eta values so that all frequencies will be
    mapped to the range
    1 to wlnpts and w2npts. This way one can calculate a frequency,
    truncate it, and then
    use it as the array index for adding its sb1*C11 values to the freq
    domain histogram
    ***/
    delta_omega = 2.00*sw1/(double)wlnpts;
    if (output==1) printf("new sigma, delta and omega values -->\n");
    sigma = (double)(wlnpts/2) - sigma/delta_omega + 1.00;
    delta = -delta/delta_omega;
    eta = -eta;
    if (output==1) printf("sigma=%lf delta=%lf
eta=%lf\n",sigma,delta,eta);

    /*** initialize matrices for spectrum ***/
    spectrum=dcmatrix(1,wlnpts,1,w2npts);

```



```

spectrumReal=dmatrix(1,w1npts,1,w2npts);
for (i=1;i<=w1npts;i++)
  for (j=1;j<=w2npts;j++)
  {
    spectrum[i][j]=DComplex(0.00,0.00);
    spectrumReal[i][j] = 0.00;
  }

/** initialize angle values and increments **/
/** this is for debugging use and may be removed **/
b1=b1min;
b2=b2min;
a1=a1min;
a2=a2min;
blinc=(b1max-b1min)/(double)b1npts;
b2inc=(b2max-b2min)/(double)b2npts;
alinc=(a1max-a1min)/(double)a1npts;
a2inc=(a2max-a2min)/(double)a2npts;
if (output==1)
printf("alinc=%f\tblinc=%f\ta2inc=%f\tb2inc=%f\n",alinc,blinc,a2inc
      ,b2inc);

/** initialize cosine table **/
if (output==1) printf("Making Cosine table\n");
CT=dvector(-2*(a2npts+a1npts),2*(a2npts+a1npts));
CTsq=dvector(-2*(a2npts+a1npts),2*(a2npts+a1npts));
for (i=-2*(a2npts+a1npts);i<=2*(a2npts+a1npts);i++)
  {
    CT[i]=cos(a2inc*(double)(i));
    CTsq[i]=CT[i]*CT[i];
  }
/** initialize sine table to compute sin(b1) **/
if (output==1) printf("Making Sine table\n");
ST=dvector(0,b1npts-1);
for (i=0;i<=b1npts-1;i++)
  {
    ST[i]=sin(blinc*(double)(i));
  }
if (output==1) printf("Completed Sine table\n");

/**
Compute 2d exchange spectrum in the frequency domain
***/

/**
note on indices :
i is for b2
j is for a1
k is for b1
l is for a2

should integrate over the following ranges:
a1 0 to Pi/2
b1 0 to Pi/2
a2 0 to 2Pi
b2 0 TO Pi/2
***/

```

```

/** next two statements used for an output of the real
time elapsed for each i iteration **/
Tbefore=0;
Tafter=0;
for(i=0;i<=b2npts-1;i++)
{
    sb1_holder=0.00;
    if (output==1) printf("%d) b2 = %f ",i,b2min + ((double)i)*b2inc);
    Tbefore=time(0);
    if (nCorrTimes>1)
    for(ii=1;ii<=nCorrTimes;ii++)
        sb1_holder+=C11_dist[ii][i];
    else
    sb1_holder=C11_dist[1][i];
    for(j=0;j<=alnpts-1;j++)
    {
        for(k=0;k<=blnpts-1;k++)
        {
            omega1=gCSA(CT,CTsq,j,k,sigma,delta,eta)+0.5;
            sb1=ST[k]*sb1_holder;
            for(l=0;l<=a2npts-1;l++)
            {
                omega2=(hCSA(CT,CTsq,l,i,j,k,sigma,delta,eta))+0.5;
                spectrum[(int)omega1][(int)omega2].r+=sb1;
            }
        }
    }
    Tafter=time(0);
    if (output==1) printf(" in %d seconds\n",Tafter-Tbefore);
}

/** symmetrize about the w1=w2 diagonal **/
DCsymmetrize_diag_2d(spectrum,w1npts,w2npts,1);

/** output non-line broadened data to spec_file **/
for(i=1;i<=w1npts;i++)
    for(j=1;j<=w2npts;j++)
        spectrumReal[i][j] = spectrum[i][j].r;

Dnormalize_2d(spectrumReal,w1npts,w2npts,normalization);

if ((output_type==0)|| (output_type==2))
    wr_fld2dD(spectrumReal,w1npts,w2npts,spec_file);
if ((output_type==1)|| (output_type==2))
    wr_expl2d_ascii(spectrumReal,w1npts,w2npts,spec_file);

/** about units - assumes lb units are the inverse of the dwell units
***/

DGaussian_Broadening_Freq_2d(spectrumReal,w1npts,w2npts,1.00/(2.00*sw1),
1.00/(2.00*sw2),lb1,lb2);

/** output data to spec1b file **/
Dnormalize_2d(spectrumReal,w1npts,w2npts,normalization);
if ((output_type==0)|| (output_type==2))
    wr_fld2dD(spectrumReal,w1npts,w2npts,spec1b_file);
if ((output_type==1)|| (output_type==2))
    wr_expl2d_ascii(spectrumReal,w1npts,w2npts,spec1b_file);

```

```

/** free matrices and vectors */
free_dcmatrix(spectrum,1,wlnpts,1);
free_dmatrix(spectrumReal,1,wlnpts,1);
free_dmatrix(C11_dist,1,nCorrTimes,0);
free_dvector(C11_dist_holder,0);
free_dvector(CT,1);
free_dvector(CTsq,1);
}

/**
  Compute the angle dependent nmr frequency for a singly rotated
  CSA.
  */
double gCSA(CT,CTsq,i,j,sigma,delta,eta)
  double *CT,*CTsq;
  int i,j;
  double sigma,delta,eta;
{
  double gtemp;

  gtemp = sigma + delta*((3.0*CTsq[j]-1.00) - eta*(1.00-CTsq[j]))*\
    CT[2*i])/2.00;

  return gtemp;
}

/**
  Compute the angle dependent nmr frequency for a doubly rotated
  CSA.

  Convention -- Uses eq (56) in Wefing, JCP, vol 89, no 3, p 1219-1233.

  a1 is alphaprime - difference
  b1 is betaprime - difference
  a2 is alpha1 - LS 1
  b2 is beta1 - LS 1
  */
/**
  i is a1 --> a2
  j is b1 --> b2
  k is a2 --> a1
  l is b2 --> b1
  */
double hCSA(CT,CTsq,i,j,k,l,sigma,delta,eta)
  double *CT,*CTsq;
  double sigma,delta,eta;
  int i,j,k,l;
{
  double htemp;

  htemp=sigma + delta*(0.75*(1.00-CTsq[j])*(1.00-CTsq[l])*CT[2*i] -\
    3.00*sqrt((1.00-CTsq[j])*(1.00-
  CTsq[l]))*CT[j]*CT[l]*CT[i]+\
    0.25*(3.00*CTsq[j]-1.00)*(3.00*CTsq[l]-1.00)\
    -0.5*eta*\

```

```

        (\
        (1.00-CTsq[j])*\
        (\
        0.25*(1.00+CT[l])*(1.00+CT[l])*CT[2*(i+k)] +\
        0.25*(1.00-CT[l])*(1.00-CT[l])*CT[2*(i-k)]\
        )+\
        2.00*sqrt((1.00-CTsq[j])*(1.00-CTsq[l]))*CT[j]*\
        (\
        0.5*(1.00+CT[l])*CT[i+2*k]-\
        0.5*(1.00-CT[l])*CT[i-2*k]\
        )+\
        0.5*(3.00*CTsq[j]-1.00)*(1.00-CTsq[l])*CT[2*k]\
        )\
        );
    return htemp;
}

/****
  Compute the marginal distribution C(g)|1|1 (same as gamma(g) 1|1)
****/
void C11(C11_dist,b2min,b2max,b2npts,tm,Dr,Lmax,output)
    double *C11_dist;
    double b2min,b2max,tm,Dr;
    int b2npts,Lmax,output;
{
    double Legendre(),psi,ltemp,C11Temp,prevC11_dist;
    double b2,b2inc;
    int i,l,m;

    b2inc=(b2max-b2min)/(double)b2npts;
    b2=b2min;
    for(i=0;i<=b2npts-1;i++)
    {
        C11_dist[i]=0.00;
        for(l=0;l<=Lmax;l++)
        {
            prevC11_dist = C11_dist[i];
            ltemp=(double)l;
            psi=(2.00*ltemp+1.00)*exp(-ltemp*(ltemp+1.00)*Dr*tm);
            C11Temp=0.5*sin(b2)*psi*(Legendre(cos(b2),l)+Legendre(cos(Pi-
b2),l));
            C11_dist[i]+=C11Temp;
        }
        b2+=b2inc;
    }
}

/****
  Compute Legendre polynomials of order l. May crap out at large
  values of l (15-20).
****/
double Legendre(x,l)
    double x;
    int l;
{
    double Legendre_temp[100];

```

```
int m;

Legendre_temp[0]=1.00;
if (l==0) return Legendre_temp[0];
Legendre_temp[1]=x;
if (l==1) return Legendre_temp[1];
for (m=2;m<=l;m++)
    Legendre_temp[m]=((2.00*(double)m-1.00)*x*Legendre_temp[m-1]-\
        ((double)m-1.00)*Legendre_temp[m-2])/((double)m);
return Legendre_temp[l];
}
```

C.2 External Subroutines

The following subroutines are used by `csaexch` but are not specific to that program. They have been collected from my subroutine libraries in order to build a self-contained version of the source code for the simulation. The basic function of each subroutine is contained in the comments.

```
#include "./complex.h"
#include "./memalloc.h"
#include "./csaexchsubs.h"
#include <stdio.h>
#include <math.h>
#define Pi (3.141592654)
#define SWAP(a,b) tempr=(a);(a)=(b);(b)=tempr

/** some subroutines used by csaexch.c **/

/***** I/O SUBROUTINES *****/

/** Write a 1d ascii data file for explorer ***/
/** Array from nmin to nmax ***/
void wr_expl1d_ascii_general(a,nmin,nmax,filenm)

double *a;
int nmin,nmax;
char filenm[];

{
    FILE *outfile_h,*outfile_d;
    char header_file[64],data_file[64];
    int i,j;

    strcpy(header_file,filenm);
    strcpy(data_file,filenm);
    strcat(header_file,".dim");
    strcat(data_file,".asc");

    /* Write the header file for the uniform 1D vector */
    outfile_h = fopen(header_file,"w");
    fprintf(outfile_h,"%d\n",abs(nmax-nmin+1));
    fclose(outfile_h);

    outfile_d = fopen(data_file,"w");
    /* Write the data file in ascii format */
    for(i=nmin;i<=nmax;i++)
        fprintf(outfile_d,"%f\n",a[i]);
    fclose(outfile_d);
}
```

```

/****
 write an avs binary data file (single precision floating point) and
 field using a double precision input
****/
void wr_fld2dD(ain,nrow,ncol,filenm)

double **ain;
int nrow,ncol;
char filenm[];

{
 float **a;
 FILE *outfile_h,*outfile_d;
 char header_file[64],data_file[64];
 int ndim=2,nspace=2,veclen=1,i,j;

 a = matrix(1,nrow,1,ncol);
 DintoF_2d(a,ain,nrow,ncol);
 strcpy(header_file,filenm);
 strcpy(data_file,filenm);
 strcat(header_file,".fld");
 strcat(data_file,".d");

 /* Write the header file for the uniform 2D matrix */
 outfile_h = fopen(header_file,"w");
 fprintf(outfile_h,"# AVS field file\n");
 fprintf(outfile_h,"ndim = %d\n",ndim);
 fprintf(outfile_h,"dim1 = %d\n",ncol);
 fprintf(outfile_h,"dim2 = %d\n",nrow);
 fprintf(outfile_h,"nspace = %d\n",nspace);
 fprintf(outfile_h,"veclen = %d\n",veclen);
 fprintf(outfile_h,"data = float\n");
 fprintf(outfile_h,"field = uniform\n");
 fprintf(outfile_h,"variable 1 file=%s filetype=binary\n",data_file);
 fclose(outfile_h);

 outfile_d = fopen(data_file,"w");
 /* Write the data file in floating point binary format */
 for(i=1;i<=nrow;i++)
   for(j=1;j<=ncol;j++)
     {
      fwrite((char *)&a[i][j],sizeof(float),1,outfile_d);
     }

 fclose(outfile_d);
 free_matrix(a,1,nrow,1);
}

/**** Write a 2d ascii data file for explorer - tab delimited text ****/
void wr_expl2d_ascii(a,nrow,ncol,filenm)

double **a;
int nrow,ncol;
char filenm[];

{
 FILE *outfile_h,*outfile_d;
 char header_file[64],data_file[64];

```

```

int i,j;

strcpy(header_file,filenm);
strcpy(data_file,filenm);
strcat(header_file, ".dim");
strcat(data_file, ".asc");

/* Write the header file for the uniform 2D matrix */
outfile_h = fopen(header_file, "w");
fprintf(outfile_h, "%d\t%d\n", ncol, nrow);
fclose(outfile_h);

outfile_d = fopen(data_file, "w");
/* Write the data file in ascii format */
for(i=1; i<=nrow; i++)
{
    for(j=1; j<=ncol; j++)
    {
        fprintf(outfile_d, "%f\t", a[i][j]);
    }
    fprintf(outfile_d, "\n");
}

fclose(outfile_d);
}

/***** FFT and LINE BROADENING SUBROUTINES *****/

/**
  DGaussian_Broadening_Freq_2D - takes a real spectrum, does an IFFT
  with swapping, performs a 2d gaussian apodization centered about (npx/2
  + 1, npy/2 + 1), unswaps the data, and does a FFT back in to the
  frequency domain.
  ***/

void DGaussian_Broadening_Freq_2d(a, npx, npy, dwx, dwy, lbx, lby)
    double **a;
    int npx, npy;
    double dwx, dwy, lbx, lby;
{
    int i, j;
    dcomplex **atemp, holder;
    double x0, y0;
    atemp = dcmatrix(1, npx, 1, npy);
    for(i=1; i<=npx; i++)
        for(j=1; j<=npy; j++)
        {
            atemp[i][j].r = a[i][j];
            atemp[i][j].i = 0.00;
        }

    dcfft2d(-1, atemp, npx, npy);

    x0 = ((double)npx/2.00)+1.00;
    y0 = ((double)npy/2.00)+1.00;
    DCGaussian_Broadening_2d(atemp, npx, npy, dwx, dwy, lbx, lby, x0, y0);
}

```



```

DCswap2d(atemp, npx, npy);
dcfft2dns(1, atemp, npx, npy);
DCintoD_2d(atemp, a, npx, npy, 'r');
free_dcmatrix(atemp, 1, npx, 1);
}

/** performs a gaussian multiplication on a 2d double precision matrix
    Origin at point (x0,y0) where (1,1) is the first row-column point
    ***/
void DCGaussian_Broadening_2d(a, npx, npy, dwx, dwy, lbx, lby, x0, y0)
{
    dcomplex **a;
    int npx, npy;
    double dwy, dwx, lbx, lby, x0, y0;
    {
        int i, j;
        double tx, ty, dtemp;

        for(i=1; i<=npx; i++)
            for(j=1; j<=npy; j++)
                {
                    tx = ((double)(i) - x0)*dwx;
                    ty = ((double)(j) - y0)*dwy;
                    dtemp = exp((-tx*tx*lbx*lbx - ty*ty*lby*lby)/2.00);
                    a[i][j].r *= dtemp;
                    a[i][j].i *= dtemp;
                }
    }
}

/** noraml 2d fft of complex matrix ***/
void dcfft2d(ii, a, npx, npy)
{
    dcomplex **a;
    int ii, npx, npy;
    {
        int i, j, k, ndim;
        double *atemp;
        unsigned long *nn;

        nn = ulvector(1, 2);
        nn[1] = npx;
        nn[2] = npy;
        ndim=2;
        atemp = dvector(1, 2*npx*np);
        for(i=1; i<=npx; i++)
            for(j=1; j<=npy; j++)
                {
                    atemp[2*(i-1)*npy + 2*j-1]=a[i][j].r;
                    atemp[2*(i-1)*npy + 2*j]=a[i][j].i;
                }
    }
}

/** n-dimensional numerical recipes fft **/

fourn(atemp, nn, ndim, ii);

for(i=1; i<=npx; i++)
    for(j=1; j<=npy; j++)
        {

```

```

        a[i][j] = DComplex(atemp[2*(i-1)*npy + 2*j-1],atemp[2*(i-1)*npy +
2*j]);
    }
    DCswap2d(a,npx,npy);
    free_dvector(atemp,1);
    free_ulvector(nn,1);
}

```

```

/** noraml 2d fft of complex matrix -- no quadrant swap**/

```

```

void dcfft2dns(ii,a,npx,npy)

```

```

dcomplex **a;

```

```

int ii,npx,npy;

```

```

{
    int i,j,k,ndim;
    double *atemp;
    unsigned long *nn;

```

```

    nn = ulvector(1,2);

```

```

    nn[1] = npx;

```

```

    nn[2] = npy;

```

```

    ndim=2;

```

```

    atemp = dvector(1,2*npx*npy);

```

```

    for(i=1;i<=npx;i++)

```

```

        for(j=1;j<=npy;j++)

```

```

            {
                atemp[2*(i-1)*npy + 2*j-1]=a[i][j].r;

```

```

                atemp[2*(i-1)*npy + 2*j]=a[i][j].i;
            }

```

```

/** n-dimensional numerical recipes fft **/

```

```

    founn(atemp,nn,ndim,ii);

```

```

    for(i=1;i<=npx;i++)

```

```

        for(j=1;j<=npy;j++)

```

```

            {
                a[i][j] = DComplex(atemp[2*(i-1)*npy + 2*j-1],atemp[2*(i-1)*npy +
2*j]);
            }

```

```

    free_dvector(atemp,1);

```

```

    free_ulvector(nn,1);

```

```

}

```

```

/*****
**

```

```

void founn() - numerical recipes n-dimensional complex fft

```

```

Replaces data by its ndim-dimensional discrete fourier transform,
if isign is input as 1. Inverse FFT is isign is -1.

```

```

*****
*/

```

```

void founn(datain,nn,ndim,isign)

```

```

double *datain;

```

```

unsigned long *nn;

```

```

int ndim,isign;

```

```

{

```

```

    int idim;

```

```

unsigned long i1,i2,i3,i2rev,i3rev,ip1,ip2,ip3,ifp1,ifp2;
unsigned long ibit,k1,k2,n,nprev,nrem,ntot;
double tempi,temp;
double theta,wi,wpi,wpr,wr,wtemp;

for(ntot=1,idim=1;idim<=ndim;idim++)
    ntot *= nn[idim];
nprev=1;
for(idim=ndim;idim>=1;idim--)
    {
        n = nn[idim];
        nrem = ntot/(n*nprev);
        ip1=nprev << 1;
        ip2=ip1*n;
        ip3=ip2*nrem;
        i2rev=1;
        for(i2=1;i2<=ip2;i2+=ip1)
            {
                if (i2 < i2rev)
                    {
                        for(i1=i2;i1<=i2+ip1-2;i1+=2)
                            {
                                for(i3=i1;i3<=ip3;i3+=ip2)
                                    {
                                        i3rev=i2rev+i3-i2;
                                        SWAP(datain[i3],datain[i3rev]);
                                        SWAP(datain[i3+1],datain[i3rev+1]);
                                    }
                                }
                            }
                    }
                ibit=ip2>>1;
                while(ibat>=ip1&&ibit>=i2rev)
                    {
                        i2rev -= ibit;
                        ibit >>=1;
                    }
                i2rev += ibit;
            }
        ifp1=ip1;
        while(ifp1<ip2)
            {
                ifp2=ifp1<<1;
                theta=sign*6.28318530717959/(ifp2/ip1);
                wtemp=sin(0.5*theta);
                wpr=-2.0*wtemp*wtemp;
                wpi=sin(theta);
                wr=1.0;
                wi=0.0;
                for(i3=1;i3<=ifp1;i3+=ip1)
                    {
                        for(i1=i3;i1<=i3+ip1-2;i1+=2)
                            {
                                for(i2=i1;i2<=ip3;i2+=ifp2)
                                    {
                                        k1=i2;
                                        k2=k1+ifp1;
                                        tempr=wr*datain[k2]-wi*datain[k2+1];
                                        tempi=wr*datain[k2+1]+wi*datain[k2];
                                    }
                                }
                            }
                    }
            }
    }

```

```

        datain[k2]=datain[k1]-tempr;
        datain[k2+1]=datain[k1+1]-tempi;
        datain[k1] += tempr;
        datain[k1+1] += tempi;
    }
}
wr=(wtemp=wr)*wpr-wi*wpi+wr;
wi=wi*wpr+wtemp*wpi+wi;
}
ifp1=ifp2;
}
nprev *= n;
}
}

```

/** quadrant swapping routine for use with fft routines **/

```
void DCswap2d(a,npx,ncpy)
```

```
    dcomplex **a;
```

```
    int npx,ncpy;
```

```

{
    int i,j,npx2,ncpy2;
    dcomplex holder;

    npx2=(int)(npx/2);
    ncpy2=(int)(ncpy/2);
    for(i=1;i<=npx2;i++)
        for(j=1;j<=ncpy2;j++)
        {
            holder = a[i][j];
            a[i][j] = a[i+npx2][j+ncpy2];
            a[i+npx2][j+ncpy2] = holder;
            holder = a[i+npx2][j];
            a[i+npx2][j] = a[i][j+ncpy2];
            a[i][j+ncpy2] = holder;
        }
}

```

/****** MATRIX MANIPULATION SUBROUTINES

******/

```

/*****
DCsymmetrize_diag_2d(a,npx,ncpy,direction) -

```

Symmetrizes a double matrix about the diagonal. If direction is 0 then the anti-diagonal is used (1,n), (2,n-1) etc... If direction is 1 then the true diagonal is used (1,1), (2,2) etc...

*****/

```
void DCsymmetrize_diag_2d(a,npx,ncpy,direction)
```

```
    dcomplex **a;
```

```
    int npx,ncpy,direction;
```

```

{
    int i,j;
```

```
    if (direction==0)
```

```
        dcrot90_sq(a,npx,ncpy);
```

```

for(i=1;i<=npx;i++)
  for(j=i;j<=npy;j++)
    {
      if (i==j)
        a[i][j] = DCadd(a[i][j],a[i][j]);
      else
        {
          a[i][j] = DCadd(a[i][j],a[j][i]);
          a[j][i] = a[i][j];
        }
    }
if (direction==0)
  dcrot90_sq(a,npx,npy);
}

/*
Returns a 90 degree rotation of a. For square matrices.
*/
void dcrot90_sq(a,npx,npy)
  dcomplex **a;
  int npx,npy;
{
  int i,j;
  dcomplex **a_holder;

  a_holder = dcmatrix(1,npx,1,npy);
  for(i=1;i<=npx;i++)
    for(j=1;j<=npy;j++)
      a_holder[i][j] = a[i][j];
  free_dcmatrix(a,1,npx,1);
  a = dcmatrix(1,npy,1,npx);
  for(i=1;i<=npx;i++)
    for(j=1;j<=npy;j++)
      a[npy-j+1][i] = a_holder[i][j];
  free_dcmatrix(a_holder,1,npx,1);
}

/**/ normalize a 2d double precision matrix to a maximum value of norm.
***/
void Dnormalize_2d(a,npx,npy,norm)
  double **a;
  int npx,npy;
  double norm;
{
  int i,j;
  double max;

  max=0.00;
  for(i=1;i<=npx;i++)
    for(j=1;j<=npy;j++)
      {
        if (fabs(a[i][j])>=max) max=fabs(a[i][j]);
      }
  for(i=1;i<=npx;i++)
    for(j=1;j<=npy;j++)
      {

```

```

        a[i][j]=a[i][j]*norm/max;
    }
}

/** Change a double precision 2d matrix to a single precision floating
point matrix. */
void DintoF_2d(ar,ad,npx,npj)
    double **ad;
    float **ar;
{
    int i,j;

    for(i=1;i<=npx;i++)
        for(j=1;j<=npj;j++)
            ar[i][j]=(float)ad[i][j];
}

/****
    put real or imaginary part of a 2d dcomplex matrix into
    a double precision floating point matrix.
****/
void DCintoD_2d(adc,ad,npx,npj,real_imag)
    dcomplex **adc;
    double **ad;
    int npx,npj;
    char real_imag;
{
    int k,l;

    if (real_imag=='i')
    {
        for(k=1;k<=npx;k++)
            for(l=1;l<=npj;l++)
            {
                ad[k][l]=adc[k][l].i;
            }
    }
    else if (real_imag=='r')
    {
        for(k=1;k<=npx;k++)
            for(l=1;l<=npj;l++)
            {
                ad[k][l]=adc[k][l].r;
            }
    }
    else if (real_imag=='m')
    {
        for(k=1;k<=npx;k++)
            for(l=1;l<=npj;l++)
            {
                ad[k][l]=DCabs(adc[k][l]);
            }
    }
}

```

C.3 Sample Parameter File

This parameter file is that used by "csaexch". "csaexch" reads each line as a string up until the first whitespace. Each number or string separated by whitespaces after the first whitespace is then read into the appropriate variable in the simulation. Each line gives the simulation the following information:

1) CSA parameters σ , δ and η with σ and δ in units of Hertz.

2-5) Limits of integration over the angle variables in Eq. (5.48). $a1$ and $b1$ correspond to α_1 and β_1 , and $a2$ and $b2$ correspond to α' and β' in Eq. (5.48). The last number in each line is the number of points sampled in the corresponding integration interval. For equal sampling by angle, $a1npts$, $b1npts$ and $b2npts$ should be the same with $a2npts$ four times greater.

6) Spectral width in Hertz (frequency range is $2*sw$), number of points and amount of Gaussian line-broadening in Hertz for both frequency dimensions. All of these numbers should appear on the same line.

7) Name of the spectrum file which contains the non-Gaussian line broadened spectrum.

8) Name of the spectrum file which contains the Gaussian line broadened spectrum.

9) For a binary single-precision floating point file *output* should be 0. For ASCII tab-delimited text, *output* should be 1. To get both, set *output* equal to 2. The binary file will be output as the file name plus the extension ".d". The ASCII file will have the extension ".asc".

10) The maximum amplitude point in the spectrum will have the value of *normalization*. To do a volume normalization, another program must be run on the spectrum file.

11) If *output* is 0, the program will output no information to the computer monitor or standard output. With *output* equal to 1, the program will display its progress to the

standard output. When running the simulation in the background, one should set *output* equal to 0.

12) Number of correlation times to be represented by the spectrum. For the simulation of two particle sizes, *nCorrTimes* should be 2.

13.i) Relative population, mixing time (t_m in seconds), rotational diffusion coefficient (D' in Hertz), and summation limit of Eq. (5.49) for each site i . For smaller values of $D't_m$, $Lmax$ should be made larger. The simulation program will output a warning if the sum given by Eq. (5.49) does not converge sufficiently.

```

1) sigma,delta,eta=          -468.8    -6796.9    0.448
2) a1min,a1max,a1npts(0,Pi/2)=      0  1.5707963    32
3) a2min,a2max,a2npts(0,2Pi)=       0  6.2831853   128
4) b1min,b1max,b1npts(0,Pi/2)=      0  1.5707963    32
5) b2min,b2max,b2npts(0,Pi/2)=      0  1.5707963    32
6) sw1,w1npts,lb1,sw2,w2npts,lb2= 15000      128    2000   15000
                                128      2000
7) spec_file=                  ./spec1b
8) spec1b_file=                 ./spec1b1b
9) output:0avs,1ascii,2both=     0
10) normalization=              1
11) output(1/0)=                 1
12) nCorrTimes=                  2
13.1) population,tm,Dr,Lmax=     0.5    0.011    40    100
13.2) population,tm,Dr,Lmax=     0.5    0.011     2    100

```


Bibliography

- (1) P. A. M. Dirac, *Quantum Mechanics*, 4th ed., Oxford Univ. Press, London, 1958.
- (2) J. J. Sakurai, *Modern Quantum Mechanics*, Addison-Wesley, Reading, MA, 1985.
- (3) P. T. Callaghan, *Principles of Nuclear Magnetic Resonance Microscopy*, Clarendon Press, Oxford, 1991.
- (4) P. Mansfield and P. G. Morris, *NMR Imaging in Biomedicine*, Academic Press, New York, 1982.
- (5) A. Abragam, *Principles of Nuclear Magnetism*, Clarendon Press, Oxford, 1961.
- (6) R. N. Bracewell, *The Fourier Transform and its Applications*, 2nd ed., McGraw Hill, New York, 1978.
- (7) D. B. Twieg, J. Katz and R. M. Peshock, *Magn. Reson. Med.* **5**, 32 (1987).
- (8) H. Geen, S. Wimperis and R. Freeman, *J. Magn. Reson.* **85**, 620 (1989).
- (9) L. Emsley and G. Bodenhausen, *Chem. Phys. Lett.* **165**, 469 (1990).
- (10) D. I. Hoult, *J. Magn. Reson.* **35**, 69 (1979).
- (11) M. S. Silver, R. I. Joseph and D. I. Hoult, *J. Magn. Reson.* **59**, 347 (1984).
- (12) C. B. Ahn, J. H. Kim and Z. H. Cho, *IEEE Tans. Med. Imaging* **5**, 2 (1986).
- (13) P. C. Lauterbur and C. M. Lai, *IEEE Trans. Nucl. Sci.* **27**, 1227 (1980).
- (14) A. Khintchin, *Math. Ann.* **109**, 604 (1934).
- (15) N. Wiener, *The Fourier Integral and Certain of Its Applications*, Dover, New York, 1958.
- (16) D. I. Hoult and R. E. Richards, *J. Magn. Reson.* **24**, 71 (1976).
- (17) P. T. Callaghan and C. D. Eccles, *J. Magn. Reson.* **71**, 426 (1987).
- (18) A. L. Patterson, *Phys. Rev.* **46**, 372 (1934).

- (19) P. Mansfield, P. K. Grannell, A. N. Garroway and D. C. Stalker, Proc. Coll. Ampere (*Krakow*) 1, 16 (1973).
- (20) P. Mansfield and P. K. Grannell, J. Phys. C: Sol. St. Phys. **6**, L422 (1973).
- (21) P. Mansfield, P. K. Grannell and A. A. Maudsley, Proc. Coll. Ampere (*Nottingham*) 2, 431 (1974).
- (22) P. Mansfield and P. K. Grannell, Phys. Rev. B **12**, 3618 (1975).
- (23) P. Mansfield, Contemp. Phys. **17**, 553 (1976).
- (24) H. Y. Carr and E. M. Purcell, Phys. Rev. **94**, 630 (1954).
- (25) E. L. Hahn, Phys. Rev. **80**, 580 (1950).
- (26) J. E. Tanner and E. O. Stejskal, J. Phys. Chem. **49**, 1768 (1968).
- (27) E. O. Stejskal, J. Chem. Phys. **43**, 3597 (1965).
- (28) J. Kärger and W. Heink, J. Magn. Reson. **51**, 1 (1983).
- (29) D. G. Cory and A. N. Garroway, Magn. Reson. Med. **14**, 435 (1990).
- (30) L. H. Schwartz and J. B. Cohen, *Diffraction from Materials*, 2nd ed., Springer-Verlag, Berlin, 1987.
- (31) P. T. Callaghan, D. MacGowan, K. J. Packer and F. O. Zelaya, J. Magn. Reson. **90**, 177 (1990).
- (32) P. T. Callaghan, A. Coy, D. MacGowan and K. J. Packer, J. Mol. Liq. **54**, 239 (1992).
- (33) P. T. Callaghan, A. Coy, T. P. J. Halpin, D. MacGowan, K. J. Packer and F. O. Zelaya, J. Chem. Phys. **97**, 651 (1992).
- (34) P. T. Callaghan, A. Coy, D. McGowan, K. J. Packer and F. O. Zelaya, Nature **351**, 467 (1991).
- (35) R. M. Cotts, Nature **351**, 443 (1991).
- (36) G. C. Chingas, L. Frydman, G. A. Barrall and J. S. Harwood In *Magnetic Resonance Microscopy : Methods and Applications in Materials Science*,

Agriculture and Biomedicine, B. Blümich and W. Kuhn, Ed., VCH, Weinheim, 1992.

- (37) G. A. Barrall, L. Frydman and G. C. Chingas, *Science* **255**, 714 (1992).
- (38) *Scattering Techniques Applied to Supramolecular and Nonequilibrium Systems*; S. H. Chen, B. Chu and R. Nossal, Ed., Plenum Press, New York, 1980.
- (39) J. E. Tanner, *Rev. Sci. Instrum.* **36**, 1086 (1965).
- (40) I. Zupancic and J. Pirs, *J. Phys. E* **9**, 79 (1976).
- (41) D. S. Webster and K. H. Marsden, *Rev. Sci. Instrum.* **45**, 1232 (1974).
- (42) W. A. Edelstein, J. M. S. Hutchison, G. Johnson and T. Redpath, *Phys. Med. Biol.* **25**, 751 (1980).
- (43) L. D. Landau and E. M. Lifshitz, *The Classical Theory of Fields*, Addison-Wesley, New York, 1962.
- (44) L. M. Smith and D. R. Keefer, *J. Quant. Spectrosc. Radiat. Transfer* **39**, 367 (1988).
- (45) R. N. Bracewell, *Aust. J. Phys.* **9**, 198 (1956).
- (46) M. J. Cree and P. J. Bones, *Computers Math. Applic.* **26**, 1 (1993).
- (47) A. D. Chave, *Geophysics* **48**, 1671 (1983).
- (48) N. B. Christensen, *Geophys. Prosp.* **38**, 545 (1990).
- (49) W. L. Anderson, *ACM Trans. Math. Softw.* **8**, 344 (1982).
- (50) B. W. Suter, *Quart. Appl. Math.* **49**, 267 (1991).
- (51) P. K. Murphy and N. C. Gallagher, *J. Opt. Soc. Am. A* **73**, 1130 (1983).
- (52) E. W. Hansen, *IEEE Trans. Acoust., Speech Signal Proc.* **ASSP-33**, 666 (1985).
- (53) S. M. Candell, *Comp. Phys. Comm.* **23**, 342 (1981).
- (54) G. N. Minerbo and M. E. Levy, *SIAM J. Numer. Anal.* **6**, 598 (1969).
- (55) R. S. Anderssen, *J. Inst. Maths Applics* **17**, 329 (1976).
- (56) E. W. Hansen and P.-L. Law, *J. Opt. Soc. Am. A* **2**, 510 (1985).
- (57) L. M. Smith, *IEEE Trans. Inf. Theory* **34**, 158 (1988).

- (58) P. D. Majors and A. Caprihan, *J. Magn. Reson.* **94**, 225 (1991).
- (59) L. C. Graton and H. J. Fraser, *J. Geol.* **43**, 785 (1935).
- (60) P. C. Lauterbur, *Nature* **242**, 190 (1973).
- (61) A. Kumar, D. Welti and R. R. Ernst, *J. Magn. Reson.* **18**, 69 (1974).
- (62) D. I. Hoult, *J. Magn. Reson.* **33**, 183 (1979).
- (63) M. J. E. Golay, *Rev. Sci. Instrum.* **29**, 313 (1958).
- (64) G. A. Barrall, Y. K. Lee and G. C. Chingas, *J. Magn. Reson. A* **106**, 132 (1994).
- (65) D. Boudot, D. Canet and J. Brondeau, *J. Magn. Reson.* **87**, 385 (1990).
- (66) D. I. Hoult, *Progr. Nucl. Magn. Reson. Spectrosc.* **12**, 41 (1978).
- (67) S. J. Cox and P. Styles, *J. Magn. Reson.* **40**, 209 (1980).
- (68) M. J. Blackledge, B. Rajagopalan, R. D. Oberhaensli, N. M. Bolas, P. Styles and G. K. Radda, *Proc. Natl. Acad. Sci. U.S.A.* **84**, 4283 (1984).
- (69) J. P. Boehmer, K. R. Metz, M. Jintong and R. W. Briggs, *Magn. Reson. Med.* **16**, 335 (1990).
- (70) C. S. Yannoni and R. A. Wind, *J. Magn. Reson.* **38**, 493 (1980).
- (71) C. S. Yannoni and R. D. Kendrick, *J. Chem. Phys.* **74**, 747 (1981).
- (72) J. D. Jackson, *Classical Electrodynamics*, John Wiley & Sons, New York, 1962.
- (73) D. J. Griffiths, *Introduction to Electrodynamics*, 2nd ed., Prentice-Hall, Englewood Cliffs, NJ, 1989.
- (74) W. Sinnema, *Electronic Transmission Technology*, 2nd ed., Prentice Hall, Englewood Cliffs, 1988.
- (75) R. A. Chipman, *Schaum's Outline of Theory and Problems of Transmission Lines*, McGraw-Hill, New York, 1968.
- (76) E. Fukushima and S. B. W. Roeder, *Experimental Pulse NMR : A Nuts and Bolts Approach*, Addison-Wesley, Reading, 1981.
- (77) J. Bear, *Dynamics of Fluids in Porous Media*, Dover, New York, 1972.

- (78) F. A. L. Dullien, *Porous media : fluid transport and pore structure*, 2nd ed., Academic Press, San Diego, 1992.
- (79) R. A. Greenkorn, *Flow Phenomena in Porous Media*, Marcel Dekker, New York, 1983.
- (80) R. Lenormand, *J. Phys.: Condens. Matter* **2**, SA79 (1990).
- (81) N.-W. Han, J. Bhakta and R. G. Carbonell, *A.I.Ch.E. Journal* **31**, 277 (1985).
- (82) G. Guillot, A. Trokiner, L. Darrasse, A. Dupas, F. Ferdossi, G. Kassab, J. P. Hulin, P. Rigord and H. Saint-Jalmes, *Magn. Reson. Imaging* **9**, 821 (1991).
- (83) J. L. A. Williams, G. Maddinelli, D. G. Taylor, P. Enwere and J. S. Archer, *Magn. Reson. Imaging* **9**, 869 (1991).
- (84) P. Mansfield, R. Bowtell, S. Blackband and D. N. Guilfoyle, *Magn. Reson. Imaging* **10**, 741 (1992).
- (85) C. Chardaire-Rivière and J. C. Roussel, *Magn. Reson. Imaging* **9**, 827 (1991).
- (86) S. Chen, K.-H. Kim, F. Qin and A. T. Watson, *Magn. Reson. Imaging* **10**, 815 (1992).
- (87) S. Chen, F. Qin, K.-H. Kim and A. T. Watson, *A.I.Ch.E. Journal* **39**, 925 (1993).
- (88) G. J. Nesbitt, T. W. Fens, J. S. van den Brink and N. Roberts In *Magnetic Resonance Microscopy : Methods and Applications in Materials Science, Agriculture and Biomedicine*, B. Blümich and W. Kuhn, Ed., VCH, Weinheim, 1992.
- (89) G. J. Nesbitt, A. DeGroot, T. W. Fens and J. H. M. Bonnie, *Magn. Reson. Imaging* **9**, 779 (1991).
- (90) D. N. Guilfoyle and P. Mansfield, *J. Magn. Reson.* **97**, 342 (1992).
- (91) T. J. Schaffsma, H. Van As, W. D. Palstra, J. E. M. Snaar and P. A. de Jager, *Magn. Reson. Imaging* **10**, 827 (1992).

- (92) P. Callaghan, D. MacGowan, K. J. Packer and F. O. Zelaya, *Magn. Reson. Imaging* **9**, 663 (1991).
- (93) J. Kärgler, H. Pfeiffer and W. Heink, *Adv. Magn. Reson.* **12**, 1 (1988).
- (94) P. Stilbs, *Progr. Nucl. Magn. Reson. Spectrosc.* **19**, 1 (1987).
- (95) Y. Xia and P. T. Callaghan, *Macromolecules* **24**, 4777 (1991).
- (96) P. T. Callaghan, C. D. Eccles and Y. Xia, *J. Phys. E* **21**, 820 (1988).
- (97) P. T. Callaghan and Y. Xia, *J. Magn. Reson.* **91**, 326 (1991).
- (98) L. Frydman, J. S. Harwood, D. N. Garnier and G. C. Chingas, *J. Magn. Reson. A* **101**, 240 (1993).
- (99) L. Li and C. H. Sotak, *J. Magn. Reson.* **92**, 411 (1991).
- (100) K. J. Packer, C. Rees and D. J. Tomlinson, *Mol. Phys.* **18**, 421 (1970).
- (101) R. Tycko, H. M. Cho, E. Schneider and A. Pines, *J. Magn. Reson.* **61**, 90 (1985).
- (102) A. J. Shaka, S. P. Rucker and A. Pines, *J. Magn. Reson.* **77**, 606 (1988).
- (103) A. A. Maudsley, *J. Magn. Reson.* **69**, 488 (1986).
- (104) T. Gullion, D. B. Baker and M. S. Conradi, *J. Magn. Reson.* **89**, 479 (1990).
- (105) R. G. Carbonell and S. Whitaker, *Chem. Eng. Sci.* **38**, 1795 (1983).
- (106) S. Whitaker, *A.I.Ch.E. Journal* **18**, 361 (1972).
- (107) H. Rouse, *Elementary Mechanics of Fluids*, Dover, New York, 1946.
- (108) J. D. Seymour, M. J.E., K. L. McCarthy, R. L. Powell and M. J. McCarthy, *J. Texture Stud.* **26**, 89 (1995).
- (109) R. B. Bird, R. C. Armstrong and O. Hassager, *Dynamics of Polymeric Liquids*, Wiley, New York, 1977, Vol. 1.
- (110) T.-Q. Li, J. D. Seymour, R. L. Powell, M. J. McCarthy, K. L. McCarthy and L. Ödberg, *A.I.Ch.E. Journal* **40**, 1408 (1994).
- (111) J. D. Seymour, J. E. Maneval, K. L. McCarthy, M. J. McCarthy and R. L. Powell, *Phys. Fluids A - Fluid Dyn.* **5**, 3010 (1993).

- (112) C. Van den Brock, *Physica A* **168**, 677 (1990).
- (113) E. N. Ivanov, *Sov. Phys. JETP* **18**, 1041 (1963).
- (114) D. L. Favro, *Phys. Rev.* **119**, 53 (1960).
- (115) R. Piazza and V. Degiorgio, *Phys. Rev. B* **42**, 4885 (1990).
- (116) R. Piazza and V. Degiorgio, *Physica A* **182**, 576 (1992).
- (117) *Dynamic Light Scattering: Applications of Photon Correlation Spectroscopy*; R. Pecora, Ed., Plenum, New York, 1985.
- (118) C. Schmidt, B. Blümich and H. W. Spiess, *J. Magn. Reson.* **79**, 262 (1988).
- (119) K. Schmidt-Rohr and H. W. Spiess, *Multidimensional Solid-State NMR and Polymers*, Academic Press Inc., San Diego, 1994.
- (120) S. Wefing and H. W. Spiess, *J. Chem. Phys.* **89**, 1219 (1988).
- (121) S. Wefing, S. Kaufmann and H. W. Spiess, *J. Chem. Phys.* **89**, 1234 (1988).
- (122) U. Haebleren, *High Resolution NMR in Solids: Selective Averaging*, Academic Press, New York, 1976.
- (123) M. E. Rose, *Elementary Theory of Angular Momentum*, 1st ed., John Wiley & Sons, Inc., New York, 1957.
- (124) C. P. Slichter, *Principles of Magnetic Resonance*, 3rd ed., Springer-Verlag, New York, 1990.
- (125) J. Jeener, B. H. Meier, P. Bachmann and R. R. Ernst, *J. Chem. Phys.* **71**, 4526 (1979).
- (126) P. J. W. Debye, *Polar Molecules*, The Chemical Catalog Company, New York, 1929.
- (127) R. B. Jones, *Physica A* **150**, 339 (1988).
- (128) B. J. Berne and R. Pecora, *Dynamic Light Scattering*, Wiley, New York, 1976.
- (129) R. B. Jones, *Physica A* **157**, 752 (1989).
- (130) K. Schmidt-Rohr and H. W. Spiess, *Phys. Rev. Lett.* **66**, 3020 (1991).
- (131) F. Perrin, *J. de Phys. et Rad.* **5**, 497 (1934).

- (132) F. Perrin, *J. de Phys. et Rad.* **7**, 1 (1936).
- (133) M. Hasegawa, S. Ohyabu, T. Ueda and M. Yamaguchi, *J. Labelled. Compd. Radiopharm.* **18**, 643 (1981).
- (134) K. Schmidt-Rohr, A. S. Kulik, H. W. Beckham, A. Ohlemacher, U. Pawelzik, C. Boeffel and H. W. Spiess, *Macromolecules* **27**, 4733 (1994).
- (135) D. J. States, R. A. Haberkorn and D. J. Ruben, *J. Magn. Reson.* **48**, 286 (1982).
- (136) Y. K. Lee Doctoral Thesis, University of California at Berkeley, 1994.
- (137) F. Fujara, S. Wefing and H. W. Spiess, *J. Chem. Phys.* **84**, 4579 (1986).
- (138) W. H. Press, *Numerical Recipes in C : The Art of Scientific Computing*, Cambridge University Press, Cambridge, 1988.

LAWRENCE BERKELEY LABORATORY
UNIVERSITY OF CALIFORNIA
TECHNICAL INFORMATION DEPARTMENT
BERKELEY, CALIFORNIA 94720